Layered intrusions: Fundamentals, novel observations and concepts, and controversial issues

Rais M Latypov, O Namur, Y Bai, S J Barnes, Syu Chistyakova, M B Holness, Giada Iacono-Marziano, W a J Kruger, B O'Driscoll, W D Smith, et al.

Invited Review

Layered intrusions: Fundamentals, novel observations and concepts, and controversial issues

R.M. Latypov [a,*], O. Namur [b], Y. Bai [c], S.J. Barnes [d], SYu Chistyakova [a], M.B. Holness [e], G. Iacono-Marziano [f], W.A.J. Kruger [a], B. O'Driscoll [g], W.D. Smith [h], V.J. Virtanen [i], C.Y. Wang [j], C.-M. Xing [j], B. Charlier [k]

[a] *University of the Witwatersrand, Johannesburg, South Africa* [b] *KU Leuven, 3001 Leuven, Belgium*
[c] *Institute of Geology and Geophysics, Chinese Academy of Sciences, Beijing, China* [d] *CSIRO Mineral Resources, Kensington, Perth, WA, Australia*
[e] *University of Cambridge, Cambridge CB2 3EQ, UK* [f] *CNRS-Universit´e d'Orl´eans-BRGM, Orl´eans Cedex 2, France*
[g] *The University of Ottawa, Ottawa, Canada* [h] *Carleton University, Ottawa, Canada* [i] *University of Helsinki, Helsinki, Finland*
[j] *Guangzhou Institute of Geochemistry, Chinese Academy of Sciences, Guangzhou, China* [k] *University of Liege, Belgium*

ABSTRACT

Layered intrusions are fossilized natural laboratories that historically have constrained many fundamental principles of igneous petrology. Layered intrusions are typically stratiform, usually sill-like bodies of cumulate rocks, at least a few hundred metres to as much as 10 km thick, characterized by the presence of a variety of different types of layering over a range of length scales. They are the solid record of crystallization, differentiation and solidification processes of mainly basaltic magmas. The importance of layered intrusions also lies in hosting a significant proportion of the world's known reserves and resources of important critical metals: particularly, the majority of the global resource of platinum-group elements (PGE), chromium (Cr) and vanadium (V) and also very large resources of nickel (Ni), copper (Cu) and cobalt (Co). This paper summarizes the progress that has been made in the study of layered intrusions during the last three decades. The progress is marked by a number of novel observations from layered intrusions. Among them are: (1) draping of igneous layering over a few-km-high sloping step in the chamber floor; (2) development of igneous layering on the overturned to undercutting portions of a chamber floor; (3) magmatic karstification of the floor cumulates, (4) existence of threedimensional framework of crystals in (oxide) cumulates; (5) systematic variations in dihedral angles between touching grains, and other microtextural features; (6) Cr-rich structures at the base of magnetitite layers; (7) coexistence of melt inclusions of contrasting composition in minerals; (8) thermal and chemical histories recorded by plagioclase; (9) textural and chemical features of minerals revealed by X-ray microscopy, (10) intrusion-scale to mineral-scale isotopic heterogeneity; (11) out-of-sequence zircon ages; and (12) skeletal/dendritic growth of minerals revealed by minor element zonation. The progress is also evident from development of several new concepts and refinement of some established ones. These include: (1) time and length scales in layered intrusion processes, (2) catastrophically fast growth of magma chambers, (3) out-of-sequence emplacement in layered intrusions, (4) large-scale slumping and mineral sorting in layered intrusions, (5) production of monomineralic cumulates from single phase-saturated melts, (6) origin of non-cotectic cumulate by in situ growth, (7) the arrival of new phases on the liquidus, (8) inward propagation of solidification fronts, (9) mushy and hard chamber floor, (10) absence of roof sequences due to their disruption, (11) basal reversals and chilled margins, (12) adcumulus growth theory, (13) compositionally stratified magma chambers, (14) melt-sediment interactions during magma chamber growth, (15) lateral reactive infiltration in a crystal mush, (16) reactions involving conjugate immiscible liquids in crystal mushes, and (17) constraints on subsolidus processes from non-traditional Fe-Mg-Cr stableisotopes. Finally, we show that the major controversies regarding layered intrusions currently revolve around whether: (a) the microstructure of igneous rocks are primary or secondary and (b) compaction in layered intrusions is pervasive or non-existent (c) large, long-lived and entirely-molten magma chambers exist or not. The review shows that layered intrusions provide ground-truth information on the processes of magma crystallization, differentiation, and solidification in crustal chambers as well as on mechanisms of ore-forming elements concentration into economically viable mineral deposits. We propose a few lines for future research that may potentially raise igneous petrology to a new level of understanding of the processes that govern the evolution of terrestrial magmatic systems.

1. Introduction

Conventionally, layered mafic intrusions have been regarded as fossil magma chambers since their recognition as a distinct category of igneous rock body in the 1930s by Wager and co-workers (e.g., Wager and Deer, 1939). They have been studied intensively ever since as natural laboratories for examining such fundamental igneous processes as fractional crystallization; crystal nucleation and growth; major and trace element geochemistry of mafic magmas; concentration of platinum group elements, Cr, V and Ti to ore grades; liquid immiscibility; and a range of other related processes. Hence, while relatively rare in the geological record, layered intrusions occupy a central place in the history of igneous petrology and geochemistry.

The cumulate rocks of which layered intrusions are mainly composed were initially regarded as having formed almost entirely by sedimentation of crystals from relatively large bodies of crystal-poor magma. This view was strongly influenced by the meticulous documentation by Wager, Deer, Brown, Irvine, Morse and others (Wager and Brown, 1968; Wager and Deer, 1939; Wager et al., 1960; Irvine, 1970a, 1970b, 1980a, 1980b; Morse, 1969, 1979) of sedimentary-like structures such as modal grading of layers from ultramafic to plagioclase-rich, sedimentary trough layering and size-graded bedding. The gravity-accumulation paradigm remained unchallenged until the late 1970s as evidence emerged of features incompatible with this universal origin, such as layering on steep walls and overhanging roofs of intrusions, density relationships of plagioclase and Fe-rich magma and detailed textural features of cumulates (Donaldson, 1974; Campbell, 1978; Campbell et al., 1978; McBirney and Noyes, 1979). This led to the suggestion that, at least, some of the features of layered intrusion cumulates argued to have been produced by crystal accumulation via sedimentation were produced by in situ crystal nucleation and growth from the convecting bulk magma. Complicating the picture further are hypotheses that some features of igneous layering are not primary crystallization features at all, but rather are due to post-cumulus replacement and wholesale recrystallization (e.g., McBirney, 1987; Boudreau, 2016, 2019). The argument about the relative role of igneous sedimentation, in situ crystallization and post-cumulus recrystallization continues to this day and informs much of this contribution.

In recent years, the paradigm of layered intrusions as fossil magma chambers has come under attack, from two directions. One of these, based on high-precision U–Pb geochronology, holds that cumulate sequences such as those of the Bushveld and Stillwater Complexes were not deposited sequentially from the bottom up, a contention discussed in detail later in this contribution, but rather as sequential out-of-sequence injections of crystal-rich magma (B´edard et al., 1988; Mungall et al., 2016; Wall et al., 2018; Scoates et al., 2021). The second holds that layered intrusions represent bodies of crystal-rich mush infiltrated by upward percolating magmas, and that magma differentiation proceeds by reaction between percolating magmas and the crystal component of the mush (e.g., Cashman et al., 2017). This view has been largely driven from the point of view of volcanologists studying arc magmatism, where geophysical observations have consistently failed to locate large bodies of crystal-poor magma beneath active volcanoes, and also by mantle and ophiolite petrologists who regard what layered intrusion petrologists call orthocumulate textures as being evidence of magmatic metasomatism.

The "mush column" interpretation is likewise discussed in detail in what follows. This point of contention reduces to the question of whether layered intrusions develop primarily as large thickness of porous crystal mushes, or as accreting piles of nearly solid rock analogous to hardgrounds in chemical sediments (e.g., Latypov et al., 2020b, 2022a, 2022b). This question is at the heart of igneous petrology and is covered in this paper.
In the sections that follow, we address the fundamental observational basis of layered intrusion petrology, starting at the broadest scale and moving down to petrological, petrographic and mineralogical details. A running theme is the extent to which classical observations using 19th and 20th century techniques – field observations and petrography – remain crucial but have gained power in combination with modern microanalytical techniques showing previously unseen and sometimes remarkable features. Layered intrusion petrology thus remains a field where we need a range of tools from rock hammers to synchrotrons. It should be emphasised that this review mostly centres on various observations and concepts regarding the processes operating in basaltic magma chambers, including those that produce mineral deposits. Also, we tried to avoid emphasis on some specific magmatic complexes but rather the focus is on petrological findings/discoveries that have general significance for all layered intrusions. And finally, we recognise that this review is inevitably biased towards research topics close to the hearts of the contributors.

2. Fundamentals of layered intrusions

2.1. Distribution in space and time

Layered intrusions have been reported throughout space and geological time (Fig. 1), with many more hypothesized to exist in relatively unexplored regions of Earth (Smith and Maier, 2021). Many of the world's layered intrusions occur within or proximal to the margins of Archean cratons and are associated with large igneous province magmatism (Fig. 1; Bleeker, 2003; Begg et al., 2010; Ernst et al., 2019). Some key mineralised cratons include the Kaapvaal (associated with the Bushveld Complex, Uitkomst, and Molopo Farms Complex), Superior (associated with the Lac des Iles and East Bull Lake suites), Zimbabwe (associated with the Great Dyke), and Pilbara (associated with Munni Munni and Radio Hill intrusions) cratons (Hoatson and Sun, 2002; Maier and Groves, 2011).
The emplacement of layered intrusions spans most of geological time and there is no secular variation in their size or metal endowment, although Archean and Proterozoic layered intrusions have a greater proclivity for hosting chromitites and (or) reef-style PGE mineralization (Maier, 2005; Smith and Maier, 2021). Some of the oldest layered intrusions include the ~3.03 *Ga* Stella (South Africa), ~ 3.1 *Ga* NuasahiSukinda (India), and the ~2.9 *Ga* West Pilbara layered intrusions (including Munni Munni, Radio Hill and Andover, yet Andover could be as old as 3016 ± 4 *Ma*; Hoatson and Sun, 2002). In contrast, some of the youngest include those associated with the Tertiary North Atlantic Igneous Province (e.g., Skaergaard of Greenland and Rum of Scotland) and Mesozoic Karoo-Ferrar large igneous province (e.g., Dufek of Antarctica and Mount Ayliff of South Africa). The emplacement ages for many intrusions correlate with the break-up and amalgamation ofsupercontinents as well as the formation rate of juvenile crust (Maier and Groves, 2011; Smith and Maier, 2021). In other words, relatively few layered intrusions are produced when supercontinents are stable. Many layered intrusions are associated with large igneous province (LIP) magmatism which, in turn, correlates with global mass extinction events (Courtillot et al., 1994; Bond and Wignall, 2014). Bond and Wignall (2014) have shown that the emplacement of the Emeishan LIP, Siberian Traps, Central Atlantic Magmatic Province, Karoo-Ferrar LIP, and Deccan Traps all correlate with episodes of mass extinction.

The growing popularity of the mineral systems approach (Wyborn et al., 1994; McCuaig et al., 2010; Barnes et al., 2016a) in understanding how deposit-scale ores concentrate within crustal-scale systems means that some recent studies focus on using lower-, mid-, and upper-crustal intrusions as analogues for crustal-scale processes (Holwell et al., 2019; Blanks et al., 2020). Such an approach is pertinent to understanding layer-forming processes in intrusions, which not only occur horizontally
across Earth's crust, but also vertically throughout it. Most known layered intrusions were emplaced within the upper crust, such as the Bushveld Complex (Buick et al., 2001), the Muskox intrusion (Kerans, 1983), and the Paleoproterozoic Fennoscandian intrusions (Lauri et al., 2012). Fewer mid-crustal layered intrusions have been reported, and even fewer lower crustal examples. This is a function of uplift, erosion, and exposure, yet modern geophysical investigations and drilling programs are characterizing unexposed layered intrusions (e.g., Xade of Botswana [Pouliquen et al., 2008; Chisenga et al., 2020] and intrusions in Brazil's Porto Nacional area [Lima et al., 2008]). Examples of lower to mid-crustal layered intrusions include the Hasvik intrusion of the Seiland Igneous Complex (Norway; Tegner et al., 1999), the alkaline Mordor Complex (Australia; Holwell and Blanks, 2021), the upper NovaBollinger intrusion (Taranovic et al., 2022), Fongen-Hyllingen Complex (Norway; Meyer and Wilson, 1999) and layered intrusions in the Halls Creek Orogen (e.g., Savannah and Panton; Bodorkos et al., 1999; Le Vaillant et al., 2020).

2.2. Size and shape

Layered intrusions come in all shapes and sizes, yet in most cases, their original physical parameters are obscured by post-magmatic deformation and erosion. There are several examples of tectonically dismembered layered intrusions including the Stella (Maier et al., 2003), Kondapalle (Meshram et al., 2015), Mantamaru (Maier et al., 2015), Stillwater (Jackson, 1961) and Koillismaa (Jarvinen ¨ et al., 2020) intrusions. South Africa's Stella intrusion dips sub-vertically and is thought to represent the upper portion of a larger, dismembered intrusion (Maier et al., 2003). The Stillwater Complex of Montana (United States) is regarded as a tectonic remnant of a Bushveld-style intrusion, missing the upper 2–3 km of section. Finland's Koillismaa intrusion consists of several tectonically dismembered blocks, which together with the Nar ¨ ank ¨ avaara ¨ intrusion and a geophysical anomaly, comprise the Koillismaa Layered Intrusion Complex (Karinen, 2010; J¨ arvinen et al., 2020). In some cases, the shape of layered intrusions may be structurally controlled. For example, the Skaergaard Intrusion of southeast Greenland, which is a type-locality for closed-system fractionation, is laterally bound by penecontemporaneous sub-vertical faults (Nielsen, 2004).
Many of the world's layered intrusions are funnel-shaped (e.g., Muskox, Yoko-Dovyren, Mordor, Sept Iles), tabular (e.g., Panton, Bushveld), or 'lopolithic' (e.g., Bjerkreim-Sokndal, Kiglapait) in nature (Fig. 2a-c). The Bjerkreim-Sokndal (Norway; Wilson et al., 1996) and Kiglapait (Canada; Morse, 1969) intrusions have traditionally been described as lopoliths, which are lenticular, centrally sunken, and generally concordant intrusions with thicknesses that are 5–10% of their diameter (Grout, 1918). However, the applicability of the term 'lopolith' has been questioned by Cawthorn and Miller (2018), who recommended the use of terms such as funnel-, boat-, wedge-, or tabular/sheet-shaped to be more in keeping with geometries determined primarily using modern geophysical methods (see also Webb et al., 2011). Many large, layered intrusions (e.g., Bjerkreim-Sokndal, Sept Iles, Bushveld Complex) do record evidence for central subsidence, which in recent times has been determined through anisotropy of magnetic susceptibility (Bolle et al., 2021)

and electron back-scatter diffraction (Vukmanovic et al., 2019); this process may be in part responsible for gravitational phase sorting of cumulus minerals (Maier et al., 2013).
Channelized and typically tubular intrusions termed 'chonoliths' may also display igneous layering (Fig. 2d). The Uitkomst intrusion (~ 8 × 0.5 × 0.8 km) of South Africa contains several chromitite layers within harzburgite units as well as a magnetite layer in the gabbronorite unit (Maier et al., 2018b). The Nebo-Babel intrusion of Australia's Giles Complex represents two ~1 × 0.5 km tubular bodies that are offset by a normal fault (Seat et al., 2007). The rhythmic layering of alternating feldspathic pyroxenite and gabbronorite has been described in Babel (Seat et al., 2007). Other examples include the Tamarack and Current Lake intrusions of the Midcontinent Rift System (see Bleeker et al., 2020 for a thorough review). In many of these cases, the deposition of magmatic sulfide mineralization may be controlled by the geometry of the intrusion (see Lightfoot and Evans-Lamswood, 2015).
Bladed dykes, such as Savannah (formerly Sally Malay) of Australia, the Expo Intrusive Suite of Canada's Cape Smith Belt, and the Eagle's Nest deposit of Canada's McFaulds Lake Belt (Fig. 2e; Barnes and Mungall, 2018) are thought to have formed as a result of horizontal as well as vertical propagation, as commonly seen in active shield volcanoes (Barnes et al., 2016a; Barnes and Mungall, 2018). The Savannah intrusion possesses modally graded interlayered peridotite and troctolite as well as compositional layering reflecting the upward differentiation of the parent magma (Le Vaillant et al., 2020). Apparently funnelshaped intrusions, such as Australia's Munni Munni intrusion, Brazil's Mirabela intrusion and the layered sections of Jimberlana, may have formed by the flaring of dykes, creating steep-sided chambers.

2.3. Mechanism of magma emplacement

The emplacement of many layered intrusions, particularly giants such as the Bushveld (up to 100,000 km2; Hayes et al., 2017; Latypov et al., 2022a, 2022b) and Molopo Farm (up to 13,000 km2; Du Plessis and Walraven, 1990; Kaavera et al., 2020) complexes, gives rise to a space problem, which refers to how such large volumes of magma were accommodated within Earth's crust. Their presence can be accounted for by any combination of (1) mechanical deformation of country rocks, including lifting, ballooning, or depression of host rocks; (2) localized tectonic extension, such as opening of transpressional fault jogs; (3) stoping, melting and assimilation of country rocks (see O'Hara, 1998).
These factors give rise to an array of intrusion geometries (Fig. 2) that may contain irregular occurrences of country rocks that represent incomplete amalgamation in sill-dyke networks (Barnes et al., 2016a). The approximate surface extent of known terrestrial layered intrusions ranges from <1 km2 to >65,000 km2 with estimated thicknesses ranging from <0.1 km to >10 km. It is unlikely that larger and (or) thicker, exposed or near-surface layered intrusions remain to be discovered on Earth, due to the ease with which they can be detected, the space problem, and that tabular variants are inclined to lengthen rather than thicken as they grow volumetrically (Cruden et al., 2017).
Layered intrusions develop primarily by the expansion of initially smaller intrusions, usually sills (Fig. 3). If the supply is episodic (i.e., successive magma pulses arrive after extensive crystallization), the magma is likely to be emplaced as a distinct separate intrusion (Blundy and Annen, 2016). However, if a sill is fed by a supply of magma arriving on a timescale shorter than that of solidification, it will remain molten and may expand (Cawthorn, 2012). If enough cooling occurs to generate cumulates between pulses, the result is macro-rhythmic layering (Irvine, 1970b). Hence, high-flux, short duration magma supply, characteristic of large igneous provinces, is most conducive to large cyclically-layered Bushveld-scale intrusions. In intermediate situations, a series of sills may develop initially by the propagation of finger-like fronts (Magee et al., 2016), that may eventually merge to form a larger, mainly molten sheet of magma. The larger the magma body, the more likely it is to "trap" successive pulses of magma, introducing a self-organizing feedback loop that may lead to giant intrusions (Fig. 3).

In all but rare cases of rapid "one-off emplacement", as proposed by Annen et al. (2022) for the Skaergaard intrusion (but see Holness et al., 2015 for details), intrusions develop sequentially over time from multiple magma pulses, and the various space-creating mechanisms may be involved in different proportions at different times. Barnes et al. (2019a) used compositions of Ni–Cu enriched cumulus magmatic sulfide liquid as a proxy for the fluid dynamic environment of emplacement of a spectrum of ore-bearing layered intrusions. Sulfide liquid is introduced into mafic-ultramafic magmas through the assimilation of sulfides from country rock xenoliths. The sulfide liquid then acquires variable concentrations of chalcophile metals by interacting with the host silicate magma. Where the magma is convecting or flowing vigorously, this process is highly efficient, and sulfides develop high metal tenors (concentration of Ni, Cu and PGE in 100% sulfide). In the early stages of the development of an intrusive complex, magma rheology is affected by the presence of a "sludge" of partially digested xenoliths and crystals. In this case, sulfide liquid is unable to react with more than a few times its own mass of silicate melt, and Ni and Cu tenors remain extremely low.
Tanzania's Ntaka Complex, Finland's Kevitsa intrusion, and Brazil's Fazenda Mirabela intrusion record a full spectrum from the "sludge" phase to the convecting phase recorded in a trend from low-tenor sulfides associated with abundant xenoliths in a stacked sill complex (Ntaka Complex), to high-tenor sulfides in a conventional layered intrusion (Fazenda Mirabela intrusion), with Kevitsa hosting a complete spectrum from one to the other (Barnes et al., 2019a).

2.4. Tectonic setting

Many of the world's layered intrusions are associated with ancient cratons (Begg et al., 2018; Smith and Maier, 2021). The PGE-mineralised Bushveld, Stillwater, and Great Dyke intrusions occur within the Kaapvaal, Wyoming, and Zimbabwe cratons, respectively. Other layered intrusions present in the central portions of cratons include the ~2.4 *Ga* Fennoscandian intrusions in the Karelia Craton, (e.g., Penikat, Portimo, and Koillismaa) and the ~2.8 *Ga* Murchison Domain intrusions in the Yilgarn Craton (e.g., Windimurra, Narndee, and Barrambie). In many cases, these intrusions are spatially associated with intra-cratonic structures that likely facilitated the emplacement of the intrusions. For example, the Bushveld Complex is spatially associated with the Thabazimbi-Murchison Lineament (Good and De Wit, 1997), the ~2.4 *Ga* Fennoscandian intrusions occur along linear belts interpreted as ancient rift suture zones (Maier et al., 2018b), and the Murchison domain intrusions have been associated with intracontinental riftrelated magmatism (Swager, 1997), yet their formation is currently ascribed to plume-driven LIP magmatism (Ivanic et al., 2010).
A few layered mafic-ultramafic and several Ni-Cu-mineralised maficultramafic intrusions occur in proximity to (paleo)craton margins, which are typically zones of relatively thin lithosphere that comprise crustal-scale fault networks within which parent magmas may ascend (Begg et al., 2010; Barnes et al., 2016b). These intrusions are often related to LIP magmatism, which is thought to occur in response to the arrival of deflected plume material beneath the craton margins (Begg et al., 2010). Layered mafic-ultramafic intrusions of the Kibaran Belt (e. g., Kapalagulu, Musongati) occur at the margin of the Tanzania Craton and are thought to have formed from variably contaminated picritic magmas that were emplaced during an early rifting phase of the ~1.4 *Ga* Kibaran Orogeny (Maier et al.,

2008a). The Kapalagulu and Musongati layered intrusions display well defined cryptic and modal layering exhibited in rocks ranging from dunite to anorthosite (Deblond, 1994; Duchesne et al., 2004; Maier et al., 2008a). Mafic-ultramafic intrusions
associated with the ~1075 *Ma* Giles Event Australia's Musgrave Province (possibly associated with the greater Warakurna LIP) were emplaced several magmatic pulses via the so-called Ngaanyatjarra Rift (Evins et al., 2010). This region hosts >20 layered intrusions including Wingellina Hills (12 × 3 km), Pirntirri Mulari (~ 5 km wide and 3 km thick), and the tectonically dismembered Mantamaru, which may have had an original size of 3400 km2 (Maier et al., 2015). Another example includes the tholeiitic layered intrusions of the Duluth Complex (~ 5000 km2) that were emplaced during the formation of the 1.1 *Ga* Midcontinent Rift on the southern margin of the Superior Craton (Miller and Ripley, 1996).
Historically, collisional tectonic settings have been considered unfavorable for the formation of mineralised layered intrusions (Jesus et al., 2020). Currently, there are increasing numbers of layered intrusions hypothesized to have formed in convergent tectonic settings, including those occurring in collisional (e.g., Beja), island-arc (e.g., Selebi-Phikwe, Vammala, Portneuf–Mauricie Domain, Greenhills Complex), continental-arc (e.g., Kondapalle, Lac des Iles, Aguablanca, Skymo, Fiambala), ´ back-arc ([predominantly continental]; e.g., Virorco, Kl¨ appsjo, ¨ Ferguson Lake Complex, Mayville), and post-collisional (e.g., Imleih, Motaghairat, Wateranga) settings. Arc-related magmas are typically more water rich than those generated in other tectonic settings (Plank et al., 2013), yet few supposedly arc-related intrusions contain cumulus amphibole (Davidson et al., 2007). Primary amphibole has been reported in Norway's Råna (Boyd and Mathiesen, 1979), Greenland's Fiskenæsset (Huang et al., 2014), Botswana's Lechana (Mokatse, 2017) America's Willow Lake (Taubeneck and Poldervaart, 1960), and Canada's Mayville intrusion (Sotiriou et al., 2020). Australia's Narndee Complex of the Yilgarn craton is one of few intrusions that has primary amphibole but has no recognized association with arc magmatism (Ivanic et al., 2010, 2015).
Portugal's Beja layered intrusion is a Variscan synorogenic gabbroic intrusion that was emplaced during the early stages of oblique continental collision in Iberia (Pin et al., 2008; Jesus et al., 2014), concomitantly with the Ni-Cu-(PGE)-mineralised Aguablanca stock (Pina, 2019). Beja's layered sequence consists of picritic troctolite, (clino)pyroxenite, gabbronorite, gabbro, and irregularly oxide-rich ferrogabbro that contains potentially economic Fe-Ti-V ($V_2O_5 \leq 1$ wt%) mineralization (Jesus et al., 2014). Disseminated Ni- and PGE-depleted sulfides are also reported in norite and pyroxenite present in the lower portion of the layered sequence (Jesus et al., 2020).
Layered and Ni-Cu-(PGE)-mineralised mafic-ultramafic intrusions of Botswana's Tati and Selebi-Phikwe belts are thought to have crystallized from variably contaminated island arc magma (Maier et al., 2008b). Contaminated island arc tholeiitic magmas are also thought to be parental to Ni-Cu-(PGE)-mineralised mafic-ultramafic intrusions of Finland's Vammala Nickel Belt (Peltonen, 1995) and Canada's PortneufMauricie Domain (Sappin et al., 2011). The Greenhills Complex that occurs in the Brook Street Terrane of New Zealand is a relatively small (~ 14 km2) layered mafic-ultramafic intrusion that crystallized from low-K island arc tholeiitic magma that is comparable in composition to local cross-cutting ankaramite dykes (Spandler et al., 2000).
The Lac des Iles Complex in Ontario is thought to have formed in a continental arc setting due to its geometrical comparability to UralAlaskan-type complexes, its spatial association with sanukitoid-like magmatism, and that its cumulate and mineral compositions are most consistent with an arc-related parent magma (Brügmann et al., 1997; Barnes and Gomwe, 2010; Djon et al., 2017). Layered mafic-ultramafic cumulate rocks of India's Pangidi-Kondapalle Complex are also thought to represent the remnants of a deeply eroded magmatic arc on the basis of whole-rock and mineral chemistry (Rao and Santosh, 2011). Spain's Ni-Cu-(PGE) mineralised Aguablanca stock (Pina ˜ et al., 2010) and Argentina's Fiambala´ layered gabbroic intrusion (DeBari, 1994), as well as America's Skymo (Whitney et al., 2008) and Duke Island (Saleeby, 1992) intrusions are other possible examples of layered intrusions emplaced in continental arcs. In the case of Kondapalle complexes, orthopyroxene is the primary ferromagnesian mineral; however, olivine is dominant in the Skymo intrusion, perhaps due to its relatively shallow (< 12 km) emplacement depth (Whitney et al., 2008).
Argentina's Virorco, Las Aguilas, ´ and Las Higueras layered maficultramafic intrusions of Argentina's Pringles Metamorphic Complex hosts alternating layers of metahornblendite and pyroxenite that are thought to be the crystalline products of possibly contaminated, tholeiitic magma that was emplaced within an extensional back-arc setting (Chernicoff et al., 2009; Ferracutti et al., 2013, 2017). The >2.62 *Ga* Ferguson Lake Igneous Complex in northern Canada is also hypothesized to have crystallized from crustally-contaminated tholeiitic basalts emplaced in a back-arc setting due to their geochemical similarity with local ~2.7 *Ga* back-arc basin basalts (Acosta-Gongora ´ et al., 2018). While not well constrained, the Ferguson Lake Igneous Complex does appear to show lithological and compositional layering (Miller, 2005, 2007). Other examples of Ni-Cu-mineralised back-arc intrusions may include the Bruvann Ni–Cu deposit of Norway's Råna layered intrusion (Tucker et al., 1990) or Canada's Mayville intrusion (Sotiriou et al., 2020).
There are few global examples of layered intrusions reported to have formed in post-collisional settings, which are those that formed from typically more alkalic magmas generated during post-collisional extension in subduction zones (see Holwell et al., 2019). Examples include those of the Arabian-Nubian shield (e.g., Imleih, Motaghairat), Wateranga of southeast Queensland (Australia), and possibly the Mordor Complex in Australia's Northern Territory, although an intracratonic setting is presently favored (Holwell and Blanks, 2021). Those reported in the Arabian-Nubian and Tuareg (e.g., Laouni) shields are associated with post-collisional continental tholeiitic magmas that are thought to have formed in response to post-collisional lithospheric delamination and then emplaced via *syn*-collisional fault networks (Azer and ElGharbawy, 2011; Halim et al., 2016). These intrusions possess welldefined modal layering in their lower, more ultramafic portions (e.g., pyroxenite, peridotite, troctolite), which sometimes possess finely disseminated sulfides (Cottin et al., 1998; Azer and El-Gharbawy, 2011; Halim et al., 2016). The tholeiitic Wateranga layered intrusion occurs within the New England Fold belt, which itself forms part of a continental margin setting (Henderson et al., 1993; Talusani et al., 2005). Despite its location within a fold belt, Wateranga is unmetamorphosed and occurs adjacent to major fault zones that likely facilitated its emplacement (Talusani et al., 2005).

2.5. Definition and classification of cumulate rocks

Cumulate rocks are the solid products of fractional crystallization. They represent the accumulation of crystals after partial or complete removal of the silicate liquid from which they crystallized, regardless of the mechanism of crystal-melt separation.
The extent to which the parent liquid is removed from the crystals was the basis for Wager et al. (1960) enduring definition of cumulate types. It is useful here to define the concept of "trapped liquid" as being the liquid component trapped between the cumulus crystals once the mixture has become geochemically isolated from the parent magma. Orthocumulates (Fig. 4a) with >30% trapped liquid are characterized by normally zoned cumulus phases, clearly interstitial liquid-derived grain aggregates and pockets of material such as granophyre, Ti-rich oxides, apatite and mica derived from end-stage fractional crystallization at the grain scale within the intercumulus porosity. Adcumulates consist of 100% liquidus crystals (i.e., crystals grown at the liquidus temperature of the melt) with <5 vol% trapped interstitial liquid (Fig. 4c, d), Intermediate between these are mesocumulates with 5–30% liquid (Fig. 4b). This straightforward scheme is complicated by the presence of poikilitic rocks, which lack this late-crystallizing material and whose bulk composition is inconsistent with the presence of enough interstitial liquid component to account for the modal proportion of the oikocrysts. The compositions of the oikocrysts closely resemble those of adjacent cumulus phases (Latypov et al., 2020b). These rocks

are termed heteradcumulates (Fig. 4e, f). They are easily mistaken for orthocumulates in the absence of whole-rock geochemical data or knowledge of mineral chemistry. A fourth type of cumulate, "harrisite" or "crescumulate", consists of large, commonly dendritic, oriented grains that have grown in situ, forming features such as comb layering (e.g., Robins, 1972).

This texturally-based scheme is deeply embedded in the original "cumulus paradigm", that cumulates formed by mechanical transport and deposition of crystals, followed by crystallization of interstitial liquid. Irvine (1981) attempted to circumvent this by proposing a purely descriptive scheme, but the legacy of classical cumulus theory is firmly ingrained. Cumulus nomenclature is simple to apply in cases of monomineralic adcumulates in large intrusions (e.g., Fig. 4), and orthocumulates in relatively rapidly cooled small intrusions (a) but founders on the characteristic heteradcumulate texture commonly observed in norites and gabbronorites in large intrusions (f). In these occurrences, plagioclase forms clearly idiomorphic cumulus grains whereas pyroxene shows composite grains with cumulus cores and interstitial, characteristically unzoned poikilitic overgrowths trapping plagioclase grains. These rocks are texturally and chemically heteradcumulates. They provide one of the lines of evidence, discussed in section 4.13 below, that many textural features of cumulate rocks are better explained as the result of in situ nucleation and growth in boundary layers rather than by mechanical accumulation of crystals followed by compaction and melt expulsion.

As a general rule, adcumulate and heteradcumulate textures are the hallmark of large, several km thick layered complexes such as Bushveld and Stillwater, whereas orthocumulate textures predominate in smaller bodies 100 s of m thick, such as the differentiated sills of the Norilsk region in Siberia (Barnes et al., 2019a, 2019b). This is clearly the result of differing timescales for solidification, although the precise mechanism is debatable: e.g., thicker cumulate piles are more susceptible to compaction and melt expulsion, favouring adcumulate formation, or larger magma bodies developed more vigorous convection.

Geochemically, adcumulate and heteradcumulate rocks have wholerock compositions expressed exactly as mixtures of the component cumulus and poikilitic minerals (Haskin and Salpas, 1992; Barnes et al., 2016b), with a negligible liquid component and hence very low concentrations of excluded elements. Poikilitic anorthosites, commonly referred to as plagioclase-only cumulates, are in many cases actually plagioclase-pyroxene heteradcumulates, such that there is no correlation between the proportion of "intercumulus" pyroxene and incompatible elements (McBirney and Hunter, 1995). Orthocumulates ideally are linear mixtures of cumulus crystals and trapped liquid, leading to the common practice of using incompatible element concentration as indices of trapped liquid abundance. However, it is commonly observed that incompatible trace elements are decoupled from one another (Meurer and Meurer, 2006); commonly, what appear to be texturally orthocumulate rocks are deficient in excluded components such as Zr and P. This probably arises from mobility through the residual pore space of incompatible-enriched residual liquid or fluid components at the last stages of solidification, resulting in nugget-effect heterogeneities at a scale of metres or more (Haskin and Salpas, 1992). Campbell (1987) found that sample sizes of at least 1 kg are needed in order to retain correlation between such incompatible elements as U and P (Barnes and Williams, 2023, in review). This must be considered when sampling layered intrusion rocks for whole-rock geochemical analysis. The identity of the cumulus minerals is not always obvious, particularly in heteradcumulates and multi-phase cumulates, or where rocks have undergone extensive alteration to secondary minerals. Stanley and Russell (1989) provide a set of graphical methods for determining cumulus mineral components from whole-rock geochemical data using normalised major element ratios (Fig. 5) and Barnes (2023) provides some practical discrimination plots for distinguishing cumulate from non-cumulate rocks.

The crystallization of a trapped liquid component within orthocumulates and mesocumulates gives rise to modification of mineral compositions (Barnes, 1986). This follows from the fundamentals of phase relations: ferromagnesian minerals such as olivine and pyroxene growing at equilibrium with a liquid have higher Mg/Fe rations than their parent melt; likewise for Ca/Na in plagioclase. As these phases grow from the trapped liquid, commonly as outgrowths on the cumulus grains, initially they give rise to normally zoned grains which subsequently homogenise, partly or completely, by diffusion during subsequent growth and cooling. Divalent ions in olivine and pyroxene diffuse sufficiently rapidly that complete homogenization typically occurs in the case of slow cooling in large intrusions, giving rise to a final composition with Mg/Fe or Ca/Na that is a weighted average of the primary liquidus composition and the trapped liquid component. The same principle applies to trace elements such as Ni in olivine and Cr in pyroxene. This change in composition is referred to as the "trapped liquid shift" (Barnes, 1986). The magnitude of this shift depends on the proportion of trapped liquid – the higher the proportion, the larger the shift – and the modal proportion of the phases in the cumulus assemblage: the larger the proportion the smaller the shift. Typical shifts are shown in Fig. 6. As a consequence, mineral trends in orthocumulate sequences would be expected to show discontinuous jumps corresponding to phase appearance horizons.

2.6. Parental melts, crystallization sequences and cotectic phase proportions

Mantle-derived basaltic to komatiitic magmas are commonly olivinesaturated because the Earth's mantle is mostly composed of olivine-rich peridotites. Ignoring minor and oxide phases, Irvine (1979) identified six major crystallization sequences for such olivine-saturated melts in a quaternary system Ol-Pl-Cpx-Qtz (Fig. 7). They can be subdivided into two major groups – one with a plagioclase tendency:

(1) Ol (dunite), Ol + Pl (troctolite), Ol + Pl + Cpx (olivine gabbro), and Opx + Pl + Cpx (gabbronorite) (Fig. 5a);
(2) Ol (dunite), Ol + Pl (troctolite), Opx + Pl (norite), and Opx + Pl + Cpx (gabbronorite) (Fig. 7b);
(3) Ol (dunite), Opx (orthopyroxenite), Opx + Pl (norite), and Opx + Pl + Cpx (gabbronorite) (Fig. 7c);

and another with a clinopyroxene tendency:

(1) Ol (dunite), Ol + Cpx (olivine clinopyroxene), Ol + Pl + Cpx (olivine gabbro), and Opx + Pl + Cpx (gabbronorite) (Fig. 7d);
(2) Ol (dunite), Ol + Cpx (olivine clinopyroxene), Opx + Cpx (websterite), and Opx + Pl + Cpx (gabbronorite) (Fig. 7e);
(3) Ol (dunite), Opx (orthopyroxenite), Opx + Cpx (websterite), and Opx + Pl + Cpx (gabbronorite) (Fig. 7f).

The systematic changes in crystallization sequence (from 1 to 3) in these two groups as well as within the individual sequences of these groups is largely a manifestation of an increasing amount of SiO_2 content in the parental and/or progressively evolving melts. Remarkably, most layered intrusions display cumulate stratigraphy with systematic crystallization sequences that are fully consistent with the above six theoretically expected orders of crystallization, indicating that formation of layered intrusions is governed by liquidus phase equilibria (Cawthorn, 1996; Charlier et al., 2015b; Latypov et al., 2020b; Irvine, 1976, 1979; O'Driscoll and VanTongeren, 2017a, 2017b; Parsons, 1987; Wager and Brown, 1968). This feature is crucial for petrogenesis of layered intrusions, especially in the light of the current tendency in igneous petrology to consider these intrusions as stacks of 'amalgamated sills' that were randomly emplaced into pre-existing, already solidified rocks (see section 4.3). Another important feature is that, in the absence of mechanical sorting of phases, cumulate rocks in these sequences are expected to consist of minerals in cotectic proportions, i.e., those which are predicted by cotectic lines in liquidus phase diagrams (Fig. 8). Note that in the mineral associations, plagioclase and clinopyroxene always dominate over olivine and orthopyroxene (e.g., 70% plagioclase and 30% olivine in troctolite; 90% clinopyroxene and 10% orthopyroxene in websterite) because all cotectic lines and surfaces are displaced towards a ternary plane with plagioclase and clinopyroxene (i.e., Pl-Cpx-Qtz; Fig. 7). Cumulates with cotectic proportions of phases predominate in layered

intrusions (e.g., Cawthorn, 1996; Charlier et al., 2015b; Parsons, 1987; Wager and Brown, 1968), indicating little physical separation of crystals after their formation, characteristic of solidification fronts (Marsh, 1996). However, there are some exceptions from this rule, with strikingly abnormal, non-cotectic proportions of minerals in cumulate rocks (Cawthorn, 2002; Cawthorn and Spies, 2003; Namur et al., 2011a; Jenkins and Mungall, 2018; Latypov and Chistyakova, 2020; Lundgaard et al., 2002). Such non-cotectic cumulates cannot be produced through direct in situ crystal growth within solidification fronts and, therefore, require the involvement of some additional processes such as crystal sorting in crystal-rich mushes (e.g., Jenkins and Mungall, 2018; Maier et al., 2013; Mondal and Mathez, 2007). There is, however, one recent attempt to explain some non-cotectic cumulates in the frame of solidification front models (Kruger and Latypov, 2022; see section 4.6).

2.7. Types of igneous layering and layer-forming processes

Igneous layering is a feature of plutonic bodies that is most commonly observed in mafic layered intrusions (Wager and Brown, 1968; Naslund and McBirney, 1996; Namur et al., 2015a) (Fig. 9). Layering is made up of cumulates forming individual layers which are distinctive in their compositions and/or textures (Irvine, 1982; Naslund and McBirney, 1996). Layering may be well defined (prominent layering) or poorly defined. Individual layers are usually leucocratic or melanocratic but can also be monomineralic. They can show different forms, the most common being planar but other forms such as troughshaped, synformal, antiformal, lenticular or convoluted are observed. The contact between successive layers can be sharp or gradational. Layers are vertically uniform or variable. In the latter case, they show vertical variability in crystal texture (e.g., crystal shape), size, mode, or composition (Irvine, 1982). Between successive layers, minerals can have similar compositions or may be different. This can be due to a range of processes: i.e., varying interstitial material fractions (Barnes, 1986), magma chamber replenishment (e.g., individual layers crystallized from different batches of magma), reactive porous flow within the crystal mush (Holness et al., 2007a; Namur et al., 2013), change in conditions crystallization conditions (Pang et al., 2008), or melt evolution due to crystal fractionation.

Various processes may have contributed layering formation. They may take place at supersolidus or subsolidus conditions (Naslund and McBirney, 1996). We divide these major processes into a first category of dynamic processes and a second category of non-dynamic processes (Irvine, 1982; Naslund and McBirney, 1996; Namur et al., 2015a).

The dynamic layer-forming processes involve the relative movement of crystals and melt within the crystal mush or the magma chamber. These main processes involve flow segregation, gravity currents of crystal-bearing magma (McBirney and Nicolas, 1997), convection (Wager and Brown, 1968) or simple crystal sorting by settling and/or floatation (Naslund and McBirney, 1996). Magma mixing between various batches of compositionally contrasted magmas within the crystal mush can also result in layering features, such as monomineralic layers (e.g., Irvine, 1975). Silicate liquid immiscibility can also be considered as a potentially important layer-forming mechanism (Charlier et al., 2011; Namur et al., 2012).

The non-dynamic layer-forming processes take place because of changing conditions of crystallization (i.e., pressure, oxygen fugacity) or due to mineralogical re-organization in a crystal mush to minimise surface energy (Boudreau, 2011). In the latter case, the initial texture of a slightly heterogeneous rock may evolve to produce modal igneous layering. A layer with poorly defined contacts or with a weakly defined textural or mineralogical interior structure may develop strong layering as the rock texture coarsens at subsolidus conditions. Initial heterogeneities in the rock may be due to changing intensive parameters (pressure, oxygen fugacity) of crystallization but most of them are probably due to some fluctuation of nucleation rates in silicate melts.

2.8. Mineral deposits

Several recent reviews have detailed the nature and formation mechanisms of mineral deposits present in layered mafic-ultramafic intrusions (Ripley and Li, 2018; Smith and Maier, 2021; Cawthorn, 2021; Hughes et al., 2021; Chaumba, 2022). Each of these thorough contributions remarked on the role layered alkaline and maficultramafic intrusions will play in the future resourcing of materials deemed critical by global governmental bodies, including PGEs, rare earth elements (REE), Ni, Co, Cr, V, and Ti (European Commission, 2020; Natural Resources Canada, 2021; Australian Government, and Department of Industry, S. and R, 2022; UK Department for Business, E.& I.S, 2022). Below, we summarize the characteristics and proposed petrogenetic models for key mineral deposits present in global layered intrusions.

2.8.1. Chromitites

Chromitites are rocks composed predominantly of chromite. They may occur as nodules or pods, as in the case of obducted and uplifted mantle material (Arai, 1997), or as layers, seams, and lenses in layered mafic-ultramafic intrusions. These stratiform layers are most often located in the lower ultramafic-mafic portions of intrusions (e.g., Bushveld, Stillwater), yet may occur in the central to upper, often gabbroic, portions (e.g., Koitelainen and Akanvaara; Hanski et al., 2001; Fig. 10). Typically, stratiform chromitites range from a few millimeters to 10s of centimeters in thickness and may persist laterally for several 10s to 100 s of kilometers (Jackson, 1961; Cameron, 1964; Cawthorn, 2005). However, layered intrusions may also host thick (up to ~100 m) discontinuous chromitite bodies that are often hosted by ultramafic rock types (e.g., Inyala and Railway Block, Black Thor, Ipueira-Medrado sill of the Jacurici Complex, Nuasahi-Sukinda, Kemi; Mondal et al., 2006; Prendergast, 2008; Marques et al., 2017; Lesher et al., 2019; Alapieti et al., 1989). This has led to the subdivision of stratiform-type and conduit-type chromitites (Prendergast, 2008; Lesher et al., 2019). It has been hypothesized that podiform-type and stratiform-type chromitites are connected. Arai (2021) proposed that chromite crystals in stratiform-type chromitites formed in the mantle during the reaction between mantle peridotite and magma and were subsequently entrained and deposited.

Stratiform chromitites are commonly rich in PGE relative to their bracketing units and rarely associated with magmatic Ni-Cu-(PGE) mineralization (e.g., Uitkomst). Chromitites of the Great Dyke, Bushveld, and Stillwater complexes host the majority of the world's Cr reserves, and significant PGE mineralization in the case of the Bushveld's UG-2 chromitite. While chromitite ores at these localities typically host 40–45 wt% Cr_2O_3, (Stowe, 1994; Naldrett, 2004), elsewhere chromitite ores range from ~21 (Rum intrusion) to 57 wt% Cr_2O_3 (see Table 1 of Schulte et al., 2010). These chromitites may bifurcate, undulate, and persist despite irregular footwall topologies (Latypov et al., 2015a). They often share sharp to weakly diffuse, planar to cm-scale undulatory contacts with their bracketing rocks units, which typically are anorthosite, gabbronorite, and pyroxenite (Lenaz et al., 2011; Scoon and Costin, 2018; Maghdour-Mashhour et al., 2021; Smith et al., 2021b). In contrast, conduit-type chromitites occur in relatively ultramafic sill-like intrusions (e.g., Black Thor, Ipueira-Medrado, Uitkomst), and as such, are thought to be the product of komatiitic magmas (Yudovskaya et al., 2015; Marques et al., 2017; Lesher et al., 2019). Their Cr_2O_3 grades are comparable to that of stratiform-type chromitites (35–40 wt% at Ipueira, Marques

et al., 2017; ~ 33.5 wt% at Uitkomst, Maier et al., 2018a). Many layered intrusions with chromitites are Archean to Proterozoic in age, with few Phanerozoic examples (e.g., Rum; Smith and Maier, 2021). Chromitites are arguably the most enigmatic rock type of layered intrusions. It remains unclear how these layers are generated from magmas with <0.35% Cr that are volumetrically in excess of what is preserved in the rock record (Eales, 2000; Lesher et al., 2019). Several mechanisms have been proposed for their formation, which may fall into magmatic, hydromagmatic, or hydrodynamic categories. Proponents of magmatic models argue that magmas become saturated solely in chromite via: (i) fluctuations in fO_2 content (Ulmer, 1969; Ferreira Filho and Araujo, 2009) or pressure increase (Lipin, 1993) or decrease (Latypov et al., 2018a) facilitated by magma replenishment and expulsion; (ii) the assimilation of siliceous crustal materials (Irvine, 1976; Woods et al., 2019); (iii) the mixing of compositionally distinct (possibly contaminated) magmas (Irvine, 1977; Alapieti et al., 1989; Campbell and Murck, 1993; Spandler et al., 2005) and (or) partial melts of pre-existing cumulates (O'Driscoll et al., 2010; Mathez and Kinzler, 2017; Hepworth et al., 2018; Scoon and Costin, 2018); (iv) the conversion of assimilated oxide xenocrysts by reaction with Cr-rich magma (Lesher et al., 2019). In these cases, chromite may (re-)crystallize in the magma and gravitationally settle (Naldrett et al., 2012) or accumulate at the liquidcumulate interface via in situ nucleation and growth (Latypov et al., 2017a, 2022a, 2023a, 2023b). Proponents of hydromagmatic models propose that volatile-induced hydration melting or dissolution (i.e., infiltration metasomatism) of Cr-bearing pyroxene in (leuco)gabbronoritic rocks can result in the concomitant formation of anorthosite and chromitite (Nicholson and Mathez, 1991; Boudreau, 2016, 2019; Veksler and Hou, 2020; Marsh et al., 2021). Proponents of (magmatic-) hydrodynamic models suggest that chromitites form by the settling and (or) sorting of chromitite crystals in flowing magmas (Mondal and Mathez, 2007) or slurries (Voordouw et al., 2009; Maier et al., 2013; Maier et al., 2018a, 2018b). The capability of chromite to form sharply defined layers in density currents has been circumstantially evidenced by the thickening of chromitite layers in the Kemi (a few millimeters thick at the margins and up to 90 m thick in the center; Alapieti et al., 1989) and Ipueira-Medrado (~ 5–8 m thick; Marques et al., 2017) intrusions, as well as experimentally simulated in flume-tank analogue experiments (Forien et al., 2015).

2.8.2. Magmatic sulphides

Large layered intrusions, particularly the Bushveld, Stillwater and Great Dyke Complexes, contain a large proportion of the world's resource endowment of platinum group elements, within a class of deposit defined by the accumulation of immiscible sulfide liquid in a variety of settings. The most significant PGE repositories are in the form either of disseminated sulfide accumulations near the margins of intrusions, the Platreef of the Bushveld Complex being overwhelmingly the dominant example, or stratiform so-called reef-style accumulations such as the Merensky Reef of Bushveld or the J-M Reef of Stillwater. These are thin layers, <1 m thick, typically of remarkable lateral extent and continuity, containing small proportions of Ni-Cu-Fe sulfides in close spatial association with PGE minerals. Both contact and reef-style deposits are marked by having exceptionally high PGE 'tenors', i.e., metal concentrations normalised to 100% sulfide (Fig. 11; Barnes et al., 2017).

2.8.2.1. Contact-style PGE-Cu-Ni mineralization. Contact-style mineralization manifests at or close to the margins of layered intrusions and may extend into the country rocks. The sulfides are typically disseminated (< 5 vol%; e.g., Bushveld's Platreef, and East Bull Lake Suite's River Valley intrusion), yet massive sulfide occurrences have been described (e.g., Portimo Complex's Suhanko intrusion). While six PGE tenors of this deposit-style (1 s to 10s of ppm) are generally smaller than those of reefstyle occurrences (10s to 100 s of ppm), mineralization can persist for 10s to 100 s of meters above the lithological contact. The igneous host rocks are typically gabbroic, rarely ultramafic, and vari-textured, i.e., show significant variability in mineral mode, texture, and grain size (Maier, 2005). They often comprise xenoliths of the local country rock (e.g., Platreef), autoliths of antecedent magma pulses (e.g., Fedorova of Russia; Groshev et al., 2021), and patches of texturally distinct felsic material thought to represent country rock partial melts (i.e., xenomelts; e.g., Platreef; Johnson et al., 2010). In situ assimilation is thought to have triggered S-saturation in many intrusions (e.g., Portimo Complex, Fedorova-Pana, Stillwater Basal Series), yet the role of pre-emplacement S-saturation and transport of sulfide melt is increasingly being ascribed to contact-style occurrences (e.g., Platreef, McDonald and Holwell, 2011; River Valley, Holwell et al., 2014; Monchegorsk, Karykowski et al., 2018a; Labrador Trough intrusions, Smith et al., 2020, 2021a).

The Platreef of the Bushveld Complex is the only example of contactstyle PGE mineralization that is currently mined (Fig. 10). It represents a ~ 10 to 400-m-thick package of mineralised vari-textured pyroxenites, norites, and gabbros that overlie Transvaal dolomitic country rocks and Archean basement rocks at the base of the Bushveld's northern limb (Kinnaird et al., 2005; McDonald and Holwell, 2011). The reef displays significant lateral variability in host rock (lithology and texture) and PGE grade, where the highest grades (~ 3 ppm; Pd/Pt = 0.5–2) occur at the Sandsloot Mine, stratigraphically overlying dolomitic country rocks (Holwell et al., 2006). The world-class Flatreef deposit (346 Mt. at 3.8 g/ t ΣPGE, 0.32% Ni, and 0.16% Cu), discovered in 2007, is the down-dip extension of the Platreef (Grobler et al., 2019), and as such, shares several lithological, geochemical, and isotopic similarities with the Platreef (Harris and Chaumba, 2001; Pronost et al., 2008; Abernethy, 2019). It is believed that sulfide melt formed in a mid- to upper-crustal staging chamber, with (Ihlenfeld and Keays, 2011) or without (Holwell et al., 2007; McDonald and Holwell, 2011) assimilation, and was then transported upwards.

Contact-style PGE mineralization in the Portimo, Monchegorsk, and Fedorova-Pana complexes occurs in vari-textured gabbronoritic rocks (~ 50 to 280 m thick) that overlie Archean basement rocks and host abundant country rock xenoliths and xenomelts (Iljina et al., 1992; Iljina and Lee, 2005; Karykowski et al., 2018a; Groshev et al., 2019). These occurrences comprises ~3–5 vol% sulfide, where the higher-grade zones (~ 2–3 g/t Pt + Pd) are associated with higher abundances of xenoliths and xenomelts (Karykowski et al., 2018a; Groshev et al., 2019). It has been recognized that the deposition of relatively high-grade contactstyle mineralization follows the emplacement of relatively unmineralized rocks (see Karykowski et al., 2018a). For example, relatively highgrade contact-style mineralization in the Bushveld's northern limb coincides with the appearance of Lower Zone cumulates (McDonald et al., 2017), mineralization in the Portimo Complex followed the emplacement of the Portimo dykes (Iljina and Lee, 2005), and Federova's thick mineralised package was deposited after the 4-km-thick main maficultramafic body of the intrusion (Groshev et al., 2009). Not only could the antecedent magmas have interacted with proto-ores at depth, they may have also sufficiently heated the upper crustal host rocks to facilitate the concentration of contact-style orebodies (Karykowski et al., 2018a; Groshev et al., 2021).

2.8.2.2. Reef-style PGE mineralization.

Following the discovery of the Bushveld's Merensky Reef in 1924, reef-style PGE deposits superseded Ural-Alaskan placers as the world's principal source of PGEs. Reef-style PGE mineralization can occur in the lower, typically ultramafic, portions of intrusions (e.g., Great Dyke's Main Sulfide Zone, Kapalagulu), the central, typically mafic, portions of intrusions (e.g., Bushveld's Critical Zone reefs, Stillwater's JM Reef), and the upper evolved portions of intrusions (e.g., Koitelainen, Stella, and Skaergaard's Platinova Reef). It can be hosted in peridotite (e.g., Luanga, Kapalagulu), pyroxenite (e.g., Great Dyke's MSZ, Munni Munni, Bushveld's Volspruit), chromitite (e. g., Bushveld's UG-2, Stillwater's A-chromitite, Panton Sill), gabbroic units (e.g., Skaergaard, Rincon del Tigre), anorthosite (e.g., Penikat,

Monchegorsk), and magnetitite (e.g., Stella, Maier, 2005). Their host rock diversity attests to their potential to form from a range of magma types, from komatiitic (e.g., Mochila), picritic (e.g., Rum) siliceous highMg basalt (e.g., Bushveld, Stillwater, Penikat), (ferro)basaltic (e.g., Skaergaard), to alkaline (e.g., Mordor). While reef-style mineralization typically manifests in Archean (e.g., Great Dyke, Stillwater, Munni Munni, Stella) and Proterozoic (e.g., Bushveld, Penikat) intrusions, it is also known in rare examples in Phanerozoic intrusions (e.g., Skaergaard, Rum).

Ultramafic-type reef-style: PGE mineralization in the lower ultramafic portions of layered intrusions is characterized by ~1 m to 100 s of meters of disseminated sulfides (< 5 vol%) associated with peridotite and pyroxenite. Examples include the Great Dyke's Main Sulfide Zone (Oberthür, 2011; which may also be classified as offset-type), Bushveld's Volspruit Zone (Harmer, 2004), and Kapalagulu's Makambo Zone (Maier et al., 2008a; Prendergast, 2021). The offset PGE mineralization in the Great Dyke's Main Sulfide Zone occurs atop pyroxenite of the Ultramafic Cyclic Unit (Fig. 10; Godel, 2015) just below the contact with the thick overlying gabbroic sequence. There is no evidence that contamination plays a role in inducing sulfide melt segregation ($\delta^{34}S$ = 0.1–1‰), which instead is thought to have arisen from differentiation.

The Munni Munni PGE reef, also an offset type closely similar to the Great Dyke MSZ, was interpreted by Barnes and Hoatson (1994) to be the result of mixing of a new influx of more fractionated magma into an expanding chamber. Conversely, sulfide melt segregation at Kapalagulu ($\delta^{34}S$ + 4.2 - +20 ‰; Maier et al., 2008a) and at Volspruit ($\delta^{34}S$ = +3.8 - +4.3‰; Hulbert, 1983) is thought to have been triggered by the assimilation of crustal rock and possibly the concomitant crystallization of chromite (see Tanner et al., 2019). Furthermore, Maier (2005) proposed that parent magmas may have reached S-saturation prior to emplacement (i.e., in a staging chamber or conduit) and that immiscible sulfide melt was entrained upward. The derivation of the S is impossible to determine in most cases: reef-style sulfides form by equilibration of sulfide liquids with tens to hundreds of thousands of times their own mass of silicate melt (Campbell and Barnes, 1984; Mungall and Brenan, 2014) such that any crustal S isotopic signal becomes diluted to undetectability by mantle S from the silicate melt (Lesher and Burnham, 2001).

Chrome-type reef-style: Stratiform chromitite layers in several layered intrusions (e.g., Bushveld's UG-2, Stillwater's A- and B-chromitite, Great Dyke, Rum) possess elevated concentrations of all the PGE, typically ranging from 0.1 to 50 ppm (Maier, 2005 and references therein). In most cases, these occurrences are thin (few cm to dm), Spoor (< 1 vol%), and contain assemblages of IPGE-Pt-alloys and PPGEsulfides with small proportions of pentlandite-chalcopyrite (Junge et al., 2014). Bushveld's UG-2 chromitite is the world's largest PGE resource and the only chromitite presently mined for PGE. The UG-2 contains 5–10 ppm PGE over ~1 m and extends laterally for several 100 s km within the Upper Critical Zone of the Bushveld Complex (see Mondal and Mathez, 2007). Like Bushveld chromitites, the Rum chromitites are thin (< 1 cm), rich in PGE (2–3 ppm Pd + Pt), and are laterally, uniformly continuous despite changes in floor rock topology and lithology (O'Driscoll et al., 2009b; Latypov et al., 2013). The petrogenesis of this style of mineralization is less clear. The precipitation of FeO-bearing minerals removes ligands for S to bond within the magma, thus, lowering S solubility and possibly triggering sulfide melt segregation. This process alone cannot explain the low-S-high-PGE nature of this style, which has been explained by: (i) desulfurization of sulfides and retention of highly chalcophile metals following Fe-loss in chromite (Naldrett and Lehmann, 1988; Maier et al., 2003); (ii) direct precipitation of PGE minerals and alloys prior to S-saturation, perhaps in response to localized reduction induced by chromite precipitation (Mungall, 2002; Godel et al., 2007; Finnigan et al., 2008); (iii) the (incongruent) dissolution of sulfides during reaction with S-undersaturated magmas or fluids (Von Gruenewaldt et al., 1986; Nicholson and Mathez, 1991; Kerr and Leitch, 2005; Naldrett et al., 2009; Smith et al., 2022); (vi) in situ crystallization of chromite and sulfide at the base of a large body of convecting magma (Latypov et al., 2013); (iv) (re)dissolution of sulfide produced by transient sulfide saturation events during chromite precipitation, accompanied by the growth of magmatic PGMs (Barnes et al., 2021).

Mafic-type reef-style: The style of PGE mineralization is typically found at lithological and (or) compositional transitions in the central portions of layered intrusions, and can be hosted in gabbro(norite), norite, troctolite, pyroxenite, and (or) anorthosite. The Bushveld's Merensky Reef and the Stillwater's JM Reef are key examples of this type (Fig. 10), but notable occurrences have been reported in the Penikat (Iljina et al., 2015 and references therein), Monchegorsk (Karykowski et al., 2018b), and Luanga (Mansur et al., 2020) intrusions. The Merensky Reef is a ≤ 1-m-thick unit of coarse-grained pyroxenite that is bracketed by mm- to cm-scale chromitites, underlain by norite and anorthosite, and overlain by pyroxenite and norite (Smith et al., 2021b). The grades range from 5 to 10 ppm Pd + Pt (Pd/Pt ~ 0.6; Barnes and Maier, 2002) and it is evident that sulfide melt has percolated downward through the rock sequence on a scale of centimeters (Godel et al., 2006a, 2006b; Smith et al., 2021b). Several models have been proposed to explain the Merensky Reef (see reviews by Cawthorn, 2015 and Kinnaird, 2005). In general, the proposed models fall into orthomagmatic or hydrothermal categories. Proponents of orthomagmatic models argue for the accumulation of chromite and PGE-rich sulfides either through gravitational settling (Campbell et al., 1983; Barnes and Maier, 2002; Naldrett et al., 2009), in situ crystallization (Eales and Reynolds, 1986; Latypov et al., 2015a, 2017a, 2017b; Hunt et al., 2018; Vukmanovic et al., 2018), or granular flow (Maier et al., 2013) in response to processes such as magma mixing (Campbell et al., 1983), sill injection (Lee and Butcher, 1990; Mitchell and Scoon, 2007; Mungall et al., 2016) or fractionation (Maier et al., 2013). In contrast, proponents of hydromagmatic models argue that the reef formed during the interaction between ascending magmatic fluids and a fluid-undersaturated protoreef (Ballhaus and Stumpfl, 1986; Boudreau and McCallum, 1986; Nicholson and Mathez, 1991; Mathez, 1995; Boudreau, 2008). Stillwater's JM Reef occurs in troctolite, (ol-) gabbronorite, and anorthosite of the lower Banded Series (Zientek et al., 2002; Jenkins et al., 2021). It comprises 0.5–5 vol% sulfides that have the highest Pd–Pt grades of all known reef-style occurrences (~ 18 ppm) and elevated Pd/Pt values (~2–4; Zientek et al., 2002; Godel and Barnes, 2008). Several of the aforementioned models have been applied to the JM Reef (see Boudreau, 1999; Zientek et al., 2002; Godel and Barnes, 2008; Boudreau et al., 2020). Alternatively, Jenkins et al. (2021) proposed that the JM Reef formed in response to the progressive infiltration of buoyant contaminated komatiitic magmas that interacted with PGE-bearing footwall cumulates.

Offset-type reef-style: While rare, this style of mineralization occurs in two settings: at the contact between ultramafic and mafic cumulates sequences, as in the Great Dyke and Munni Munni intrusions (Fig. 10; Barnes et al., 1992); and in the upper, typically gabbroic, portions of evolved layered intrusions, as in the Skaergaard and Stella intrusions (Fig. 10; Andersen et al., 1998; Maier et al., 2003). The term 'offset' arises from the sequential occurrence of peak metal grades over 1 s to 10s of m, where Pd + Pt concentrations peak at the base, followed by Au (–Te) and then Cu(–Se) (Barnes, 1993; Prendergast, 2000; Holwell et al., 2016). The assemblages in the case of the upper-level examples consist of low volumes of Cu-sulfides (bornite-chalcocite-chalcopyrite), rare Fe-sulfides, as well as abundant Pd-Au-Cu alloys and tellurides that occur at the margins of sulfide blebs (Prendergast, 2000; Holwell et al., 2014, 2016). Examples of this style of mineralization include Skaergaard's Platinova Reef (Andersen et al., 1998; Holwell et al., 2016), Sonju Lake's Reef Horizon (Lundstrom and Gajos, 2014), Rincon del Tigre's Precious Metal Zone (Prendergast, 2000), and in the Sotkavaara intrusion (Guice et al., 2017). More unconventional offset-type reefs occur in the Stella (Maier et al., 2003) and Kapalagulu intrusions (Prendergast, 2021). Their typical presence in the upper portions of intrusions, together with the low-S characteristic, suggests S-saturation was achieved via in situ fractional crystallization (Holwell et al., 2016), regardless of contamination (Guice et al., 2017), with removal of FeO by magnetite crystallization being a key factor. The offsets are then ascribed to the relative order of silicate:sulfide liquid partition coefficients ($D_{PGE} > D_{Au-Te} > D_{Cu-Se}$), as modelled by Barnes (1993). Mungall (2002) showed that offset profile could

also be explained by kinetic factors, specifically different diffusivities of the chalcophile elements. However, the exceptionally high PGE tenors of the Platinova Reef suggest that some degree of sulfide dissolution may have subsequently upgraded primary sulfides (Holwell et al., 2015; Mungall et al., 2020), consistent with detailed 3D observations of the micro-scale distribution of Pd-Au-Cu minerals and Cu sulfides (Godel et al., 2014). A key factor in the unusual nature of the Platinova Reef is that highly fractionated magmas become saturated in Cu-sulfide rather than Fesulfide liquids (Ripley et al., 2002). The PGE mineralization in the ~3.03 *Ga* Stella intrusion (~ 4.4 g/t Pd + Pt over 5–8 m) is hosted in interlayered semi-massive magnetitite and magnetite-bearing leucogabbro-anorthosite in the upper portion of the intrusion (Maier et al., 2003). It is thought to have formed in response to ascending chalcophilebearing deuteric fluids, which became trapped in magnetite layers (Maier et al., 2023). The offset Lubalisi Reef in the Kapalagulu intrusions occurs within basal chromitiferous harzburgites and is thought to have formed in response to chromite crystallization triggering sulfide melt segregation (Prendergast, 2021).

2.8.2.3. Breccia-style PGE mineralization.

The southern portion of the Lac des Iles Complex is the world's best example of breccia-style PGE mineralization that is primarily hosted in heterolithic magmatic breccia, vari-textured gabbro, and chlorite-actinolite schist (Barnes and Gomwe, 2011). Similar styles of PGE mineralization have been described at Nuasahi of India (Mondal et al., 2001), Legris Lake of Canada (Pettigrew and Hattori, 2002), Mayville of Canada (Yang et al., 2011), and Swan Lake of Canada (Maxeiner and Rayner, 2017); all of which were emplaced in Archean magmatic arcs. Mineralised breccias of the funnelshaped Aguablanca intrusion also formed in a continental arc setting, yet this intrusion contains relatively higher volumes of sulfide (up to massive) and grades (15.7 Mt. at 0.66% Ni, 0.46% Cu, and 0.47 g/t PGE; Tornos et al., 2001; Pina ˜ et al., 2006). Palladium-rich mineralization in the southern portion of the ~2.69 *Ga* Lac des Iles Complex occurs within sub-vertical (gabbro)noritic breccia pipes that are ~50–100 m in diameter and ~ 200–500 m in vertical extent (Stone et al., 2003). The ore zones are characterized by low volumes of finely disseminated sulfides (~ 0.5–3 vol%) with relatively high Pd/Pt (~ 7–14 compared to typical PGE reef-style deposits with ~0.5–2) values (Barnes and Gomwe, 2011). The gabbro-breccia zone of the Nuasahi intrusion also contains patchy sulfide mineralization with variable Pd/Pt values (1–73; Mondal and Zhou, 2010). While the exact mechanism(s) responsible for generating this Pd-rich breccia-style mineralization remains unclear, it is clear that they formed in response to several pulses of volatile-rich magma, which may be andesitic (e.g., Lac des Iles; Barnes and Gomwe, 2011) or boninitic (Mondal and Zhou, 2010). At Lac des Iles, it has been proposed that deuteric fluids upgraded pre-existing sulfides in Pd (Watkinson and Dunning, 1979; Hinchey et al., 2005) or that fluids have redistributed Pd to the mineralised zones (Djon and Barnes, 2012).

2.8.3. Stratiform Fe-Ti-V(–P) deposits

While chromitites and magmatic sulfides typically concentrate in the lower portions of layered mafic-ultramafic intrusions, stratiform Fe-Ti-V (–P) deposits typically occur in the central to upper portions of layered intrusions. They may manifest as massive layers, lenses, or pods of (titano)magnetite (i.e., magnetitite; e.g., Bushveld (Reynolds, 1985), Panzhihua (Zhou et al., 2005), Lac Dore (Mokchah and Mathieu, 2022), Sept Iles (Namur et al., 2010) and Windimurra (Ivanic et al., 2018) and (or) ilmenite (i.e., ilmenitite; e.g., Egypt's Korab Kansi and Abu Ghalaga intrusions; Khedr et al., 2022). Some of these examples are associated with apatite-rich oxide layers (i.e., nelsonite), such as the Bushveld (Tegner et al., 2006), Grader (Charlier et al., 2008), and Sept Iles (Namur et al., 2010, 2012, 2015b; Charlier et al., 2011) intrusions. The oxide layers typically have cm- to m-scale thicknesses (up to 18 m in the Jameson Range intrusion; Karykowski et al., 2017a), and typically share sharp to weakly diffuse contacts with bracketing rock units. Their bracketing units are often feldspathic, such as anorthosite (e.g., Bushveld Complex; Reynolds, 1985) or (leuco)gabbro (e.g., Rio Jacar´ e; Sa´ et al., 2005; Windimurra; Habteselassie et al., 1996; Fig. 10). However, oxide-rich layers may also occur within melagabbro (e.g., Panzhihua and Taihe; Zhou et al., 2005; Liu et al., 2015), norite (e.g., Abu Ghalaga; Basta and Takla, 1968; Bjerkreim-Sokndal; Duchesne and Charlier, 2005), troctolite (e.g., Baima, Liu et al., 2015), and rarely pyroxenite (e. g., Anyi and Hongge; Liu et al., 2015; Bell River Complex; Goutier, 2005).

The Bushveld's Main Magnetite Layer is one of 26 magnetitites (and six nelsonites) in the Upper Zone that range in thickness from 0.1 to 10 m (Reynolds, 1985; Tegner et al., 2006). It contains 5 to 20% TiO_2, and 1.5 to 1.8% V_2O_5 (Reynolds, 1985; Scoon and Mitchell, 2012) and once accounted for >50% of the world's annual V_2O_5 production (Crowson, 2001; Simandl and Paradis, 2022). The Lac Dor´e Complex is a thick (7–8 km) Neoarchean layered intrusion that possesses a 60–100-m-thick sequence of interlayered magnetitites with magnetite-bearing anorthosite, gabbro, and pyroxenite that persists laterally for ~17 km (Mathieu, 2019; Mokchah and Mathieu, 2022). The Mustavaara V-Fe-Ti deposit is an ~80-m-thick ilmenite-magnetite-rich layer that occurs with the lower part of a magnetite gabbro unit in the upper portion of the ~2440 *Ma* Koillismaa intrusion (Juopperi, 1977; Karinen et al., 2022). Many other Fe-Ti-V deposits are hosted in Proterozoic massif-type anorthosites, such as Korosten (Fedorivka, Ukraine; Duchesne et al., 2006), Damiao (Damiao, Maying, and Heishan, China), and Kunene (Oryeheke in Angola-Namibia; see review by Charlier et al., 2015a).

There are few global examples where magnetitites in the upper portions of layered intrusions possess anomalous PGE concentrations, such as Rio Jacar´e (Their bracketing units are often feldspathic, such as anorthosite; Sa´ et al., 2005), Freetown (Bowles et al., 2013), Nuasahi (Prichard et al., 2018), and Stella (Maier et al., 2003). In these examples, the Pt/Pd values of magnetitites may be low (~ 0.15 in Nuasahi; Prichard et al., 2018) or relatively high (~ 1.4 in Rio Jacar´e; Sa´ et al., 2005). The PGE are predominantly hosted in Pd-antimonides and bismuthides as well as Pt-arsenides that generally occur among interstitial silicates (Sa´ et al., 2005; Prichard et al., 2018). It is believed that the relatively late-stage saturation of magnetite and concomitant removal of Fe^{2+} from the liquid triggered sulfide melt segregation, where deposited sulfides and PGM may be converted to antimonides and arsenides during post-magmatic alteration (Prichard et al., 2018).

In several cases, the deposition of Fe–Ti oxide-rich layers has been ascribed to fluctuations in fO_2 (see Toplis and Carroll, 1995), triggered either through pressure increase and phase boundary shift (e.g., Bushveld, Klemm et al., 1985), differentiation (e.g., Baima, Zhang et al., 2012), and assimilation-crystallization (e.g., Panzhihua, Ganino et al., 2013; Lac Dore, Mathieu, 2019). Like chromitites, an increase in total pressure has been proposed for the formation of Bushveld magnetitites (e.g., Cawthorn and McCarthy, 1980; Cawthorn and Ashwal, 2009). Models involving fluctuations in intensive parameters do not preclude the occurrence of density-driven crystal settling and kinetic sorting (e.g., Wager and Brown, 1968). Density-driven segregation of oxides and silicates may have facilitated layer formation at the Grader (Charlier et al., 2008), Jameson Range (Karykowski et al., 2017a), and Bushveld (Vukmanovic et al., 2019) layered intrusions. Iron-titanium oxide-rich layers may be the crystalline or cumulate products of dense immiscible Fe-Ti-P liquid that segregates from, or emulsifies with, relatively buoyant Si-rich immiscible conjugate (Namur et al., 2012; Charlier et al., 2011, 2013; Veksler and Charlier, 2015; Hou et al., 2017, 2018; Zhang et al., 2023).

This petrogenesis has been applied to Fe-Ti-V layers in the Bushveld (Reynolds, 1985; Fischer et al., 2016), Skaergaard (e.g., Jakobsen et al., 2005), Sept Iles (Namur et al., 2012), Panzhihua (Zhou et al., 2013), and Baima (Liu et al., 2016) intrusions. Nelsonites of the Duluth Complex may also be a product of Fe-Ti-P liquid immiscibility (Ripley et al., 1998). The saturation of Fe–Ti oxides or segregation

of an immiscible Fe-Ti-P liquid may have been facilitated by magma mixing (Harney et al., 1990; Von Gruenewaldt, 1993). Magnetitite layers of the Bushveld's Upper Zone may have formed during bottom-up growth in the form of nodes (McCarthy et al., 1985; Cawthorn, 1994; Kruger and Latypov, 2020). This may have occurred via in situ crystallization in a liquid-rich system (Kruger and Latypov, 2020) or via crystal settling followed by upwelling of intercumulus melt and compositional convection (Yao and Mungall, 2022).

2.8.4. Non-conventional mineral deposits of layered intrusions

Layered intrusions may also be prospective for Ni–Co laterite deposits, REE-U-Th-Ta-Zr-Nb mineralization, andalusite, aggregates, and dimension stone. Approximately 15% of the world's Ni–Co laterite resources occur within serpentinised ultramafic cumulates of igneous intrusions, such as Wingellina Hills, Kapalagulu-Musongati, and Niquelandia (Butt and Cluzel, 2013; Smith and Maier, 2021). They form during the chemical and mechanical weathering of Ni-rich olivine cumulates, which works to concentrate Ni (average ~ 5%) and possibly Co (average ~ 0.06%) via the removal of soluble elements (Marsh and Anderson, 2011). Layered alkaline intrusions, such as those of the Gardar Province (Greenland) and Kola Peninsula (NW Russia) may be prospective for REE-U-Th-Ta-Zr-Nb mineralization (Marks et al., 2011). These elements become concentrated in peralkaline residual liquids during differentiation, which gives rise to mineralised (sometimes pegmatitic) syenitic roof rocks (Marks et al., 2011; Paulick et al., 2015). The metamorphosed country rocks bracketing the Bushveld Complex are the world's largest reserve of andalusite, which is extracted at Thabazimbi, Penge, and Lydenburg (Botha, 2010).

3. Novel observations from layered intrusions

3.1. Igneous layering draping over a few-km-high sloping step in the chamber floor

Igneous layering in mafic intrusions (see section 2.7) often results from the deposition of crystals from the overlying resident melt due to gravitational settling (Irvine, 1980a; Latypov and Chistyakova, 2020; Morse, 1986; Wager and Brown, 1968) or in situ crystallization (Campbell, 1978, 1996; Latypov et al., 2015a, 2020a, 2020b; McBirney and Noyes, 1979) on the c hamber floor that is planar and sub-horizontal in most magma chambers. As a result, igneous layering in maficultramafic intrusions normally has a sub-horizontal orientation. There are, however, exceptions from this general rule (e.g., Cawthorn, 2018) and one of the most notable is documented in the Bushveld Complex (Latypov et al., 2022b). Fig. 12a presents a section along strike across the Tonteldoos area in the southeastern Bushveld Complex that is subdivided into two major portions - the Roossenekal and Belfast subchambers. The floors to both sub-chambers curve upwards and are placed on an intervening Stoffberg remnant of non-deformed host rocks.

The floor contact of the Roossenekal sub-chamber has a spectacular ~6-km-high shelf relief (referred to as the Tonteldoos step) with a ~ 10 · slope across ~35 km up to the top of the Stoffberg remnant. This topographic relief of the floor contact controls a sub-chamber that was formed along an angular discordance to its host rock stratigraphy (Button, 1976). From north to south, the floor of the Roossenekal subchamber first coats the Steenkampsberg Formation, then truncates through the Houtenbek Formation and finally cover the Dullstroom Formation. The Roossenekal sub-chamber thus reaches its highest thickness in the north and becomes increasingly thinner towards the south where the Critical Zone (CZ) finally terminates against the intrusion floor. The Main Zone (MZ) and Upper Zone (UZ) extend across the entire area of the two sub-chambers. The MZ in the Roossenekal subchamber drapes over the sedimentary and volcanic floor rocks (Fig. 12a).

The most remarkable feature of this section is its igneous layering that is defined by prominent stratiform layers referred to as the Lower, Middle and Upper Mottled Anorthosites (LMA, MMA and UMA) (Van der Merwe, 2007). The layers are located close to the base of the MZ. The MZ layering is widely believed to abut the floor contact of the country rocks (e.g., Sharpe, 1985; Cawthorn et al., 2016; Setera and VanTongeren, 2018). However, the Anorthosite Markers do not actually disappear here but rather drape across the entire Roossenekal and Belfast subchambers, including the Stoffberg remnant (Van der Merwe, 2007). Several field traverses through the basal part of the MZ in both subchambers have been undertaken to map the Anorthosite Markers along strike (Latypov et al., 2022b). Field mapping shows that from north to south the thickness of the Anorthosite Markers decreases with no systematic changes in the texture of rocks. The occurrence of the Anorthosite Markers across the entire area is indicative of the deposition of MZ cumulates synchronously across the shallowest (i.e., Stoffberg remnant summit) and deepest (i.e., Roossenekal sub-chamber base) parts of the sub-chamber (Fig. 12b). This took place despite the two depositional places have a difference in elevation of ~4 km (Fig. 12b). It is important to stress that the local and regional geology shows no evidence for the depression of the floor rocks (e.g., through faulting or magma emplacement) and therefore the observed relationship cannot be due to *syn*- or post-emplacement subsidence of the Roossenekal subchamber and its host stratigraphy (Fig. 12a).

A key implication of these field relations is that the column of resident melt in the Bushveld chamber must have been thicker than the ~4.0 km height of the Tonteldoos step. Otherwise, it would be physically impossible to blanket the topographic relief of a temporary floor of the chamber with the igneous layering (i.e., LMA). Internal differentiation of a resident melt column that was thicker than the crystallized sequence is also indicated by a systematic decrease in An-content of plagioclase and Mg-number of orthopyroxene through the ~3.0-kmthick stratigraphy of MZ in the Roossenekal sub-chamber (Latypov et al., 2022b; Von Gruenewaldt, 1973). The passage to the overlying Pyroxenite Marker is marked by ~0.5-km-thick reversal towards minerals with more primitive composition. The reversal has been attributed to mixing of a residual MZ melt with new magma emplaced into the chamber (Cawthorn et al., 1991; Setera and VanTongeren, 2018; Vantongeren and Mathez, 2013), causing further vertical expansion of the chamber. Based on *Sr*-isotopic data, mass balance calculations show that the residual melt comprised 60–70% of the resulting hybrid magma (Kruger, 2005; Sharpe, 1985). This melt subsequently crystallized into a > 3.0 km thick sequence that overlies the Pyroxenite Marker. This means that the residual melt of the MZ must still have been ~2 km thick prior to the Pyroxenite Marker magma influx, thereby indicating that the initial MZ melt column was ~5 km in thickness. This is in line with earlier estimates that were based on thermal modelling of the Bushveld Complex (Cawthorn and Walraven, 1998). Following some previous studies (Cawthorn, 2013; Cawthorn et al., 2016), the instantaneous top of the cumulus pile during crystal deposition in this region is inferred to have been gently basinal and the Stoffberg remnant was partially separating the Roossenekal and Belfast sub-chambers (Fig. 12c).This interpretation is supported by the concave geometry of the Pyroxenite Marker within the Roossenekal sub-chamber which results in this layer to occur ~2 km stratigraphically lower at the centre of this sub-chamber compared to the Stoffberg remnant (Fig. 12b). This field relations suggest that the ~1.0 km and ~ 3.0 km thick MZ in the Roossenekal and Belfast subchambers, respectively, was produced synchronously from the same interconnected resident magma. The conclusion is further supported by similar An-content of plagioclase at the base of the MZ at both subchambers (Lundgaard et al., 2006; Cawthorn et al., 2016; Von Gruenewaldt, 1973; Setera and VanTongeren, 2018). The high thickness of MZ cumulates in the Roossenekal sub-chamber is likely owing to redeposition of crystals inside this depression and/or predominant crystallization in the deeper parts of the magma chamber caused by an increase in the liquidus temperature of the melt associated with a pressure increase with depth (Campbell, 1978, 1996; Jackson, 1961). The discovery of the topographic relief in an

inward-growing floor of the Bushveld chamber appears to be the first field-based evidence that allows to rigorously estimate the thickness of a resident melt at a specific period of the evolution of the magma chamber.

3.2. Transport of roof- and wall-derived materials to the magma chamber floor

Mafic layered intrusions commonly preserve compositional evidence of progressive crystal accumulation on the floor, roof and walls, demonstrating that these bodies formed from the inwards solidification of an essentially crystal-free body of mobile magma. Solidification results from both in situ nucleation and growth on inwards-propagating solidification fronts (c.f. Marsh, 1996), and heterogeneous nucleation on suspended particles in the bulk magma which then accumulate elsewhere. In any intrusion, the relative importance of these two processes varies both spatially and temporally, depending on the intrusion geometry, whether it is open to new batches of magma, the fluid dynamical behaviour of the magma, and the physical properties of the mush zones. In this section, we explore the mechanisms by which floor sequences form.

There are two mechanisms by which cumulates develop on the magma chamber floor. Firstly, crystals nucleated and grown elsewhere in the body may accumulate at the floor depending on the stability of any mush zones on the wall to gravitational collapse, and the balance between settling/flotation and convective entrainment. Secondly, crystals may nucleate and grow directly at the magma-mush interface at the floor. Which of these two mechanisms is dominant is fundamentally dependent on the extent to which the intrusion is closed to further magma input.

For the specific case of horizontal tabular intrusions created from a single injection, or from a series of injections that are sufficiently close to be treated as one, the resultant splitting of the geotherm means that cooling is fastest at the roof (Morse, 1986), driving convection [both thermal and two-phase]. The differing sensitivity to pressure of the temperature of the liquidus and adiabat means that, in an intrusion of km-scale height, down-welling magma becomes super-cooled: this drives nucleation and crystal growth in a boundary layer near the chamber floor (Irvine, 1970a). The resulting predominance of crystallization in the lower part of the bulk magma, together with accumulation of crystals derived from the roof and walls, either entrained in convection currents or following the collapse of these gravitationally unstable mush zones (e.g., Holness et al., 2022, 2023), means that the dominant location for crystal accumulation is the magma chamber floor. The resultant creation of an insulating blanket of mush on the chamber floor, together with the release of latent heat as the interstitial liquid crystallises in the floor mush, amplifies the initial asymmetry of cooling. This insulating floor blanket means that the large undercooling required for in situ nucleation of crystals from the bulk magma at the floor itself cannot be attained: thus, the nucleation of primocrysts directly on the chamber floor, via heterogeneous nucleation at the magma-mush interface, is only possible in a closed intrusion of km-scale height immediately after magma emplacement. Morse (1988) suggests that these effects become discernible when only ~100 m of floor blanket has been formed. This is supported by Holness et al. (2020), who argue from microstructural evidence that only the lowest few tens of metres of the floor cumulate sequence nucleated on the floor of the Skaergaard intrusion.

The solidification behaviour of open systems that are replenished by relatively small batches of super-heated magma is different, since the arrival of hot magma into a pre-existing body will trigger abundant nucleation and crystal growth. For the case of basaltic magmas, for which primitive liquids are denser than relatively evolved liquids, the incoming magma will pond on the chamber floor, leading to in situ heterogeneous nucleation and growth at the magma-mush interface. This is thought to be the cause of the striking dendritic olivine crystals of the Rum Eastern Layered Intrusion (O'Driscoll et al., 2007a).

A further consideration pertinent to the prevalence of accumulation (e.g., by settling) on the floor of mafic magma chambers of crystals nucleated and grown elsewhere is the density of the crystals relative to that of the magma. For example, the plagioclase-magma density paradox of Morse (1973) is based on the fact that, in much of the crust, plagioclase is less dense than the magma from which it crystallises, prohibiting the settling of plagioclase on the floor (though see recent work by Krattli ¨ and Schmidt (2021), who suggest that the pressure of neutral buoyancy of relatively anorthitic plagioclase in basaltic liquids is as high as 6 kbar, permitting gravitationally driven settling of plagioclase in magma bodies emplaced in the upper half of the crust). It is now recognized, however, that plagioclase can be brought to the chamber floor as part of a poly-mineralic crystal load in gravity currents of dense liquid, sometimes referred to as two-phase convection, in which the buoyant plagioclase grains are entangled with grains of denser minerals. It may also be brought to the floor in crystal-rich density surge currents in which plagioclase buoyancy only becomes significant during the final sorting to form graded layers, (e.g., Irvine et al., 1998; Scoates, 2000). Once at the floor, the plagioclase crystals could not float away, either because they were rapidly cemented into place by crystallization of the intercumulus liquid, because the yield strength of the interstitial liquid was too high, or because the plagioclase-enriched layer tops were immediately buried beneath denser cumulates (Irvine et al., 1998).

The accumulation on the magma chamber floor of material derived from elsewhere in the intrusion is straightforwardly demonstrated by the presence of autoliths. Coherent blocks derived from the intrusion roof are common throughout much of the floor cumulates of the Skaergaard (Fig. 13a), with evidence of localized disruption of the poorly consolidated crystal mush on which they landed (Irvine et al., 1998; Conrad and Naslund, 1989). Their concentration in certain stratigraphic horizons is consistent with repeated transient episodes of tectonic activity disrupting the roof sequence.

Evidence of accumulation of crystals brought to the floor by currents flowing down the walls and across the chamber floor is preserved by the presence of modally-graded layers (Irvine, 1980a) and evidence of reworking, such as layer truncations (Fig. 13b). The upper part of the Skaergaard floor cumulates contains some remarkable, stacked, crescentic modally graded layers known as trough bands, which are argued to have resulted from sedimentation in channels formed by long-lived ridges perpendicular to the walls, created by a temporary convective pattern in the bulk magma (Irvine, 1983a, 1983b; Irvine and Stoeser, 1978) (Fig. 13c). Although the firm identification of the ultimate source of the sedimented crystals in the channels is not possible, since the wellmixed nature of the bulk magma means that mineral compositions are the same on the inner margins of all solidification fronts (e.g., Salmonsen and Tegner, 2013), the direction of flow away from the nearby vertical walls is recorded by mineral lineations parallel to the trough axis (Wager and Brown, 1968; Brothers, 1964; Vukmanovic et al., 2018). This is consistent with evidence of loss of wall material, either by a continuous rain of poorly attached grains, or of episodic catastrophic collapse caused perhaps by local tectonic activity (Holness et al., 2022). While the inwards-propagating mush on the steep, km-scale, vertical walls of the Skaergaard intrusion was a major contributor of the crystals accumulating on the chamber floor, this cannot be the case in more tabular intrusions without such extensive walls, such as the Bushveld and Rum Eastern Layered Intrusions, and many layered smaller sills. The abundant evidence of magmatic lineations in the Rum cumulates are argued not to be a consequence of settling from magmatic currents but of post-accumulation slumping due to sagging of the intrusion floor towards the feeder (O'Driscoll et al., 2007b). A similar conclusion was reached for a lopolithic body in the Ardnamurchan igneous centre of NW Scotland (O'Driscoll et al., 2006). The longevity of sill-like intrusions like

Rum and Bushveld is due to their open nature, with repeated influxes of replenishing magma: hence, although crystals accumulating on the floor of these intrusions may have been sourced from the roof, they may also have been brought by incoming magma batches, or nucleated (either in situ on the floor or in the bulk magma) as a consequence of the arrival of magma out of equilibrium with the resident liquid (e.g., Latypov et al., 2015a, 2017a, 2017b, 2022a).

3.3. Igneous layering on the overturned to undercutting portions of a chamber floor

Crystals are normally deposited on the sub-horizontal chamber floor and, therefore, modal igneous layering also tends to be sub-horizontal. A disadvantage of the planar layering is that it gives almost no clue to the mechanism of crystal accumulation (i.e., gravity settling vs in situ crystallization). The situation has drastically changed with a recent documentation of exposures in which igneous layering was found to develop on non-horizontal portions of the chamber floor of the Bushveld Complex. The non-horizontal portions of the chamber floor are found in potholes (Fig. 14a) which are near circular to elliptical depressions with gently to steeply inclined, subvertical and even overturned sidewalls in which footwall cumulates have been eroded away (Ballhaus, 1988; Boudreau, 1992; Carr et al., 1994, 1999; Latypov et al., 2015a; Smith and Basson, 2006; Viljoen, 1999). Apart from having subvertical to overturned sidewalls, the potholes also show undercutting, sill-like bodies that extend laterally from pothole margins into the footwall (Ballhaus, 1988; Latypov et al., 2015a; Leeb-Du Toit, 1986) (Fig. 14a). Potholes likely persist throughout the entire stratigraphy of the complex but are most abundant in the Critical Zone in close association with the MR, UG1 and UG2 units (Hahn and Ovendale, 1994; Latypov et al., 2015a, 2017a, 2017b, 2019b; Lomberg et al., 1999; Mitchell et al., 2019; Viljoen, 1999). Initially, it has been found that 1–3 cm thick chromitite seams of the MR develop – without any notable changes in their thickness – along the subvertical and overturned sidewalls of potholes (Latypov et al., 2015a) as well as along the upper and lower margins of undercutting MR bodies (Latypov et al., 2017b) (Fig. 14a). One of the most remarkable undercutting MR bodies consisting of sulphide-bearing harzburgite to olivine-rich orthopyroxenite extended outwards from a pothole for about 300 m at about 20 m below the normal position of the MR. The apophysis was about 30 cm thick and had 1–2 cm thick chromitite seams along both its margins (Latypov et al., 2017b). Not only the chromitite seams but even the entire MR package may develop as a 'rind' covering all the chamber floor depressions and culminations, even where these are vertical or overhanging (Chistyakova et al., 2019a, 2019b) (Fig. 14b, c). One of these exposures was studied in detail and represents one side of ~2 m deep pothole that occurs within the footwall mottled anorthosite (Fig. 14b). In this exposure, the highly irregular surface of the footwall anorthosite is consistently draped by a 20–50 cm thick package of the MR orthopyroxenite/melanorite that is well developed along sub-horizontal, steeply inclined, subvertical and overhanging sidewalls. At the base of the pothole, the MR package increases to over a meter in thickness and in one place cuts into the footwall and is wholly hosted in mottled anorthosite (Fig. 14b). Similar field relationships with host cumulates were documented for the UG and MG chromitites (Hasch and Latypov, 2021; Latypov et al., 2017a). In potholes, the entire UG1/UG2 chromitite may develop along steeply-inclined, subvertical and even locally overhanging sections of pothole walls (Fig. 14d). Importantly, such a position of the chromitite layers as well as MR is primary because igneous layering in the footwall rocks is cut by pothole's margins (Fig. 14). In one case, a 15 cm thick undercutting UG1 chromitite body was observed to laterally extend from the UG1 pothole's margin into the host anorthosite for several meters (Mukherjee et al., 2017). The discovery that the MR package and UG1/UG2 chromitites may develop on subvertical to overhanging sidewalls of potholes and especially as undercutting, sill-like bodies within footwall rocks precludes the possibility of their formation by crystal settling at the chamber floor because sinking crystals cannot penetrate the solid cumulate rocks to reach overhangs and undercutting cavities. Such relationships can be reconciled with the formation of these cumulate layers in situ, i.e., directly at the floor of a magma chamber.

3.4. Magmatic karstification of the floor cumulates

Many layered intrusions show field and textural evidence for the erosion of their floor cumulates by magmas that replenish the evolving chambers. Such field observations are especially abundant in the Bushveld Complex, in which the erosion can be observed throughout its entire stratigraphy but are particularly common at the level of the Merensky Reef (MR) and UG2 chromitite (Boudreau, 1992; Eales et al., 1988; Hunt et al., 2018; Latypov et al., 2015a; Schmidt, 1952; Van der Merwe and Cawthorn, 2005; Viljoen, 1999; Viljoen and Hieber, 1986).

This is evident on the regional scale, when ~10–20 m of cumulates that vary in composition from anorthosites to orthopyroxenites have been removed by erosion (Viljoen, 1999). It is also well seen on a local scale, when footwall cumulates have been excavated to depths of a few meters to several dozens of meters in potholes (Latypov et al., 2019b; Latypov et al., 2017a, 2017b). The erosional surface is commonly considered to be sharp and planar so that the cumulate pile is direct overlain by the resident melt (Campbell, 1996; Latypov et al., 2015a; Wager and Brown, 1968). Recent studies indicate, however, that this may not be true for magma chambers that undergo repeated replenishments. In this case, the hard chamber floor may be separated from the overlying melt by an undercut-embayed transitional zone up to a few meters in thickness (Kruger and Latypov, 2021). This transitional zone is composed of a framework of in situ erosional remnants that are fully or partially interconnected with each other and the floor rocks in 3D space (Fig. 15a).

The origin of the undercut-embayed floor has been attributed to thermochemical erosion of the floor cumulates by highly reactive, superheated melts that replenished the evolving Bushveld chamber (Latypov et al., 2015a, 2022a; Latypov et al., 2017a, 2017b). High erosive power of the replenishing melts can be due to their chemical and thermal disequilibrium with the pre-existing floor cumulates. A major reason for thermal disequilibrium is melt superheating that can be as high as 90 °C for basaltic melts that ascend near adiabatically from a deep-seated magmatic reservoir (Latypov et al., 2020a, 2020b). A few tens of metres' thick column of such a melt can erode several metres of footwall rocks even if it arrives at the chamber at a much lower degree of superheating (say, 10-15 °C) due to some cooling along the way (Latypov et al., 2017a, 2017b). This happens because a principal agent of the erosion is chemical disequilibrium between the new melts and preexisting cumulates rather than the melt superheating itself (Kerr, 1994). In other words, the predominant erosional process is chemical dissolution (with some related cooling of the melt), and not pure melting of the floor cumulates. Melt superheating is still of importance, of course, because the non-superheated replenishing melts will start crystallizing soon after entering the chamber and will therefore produce a new cumulate layer that will drape over the existing floor cumulates and terminate their erosion.

During the initial stages shortly after magmatic recharge, the thermochemical erosion may be extremely effective, causing wholesale destruction of the floor rocks. The intensity of erosion will decrease with time so that it will be able to operate only along fractures and planes of weakness of the cumulate pile. Such partial melting will result in the complex, undercut-embayed morphology of the floor cumulates (Fig. 15b-d). In this undercut-embayed floor, the blocks that appear to be isolated in the two-dimensional exposures provided by outcrops may still, however, be connected with the floor in three dimensions. See, for example, section 4.9 and Fig. 37,

where magnetitite appears to be growing in situ on a hidden anorthosite inclusion connecting two other inclusions, one near the center of the profile and a smaller one towards the left (Kruger and Latypov, 2021). This phenomenon is referred to as magmatic 'karstification' of the chamber floor cumulates because both in morphology and origin this feature is similar to karst landforms in surface sedimentary rocks that are produced by infiltrating acidic water. A major result of this process is the formation of a few meters thick framework of erosional remnants that are spatially interconnected in 3D space. This framework separates the floor cumulates from the overlying resident melt.

The magmatic karstification (i.e., erosion by dissolution) of the floor cumulates by magmas that replenish the evolving chambers may be a common feature because most, if not all, large plutonic complexes grow incrementally via numerous events of magma emplacements (Campbell, 1996; Cawthorn, 1996; Charlier et al., 2015b; Irvine, 1975; Maier et al., 2018a; Nebel et al., 2013; Wager and Brown, 1968). These replenishing magmas can erode the chamber floor cumulates. Many more examples of the undercut-embayed floor may be reported from layered intrusions that show evidence for large-scale erosional unconformities (e.g., Stillwater, Rum, Penikat, Windimurra).

3.5. Three-dimensional framework of crystals in (oxide) cumulates

Many igneous cumulates in magmatic systems, including layered intrusions, appear to be composed of crystal aggregates – i.e., clusters of randomly oriented crystals (Philpotts et al., 1998, 1999; Philpotts and Dickson, 2000; Wieser et al., 2019). Such crystal clusters may be the basic 'building blocks' that form high porosity crystal frameworks that are the starting point for the development of igneous cumulates (Jerram et al., 2003). A major question that has been debated for the past several decades and remains unanswered: is this initial high porosity crystal framework produced by in situ growth (e.g. Campbell, 1978, 1987, 1996; Marsh, 1996, 2006; McBirney and Noyes, 1979), or did it form by the dynamic accumulation of grains grown elsewhere, and, if the latter, was the accumulation formed of individual grains or clusters (e.g. Holness et al., 2023; Philpotts et al., 1998, 1999; Philpotts and Dickson, 2000; Wieser et al., 2019)? An illustration of the controversy is the divergence of opinion concerning the formation of chromitites.

The UG1 chromitite of the Bushveld intrusion comprises 27 vol% of chromite grains <0.1 mm in diameter enclosed within oikocrysts of plagioclase up to 5–10 cm across (Figs. 16a, b). High-resolution X-ray computed tomography confirms the suggestion of Eales and Reynolds (1986) and Jackson (1961) that the chromite grains form a continuous framework in 3D space, extending through multiple plagioclase and pyroxene oikocrysts (Latypov et al., 2022a: section 3.10; Fig. 23a). As expected for such an open framework, the relationship between coordination number (the number of grains that each grain touches) and grain size differs from that expected for accumulations formed of originally isolated particles. For a maximum random packing of spheres of variable size, the coordination number increases systematically with grain size (Fig. 16d) because the larger surface area of the larger grains means they are likely to be in contact with many smaller grains. In the open chromite framework of UG1, however, the coordination number remains roughly constant at about 10 for grains larger than 150 μm.

The low packing density, and the relationship between coordination number and crystal size, in the UG1 chromite framework are not consistent with mechanical accumulation of separate, non-interacting chromite grains. Models involving accumulation of isolated grains, either via crystal settling (Irvine, 1977; Kinnaird et al., 2002; Lesher et al., 2019; Spandler et al., 2005; Wieser et al., 2019) or by kinetic sieving in a crystal-laden slurry (Maier et al., 2013; Mondal and Mathez, 2007; Mungall et al., 2016), followed by crystallization of plagioclase and orthopyroxene from the interstitial liquid, are therefore incorrect.

There remain two possible models. Firstly, the low packing density of the chromite framework may be achieved via mechanical accumulation (e.g., settling) of chains or aggregates of crystals (Holness et al., 2023; Philpotts et al., 1998, 1999; Philpotts and Dickson, 2000). The resultant high porosity is therefore a consequence of the highly irregular shape of the chains and clusters, illustrated by the strong effects of particle aspect ratio on the maximum random packing density (e.g., Williams and Philipse, 2003). Clusters of minerals other than chromite are common in extrusive rocks, and that they formed by aggregation (synneusis; Schwindinger and Anderson, 1989) of previously isolated grains is demonstrated by the presence in monomineralic clusters of zoned grains with different core compositions (Ferguson et al., 2015) or different outer compositional zones (Philpotts and Dickson, 2000). Grain clusters and chains of spinel-group minerals are also found in erupted lavas (e.g., Figs. 17a, b; Jackson, 1961), with post-accumulation sintering resulting in a coherent framework in associated cumulates (e.g., Fig. 17c). However, the ubiquity of this process is inconsistent with the development of some chromitite layers/seams along the overturned sidewalls of potholes and along the contacts of undercutting bodies, some of which are thought to have formed within the cumulate pile a few meters below the temporary chamber floor (Latypov et al., 2017a, 2017b). Detailed microstructural examination of a chromitite sample from a vertical Merensky Reef pothole wall also shows a relationship between coordination number and grains size significantly different from that of a random grain pack and similar to that of the UG1 (Latypov et al., 2022a). An alternative explanation is that the chromite framework formed by nucleation and growth of chromite in situ at the cooling magma chamber margins (Campbell, 1978, 1987, 1996; Marsh, 1996, 2006; McBirney and Noyes, 1979). Following Campbell (1978, 1986), Latypov et al. (2022a) proposed it occurs by heterogeneous nucleation on the pre-existing crystals.

The classical treatment of heterogeneous nucleation considers a spherical cap of the nucleating phase on a planar substrate: for such a system, the thermodynamic barrier to nucleation is reduced by a factor which is a function of the wetting angle, ϕ, of the nucleating phase. If the nucleating phase forms a continuous layer on the substrate surface, this wetting angle is zero and nucleation is effectively an adsorption process (e.g., Cantor, 2003). For non-zero wetting angles, the undercooling required to drive nucleation is smallest when there is a close match between the crystal lattices of the substrate and the nucleus: this is known as epitaxial nucleation and growth (Hammer et al., 2010; Mithen and Sear, 2014).

The accepted understanding of heterogeneous nucleation is that the substrate is of a different material to the nucleating phase. However, Campbell (1978) suggested that it could occur on a substrate of the same phase, resulting in the formation of monomineralic clusters and chains. He termed this process self-nucleation (later amplified to heterogeneous self-nucleation by Campbell (1987)), although there is no thermodynamic basis to support it. For example, the wetting angle is indeed 0° when the lattice of the nucleus is exactly aligned with that of the substrate of the same phase, but this situation actually describes continued growth of the substrate and not the nucleation of a new grain. A non-zero wetting angle occurs if the nucleus is misaligned with the substrate, related to the fluid-solid-solid dihedral angle, θ, via:

$$2\cos(\theta/2) = 1 - \cos\phi$$

Melt-bearing systems of geological interest have melt-solid-solid dihedral angles in the range $10–40^\circ$ for junctions formed by highangle grain boundaries (see compilation in Holness, 2006): these dihedral angles result in wetting angles of misaligned grains in the range $152–178^\circ$. These high wetting angles cause only minimal reduction in the kinetic barrier to nucleation, with continued growth of the existing substrate always energetically favored. If the lattice of the nucleating grain is aligned with that of the substrate, or has a twin orientation relationship, this would result in a low-energy grain boundary (and a high solid-solid-melt dihedral angle), and a consequent decrease of the kinetic barrier compared to a misaligned substrate: however, it will nevertheless always be favourable to

continue growth of the substrate rather than to nucleate and grow a new grain of the same phase. The concept of "heterogeneous self-nucleation" proposed by Campbell (1978, 1987) is not physically plausible, and the concept of growth of open monomineralic crystal frameworks by in situ nucleation needs to be revisited. A possible alternative mechanism, as yet untested for magmatic systems, is secondary nucleation (e.g., Ahn et al., 2022a, 2022b; Bosetti et al., 2022), by which pre-existing parent crystals of the same solute in the solution act as catalysts for further nucleation (Agrawal and Paterson, 2015; Myerson et al., 2019; Qian and Botsaris, 1997).

3.6. Clinopyroxene-plagioclase-plagioclase dihedral angle variations in layered intrusions

In textural equilibrium, three-grain junctions are formed by the meeting of three grain boundaries of constant mean curvature. For three-grain junctions comprising two phases, the angle between the two inter-phase grain boundaries is known as the dihedral angle and is controlled by the balancing of interfacial energies. For the specific case of three-grain junctions formed by the meeting of two grains of plagioclase and one of clinopyroxene (augite), the resultant dihedral angle, θ_{cpp}, is given by:

$$\gamma_{pp} = 2\,\gamma_{pc}\,cos\,(\theta_{cpp}/2)$$

where γ_{pp} is the energy of the plagioclase-plagioclase grain boundary and γ_{pc} is that of the plagioclase-clinopyroxene grain boundary (Fig. 18a).

Grain boundary energy for silicate minerals is anisotropic, resulting in a range of energies depending on the crystallographic orientation of the two grains involved, and a range of equilibrium dihedral angles. The median value of (true, 3D) equilibrium clinopyroxene-plagioclaseplagioclase dihedral angles, Θ_{cpp} (measured using a universal stage mounted on a transmitted light microscope), is ~109° with a standard deviation of ~1° (Holness et al., 2012a). Although this value of Θ_{cpp} is observed in granulites, that in dolerites and gabbros is generally out of equilibrium, with the three-grain junction geometry controlled instead by the kinetics of growth during solidification and falling in the range 78° - 105°. In most dolerites, three-grain junctions are formed by the meeting of planar augite–plagioclase grain boundaries (Fig. 18b), whereas in more slowly cooled mafic rocks the grain boundaries curve into the junction, creating higher angles (Fig. 18c). This difference is the consequence of variations in the anisotropy of plagioclase growth rates in response to changes in the cooling rate. In rapidly cooled rocks, there is very little growth on the plagioclase (010) faces that commonly form the walls of melt-filled pockets, resulting in the original melt-filled space being almost perfectly pseudomorphed by augite. The narrower junctions, formed by impingement of two plagioclase grains at a low angle, are commonly filled with glass or mesostasis, leading to a median value of Θ_{cpp} of 78° instead of the 60° expected for perfect pseudomorphing of pores formed by the impingement of randomly oriented plagioclase grains. Rocks with $\Theta_{cpp} > 78°$ have angles formed by the simultaneous growth of the plagioclase forming the walls of the pore in which the augite is growing, manifest by a change in curvature of the two augiteplagioclase grain boundaries as the three-grain junction is approached (Holness and Fowler, 2022; Fowler and Holness, 2022). This dependence on cooling rate means that Θ_{cpp} varies systematically in nonfractionated dolerite sills, with the highest values in the centre (Holness et al., 2012b).

Θ_{cpp} varies in a fundamentally different way in fractionated bodies such as layered intrusions. In such bodies, Θ_{cpp} has a constant value over considerable stretches of stratigraphy, with discrete stepwise changes in this constant value associated with changes in the liquidus assemblage.

Θ_{cpp} increases when a phase is added to the liquidus assemblage and decreases when the liquidus assemblage loses a phase (Holness et al., 2013). This behaviour is argued to be caused by stepwise changes in the cooling rate caused by changes in the contribution of the latent heat of crystallization to the enthalpy budget (Morse, 2011; Holness et al., 2013).

The most evolved regions of the floor cumulates of the Skaergaard Intrusion, East Greenland depart from the generally observed stepwise behaviour of Θ_{cpp} in layered intrusions. This part of the stratigraphy was the last to crystallize, with a consequently slow solidification rate and an expected high value of Θ_{cpp}. However, in the vicinity of the three-grain junctions the grain boundaries between plagioclase and (ferro-)augite are planar, with many of the narrower spaces between plagioclase grains filled with granophyre instead of augite (Fig. 18d). These features are typical of rapidly cooled dolerites (Holness et al., 2007a, 2007b, 2007c, 2013) and lead to a value of Θ_{cpp} of 78°. The departure from the behaviour of less evolved gabbros was attributed by Holness et al. (2013) to the cessation of plagioclase growth during final solidification of highly evolved interstitial liquid at the base of the mushy layer.

3.7. Cr-rich structures at the base of magnetitite layers

A common feature in many layered mafic intrusions is the occurrence of oxide-rich layers, such as chromitites and magnetitites. Because of their economic significance and importance for understanding magma chamber dynamics, their petrogenesis has garnered much attention. Many models invoke some process involving crystal settling or sorting to explain their origin (Bilenker et al., 2017; Maier et al., 2013; Scoon and Mitchell, 2012; Vukmanovic et al., 2019; Yao and Mungall, 2022; Yuan et al., 2017), partly because they consist of minerals with relatively high densities (e.g., 4.8 g cm^{-3} for Bushveld magnetite (Molyneux, 1972), compared to the more typical 2.7–3.3 g cm^{-3} for silicate minerals).

However, in the 1980s and 90s, remarkable discoveries were made (Cawthorn and McCarthy, 1980, 1981; Cawthorn et al., 1983; McCarthy et al., 1985; Cawthorn, 1994) that challenged some of the most popular ideas on how minerals accumulate to form oxide-rich layers.

Cawthorn and McCarthy (1980)'s work focussed primarily on the socalled Main Magnetite Layer (MML) from the Upper Zone of the eastern Bushveld Complex (see Fig. 12 for Bushveld stratigraphy), which is well exposed in a stream section from the Magnet Heights locality. By sampling this ~2 m thick, monomineralic layer consisting of almost pure titanomagnetite, they unveiled an extremely rapid yet surprisingly regular depletion in the Cr content upwards. To explain the rapid depletion, they argued that the layer had to form by fractional crystallization of magnetite from a relatively limited quantity of liquid, aided by the extremely high partition coefficient of Cr into magnetite (ranging from 100 to 2000, Shepherd et al., 2022). However, the remarkable regularity of the depletion presented a problem for the more commonly favored mechanism for fractional crystallization, i.e., crystal settling, a process that they argued would produce a homogeneous or more chaotic distribution in the Cr contents. Instead, they proposed the magnetitite layer had to grow predominantly by in situ crystallization or by settling that occurred over only very short distances (Cawthorn and McCarthy, 1980).

Cawthorn (1994) found additional evidence for in situ crystallization when he returned to collect samples along lateral profiles at the base of the MML. Another surprising result emerged; dramatic variations were present at the base of layer in the Cr_2O_3 contents which range from 1.0 wt% to >4.0 wt%. Cawthorn (1994) proposed that high-Cr areas represent the spots where magnetitite started nucleating and growing on the underlying anorthosite layer. As the magnetitite spread out laterally from the first nuclei, the Cr content became depleted. By analogy, this growth pattern was likened to mold growing on cheese. Cawthorn (1994) envisioned that the growth would proceed in such a way as to produce dome-shaped, high Cr structures at the base of the magnetitite layer. However, the data appeared highly irregular with the 10-m sampling spacing originally employed. To see if a more regular pattern would emerge, another

attempt was made to collect samples at progressively smaller sample spacings, ending up with a minimum sample spacing of 50 cm. Nevertheless, the patterns remained erratic. Cawthorn (1994) proposed that this was either because the 50 cm sample spacing was still too large or convective activity may have disturbed the melt's Cr-contents at the magma chamber's basal part.
In the following decades, portable X-ray fluorescence spectrometers (pXRF) became more compact, more powerful, and much more accurate, and were enabling the direct chemical analysis of rocks directly on field outcrops. Using this technology, Kruger and Latypov (2020) revisited Magnet Heights and performed chemical analysis of the magnetitite. One approach was to perform two-dimensional chemical mapping on the MML using a much-improved sample spacing of 4 cm. Their results confirmed Cawthorn (1994) initial prediction: several Cr-rich, domeshaped structures were found decorating the base of the MML (Fig. 19). These domes are about 20 cm wide, explaining why previous sampling attempts only resulted in irregular chemical patterns. Following Cawthorn (1994), Kruger and Latypov (2020) referred to these structures as growth nodes and agreed that they indicate the in situ crystallization of the magnetitite layer. Since then, Kruger and Latypov (2021) found similar structures in the lowermost magnetitite layer in the western Bushveld Complex (Fig. 37).
Because these discoveries were interpreted to suggest the in situ crystallization of the MML, the question arose as to how magmatic differentiation took place to produce the Cr-depletion upwards if crystal settling was not responsible. Cawthorn and McCarthy (1980) proposed the idea of diffusive bottom growth, stating that diffusion of Cr towards a growing magnetitite layer caused the lowermost part of the magma chamber to become depleted in Cr. Based on some experimental and theoretical studies (Martin et al., 1987; Seedhouse and Donaldson, 1996), Kruger and Latypov (2020) suggested that it may occur by the convective removal of thin (a few mm) liquid boundary layers surrounding magnetitite crystals. These boundary layers are formed by the diffusive extraction of mostly iron directly adjacent to the magnetitite layer, causing it to become lower in density until it is removed by the effects of gravity. Mixing of these boundary layers with the supernatant melt would cause magmatic differentiation of the overlying liquid, which was presumed to be a relatively thin (40–100 m) layer of melt that arose as a basal flow during a magmatic recharge event.
Yao and Mungall (2022) recently proposed an alternative model to explain these geochemical features of magnetitite layers that involve crystal settling. They proposed that crystal settling initially produced a blanket of magnetitite crystals with a uniform Cr concentration. Later, Cr-rich melts percolated upwards through the magnetitite layer, upgrading its Cr contents. A greater flux of Cr-rich liquid occurred where the underlying rock had a higher porosity, producing the dome-shaped, Cr-rich structures. This model received some criticism from Cawthorn and McCarthy (2023) who stated that it would be unable to explain the reversals in Cr that commonly occur within magnetitite layers.

3.8. Co-existing melt inclusions of contrasting composition in minerals

Melt inclusions of contrasting composition have been recognized as being trapped in various phases of cumulate rocks. Such observations have first been made in lunar rocks by Roedder and Weiblen (1970). These authors interpreted those inclusions as evidence for late-stage silicate liquid immiscibility producing paired Si-rich and Fe-rich melts. Similar textures were also identified in a broad range of terrestrial basalts, either as inclusions in phenocrysts or in the mesostasis (Philpotts, 1981, 1982). Fully recrystallized melt inclusions have then been found trapped in cumulus phases of Skaergaard (Jakobsen et al., 2005, 2011), Sept Iles (Charlier et al., 2011), Bushveld (Fischer et al., 2016), Baima (Liu et al., 2014), and Panzhihua layered intrusions (Wang et al., 2018). Host phases are usually plagioclase, pyroxenes and apatite. Similar inclusions were found in the Sudbury Igneous Complex (Watts, 2014) but the bimodal compositions have been interpreted to result from emulsion of superheated norite and granophyre source rocks (Zieg and Marsh, 2005). They would rather represent incomplete mingling rather than unmixing.
Inclusions are fully crystallized and contain different daughter minerals in various proportions. Feldspar, pyroxenes, olivine Fe–Ti-oxides, apatite, and amphibole are most common. Minor phases such as ilvaite, chlorite, biotite, and quartz have also been identified. Homogenization temperatures of melt inclusions are in the range 1040–1100 ◦C. Compositional variability observed for those inclusions is usually more extensive than those in paired experimental melts (Fig. 20). The origin of the compositional diversity may be produced by several processes. Trapped melt may re-equilibrate with the host phase (usually pyroxene, plagioclase and apatite) and crystal nuclei may be trapped with the melt. The presence of hydrous phases is commonly interpreted as resulting from post-entrapment alteration processes, commonly observed in highly cracked apatite grains. The hightemperature re-homogenization process of the multiphase inclusions may also produce the incorporation of a higher component of the host phase in the quenched glass. The variability has also been interpreted as a result of the liquid immiscibility process (Jakobsen et al., 2011). Indeed, the absence of a clear compositional gap between the Si-rich and the Fe-rich melts is explained by heterogeneous trapping of an emulsion of immiscible liquids. This interpretation has been corroborated by the imaging of nano-emulsions in ferrobasalts (Honour et al., 2019a) supporting that incomplete separation of the immiscible melts is a common phenomenon.
The occurrence of multiphase inclusions of contrasting composition can be used as an indicator for the onset of immiscibility along the liquid line of descent. In Skaergaard, abundant inclusions in plagioclase from Lower Zone c are witnesses of entrapment of immiscible liquids from this zone. Early immiscibility would thus start after 60–65% crystallization at 1100–1115 ◦C (Thy et al., 2009). This temperature is significantly higher than the onset predicted by experimental studies (maximum 1040 ◦C, see e.g., Honour et al. (2019b), Zhang et al. (2023) and references therein) but is fully supported by emulsion observed in ferrobasalts from Hawaii, Iceland and Snake River Plain with estimated temperature of 1100–1115 ◦C (Honour et al., 2019a). Studies of inclusions trapped in apatite have lower estimated temperatures (1060–1020 ◦C; Fischer et al., 2016; Wang et al., 2018) but immiscibility may have started before apatite becomes a liquidus phase.
The novel observation of the common occurrence of multiphase inclusions in liquidus phases of relatively evolved cumulates in several layered intrusions is an obvious support for the importance of immiscibility in ferrobasaltic melts. The inclusions are snapshots of the equilibrium immiscible melts, thus linking observations made in basalts and experimental studies to those in slow cooling magma chambers of plutonic environments.

3.9. Thermal and chemical histories recorded by plagioclase

The shape of plagioclase grains is dependent on growth conditions, particularly undercooling. Under conditions of small undercooling, grain growth is controlled by the kinetics of attachment at interfaces (Kirkpatrick et al., 1976; Kirkpatrick, 1977; Cabane et al., 2005). A detailed study of plagioclase microlites in intermediate volcanic rocks shows that the shape of plagioclase grains grown under interfacecontrolled conditions evolves from a prismatic shape of the smallest microlites towards tabular shapes flattened parallel to (010) for the larger grains (Mangler et al., 2022). The shape of the tablets is dependent on cooling rate, being more equant in more slowly-cooled rocks (Coish and Taylor, 1979; Shea and Hammer, 2013). Extracting information about the true 3D shape, or range of shapes, from single 2D thin sections necessitates assuming that all grains (or size groups of grains) have the same shape (e.g., Higgins, 1994, 2000; Mangler et al., 2022) but a useful comparison of the overall difference in plagioclase shape between samples is the average

apparent aspect ratio (the arithmetic mean of the population of length/width ratios) of the grain intersections in a thin section, AR (Meurer and Boudreau, 1998; Boorman et al., 2004; Holness, 2014, 2015).
Although AR cannot be used to quantify the true 3D grain shape (or range of shapes) present in a sample, it varies in a systematic manner through non-fractionated tabular mafic intrusions in which there is no preferred grain orientation and in which grain growth primarily took place in inwards-propagating marginal solidification fronts. It is strongly correlated with the time taken to crystallize according to the relationship:
AR = 0.5586 [6.34–*log*(crystallization time in years)]
where the crystallization time is calculated assuming diffusive heat transport, a country rock temperature of 0 ◦C, and a crystallization interval of 1200–1000 ◦C during which latent heat is released at a constant rate (Holness, 2014). It is this sensitivity to cooling rate of the anisotropy of attachment kinetics during plagioclase growth which controls the geometry of clinopyroxene-plagioclase-plagioclase three-grain junctions formed during solidification, resulting in the variation of median dihedral angle, Θ_{cpp}, with cooling rate.
In layered intrusions, the shape of plagioclase grains is controlled not only by cooling rate, but also by the location of growth. Randomly oriented grains nucleating in situ at the magma-mush interface are characterized by highly irregular grain boundaries showing no relationship to planar growth faces (Fig. 21a), due to impingement against neighbouring grains. Impingement also affects the overall shape, since it results in the cessation of growth in the primary growth direction, meaning that further growth must occur on the slower-growing faces (e. g., Schiavi et al., 2009): thus grains growing in isolation are commonly more non-equant than those which underwent early impingement (Martin et al., 1987). In contrast, plagioclase primocrysts that nucleated and grew elsewhere and accumulated by sedimentation or flotation are tabular, with grain boundaries closely corresponding to growth faces (Fig. 21b), particularly in orthocumulates with abundant interstitial phases. If such crystals have a preferred alignment, adjacent grains are likely to be in contact on their slow-growing faces, resulting in an increasingly non-equant habit during continued growth (Brown, 1956).
Changes in plagioclase growth conditions are also recorded by compositional zoning. The conventional understanding of interstitial overgrowth is that plagioclase rims record an evolution from the essentially constant core composition towards more albitic compositions as the interstitial liquid progressively fractionated. However, detailed work on the Skaergaard intrusion shows that while the expected normally zoned plagioclase crystals are indeed present, there is a significant number of grains for which the overgrowth has an outer region of constant composition. This was attributed to compositional buffering during extensive convection within the mush by Toplis et al. (2008), but Namur et al. (2014) showed that the composition of this outer region changes in a stepwise fashion through the stratigraphy, being An_{56} in the lowest parts, changing to An_{51} and then to An_{40} at higher levels. In the main magma body, these compositions correspond to those of plagioclase primocrysts (e.g., cores) at the appearance of cumulus clinopyroxene (An_{56}), Fe–Ti oxides (An_{51}) and apatite (An_{40}). This compositional buffering was therefore interpreted by Namur et al. (2014) as a consequence of enhanced release of latent heat of crystallization at the appearance of a new interstitial phase in the crystal mush, resulting in thermal buffering and the adcumulus growth of plagioclase rims of constant An-content in an analogous process to that creating the stepwise variations of Θ_{cpp} described above. That not all grains in any sample show this constant rim, with some displaying normal zoning and others with no marginal zoning, is dependent on local porosity variations in the mush. The distribution of the various types of plagioclase grains throughout the Skaergaard intrusion can therefore be used to infer the spatial variability in the physical properties of the crystal mush, such as the residual porosity, both at an intrusion-wide scale and at a millimetre- to centimetre-scale.

The trace element composition of interstitial overgrowth of plagioclase primocrysts record valuable information about processes occurring in the mush. Humphreys (2009) showed that the saturation of the interstitial liquid in Fe–Ti oxides is recorded in normally-zoned rims by a change from one of increasing Ti content with decreasing An-content, to one of decreasing Ti content. This change occurs at An_{55}, which is the composition growing from the bulk magma at the moment of saturation in Fe–Ti oxides. In detail, however, the interstitial plagioclase within a single thin section displays two distinct trends that correlate with the mineral assemblage in adjacent pockets of fine-grained interstitial material, with reverse An zoning associated with Fe-rich mineral assemblages, and normal zoning associated with pockets of granophyre (Humphreys, 2011). These are interpreted as late-stage pockets of unmixed immiscible liquids: the plagioclase that crystallises from these two liquids diverges once chemical communication between the two immiscible conjugates is lost. The distribution and compositions of these plagioclase zoning trends vary systematically as a function of stratigraphic height and spatial location within the intrusion, with the potential to constrain the spatial distribution and differential movement of interstitial immiscible liquids.
Namur and Humphreys (2018) investigated the behaviour of highly incompatible trace elements in plagioclase during solidification of the Skaergaard floor cumulates (known as the Layered Series). They observed that rare earth elements (REE) concentrations in plagioclase cores do not follow a stratigraphic evolution that is compatible with simple fractional crystallization of the ferro-basaltic parental magma. In particular, they noticed that, in the upper 20% of the Layered Series, plagioclase cores are depleted in REE compared to what would be expected from fractional crystallization. They argue that this indicates that at this stage of magma chamber solidification, fractional crystallization became less efficient, with significant in situ equilibrium crystallization. In contrast to what is observed in plagioclase cores, REE show very large compositional variations in plagioclase overgrowths which crystallized from the interstitial melt. REE are present in plagioclase rims in concentrations that strongly exceed the highest concentrations observed in plagioclase cores at the top of the Layered Series. This is likely related to the development of silicate liquid immiscibility in the crystal mush and crystallization of plagioclase rims dominantly from the Fe- (and REE-) rich melt (Namur and Humphreys, 2018). Note, however, that other processes such as delayed apatite nucleation or clinopyroxeneplagioclase subsolidus diffusive equilibration could also contribute to the formation of REE-rich plagioclase rims (Kieffer et al., 2023).

3.10. Textural and chemical features of minerals revealed by X-ray microscopy

Zoning in cumulus minerals is ideally only present in orthocumulates, in cases where diffusion is too slow to allow for continuous equilibration during crystallization of intercumulus material. It is typically only noted in plagioclase due to the slow diffusion of coupled NaAl-Ca-Si components. However, advent of thin section scale microbeam element mapping by laser ablation (TOF)-ICP-MS and particularly by synchrotron microbeam XRF has revealed hitherto cryptic zonation in slow-diffusing minor elements such as Cr and Ti in pyroxene (Schoneveld et al., 2020). This zoning tends to be more evident in smaller intrusions but can also be seen in large ones (Fig. 22). It takes various forms including normal zoning (Cr-depleted, Ti-enriched rims), sector zoning, oscillatory zoning and combinations thereof. The presence of sector zoning within pyroxene oikocrysts is further evidence for their growth under undercooled or otherwise supersaturated conditions where growth outstrips diffusion. Prominent oscillatory and reverse zoning as

at Kevitsa (Fig. 22c) testifies to disruption of crystal mush by multiple injections of magma; the unusually strong development of this feature at Kevitsa is accompanied by general lack of clear layering and chaotic cryptic variations in sulfide composition.
A further observation elucidated by synchrotron XRF is the presence of reverse zoning of plagioclase, previously noted by Morse et al. (2017). This feature is particularly well developed in anorthosite immediately beneath the Merensky Reef where it may be indicative of extraction of partial melt at an erosional contact (Latypov et al., 2023a, in review). The geometry of zoning in Skaergaard intrusion plagioclase has been used to argue against gravitationally-driven compaction involving changes in grain shape (Holness et al., 2017c).
High-resolution X-ray microtomography (HXRT) was first applied to mafic igneous rocks by Philpotts and Dickson (2000), who identified open three-dimensional plagioclase frameworks in dolerites. Subsequent HXRT studies have focussed on the structure of magmatic sulfide aggregates (Godel et al., 2006a, 2006b) and disseminated chromite (Godel et al., 2013; Latypov et al., 2022a). Chromite in particular displays a very strong tendency to form interconnected 3D "chicken-wire" chains that cannot be explained as the result of random accumulation of individual crystals (Fig. 23a). The origin of these features remains a matter of debate (see section 3.5).
A particularly informative application of MicroCT has been on the distribution of sulfides and platinum group element minerals (PGMs) within oxide-hosted PGE reefs. In the case of the Merensky Reef, larger PGMs are found preferentially associated with 3D triple points between chromite, silicate and sulfide (Fig. 23a, b), indicating that PGMs nucleated and grew in place from sulfide at preferential nucleation sites, rather than being mechanically collected by settling sulfide droplets (Godel et al., 2010). In the Pd-rich layers of the Platinova Reef, Pd takes the form of Pd–Cu alloy (skaergaardite) attached to spherical droplets of bornite-chalcocite, indicating collection by a Cu-rich sulfide liquid. The best-developed droplets are enclosed within cumulus ilmenite grains, suggesting that they formed early as highly Pd-enriched Cu sulfide liquid; droplets outside ilmenite grains show widely variable Pd–Cu proportions attributable to partial redissolution of the Cu sulfide component leaving the alloy phase behind (Godel et al., 2014). Very similar textures, but with Au–Cu alloy, are found in the Au-rich layers of the unit, indicating a similar mechanism (Holwell et al., 2016).

3.11. Intrusion-scale to mineral-scale isotopic heterogeneity

Radiogenic isotope systems have been used to date layered intrusions and evaluate magma (mantle) source characteristics. Magma fractionation alone does not affect these isotope compositions, so they are also potentially powerful tracers of parental melt composition and, where there is evidence of isotopic heterogeneity, crustal contamination and/ or new magma replenishment. In early studies of the Stillwater, Muskox, Bushveld and Rum layered intrusions, open-system magmatic behaviour was confirmed by fluctuations in initial $^{87}Sr/^{86}Sr$ and $^{143}Nd/^{144}Nd$ values through the cumulate record, generally attributed to (the input and) mixing of isotopically distinct magmas (DePaolo and Wasserburg, 1979; Stewart and DePaolo, 1992; Kruger and Marsh, 1982; Palacz, 1985). By contrast, large sections of the Skaergaard and Kiglapait intrusion cumulate piles were found to exhibit relatively homogeneous $^{87}Sr/^{86}Sr_i$ and $^{143}Nd/^{144}Nd_i$ isotopic compositions (Stewart and DePaolo, 1990; DePaolo, 1985), lending considerable weight to the existing interpretations of these bodies as the products of closed system fractionation. In the aforementioned studies, the setting of correlated isotopic data in the context of layered intrusion stratigraphy proved a powerful approach to understanding solidification history. Many intrusions have benefitted from studies of their isotope geochemistry over the past 45 years, both with respect to the isotope systems mentioned above and others (e.g., Os, Pb, Hf). The iterative nature of everimproving field and petrological constraints, as well as technological advances (e.g., increased sample throughput) means that isotopic variation has been scrutinized at ever decreasing length-scales, and multisystem 'isotope stratigraphies' with complementary major and trace element data, now exist for many layered intrusions. In general, differences in radiogenic isotope characteristics from one intrusion to another are a consequence of mantle source and parental melt composition, as well as the composition (and degree of interaction with) the surrounding country rocks (O'Driscoll and VanTongeren, 2017a, 2017b).
A key theme emerging from recent isotope geochemical studies on layered intrusions is that the analysis of multiple isotope systems in the same (hand specimen) samples is extremely insightful. For example, Fourny et al. (2019) applied an integrated Pb-Sr-Nd-Hf approach to the Kiglapait intrusion that they set in the framework of the classic upwardincreasing percent solidified (PCS) classification of Morse (1969). Kiglapait solidified mainly as a closed system, verified by relatively uniform $^{143}Nd/^{144}Nd_i$ and $^{176}Hf/^{177}Hf_i$ profiles through the body, but may have experienced progressively increasing amounts of crustal contamination (evident in $^{87}Sr/^{86}Sr_i$) and late-stage hydrothermal alteration (deduced from Pb isotope disequilibrium between plagioclase and mafic phases).
Another important finding is that different mineral phases within cumulates may not be in isotopic equilibrium with each other. Roelofse and Ashwal (2012) reported that separates of plagioclase and mafic silicates (e.g., orthopyroxene) from the lower Main Zone of the Bushveld intrusion yield different $^{87}Sr/^{86}Sr_i$ at hand sample lengthscales. The latter authors used these data, together with other petrological constraints, to propose that the lower Main Zone, which does not show significant evidence for large-scale differentiation, must have formed by repeated replenishment of crystal mush batches. The different batches contained isotopically distinct crystal populations because they tapped different (compartmentalized) staging chamber(s) each containing magma that had undergone different degrees of interaction with the surrounding crust.
The osmium isotope system is different to those discussed above in being strongly controlled by sulfide (and platinum-group mineral) phases, typically present in very low abundances in silicate-dominated cumulates, demonstrating that even trace quantities of a given phase can dominate bulk rock isotope composition(s). Day et al. (2008) analyzed Os isotopes through the Muskox cumulate sequence, integrated these with other geochemical data, and quantified crustal contamination associated with specific (cyclic) replenishment magma events. The latter study also reported relatively radiogenic $^{187}Os/^{188}Os_i$ for Muskox chromitites and attributed chromitite formation to magma-crust interaction. The important observation that layered intrusion chromitites have a relatively radiogenic Os isotope composition has been noted for other localities (e.g., Rum; O'Driscoll et al., 2009a) and was combined with *Sr* isotopes to unequivocally demonstrate that Bushveld chromitites formed by the interaction of isotopically distinct components (Fig. 24; Schoenberg et al., 1999).
The examination of individual crystals for intra-crystal isotopic heterogeneity has had important consequences for our understanding of crystal mush assembly and solidification. Tepley and Davidson (2003) showed, via a high-precision micro-milling and ID-TIMS approach to cumulus plagioclase from the Rum intrusion, that individual crystals in troctolite samples contained zones with resolvable, different $^{87}Sr/^{86}Sr$ compositions that correlated with variation in anorthite content. These authors proposed that crystal cargoes convected around the putative Rum magma chamber, such that they were exposed to melts characterized by different isotopic compositions (see also Morse et al., 2017). Though initially beset by laser/instrument-induced isotopic fractionations and molecular interferences (e.g., ^{87}Rb), technological advances in laser ablation systems have led to an increase in the application of LAICP-MS to $^{87}Sr/^{86}Sr$ studies of layered intrusions in recent years. An advantage of LA-ICP-MS over micro-milling and ID-TIMS is the rapid throughput and coverage of more sample material. From such studies, intra-crystal isotopic heterogeneity does not appear to be ubiquitous in layered intrusions. Hagen-Peter et al. (2019) observed homogeneous $^{87}Sr/^{86}Sr_i$ in plagioclase at hand-specimen length-scales, over much (~2 km) of the thickness of the Skaergaard cumulate pile and argued that the intrusion evolved with only minor

crustal assimilation and no new magma input during its solidification. These findings contrast somewhat with the earlier study of McBirney and Creaser (2003), who reported mineral scale Sr and Nd isotopic heterogeneity in cumulates throughout the Skaergaard intrusion; however, these data were interpreted as reflecting postcumulus high-temperature metasomatism and not opensystem magmatic behaviour in the conventional sense. Wilson et al. (2017) analyzed cumulates from the lowermost (Basal Ultramafic Series, Marginal Zone and Lower Zone) portions of the Bushveld and found that though $^{87}Sr/^{86}Sr_i$ ranged over 0.7042–0.7076 in the sequence studied, plagioclase $^{87}Sr/^{86}Sr_i$ isotope composition did not vary significantly at the hand specimen scale.
Karykowski et al. (2017b), reported intra-plagioclase $^{87}Sr/^{86}Sr_i$ analyses from samples spanning ~6 km of the Bushveld stratigraphy (Marginal, Lower, Critical, Main and Upper Zones) and, in contrast to Wilson et al. (2017), reported complex intra-crystal heterogeneity in most of their samples, that they attributed to the input of mafic magma into the crystal mush, displacing the resident interstitial melt, i.e., at the postcumulus stage. An intriguing conclusion from the Karykowski et al. (2017b) study is that an apparent decoupling between the evolution to relatively radiogenic $^{87}Sr/^{86}Sr_i$ and indices of magma differentiation might be due to contamination by relatively small amounts of carbonate footwall country rock. Hepworth et al. (2020a) returned to the micromilling and ID-TIMS approach of Tepley and Davidson (2003) and applied this to intercumulus plagioclase and clinopyroxene associated with thin PGE-enriched chromitite seams in peridotites of the Rum intrusion. Hepworth et al. (2020a) identified resolvable isotopic heterogeneity within crystals of both phases and proposed a model where chromitite seams crystallized via repeated intrusion of the crystal mush by thin sheets of primitive (reactive) melt, recycling crustal isotopic signatures from older cumulate as they did so. The implication for the Rum intrusion is that much of it may have been constructed as a sill complex, rather than solidifying from a magma chamber.
Isotope geochemistry continues to offer a powerful means of interrogating the crystallization record of layered intrusions. Future advances will certainly come from additional studies that apply multiple isotope systems to the same cumulate sequences. Understanding the contributions from different mineral phases is also extremely important.
For example, Day and O'Driscoll (2019) recently showed that the longlived $^{186}Os/^{188}Os$ system distinguished an Archean component in sulfide-bearing cumulates of the ~60 *Ma* Rum intrusion. There is also significant scope for the application of stable isotope geochemistry. Although the sulfur isotope system is well established as a means of tracking crustal contaminants in sulfide-bearing cumulates (including ore deposits), the use of other, novel stable isotope systems to layered intrusions is in its infancy (see sections 4.18, 4.19). To date, iron isotopes have been used to evaluate magmatic differentiation with respect to Fe–Ti oxide fractionation in the upper part of the Bushveld Complex (Bilenker et al., 2017), as well as postcumulus isotopic equilibration in the Baima layered intrusion (Chen et al., 2014). Other systems (e.g., Mo, Zn) have enormous potential for fingerprinting different crustal contaminants and elucidating ore-forming processes.

3.12. Out-of-sequence zircon ages

The recent application of high-precision U–Pb TIMS dating to the Bushveld and Stillwater Complexes (Mungall et al., 2016; Scoates et al., 2021; Wall et al., 2018) has resulted in a quite unexpected discovery that may have dramatic implication for our understanding of the formation of layered intrusions. The essence of this finding is outlined here using, as an example, the Stillwater Complex, USA. Wall et al. (2018) have presented results of U–Pb zircon geochronology through the entire magmatic stratigraphy of this layered intrusion (Fig. 25). This is arguably the most detailed high-precision geochronologic study ever undertaken for a mafic-ultramafic layered intrusion. The results are notable for two reasons. Firstly, the weighted mean $^{207}Pb/^{206}Pb$ dates of zircons from the studied rocks is turned out to span an interval of ~3 million years from 2712 to 2709 *Ma*. This enormous age interval is in sharp contrast to a common notion that emplacement and crystallization time of a typical layered intrusion, even as large as the Bushveld Complex, is unlikely to exceed 0.1–0.2 *Ma* (e.g., Cawthorn and Walraven, 1998). Secondly, and even more surprisingly, the isotopic ages of zircons do not become progressively younger from the base towards the top of the complex, as it would be expected from the stratigraphic law of superposition. Rather, the ages are out-of-sequence, i.e., they change a few times from old to young ones and backwards with moving up-section of the Stillwater Complex. Four main time episodes are postulated from the ages, with the interval between the episodes being about 1 *Ma*. From older to younger, the time episodes are as follows: (1) 2712 *Ma* for the Basal series, (2) 2711 *Ma* for the entire Bronzitite zone together with the uppermost part of the Peridotite zone; (3) 2710 *Ma* for cyclic units of the lower Peridotite zone and Norite 1 of the Lower Banded series and finally (4) 2709 *Ma* for the rest of the Banded series, including Olivinebearing zones 1 to 5, Gabbronorite zones 1 to 3 and Norite 2 (Fig. 25). Similar life span and out-of-sequence ages have also been reported for the Bushveld Complex (Mungall et al., 2016; Scoates et al., 2021). In particular, Scoates et al. (2021) concluded that this complex was built incrementally over an ~5 Myr interval from 2060 to 2055 *Ma*. They postulated four main time episodes, with the interval between the episodes ranging between 1 and 2 *Ma*. From older to younger, the time episodes are as follows: (1) 2059–2060 *Ma* for multiple orthopyroxenitic units (e.g., Merensky Unit or UG2) in the Upper Critical Zone, (2) 2057 *Ma* for multiple orthopyroxenitic units (e.g., LG1 to LG6) forming the Lower Critical Zone; (3) 2055–2056 *Ma* for multiple ultramafic sills forming the Lower Zone and multiple gabbronorite units forming the Main Zone. (4) 2055 *Ma* for the multiple ferrogabbro units forming the Upper Zone. There are expectations that similar out-of-sequence geochronology will be reported in the future from other maficultramafic layered intrusions. The interpretation of these new fundamental observations is currently a matter of a hot debate (see section 4.3), but regardless of its outcome, the realization that geochronological ages of zircons may vary in a random manner across the stratigraphy of layered intrusions is clearly a "wake-up call" for researchers of layered intrusions. Owing to these findings, we are now aware that any single, highly precise U–Pb isotopic age obtained from some igneous rock of a layered intrusion (and likely other magmatic complexes), irrespective of how small its error is, must be regarded and interpreted with extreme caution. This is because (a) we do not know how long a life span of the intrusion is (at least 3 to 5 *Ma*) and (b) we do not understand what events/processes in the history of this intrusion this age actually dates (Latypov et al., 2017c; Latypov, 2019; Latypov and Chistyakova, 2022).

3.13. Skeletal/dendritic growth revealed by phosphorus zonation

Olivine generally occurs as a major phase in layered intrusions. It rarely displays growth zoning of major and some minor elements, such as Fe, Mg and Ni, due to fast diffusion of these elements at high temperatures. Phosphorus (P) is generally incompatible to olivine and is very low in concentration (<0.1 wt%) but diffuses extremely slowly, making P zoning of olivine resistant to diffusion equilibration at magmatic temperatures over millions of years (Watson et al., 2015). The P zoning of olivine can thus be a powerful tool to decode the hightemperature crystallization and cooling histories of layered intrusions.
The P zoning of olivine in natural rocks can be easily identified by the X-ray elemental mapping using electron probe micro-analyzer (EPMA). Distinct P zoning patterns of olivine have been revealed for the ca. 260 *Ma* Baima layered intrusion in SW China and the ca. 564 *Ma* Sept Iles layered intrusion in Canada (Xing et al., 2017, 2022). The rounded olivine grains from the net-textured, Fe–Ti oxide ores of the Baima intrusion commonly have irregular P-rich patches/bands crosscut and interlocked by P-poor olivine domains, with typical skeletal branches in the P-rich patches (Fig. 26a, b). Distinct P zoning of olivine is ubiquitous throughout the ~4.7 km thick

layered series of the Sept Iles intrusion (Fig. 26c-f). Despite variable degrees of corrosion, typical P zoning patterns in the Sept Iles intrusion can be identified as P-rich dendrites (Fig. 26c, d) and sector zoning (Fig. 26e, f) in a broad P-poor olivine. The P-rich dendrites are composed of primary branches propagating from the crystal center towards crystal corners of olivine and secondary branches developing along the crystal plane (Fig. 26d). Distinctly skeletal P zoning is also found in the olivine from the Upper Zone of the Bushveld Complex in South Africa (Fig. 26g, h). Given the different sizes of these intrusions, it is likely that P zoning of olivine is common in layered intrusions regardless of their scale and can be looked for in intrusions elsewhere.

The P zoning patterns of olivine in layered intrusions resemble those documented for the olivine in volcanic rocks (e.g., Milman-Barris et al., 2008; Welsch et al., 2013, 2014). Milman-Barris et al. (2008) conducted the pioneering study on the P zoning of olivine from the volcanic rocks in different tectonic settings and meteorites, and recognized skeletal, hopper, oscillatory and sector P zoning. Welsch et al. (2013, 2014) examined the crystal habits and P zoning of olivine in volcanic rocks and suggested that the P zoning of olivine actually fingerprints skeletal and dendritic growth of olivine. They proposed a dendritic model to explain the continuous growth of olivine that initiates with rapid growth of Prich dendrites, followed by slow ripening and infilling of P-poor domains.

Rapid growth of olivine can be facilitated by fast cooling of magma in a magma chamber. Experimental studies demonstrate that there is a systematic change of olivine morphologies from polyhedral to hopper/ skeletal habit and then to dendritic habit as a function of increasing cooling rate and degree of undercooling, i.e., - $\Delta T = T_{\text{liquidus}} - T_{\text{crystallization}}$ (e.g., Faure et al., 2003, 2007). Recent experimental results also demonstrate that low-to-moderate undercooling (- ΔT = 25–60 ◦C) are sufficient to result in skeletal growth of olivine (Shea et al., 2019). At high degrees of undercooling (- ΔT > 60 ◦C) and high cooling rates (>47 ◦C/h), dendritic growth of olivine occurs (e.g., Faure et al., 2003, 2007; Lang et al., 2022). The various P zoning patterns of olivine grains in layered intrusions indicate that variable degrees of undercooling may exist in the magma chamber, which could be induced by conductive cooling of magma in the margin of the chamber (i.e., floor, roof and walls), or mixing of hot primary magma and relatively cold evolved magma in the magma chamber (e.g., Welsch et al., 2013; Shea et al., 2019; Xing et al., 2022). Particularly, the presence of dendritic morphology of olivine in the harrisite of the Rum layered intrusion (O'Driscoll et al., 2007a), the distribution of skeletal/hopper magnetite, ilmenite and apatite from the Upper Border Series of the Skaergaard intrusion (Naslund, 1984), and the preservation of sector-zoned clinopyroxene in the Xinjie layered intrusion (Cao et al., 2023) indicate that undercooling-induced disequilibrium growth of minerals in layered intrusions may be more common than we usually thought.

A common feature for the olivine of layered intrusions is that the Prich zones of olivine experienced variable degrees of dissolution, recording a two-stage growth process of olivine, i.e., initially skeletal/ dendritic growth and ripening, followed by late-stage dissolution and reprecipitation (Fig. 26i). Distinct resorption surface (R) can be recognized between P-rich zones and P-poor olivine domains (Fig. 26b, d, f, h). The dissolution process was likely triggered by the evolved interstitial liquid that may have become Fe-rich and in chemical disequilibrium with early crystallized olivine (Xing et al., 2017). In addition, finegrained inclusions of magnetite and plagioclase are all enclosed in Ppoor olivine domains (Fig. 26d, f), indicating late crystallization of these minerals. P-poor olivine domains containing rounded Ti-rich magnetite and Fe-rich melt inclusions provide concrete evidence for late crystallization of magnetite to form Fe–Ti oxide ore bodies hosted in the Baima layered intrusion (Xing et al., 2017).

The P concentration of olivine is relatively less constrained compared to other trace elements of olivine (e.g., Ni, Co, Mn) due to limited dataset for P in olivine. The P-rich zones of olivine from the Sept Iles intrusion have P concentrations varying from 200 to 450 ppm with a maximum of >1000 ppm, more than ten times higher than that of P-poor olivine domains (50–145 ppm P, Xing et al., 2022). The P-rich zones of olivine from the Baima intrusion contain 250 to 612 ppm P, higher than that of P-poor olivine domains (123–230 ppm P, Xing et al., 2017). In contrast, the olivine from the Stillwater Complex only contains 10 to 100 ppm P (Wang et al., 2021). In the binary plot of Fo-content versus P concentration for olivine, the olivine grains from layered intrusions, Ni–Cu sulfide-bearing mafic-ultramafic intrusions, Alaskan-type intrusion and volcanic rocks all commonly show a large range of P concentrations against certain Fo-content (Fig. 27a). Such a feature is indicative of the disequilibrium growth of olivine in the absence of P distribution map of olivine. Experimental results demonstrate that the partitioning coefficient of P between olivine and silicate melt ($D^{Ol/melt}_{P}$) increases from 0.01 to 1 with increasing growth rate of olivine, and P concentration of olivine can be enriched by a factor of >40-fold in the same crystal (Shea et al., 2019).

The well-preserved P gradients in olivine can be also used to estimate the diffusion timescale of P, which, in turn, can be used to calculate the cooling rate of magma chambers. 1-D diffusion modelling for the P gradients across different planes of olivine from the Sept Iles layered intrusion yields a diffusion timescale of 66–79 kyr. (Fig. 27b-e), resulting in an averaged cooling rate of 2.7 to 3.3 × 10^{-3} ◦C/year from 1105 to 890 ◦C (Xing et al., 2022), similar to the averaged cooling rate of other layered intrusions (e.g., Bushveld, Stillwater and Skaergaard) at high temperatures reported in previous studies.

4. Developing concepts about layered intrusions

4.1. Time and length scales in layered intrusion processes

Magmatic processes involve the redistribution of heat, mass and momentum by a wide range of interconnected processes operating at different time and length scales. Slow processes such as the growth and solidification of layered intrusions can be resolved into multiple faster processes operating episodically at short time scales. The fastest process at any given length scale tends to be the dominant control, and for one process to be the cause of another they must both be operating at similar time and length scales. This principle has been applied to the formation of magmatic sulfide ore deposits in igneous intrusions by Barnes and Robertson (2019) and their approach is taken here (Fig. 28).

Processes can be divided into three types: more-or-less linear processes governed by flow of magma, constrained largely by viscosity and other influences of rheology; processes related to heat flow, governed primarily by thermal diffusivity; and processes governed by chemical diffusivity. The latter two obey a universal scaling law, whereby the length scale of diffusive process scales with the square root of the diffusivity times the timescale, i.e., diffusive processes plot on the scaling diagram along lines with slopes of ½ and vertical position determined by the relevant diffusivity. Hence, chemical diffusion processes such as crystal growth and dissolution are intrinsically several orders of magnitude slower than heat transfer by conduction, and orders of magnitude slower again than processes of magma flow. The position of the different process fields on the plots is in many cases relatively poorly constrained, but the arguments apply at order-of-magnitude scales so in most cases the uncertainty is acceptable. Detailed discussion of the implications of this approach are beyond the scope of this review, but some examples are given here of arguments that can be derived from it.

Crystal growth rates are very slow compared with the rates of magma flow. Hence, a flowing pulse of magma across the floor of an intrusion (Eales et al., 1988) on scale of tens of km would not undergo a detectable amount of heat loss or crystallization during flow. In other words, lateral differentiation of magma pulses during flow is not expected. If so, the subdivision of cumulate sequences in the

Bushveld Complex into proximal and distal facies relative to the position of putative feeders into the chamber (Eales et al., 1988) makes little sense.

Crystal settling rates are low compared with convective velocities, such that a high degree of entrainment of crystals would be expected in a convecting magma body, to the point where the crystal density begins to reduce the effective viscosity of the suspension. For a km thick intrusion, the time scale of this transition would be similar to the timescale for the solidification of the intrusion, thousands to tens of thousands of years. The timescale for crystal accumulation from a convective magma depends on the rate of "escape" of crystals at the bottoms of convection cells near the chamber floor (Martin and Nokes, 1988).

Thermal erosion and assimilation of floor rocks and roof rocks depends strongly on the fluid dynamic regime, but in the case of rapid flow of magma through a conduit is of the order of metres in days. This is considerably faster than the rate of propagation of isotherms into the country rock due to thermal conduction, so in these circumstances magmas would erode their country rocks faster than a thermal aureole could form. This has important implications for processes of assimilation and formation of magmatic ore deposits (Robertson et al., 2015). It is likely that thermal aureoles form primarily after the intrusion has largely solidified, over 10–100 thousand year timescales of thermal conduction.

Dissolution of chamber-floor cumulates beneath a superheated convecting magma body operates on scales of metres and 10^2 to 10^3 years. This is thought to be the timescale for the distinctive erosional potholes found beneath major magma influxes in the Bushveld Complex, for example. This can be compared with the probably similar timescales for episodic major eruptions in flood basalt provinces. This is a short timescale compared with the 10^4 to 10^6 years for solidification of giant intrusions such as the Bushveld Complex. It may well be that development of cyclically layered sequences such as the Upper Critical Zone of the Bushveld Complex involves alternations of 10^2–10^3 year periods of alternating deposition and dissolution of the crystal pile. Such timescales readily allow for diffusive equilibration through crystal-liquid frameworks on a scale of metres, facilitating the formation of adcumulate and heteradcumulate "hardgrounds" at the top of the crystal pile.

4.2. Catastrophic growth of magma chambers

Knowledge of magma emplacement timescales is critical for understanding how volcanic and igneous plumbing systems operate in the Earth's crust. The timescales of processes that create space for magma chambers are particularly poorly constrained (Coleman et al., 2016; Lundstrom and Glazner, 2016). Estimates of the volumetric emplacement rates of plutonic bodies range from 10^{-3} to 10^{-1} km^3/yr (de Saint Blanquat et al., 2011; Menand et al., 2015). The vertical growth rate of basaltic magma chambers remains largely unknown with available estimates being as low as 1–5 cm/yr (Glazner, 2021). A straightforward thermal approach has recently been explored to obtain the first rigorous estimates of the growth rate of the Skaergaard layered intrusion, Eastern Greenland – a classic example of a solidified basaltic magma chamber (Hagen-Peter et al., 2019; McBirney, 1995; Namur et al., 2014; Nielsen, 2004; Salmonsen and Tegner, 2013; Wager and Brown, 1968). The Skaergaard layered intrusion is a fault-controlled igneous body made up of layered gabbro (Fig. 29a) emplaced at a depth of about 2 km within the East Greenland volcanic rifted margin. The intrusion has a surface exposure of ~8 × 11 km, a total structural height of ~4 km, and a boxlike shape with a total volume of ~300 km^3. Closed-system crystallization of this parental melt took place from all margins inward with the formation of the Layered Series (LS) in the bowl-shaped floor, the Marginal Border Series (MBS) on the walls, and the Upper Border Series (UBS) below the roof. The UBS and LS meet at the Sandwich Horizon (SH). All three series record the progressive fractional crystallization of a parental tholeiitic melt (Nielsen, 2004; Wager and Brown, 1968) as indicated by successive appearance/disappearance of cumulus phases (e.g., augite, olivine, muscovite, apatite, and bustamite, Fig. 29b) and systematic changes in their compositions (e.g., An-content of plagioclase, Fig. 29b). Cumulate mineralogy is correlated between the series and is used to subdivide them into zones and subzones (UBS subzones denoted with apostrophes, e.g., Lower Zone in UBS is LZa' whereas MBS subzones with asterisks, e.g., Lower Zone in MBS is LZa*). The LS, UBS, and MBS have similar chemical trends everywhere in the chamber indicating that the Skaergaard intrusion started crystallizing inwards from all margins only when it had been completely filled with melt. This implies that the body grew continuously to its current size by accumulation of compositionally near-homogeneous melt on a time scale that was much shorter than that of its solidification (Marsh, 2015). During this process, new melt effectively mixed with resident melt in the chamber, impeding the onset of crystallization. A key message is that the bulk of the intrusion eventually started to crystallize from one large volume of nearly crystal-free homogeneous melt. This fundamental physical constraint provides a unique opportunity to estimate the minimum rate of magma emplacement that was required to keep the Skaergaard magma body in a largely molten state (<<1% crystals), while growing to its current size.

A series of numerical simulations were carried out to determine the conditions required for the growth of a crystal-free Skaergaard magma chamber. These simulations show that for magma emplaced at its liquidus temperature (1160 °C) (Thy et al., 2009; Toplis and Carroll, 1995), the minimum vertical emplacement rate that permits a large, crystalfree chamber to grow without freezing at its roof and floor is extremely high – on the order of several 100 s to a few 1000s m/yr (Fig. 29c). This corresponds to volumetric flow rates of 10s to 100 s of km^3/yr. These estimates are comparable with those of lava production rates in giant flood basalt flows (e.g., Thordarson and Self, 1998). Slower growth rates result in a crystal-rich magma chamber. For even slower rates (less than a few 10s of cm/yr), large parts of the intrusion are already solidified when the intrusion reaches its final size. The thermal modelling thus indicates that the volumetric flow rate of magma required for the Skaergaard magma chamber to remain crystal-free is 3 to 5 orders of magnitude larger than those typically inferred from the geochronology of felsic and mafic intrusions (Coleman et al., 2004; de Saint Blanquat et al., 2011; Leuthold et al., 2012). This corresponds to an emplacement time for the entire mafic intrusion of a few years to a few decades. Such fast growth of the Skaergaard chamber can be approximately modelled by either subsidence of the floor, or lifting the roof of a rectangular tabular body with horizontal dimensions ~8 × 11 km. Based on field evidence (Irvine, 1992; Irvine et al., 1998; Nielsen, 2004), floor subsidence is the most likely mechanism for growth of the intrusion but the calculations are equally valid for both roof lifting or hybrid roof lifting/floor depression emplacement scenarios (Cruden, 1998; Norton et al., 1984). Piston- or cauldron-like subsidence is accommodated by displacement on sub-vertical faults, which could also act as conduits for magma flow from the source to the intrusion (Cruden, 1998). We assume that the base of the underlying crustal block subsided into a depleting lower magma reservoir or stack of underlying reservoirs, possibly aided by ongoing regional extension (Cruden and Weinberg, 2018; Glazner, 2021). Taking minimum vertical growth rates dh/dt = 200–2000 m/yr required to maintain a crystal-poor chamber (Fig. 29c), the time to reach the ~4 km thickness of the Skaergaard intrusion ranges between 20 and 2 yr, respectively. The corresponding volumetric magma inflow rates, Q, required to sustain these growth times varies between 17.6 and 176 km^3/yr. We can also evaluate the viability of these timescales and rates by estimating the corresponding flow rates in the magma feeder zone(s) below the Skaergaard intrusion, which we approximate here as a single vertical dyke. Volumetric flow rates in a dyke-like feeder are driven by the density difference between the magma and the host rocks and are governed by the magma viscosity and the length and width of the conduit (Petford et al., 1994). For a 1 km long dyke (i.e., the minimum length of dykes in the Skaergaard swarm), a conservative density difference of 50 kg/m^3 and a typical, crystal-free basaltic magma viscosity of 1000 Pas, volumetric flow rates of 1.3, 10.3, 161 and 1290 km^3/yr are predicted for

dyke widths of 1, 2, 5 and 10 m, respectively. Thus, our calculations show that even a single, relatively short and thin feeder dyke would have been capable of delivering magma into the growing Skaergaard intrusion at flow rates that fall well within those required for the melt to remain crystal-free (10s to 100 s of km3/yr).

Similar to Skaergaard, many layered mafic intrusions tend to have cumulate stratigraphy that displays systematic crystallization sequences and mineral chemical trends indicating their crystallization in large and mostly molten magma chambers in Earth's crust (Cawthorn, 1996; Charlier et al., 2015b; Latypov et al., 2020b; O'Driscoll and VanTongeren, 2017a, 2017b; Parsons, 1987; Wager and Brown, 1968). This suggests that the growth rate of the magma chambers of these intrusions is likely comparable to that of Skaergaard and that the filling times of such bodies might be surprisingly fast. For instance, taking a volumetric flow rate of 100 km3/yr, a body of the size of Skaergaard (300 km3) can be filled in a matter of only 3 years. Since our numerical simulations constrain the minimum rate of magma emplacement, the actual filling time for such a body may be even faster, perhaps, several months or even a few weeks. Following this logic, for bodies the size of Kiglapait (3500 km3) (Morse, 2015) and Windimurra (26,000 km3) (Ivanic et al., 2018), the filling times could have been <35 and 260 years, respectively. Again, the filling times for these intrusions may be on the order of a few months if greater than minimum chamber growth rates are used. Therefore, leaving aside the matchless giant Bushveld Complex (600,000 km3) (Cawthorn and Walraven, 1998), the actual filling times for many layered intrusions may be in the range of only a few months to a maximum of dozens of years. This conclusion is valid for the cases of magma chamber growth from both crystal-free (e.g., Skaergaard) and crystal-bearing magmas (e.g., Stillwater). Importantly, these estimates are consistent with the durations of basaltic eruptions, which most commonly last from about a month to a year, with the overall spectrum of times spanning about 100 years (Marsh, 2015; Simkin, 1993). We propose that the Skaergaard and possibly some other layered intrusions can be viewed as products of catastrophic events associated with rapid and voluminous emplacement of basaltic magmas into the Earth's crust.

In other words, some layered mafic intrusions may represent the plutonic analogues of LIP-related volcanoes that are responsible for eruptions of enormous volumes of flood basalts on the Earth's surface (Coffin and Eldholm, 1994; Ernst, 2014; Svensen et al., 2019).

4.3. Out-of-sequence emplacement in layered intrusions

This classical paradigm considers the layered intrusions as crystallized in 'big magma tank' chambers, i.e., in large, long-lived, mostly molten bodies in Earth's crust (Fig. 30a). However, a recent discovery that zircon isotope ages may display the 'out-of-sequence' behaviour, i.e., jumping back and forth from younger to older ages, as one moves upsection through the Bushveld and Stillwater Complexes (see section 3.12) has prompted an emergence of a new alternative concept for the formation of layered intrusions (Fig. 30b). It has been proposed that these two complexes were built non-sequentially through the emplacement of a stack of amalgamated sill-like bodies over a period of ~3–5 million years, and that no large magma chamber ever existed (Mungall et al., 2016; Scoates et al., 2021; Wall et al., 2018). Again, taking the Stillwater Complex, as an example, four main episodes of sill-like emplacement were postulated at about 2712, 2711, 2710, and 2709 *Ma*. The time interval between the episodes is considered to be each time long enough (1 *Ma*) for all earlier-formed rocks to completely solidify before the onset of the next episode of magmatic activity. The following sequence of the magmatic episodes is envisaged (see Fig. 25; section 3.12): (1) at 2712 *Ma*, the Basal series was first emplaced into country rocks; (2) at 2711 *Ma*, the entire Bronzitite zone together with the uppermost part of the Peridotite zone were emplaced along a roof contact of the Basal series with country rocks; (3) at 2710 *Ma*, cyclic units of the lower Peridotite zone were emplaced along the boundary between the Basal series and the Bronzitite zone. At the same time, Norite 1 of the Lower Banded series was emplaced along a roof contact of the Bronzitite zone with country rocks. Flotation of plagioclase from the Norite 1 towards the top of the magma chamber produced a thick pile of anorthosite - the future Anorthosite 1, 1.5 and 2 of the Middle Banded series; (3) at 2709 *Ma*, the rest of the Banded series was finally emplaced as multiple sill-like injections of magma to form Olivine-bearing zones 1 to 5, Gabbronorite zones 1 to 3 and Norite 2. If true, this emplacement scenario calls into question most current concepts regarding the crystallization histories of open-system layered intrusions and challenges our understanding of the timescales of magma emplacement in these large and petrologically important complexes (Wall et al., 2018).

There are, however, several issues which the amalgamated sill concept needs to address before they can be widely accepted by igneous petrologists. Most important among them are the following ones. First, field, textural or chemical evidence is required to document the emplacement of sill-like bodies into pre-existing rocks of the Bushveld and Stillwater Complexes. This is difficult but not impossible to do as follows from the field evidence for the chaotic sill-like emplacement of some ultramafic layers recently documented by detailed outcrop-scale mapping of the Rum Complex (Hepworth et al., 2017, 2018). Second, one needs to explain why the random emplacement of multiple sills into pre-existing solidified rocks mimic the general stratigraphies and crystallization sequences of layered intrusions that appear to be controlled by liquidus phase equilibria (Cawthorn, 1996; Charlier et al., 2015b; Latypov et al., 2020b; Parsons, 1987; Wager and Brown, 1968) (compare Fig. 30a, b). Third and most importantly, it has to be explained why interpretation based on absolute ages of zircon ages comes into a conflict with relative ages indicated by transgressive relationships in potholes of the Bushveld Complex (Latypov and Chistyakova, 2022). Addressing these and some other questions necessitates a new line of research combining geochronology and igneous petrology. The future geochronological work on layered intrusions needs not only be performed with high precision, but most importantly to be critically integrated with field, textural and petrological observations. Clearly, further progress in our understanding of the processes responsible for the generation and development of large magma chambers will be greatly dependent on the successful resolution of the pressing question regarding the 'out-ofsequence' geochronology reported from layered intrusions.

4.4. Large-scale slumping and mineral sorting in layered intrusions

Slumping and gravity flow of crystal slurries has been an important concept in layered intrusion science, particularly in the work of Neil Irvine on Duke Island intrusion (Irvine, 1987). A more pervasive and economically significant role has been promoted in recent years by Maier and Barnes (2008) and Maier et al. (2013). The essence of their model is considered here using the cumulate sequences with massive chromitites in the Bushveld Complex. Maier et al. (2013) proposed that a Bushveld chamber is replenished by pulses of phenocryst-free melt that precipitates first orthopyroxene and then chromite and this results in the formation of a 10's to 100's m thick, broadly differentiated mushy layer.

At some point, the chamber experiences central subsidence that causes downward slumping of the mushy layer during which size- and densityinduced sorting of minerals takes place in the down-dip direction. In this process, the small and dense chromite crystals percolate downwards through the crystal slurry by the process of kinetic sieving (also known as the "Brazil Nut effect"), producing a layer of massive chromitite at its base overlain by a thick orthopyroxenite layer (Fig. 31a, b). Thus, massive chromitites do not form on the instantaneous chamber floor during the magmatic stage, instead their formation takes place at the post-cumulus stage in the evolution of the solidifying magma chamber.

A process of kinetic sieving is well-known in the field of sedimentary geology. Both theory and experiments indicate that it can be accountable for several features of sedimentary rocks, i.e., inverse grading (see a review in Marsh, 2013). Since magmatic slurries of basaltic composition are composed of primocrysts of varying size and density, it is thought by some researchers that kinetic sieving and some other unmixing processes must occur nearly inevitably during their transport and deposition (Marsh, 2013). For instance, kinetic sieving is thought to be responsible for the origin of modal layering in Ferrar dolerite sills (Marsh, 2013) and massive chromitites of the Bushveld Complex (Maier et al., 2013; Mondal and Mathez, 2007). Forien et al. (2015) have undertaken an analogue experimental study to validate the operation of the kinetic sieving in a slumping crystal mush. In their experiment, they employ glycerine to mimic the melt and glass, silicone and polyacetal beads to simulate minerals of different size and density. Forien et al. (2015) produced a mineral layering by percolation of the smaller, denser particles down between the larger, less dense grains during slumping of the beads down an inclined surface in a tank. The experiments are held to have provided evidence supporting kinetic sieving in the Bushveld Complex through slumping of semi-consolidated cumulates, but questions remain as to how well these experiments apply at the 100 km lateral scale of Bushveld Complex chromitites.

The concept of large-scale slumping and mineral sorting has been recently extended to explain igneous layering in some other layered intrusions (e.g., Maier et al., 2018a, 2018b, 2020). Its wider application seems to be limited, however, by the need to address some unresolved theoretical and observational issues (e.g., Latypov et al., 2015a, 2017a, 2017b, 2023b). For instance, it needs to keep in mind that the beads that are used in experiments to imitate minerals (e.g., Forien et al., 2015; Marsh, 2013) are separate and independent particles which are not attracted to each other by any physical or chemical forces. For this reason, these particles may move freely relative to each other to result in their sorting during a slumping process. Unlike the beads, crystals in magmas are not inert as they are chemically precipitated from the parental liquid (Glazner, 2014). The minerals in cumulate rocks nucleate and grow on each other and are therefore linked both physically and chemically from the very start (e.g., Campbell, 1996; Hammer et al., 2010; Pupier et al., 2008; Spillar ˇ and Dolejˇs, 2015). This is particularly true for chromite that tends to be commonly attached to or included within crystals of olivine or orthopyroxene (e.g., Hoshide and Obata, 2014; Roeder et al., 2006). This is one of the major reasons as to why a rigid, three-dimensional network of crystals exists when basaltic melt is only about 25% crystallized (e.g., Philpotts, 1998; Philpotts and Dickson, 2000). When in an incompletely crystallized state, such a crystal mush can be deformed but the bonds existing between the minerals may prohibit their physical rearrangement and sorting on a large scale (Fig. 31). To mimic the behaviour of real cumulates in layered intrusions, a different design of analogue experiments (or computational fluid dynamic models) is therefore strongly required. The experiments must involve crystals that are bound to each another chemically by particle interactions and to the enclosing liquid by viscous forces.

4.5. Monomineralic cumulates produced from single phase-saturated melts

The Earth's mantle is composed of olivine-rich rocks and therefore mantle-derived melts, after their ascent and emplacement to a shallow level, are normally saturated in olivine and initially crystallize monomineralic dunite (Jackson, 1970). Some of these melts with further differentiation, and particularly with addition of crustal silica by contamination, may also produce monomineralic orthopyroxenite (Irvine, 1979). With subsequent evolution of these melts in crustal chambers, olivine/orthopyroxene are joined by other crystallizing phases (up to 7–8 phases) to form various polymineralic cumulates (norite, gabbronorite, pigeonite gabbro, etc.). The crystallization sequence of these melts along multi-phase cotectics/eutectics is governed by liquidus phase equilibria and is therefore considered as one of the most fundamental principles of igneous petrology (Cawthorn, 1996; Charlier et al., 2015b; Latypov et al., 2020b; Morse, 1980; Parsons, 1987; Wager and Brown, 1968). In many layered intrusions this sequence of polymineralic cumulates is, however, interrupted by an abrupt appearance of stratiform layers of various monomineralic rocks (e.g., anorthosite, clinopyroxenite, hornblendite, chromitite and magnetitite), which are not supposed to crystallize from the multi-saturated melts. Their existence is, therefore, a major challenge from a liquidus phase equilibria standpoint. Some of the monomineralic rocks can be attributed to size- and density-induced sorting of minerals in the chamber – e.g., settling of dense mafic minerals on the chamber floor (Wager and Brown, 1968), plagioclase flotation to the chamber roof (Namur et al., 2011a), kinetic sieving of crystals in crystal mushes (Maier et al., 2013; Mondal and Mathez, 2007), reactive porous flow through proto-cumulates (Maier et al., 2021) or emplacement of single phase-rich mushes into the chamber (Lesher et al., 2019; Voordouw et al., 2009), but major problems exist with such interpretations as discussed elsewhere (e.g., Cawthorn, 2015; Latypov et al., 2015a; Latypov et al., 2017a, 2017b; Namur et al., 2015a; Naslund and McBirney, 1996).

The origin of monomineralic rocks can be best explained by their crystallization directly from single-phase saturated melts, i.e., melts that are saturated in plagioclase, chromite or magnetite as the only liquidus phases (e.g., Namur et al., 2015a). A problem, however, is how to generate such melts in basaltic chambers that contain resident melts saturated in multiple phases. Let us illustrate this problem using stratiform anorthosites - the most spectacular monomineralic rocks that occur as continuous layers in many layered intrusions, including the Bushveld Complex (e.g., Cawthorn, 2015). Mantle-derived basaltic to picritic melts may have plagioclase on the liquidus only as a second, third or a fourth phase after olivine and both pyroxenes (Presnall et al., 1978). It seems, therefore, that to produce plagioclase-only-saturated liquids by fractional crystallization of primary mantle-derived melts is nearly impossible. If so, then why do stratiform layers of monomineralic anorthosites exist in nature despite these obstacles from liquidus phase equilibria? Experimental data on simple binary and ternary systems clearly show that with a decrease in lithostatic pressure dry liquids may move from the stability fields of mafic phases (e.g., pyroxene) into that of plagioclase alone (Sen and Presnall, 1984; Yoder, 1968). This happens owing to expansion of the stability volume of plagioclase at the expense of mafic phases with decreasing pressure (Yoder, 1968). In this process, the dry melts become superheated with respect to their liquidus temperature so that no phases can crystallize from these melts. Until recently, no attempts have been made to relate the generation of melts parental to stratiform anorthosites in layered intrusions to the expansion of the plagioclase stability volume with reduction in lithostatic pressure. A reason is that it has been problematic to identify a plausible mechanism for a substantial decrease in pressure *within* a magma chamber (Cawthorn and Ashwal, 2009; Naslund and McBirney, 1996): the pressure reduction is generally thought to be negligible because the crust cannot sustain large overpressure.

Using stratiform anorthosites of the Bushveld Complex, Latypov et al. (2020a) has recently proposed an alternative scenario. A key idea is that it is the new melts ascending from depth, i.e., deep-seated magma chambers, that undergo a pressure reduction, not the resident melts in the shallow-level chambers. In other words, the plagioclase-onlysaturated melts parental to stratiform anorthosites are proposed to generate on the way up from, deep-seated sites of magma storage, rather than within the shallow-level chambers. This fundamental inference from simple binary/ternary systems has been fully confirmed by MELTSbased thermodynamic modelling. The modelling has shown that some alumina-rich basaltic andesitic melts sitting close to the orthopyroxene stability field in staging

chambers become superheated during their ascent and then, upon cooling in shallow chambers, saturated in plagioclase alone (Fig. 32a, c). It was proposed that many stratiform layers of monomineralic anorthosites in layered intrusions may be attributed to a pressure-induced shift of multi-saturated melts into the plagioclase stability field during their transportation towards the Earth's surface (Latypov et al., 2020a). After arriving at a shallow level chamber and some cooling, the melt starts crystallizing and accumulating plagioclase on the chamber floor to form anorthosite (Fig. 32b). This proposal is advantageous over the earlier attempts to generate plagioclase-only-saturated melts (Hess, 1960; Morse, 1979; Naslund and McBirney, 1996) because it is based on a physical process that seems to be inevitable in nature. None of the mantle-derived melts, including those from deep-seated staging chambers, can avoid a decrease in lithostatic pressure during their ascent towards the Earth's surface. It is therefore no wonder that some ascending alumina-rich basaltic andesitic melts may reach saturation in plagioclase upon their ascent and subsequent cooling (Fig. 32c).

A similar approach has also been applied to explain the generation of chromite-only-saturated melts as parental to stratiform chromitites of the Bushveld Complex (Latypov et al., 2018a). Using three interrelated approaches – phase equilibria, thermodynamic modelling and experimental data – it has been shown that basaltic melts located alongside a so-called chromite topological trough in deep-seated reservoirs may become saturated in chromite alone upon their ascent towards the Earth's surface. This occurs due to an increase in the plagioclase stability volume as the pressure decreases, which shifts the chromite topological trough in such a manner as to force these basaltic melts into the chromite stability volume. On cooling, these melts would crystalize pure chromite forming layers of monomineralic chromitites in layered intrusions (Latypov et al., 2018a). In developing this idea further, the injection of new magma that was oversaturated in magnetite upon emplacement was proposed to explain the origin of monomineralic magnetitites in the Bushveld Complex (Kruger and Latypov, 2020, 2021). The discordant magnetite-rich pipes and reversals in mineral chemistry towards more primitive compositions were taken as evidence for the existence of such magnetite-only-saturated magmas in nature. One of the potential mechanisms that may cause a transformation of multi-saturated, broadly gabbroic melts into magnetite-only-saturated ones is changes in phase equilibria associated with ascent of melts from the deep staging reservoirs towards the Earth's surface. This appears to be a quite intriguing, although not yet explored, line of research.

It is thus proposed that the melts ascending from deep-seated staging chambers may become saturated in chromite, plagioclase, or magnetite alone in response to pressure-related changes in the liquidus phase equilibria (Kruger and Latypov, 2020; Latypov et al., 2018a, 2020a). The single phase-saturation event happens due to decompression as magmas are transferred from the deep-seated storages towards the Earth's surface. The emplacement of such single phase-saturated melts into shallow level chambers followed by adcumulus growth of chromite, plagioclase or magnetite at the chamber floor are considered as potential keys to the formation of monomineralic cumulates in layered intrusions. Monomineralic rocks may thus be regarded as "smoking guns" of processes that transform the melts ascending from deep staging chambers into those saturated in various single phases during their transcrustal transfer towards shallow level chambers.

4.6. Non-cotectic cumulates by in situ growth

One of the most challenging aspects when dealing with the origin of igneous layering is determining how crystals are deposited. This can happen by in situ crystallization, where crystals remain in position after their initial nucleation and growth, or they may have undergone transport by a wide array of mechanisms, such as crystal settling (Cawthorn and Ashwal, 2009; Hess, 1960; Jackson, 1961; Wager and Brown, 1968), flotation (Namur et al., 2011a), transport or rearrangement by magma currents (Higgins, 1991; Barnes et al., 2021), intrusion of crystal mushes from deeper-seated magmatic bodies (Latypov and Chistyakova, 2020; Yao et al., 2021), or the re-arrangement of crystal mushes by tectonic disturbances (Maier et al., 2013). There are certain features to look for in a set of cumulates to determine if crystal transport has occurred. For example, transport can cause mineral grains to become sorted by size (Holness et al., 2020), potentially leading to size grading. Hydrodynamic sorting may also cause minerals to accumulate in layers based on their density. This process has been proposed as responsible for the formation of many non-cotectic rocks in layered intrusions (Maier et al., 2013). Finally, magmatic flow may also cause a foliation to develop, where elongated mineral grains are re-arranged with their long axis parallel to the bedding plane (Higgins, 1991). These three characteristics, sorting by size, large deviations from the expected cotectic proportions of minerals, and a foliation and/or lineation are thus commonly used to infer that transport has occurred.

It is in light of the above that magnetitite layers from the Bushveld Complex are such enigmatic rocks. Upon first inspection, they may appear as though they were produced by crystal settling. At their bases, they are almost perfectly monomineralic, consisting of nearly pure titanomagnetite. However, most magnetitite layers have graded tops into magnetite anorthosite (Fig. 33a). The plagioclase within these tops also shows a clear foliation, although no lineation is evident. If cocrystallizing magnetite and plagioclase grains were held in suspension in a melt, magnetite might settle out much faster due to its much higher density (4.8 g cm^{-3}) compared to plagioclase (~2.7 g cm^{-3}). This may lead to the formation of a magnetite-enriched base that is gradually joined by an increasing amount of plagioclase crystals. A foliation may be produced as the plagioclase grains come to rest and lay flat on the crystal pile.

A closer inspection of magnetitite layers reveals, however, that the process cannot be so simple. For one, the plagioclase grains are poorly sorted, with grain sizes generally varying from 0.8 to 4.0 mm. For plagioclase grains with such dramatically different grain sizes to accumulate at the same level, settling distances would have to be very short, perhaps no more than a few cm (Kruger and Latypov, 2022). However, if that were the case, settling would not be able to separate a non-cotectic suspension of plagioclase and magnetite grains. While the exact cotectic proportions of plagioclase to magnetite are unknown, it is fair to argue that significantly more plagioclase should crystallize compared to magnetite at a cotectic, based on the fact that magnetite typically occurs in low abundances in layered intrusions throughout the world, typically no >15% (Kruger and Latypov, 2022). Settling of plagioclase and magnetite over a distance of just a few centimeters would not be able to make a rock with an excess of 20–90% magnetite across a distance of several tens of centimeters, as is observed in the upper portions of Bushveld magnetitite. There is also uncertainty if plagioclase would be able to settle at all. According to Cawthorn and Ashwal (2009), this is very dependent on the water content of the melt. If it were <1 wt%, plagioclase would float, and vice versa. Unfortunately, the water content of the melt is unknown. Even if plagioclase were able to sink, it may not be slower than magnetite due to the large differences in the primary grain size for plagioclase (>4 mm) compared to magnetite (0.007 mm). Kruger and Latypov (2022) calculated that plagioclase will only sink faster than magnetite for a very limited range in magmatic densities.

The case for crystal settling gets even more problematic when the geochemistry of magnetitites is considered. Dome-shaped, high-Cr structures (Fig. 19) occur at the bases of these layers and have been used to infer the in situ crystallization of these layers (Cawthorn, 1994; Kruger and Latypov, 2020), as described above (section 3.7). Furthermore, they are characterized by very smooth upward depletions in Cr in their gradational contacts that remain so even for an extremely detailed sample spacing of just 1–2 cm (Fig. 34). Just about all investigators (Cawthorn and McCarthy, 1980; Kruger and Latypov, 2020; Kruger and Smart, 1987; Yao and Mungall, 2022) who have looked at this depletion concluded that it is, at least in part, a product of the fractional crystallization of magnetite and the exceptionally high crystal-liquid partition coefficient of Cr in magnetite, potentially >2000 (Shepherd et al., 2022). The fact that

samples of magnetitite spaced just 1–2 cm apart, can have distinguishable Cr contents, indicates that they were deposited in packets of at least a similar or smaller size. Once again, this argues for either very short distance settling, in which case cotectic suspensions would not be able to be properly separated, or that the magnetitite grew in situ.

A means to produce non-cotectic rocks by in situ crystallization has been proposed by Kruger and Latypov (2022) (Fig. 33). The model relies on the following assumptions. First, a relatively thin (<100 m) basalt melt layer is assumed that is saturated in magnetite only with plagioclase as the second phase to join crystallization after some degree of differentiation. Second, the melt is assumed to undergo magmatic differentiation by the convective removal of thin (a few mm) compositional boundary layers directly adjacent to the solidification front (Martin et al., 1987). During magnetite crystallization, elements like Fe, Ti, Cr, and V diffuse towards a growing crystal, causing the surrounding melt to become depleted in these elements. This also results in a loss of density, causing the boundary layer to periodically break away in a convective fashion once a critical density and size are reached. Extraction of these elements also causes the boundary layers to evolve towards plagioclase saturation. Initially, these boundary layers do not reach plagioclase saturation before their convective removal, leading to the production of monomineralic magnetitite so commonly observed at the bases of magnetitite layers. As these boundary layers rise and mix with the basalt melt layer, it slowly evolves towards plagioclase saturation. Thus, each successive boundary layer comes progressively closer to crystallizing plagioclase. Eventually, somewhere along the solidification front, a boundary layer finally starts crystallizing plagioclase, but its crystallization is quickly terminated when the boundary layer is once again removed by convection. It is then replaced by a melt that is still saturated in magnetite alone. Magnetite-only crystallization resumes for a while before the new boundary layer can reach plagioclase saturation. This constant removal of a boundary layer saturated in plagioclase inhibits the crystallization of plagioclase and magnetite in the expected cotectic proportions, with magnetite dominating the modal abundance of the rock. However, with continued differentiation, plagioclase saturation is reached earlier in each successive boundary layer, causing its modal abundance to gradually increase. This results in the upper gradational contacts of magnetitite into magnetite anorthosite.

An intriguing piece of the puzzle that remains is the development of the foliation of the plagioclase. Once again, an answer may be found within the compositional boundary layers atop a magnetitite solidification front. Extraction of magnetite-building chemical components results in a compositional gradient across the boundary layer, with the highest abundance of plagioclase components occurring directly adjacent to the magnetitite solidification front. This would favor the lateral growth of plagioclase in the direction where the components to sustain crystallization are most abundant (Kruger and Latypov, 2022). The gradational upper contacts of magnetitite layers from the Bushveld Complex may thus represent an interesting case where non-cotectic and foliated rocks, so commonly inferred to arise during hydrodynamic sorting, are, in reality, produced during the process of in situ crystallization. It is not inconceivable that some other non-cotectic rocks in layered intrusions may be formed by similar processes of in situ crystallization at the chamber floor.

4.7. Superheated, normal and supercooled melts in layered intrusions

Magmas parental to layered intrusions are referred to as normal when they crystallize at their liquidus temperature. This is considered the norm because basaltic magmas usually arrive in crustal chambers being close to their liquidus temperature with or without intratelluric phenocrysts. A much less common situation is when the magmas are superheated or supercooled with respect to their liquidus (i.e., located above or below their liquidus, respectively). Superheating is commonly invoked to explain the field observations indicating that replenishing magmas are highly reactive and cause intensive erosion of the floor cumulates. It has long been established that superheating cannot be caused by fractional crystallization or mantle melting, thus necessitating some special circumstances for its appearance. There are several plausible ways by which magma in the chamber may become superheated. A first possibility is assimilation of footwall cumulates by replenishing magma lying on the opposite side of a cotectic (e.g., Latypov et al., 2015a). A second possibility is mixing of two melts of different compositions that occur on opposite sides of a thermal minimum (e.g., a eutectic or cotectic) (e.g., Campbell, 1986; Irvine et al., 1983). It has been shown that such mixing of the disparate magmas may result in hybrid magma that can be as much as 100 ◦C above its liquidus (Irvine et al., 1983).

Finally, a third possibility is a rapid ascent of a large volume of magma from depth when superheating arises due to the difference in slope between the adiabatic gradient and the liquidus. For magma ascending from a storage region located at a depth corresponding to ~10 kbar, the degree of superheating can be up to ~10-30 ◦C assuming the adiabatic gradient vs liquidus difference for olivine to be about 3 ◦C/ km. Thermodynamic modelling using MELTs has revealed, however, that some basaltic melts contaminated in deep-seated reservoirs may become superheated by up to 90 ◦C if they ascend from there nearly adiabatically (Fig. 32; section 4.5). In practice, some cooling of ascending melts still takes place and, therefore, upon arrival into a shallow-level chamber, the melts are expected to be much less superheated. Latypov et al. (2022c) have recently explored with the help of the Magma Chamber Simulator (Bohrson et al., 2014, 2020) the potential extent of chemical dissolution of the high-temperature-melting cumulates (anorthosite and orthopyroxenite) by slightly superheated (15 ◦C above the liquidus) basaltic-andesitic melts that replenished the magma chamber. The thermodynamic modelling shows that at such a modest degree of superheating the melts can consume up to 4.5–8.0 wt% of the bulk floor cumulates without causing their crystallization. This is despite that fact that the melts are much colder than the liquidus temperatures of these cumulates. Given a basal melt layer of about 350 m thick, the consumption is equivalent to regional erosion of 15–24 m of the chamber floor cumulates (Latypov et al., 2022c).

Supercooling of magma can also be induced by several mechanisms. The most obvious of them is strong cooling of inflowing magmas against cold country rocks. This type of magma supercooling is usually recorded in the formation of chilled or fine-grained rocks along the margins of layered intrusions (Latypov, 2015a; Latypov et al., 2007). Another mechanism is decompression-induced degassing of water-saturated parental melts. The isothermal degassing leads to a sudden increase in liquidus temperature of these melts inducing strong constitutional supercooling and fast crystallization (Cashman and Blundy, 2000; Waters et al., 2015). The degassed magmas are characterized by a high content of intratelluric phenocrysts of various minerals (i.e., crystal-rich slurries, often with dendritic and hollow crystals). In layered intrusions, the most intriguing type of melt supercooling is, however, the one that is caused by kinetics of crystallization. Such kinetic supercooling is an important element of an in situ crystallization model that envisages almost no crystals in the convecting magma body of the chamber (Fig. 35a). The model considers magma chambers as consisting of crystal-free magma bodies in which crystals mainly nucleate heterogeneously and grow along the cooling margins of the chamber (Campbell, 1978, 1987, 1996; Martin, 1990; Martin et al., 1987). This occurs because slow cooling of large magma chambers prevents them from reaching the degree of supercooling that is necessary for homogeneous nucleation within the resident melt. Importantly, the entire resident melt is thought to be at the metastable conditions, i.e., kinetically supercooled with respect to liquidus phases that crystallize along the chamber margins (Campbell, 1978, 1987, 1996; Latypov et al., 2020b; Martin, 1990; Martin et al., 1987). The degree of the kinetic

supercooling in a basaltic magma chamber that is cooled via conduction through its host rocks, has been shown to be in the range of 1 ◦C and 20 ◦C (Martin, 1990; Martin et al., 1987). Importantly, it is Wager (1963) who was the first to propose that resident melt in a basaltic chamber needs to be supercooled by, at least, 5 ◦ to 10 ◦C to assist in adcumulus growth in layered intrusions. The thermal and physical structure of a basal solidification front that occurs between the crystalfree resident melt and the cumulate pile is shown in Fig. 35b. It illustrates how the melt becomes increasingly more supercooled across the compositional boundary layer with respect to liquidus minerals of a crystal-liquid mush.

4.8. The arrival of new phases on the liquidus

Various textural and chemical features related to the arrival of new phases on the liquidus of a resident melt in layered intrusions have been recently compiled and discussed in detail by Latypov et al. (2020b). What follows below is a short summary from this publication. With progressive fractional crystallization of basaltic melts in layered intrusions up to ten liquidus phases (e.g., olivine, chromite, orthopyroxene/pigeonite, plagioclase, Ca-rich clinopyroxene, magnetite, ilmenite, apatite, alkali feldspar and quartz) may successively appear/ disappear and show progressive evolution in composition from margins inwards. The crystallization sequences are mostly controlled by composition of parental magmas and liquidus phase equilibria under given P-T conditions. To illustrate this concept, a simplified crosssection through a hypothetical layered intrusion is presented here (Fig. 36a). The intrusion is produced by internal differentiation of an olivine-saturated parental melt with a general crystallization trend Ol, Ol + Plag, and Ol + Plag+Cpx (Fig. 36b). This section shows most important textural, modal and chemical features that mark the arrival of a new liquidus phase in the stratigraphy of layered intrusions. This summary is based on primary textural, modal and chemical data from the Sept Iles, Rum, Rytky, Noril'sk, Bushveld, Great Dyke, Jimberlana and Skaergaard intrusions. There are two distinct stages in which liquidus phases appear in the stratigraphy of layered intrusions. At first, they emerge in the form of oikocrysts which are large, irregularlyshaped and interstitial crystals that crystallize in a crystal-liquid mush. Thereafter, they appear as primocrysts which are relatively small, idiomorphic and cumulus crystals that precipitate from a main magma body. The evolution from large oikocrysts to small primocrysts is commonly recorded in the following textural and chemical features (Fig. 36a): (1) the first primocrysts of a new phase are substantially smaller than crystals of the already existing cumulus phases; higher in the section the primocrysts of new cumulus minerals increase in grain size and become ultimately similar to those of the existing cumulus phases; (2) the arrival of primocrysts occurs over some interval and peaks with a distinct modal overabundance; this is followed by relaxation to a steady-state trend in which proportions become close to cotectic; (3) if some mafic phases (e.g., olivine) are already on the liquidus then the emerging oikocrysts and primocrysts of a new mafic phase (e.g., clinopyroxene) will show a continuous evolutionary trend. This is not, however, the case with plagioclase. Its oikocrysts tend to be poorer in An-content compared to their primocrysts but become increasingly richer in An-content at the transition towards plagioclase primocrysts. The last-forming plagioclase oikocrysts are similar in composition to the first plagioclase primocrysts; (4) the base of the cumulate layer at which primocrysts of a new phase appears, is more adcumulate (i.e., with lesser amount of an interstitial liquid enriched in incompatible trace elements such as REE, Zr or P) compared to the top of the underlying cumulate layer; (5) the arrival of primocrysts is associated with a step-like increase of the median value of dihedral angle (Θ_{cpp}) at the junctions of two grains of plagioclase and one grain of either pyroxene or olivine. This usually occurs a few meters below the level at which primocrysts emerge (Latypov et al., 2020b). These systematic changes related to the arrival of cumulus phases in layered intrusions are interpreted within a conceptual framework that views layered intrusions as large initially crystal-free bodies of parental melt that cools and crystallises through thin solidification fronts along chamber margins. The entire magma body during its internal fractionation is considered to be kinetically supercooled (i.e., occurring slightly beneath its liquidus temperature) with regards to cumulus phases that form at the cooling margins. The arrival of each new cumulus phase on the liquidus is associated with some kinetic delay. The phase nucleates and grows directly at the floor, roof and sidewalls of basaltic magma chambers. Oikocrysts of a new phase in the underlying cumulates come invariably before its primocrysts because both the interstitial melt in a crystal-rich mush and the resident melt in the chamber evolve along the same liquid line of descent. As a result, the same liquidus phase appears in both environments – first as oikocrysts in the underlying crystal-rich mush (where melt supercooling in highest) and then as primocrysts from the overlying resident melt (Latypov et al., 2020b).

4.9. Inward propagation of solidification fronts

A problem in modern igneous petrology concerns the very anatomy of magmatic systems. Two endmember scenarios are envisioned; on the one hand, recent work citing primarily geophysics and phenocryst geochemistry has suggested that magmatic systems are predominantly composed of large, vertically extensive, trans-crustal crystal mushes (e. g., Cashman et al., 2017; Osterero et al., 2021). The other is the more classical model of a magma chamber, presented as a big tank of mostly crystal-free liquid in its interior (Irvine, 1987). Examples of vertically extensive mushy systems are presented as occurring underneath the Yellowstone caldera (Cashman et al., 2017) and underneath the island of Dominica of the Lesser Antilles (Osterero et al., 2021), while one of the best examples of a large tank filled with liquid is arguably the Skaergaard intrusion of Greenland (Annen et al., 2022). For many other intrusions, such as the Bushveld Complex, determining whether or not they accumulated by the emplacement of stacks of mush (Eales and Costin, 2012; Yao et al., 2021) or by the injection of large volumes of essentially aphyric melts (Latypov et al., 2022a), has been a contentious issue.
Distinguishing between these two endmembers for ancient fossilized magmatic systems may be accomplished by finding evidence for inwardpropagating solidification fronts. In the mushy model, one should expect largely undifferentiated stacks of igneous material. In the magma chamber model, mineral grains are formed or deposited on the floor and sometimes even the walls and roof of magma chambers. Here, they form layers that are thermally located between the liquidus and solidus of the chamber and are, therefore, in a partially crystalline state. These partially solidified layers are referred to as solidification fronts (Marsh, 1996) that gradually propagate inwards during the cooling of the magma chamber. As minerals are deposited (either by settling or in situ crystallization) to the solidification front, the melt undergoes magmatic differentiation, reflected in the solid products gradually evolving to lower temperature endmembers, and the progressive addition and/or removal of liquidus phases as the solidification front propagates (Latypov et al., 2020b). The Skaergaard intrusion is exemplary of such magmatic behaviour, with geochemical and mineralogical evidence suggesting the inward propagation of a solidification front from all margins of the intrusion (Fig. 29; McBirney and Noyes, 1979).
What follows are recent observations hinting at the existence of inward-propagating solidification fronts in the Bushveld Complex. Dealing with the Bushveld Complex is significant, since there has been much debate on whether this system accumulated as stacks of mush (e. g., Yao et al., 2021), or if it crystallized from an upward-propagating solidification front from a large, essentially crystal-free magmatic reservoir (e.g., Latypov et al., 2022a). In terms of geochemistry, arguably the best evidence for the existence of solidification fronts comes from magnetitite layers. This is because of the extremely high partition coefficient of Cr into magnetite, with recent experimental work suggesting it may even be as high as 2000 (Shepherd et al., 2022). During growth of magnetite, the surrounding

melt would be quickly depleted in terms of its Cr contents. If a magnetitite layer forms in an advancing solidification front, this Cr depletion would be recorded in subsequently forming magnetite, with the Cr content becoming lower in the direction of propagation. The above is precisely what Cawthorn and McCarthy (1980, 1981) and McCarthy et al. (1985) documented in Bushveld magnetitite layers: in vertical profiles across these layers, the Cr contents rapidly decrease upwards from >1.7 wt% at their bases to <0.1 wt% across a distance of just 1 m. More recently, Kruger and Latypov (2020) mapped out the geochemistry of massive magnetitite layers in two dimensions. What emerged was a two-dimensional record of the propagation of an ancient solidification front in a magma chamber that was hidden within the magnetitite's cryptic layering patterns. On the two-dimensional contour map, the stepwise propagation of the solidification front could be observed by tracing the geochemical contours, with each contour preserving the morphology of the solidification front at a specific stage in time (Fig. 37).

The geochemistry of magnetitites thus provides evidence for the existence of an inward-propagating solidification front in a magma chamber. Evidence for the in situ crystallization of these layers (see section 3.7) also suggested that they crystallized from essentially aphyric melts. Modelling based on the Cr content of magnetitites suggested that they crystallized from melt layers several tens to more than a hundred meters in thickness (Cawthorn and McCarthy, 1980; Kruger and Latypov, 2020; Kruger and Smart, 1987; Yao and Mungall, 2022), supporting the idea of a liquid-dominated magmatic reservoir that gradually solidifies during the propagation of a solidification front. However, this scenario becomes even more dramatic when the chromitite layers of the Bushveld Complex are also considered. Numerous field and textural observations on chromitite layers have provided support for their in situ crystallization. For example, the low packing density of grains of chromite is at odds with settling models (Latypov et al., 2022a), together with the occurrence of chromitite layers on overturned contacts in some field exposures (Latypov et al., 2017a, 2017b). This suggests that Bushveld chromitites probably also crystallized as inward-propagating solidification fronts. In comparison to magnetitite layers, however, significantly more melt is required to crystallize a thick chromitite layer due to the comparatively low concentration of Cr in basaltic melts. For example, to form a chromitite layer of 1 m of thickness would require a column of melt of a few kilometers in thickness (Latypov et al., 2022a). These observations provide support to the classic view of a large, liquid-dominated magma chamber that gradually solidifies by the inward propagation of a solidification front. A more interesting case of the propagation of a solidification front can be seen where the chamber floor has undergone some degree of destruction, potentially by thermochemical erosion after magmatic recharge, to produce a floor with a highly irregular morphology. This has been referred to as the undercut-embayed chamber floor and the process that produces it magmatic karstification (see section 3.4). Kruger and Latypov (2021) documented the propagation of magnetitite solidification fronts within magmatic karst environments (Fig. 37a and 38), using the same approach as described above. They envisioned that the exact propagation pattern of the solidification front is highly dependent on the cooling regime at the chamber floor. The melt will experience most of its heat loss directly through the underlying cumulates, while interconnected fragments (in this case, anorthosite) serve as additional heat sinks. Heat loss is thus most effective directly underneath anorthosite inclusions close to the floor, and this is where the melt first cools to the point where magnetite can start to nucleate (Fig. 37b). After nucleation, concentrated growth of the magnetite occurs to produce Cr-rich, dome-shaped structures, referred to as growth nodes (Cawthorn, 1994; Kruger and Latypov, 2020). Growth nodes may also occur within small depressions in the floor that allow for more effective cooling. The solidification front then propagates in a complex manner until most inclusions of anorthosite become engulfed in magnetitite (Fig. 37c, d). Continued growth from the floor upwards and from inclusions outwards causes the undercut-embayed floor to become completely filled with solid magnetitite (Fig. 37e). This results in geochemical patterns that appear like gradual reversals in terms of the Cr content around anorthositic inclusions, but in reality, reflect the complex propagation of a solidification front (Fig. 38). Kruger and Latypov (2021) proposed that crystallization within a magmatic karst environment provides several unique insights into the dynamics of crystallization and differentiation of magma chambers, such as (1) that the propagation of a solidification front can proceed in multiple directions, producing complex cryptic layering patterns, (2) cooling is sufficient through the underlying cumulates to control nucleation and growth, and (3) liquid exchange remains effective during the crystallization of magnetite to produce adcumulates even in extremely confined spaces, probably by the convective removal of thin liquid boundary layers adjacent to magnetite crystals.

4.10. The chamber floor: hard versus mushy

There is abundant evidence that mafic layered intrusions formed by the progressive inwards growth of marginal solidification fronts, with a central crystal-poor (or crystal-free) bulk magma. A critical parameter required to understand the progressive solidification of intrusions is therefore the thickness of these marginal crystal mushy layers, which is one of the prime controls on their physical properties and behaviour, controlling the rate and extent to which the remaining bulk magma will fractionate.

Model-based constraints on mush thickness are dependent on assumptions about their physical properties (e.g., porosity, permeability and rheology). Irvine (1980a, 1980b) used the offset of compositional discontinuities across modal boundaries by infiltration metasomatism to argue that the permeable mush zone in the Muskox intrusion was several hundred metres thick. A similar thickness was calculated by McKenzie (2011) for the mush on the floor of the Skaergaard intrusion, using a theoretical compaction model to account for the observed stratigraphic variation of bulk-rock P_2O_5 content. However, Tegner et al. (2009) used metre-scale anti-correlations between the calculated fraction of trapped liquid and rock density in the same cumulate sequence to argue for a compacting mush of the order of tens of metres.

Field-based evidence for mush thickness includes the length-scales of tectonically-induced disruption of layering, which vary from a few metres (Holness and Winpenny, 2009) to several hundreds of metres (Chambers and Brown, 1995). A thickness of several metres is also inferred from mush disruption beneath blocks that have fallen to the floor (Thompson and Patrick, 1968). Observations of sharp and essentially planar lower boundaries of metre-scale monomineralic oxide layers in the Bushveld intrusion indicate minimal disruption of the underlying plagioclase-dominated cumulates, indicative of formation of the oxide layers on a mostly solidified hardground. A similar conclusion is reached from outcrop-scale evidence suggestive of erosion of the chamber floor before formation of the overlying layers (Latypov et al., 2015a; Holness et al., 2017a).

A recently developed approach (Holness et al., 2017a, 2017b) to determining mush thickness in mafic intrusions is based on the observation that the median clinopyroxene-plagioclase-plagioclase dihedral angle, Θ_{cpp}, changes in a stepwise fashion as a phase is added or removed from the liquidus assemblage of a fractionating system (see section 3.6). The position of the magma-mush interface (i.e., the top of the mush) at the instant the bulk magma becomes saturated with (or loses) a new phase (Fig. 39) is marked by the first appearance (or disappearance) of the new assemblage in the cumulate stratigraphy. This is accompanied by a step-wise change in Θ_{cpp}, as the dihedral angle changes from the value associated with the old liquidus assemblage to that associated with the new assemblage, resulting from a change in the local latent heat contribution to the enthalpy budget and a consequent change in the growth behaviour of interstitial plagioclase. Holness et al. (2012a) showed that in solidifying orthocumulates (i.e., those cumulates containing

abundant interstitial liquid), all clinopyroxene-plagioclaseplagioclase dihedral angles are formed by the time only ~10vol% liquid remains: as gabbros become more adcumulate in character, the formation of the dihedral angle population is complete when the rock is even closer to being entirely solidified. The base of the dihedral angle step therefore corresponds to the horizon at which there is so little remaining liquid that it is effectively immobile (e.g., Cheadle et al., 2004). The more adcumulate the rock, the more closely the dihedral angle step corresponds to the horizon at which the mush is fully solidified and therefore the base of the mush. Consequently, the mush thickness can be determined from the stratigraphic distance from the base of the step to the change in the liquidus assemblage (Fig. 39).

This technique can be used only at those specific stratigraphic horizons where the liquidus assemblage changes. The mush thickness on the floor of the Rustenburg Suite of the Bushveld Complex was only a few metres thick at three widely spaced stratigraphic horizons (those marking the arrival of clinopyroxene, magnetite and apatite on the liquidus of the bulk magma) (Holness et al., 2017a), consistent with outcrop evidence for a thin mush. That on the floor of the Skaergaard intrusion was ~80 m in the lower parts of the stratigraphy where the bulk magma saturated in clinopyroxene (Holness et al., 2007b, 2007c), reducing to a few metres across much of the floor in the more evolved upper parts where apatite arrives on the liquidus (Holness et al., 2017b). The thickness of the mush developing contemporaneously on the vertical walls of the Skaergaard chamber increased progressively with increasing fractionation, from only a few metres at the point of clinopyroxene saturation to ~170 m at the point of apatite saturation (Holness et al., 2022).

The mush thickness on the floor is likely to be a function of the liquidus assemblage of the bulk magma, both because this controls the difference between the temperature at the top and bottom of the mush and also because it affects the extent of any gravitationally-driven compaction. Compaction of the Skaergaard Layered Series has been argued to be negligible (Holness et al., 2017c), and the insulating effects of the thick crystal pile prevented significant downwards heat loss, so a progressively thinner mush with increasing stratigraphic height was most likely predominantly controlled by the decreasing temperature difference between the top and base of the mush. That the associated wall mush contemporaneously increased in thickness demonstrates that its thickness was predominantly controlled by the rate of heat loss through the intrusion margins.

The thickness of the crystal mush is likely to vary spatially and temporally within any magma chamber, with transient or localized changes related to gravitational instability within the chamber (particularly for those with steeply dipping walls), and more progressive changes related to the temperature interval between the liquidus and solidus and the extent of adcumulus crystallization. The mush on the floor of open-system chambers is likely to experience episodes of mechanical or chemical erosion, due to sustained flow of incoming magma. Conversely, the mush thickness may be episodically thickened by the sedimentation of the crystal cargo brought in by replenishing magma. The mush thickness on steep walls may be reduced by gravitational collapse (with an associated abrupt increase in the thickness of the mush on the nearby floor) (Holness et al., 2022). Such changes can only be detected using the Θ_{cpp} step-change method if they occur close to the stratigraphic position of changes in the liquidus assemblage: if not, then other methods, such as detailed field observations, are required.

4.11. Absence of the roof sequences due to their disruption and collapse

The modelling of thermal history of a sheet-like magmatic body indicates that heat loss predominantly takes place through its roof rather than the floor (e.g., Irvine, 1970a; Morse, 1988). This is because, from the very start, a thermal gradient at the roof is inherently larger than at the floor in a sheet-like body (Morse, 1988). This implies that magma crystallization must also prevail there producing a thick sequence of roof cumulate rocks in all layered intrusions. This is not the case, however. In reality, most of the layered intrusions (except for Skaergaard and Kiglapait intrusions) are lacking any rock sequences that would have grown from the roof downwards. Among them are the Bushveld Complex (Cawthorn, 2015; Eales and Cawthorn, 1996), Fongen-Hyllingen intrusion (Wilson and Sørensen, 1996), Penikat and Kemi intrusions (Alapieti et al., 1989; Alapieti and Lahtinen, 1986), Koillismaa intrusion (Karinen et al., 2022), Imandra intrusion (Egorova and Latypov, 2012a), Muskox (Irvine, 1977), Sudbury Complex (Lightfoot, 2016), Sept Iles (Namur et al., 2010) and many others. A pertinent question is why are roof sequences absent from all these intrusive complexes if they are theoretically supposed to be there? A clue to this long-standing paradox appears to have been provided by a recent re-mapping of the Sudbury Igneous Complex (SIC) (Latypov et al., 2019a).

From the base upwards, the SIC shows a notable magmatic stratigraphy in which a lower noritic layer passes through a gabbroic layer into an upper granophyric layer. This stratigraphy has been traditionally interpreted as resulting from internal unidirectional differentiation of an originally homogeneous impact melt sheet (Lightfoot, 2016; Lightfoot and Zotov, 2005; Therriault et al., 2002) (Fig. 40a). The re-mapping has unexpectedly resulted in the discovery of discrete blocks (10 to 100 s meters in size) of melanorites that occur throughout much of the stratigraphy of the SIC and are, even locally, developed along its roof (Latypov et al., 2019a). Both chemically and mineralogically the melanorite blocks are an integral part of the SIC. On this basis, the melanorite blocks were interpreted as fragments of a roof (mela)noritic sequence of the SIC which initially grew from the top of the melt sheet downwards but was later disrupted and collapsed onto the temporary floor (Latypov et al., 2019a). This has resulted in the recognition that the Sudbury melt body crystallized from both margins inwards from the very beginning, producing floor and roof sequences of the same cumulates synchronously (Fig. 40b). The roof sequence was gravitationally unstable and tectonic activity resulted in its nearly complete dislocation and collapse, as angular blocks settling on the upwards-growing chamber floor (Fig. 40c). The roof autoliths may thus be quite abundant in the SIC and may substantially contribute to the overall thickness of noritic/gabbroic zones by forming ~15 vol% of their sequence (Latypov et al., 2019a). Interestingly, the collapse of large discrete blocks on the chamber floor of the SIC is expected to result in local irregularities of its topography so that crystal deposition onto and between the neighbouring blocks may produce pothole-like depressions that have been recently reported from the complex (Chistyakova and Latypov, 2022).

A major implication from the SIC is that the initial roof sequences in most layered intrusions may have been destroyed and collapsed as angular blocks on the chamber floor. This explains why most layered intrusions lack any rocks that grew from the roof downwards. The remnants of the former roof sequences may be, however, found as separate blocks scattered among the rocks of the floor sequences. Such angular blocks in the floor sequence were found and interpreted as coming from the former roof sequence in the Akanvaara intrusion, Finland (Mutanen, 2005). The blocks of the roof sequences are also found among the rocks of the floor sequences in Sarqata Qaqa Complex (Thompson and Patrick, 1968), Stillwater Complex (Hess, 1960), and Skaergaard intrusion (Irvine et al., 1998). Future research will likely reveal many more examples of layered intrusions in which roof-derived blocks are sitting within the floor rock sequences. The field reexamination of the SIC (Latypov et al., 2019a) indicates that twodimensional (re-)mapping of layered intrusions is a very powerful tool to improve our understanding of internal dynamics of evolving magma chambers (Kruger and Latypov, 2020, 2021; Tegner et al., 1996; Wilson and Larsen, 1985).

4.12. Basal reversals and chilled margins

Basal reversals are a characteristic feature of both mafic-ultramafic sills (Frenkel' et al., 1988; Galerne et al., 2010; Latypov and Egorova, 2012; Egorova and Latypov, 2013; Simkin, 1967) and layered intrusions (Campbell, 1978; Egorova and Latypov, 2012a, 2012b; Jaupart and Tait, 1995; Wilson and Engell-Sørensen, 1986). They occur along the margins of igneous intrusions and show rocks and minerals that become increasingly more primitive upwards. The reversals are commonly marked by a decrease in the number of crystallizing (liquidus) phases in successively formed rocks (e.g., *Ol + Pl + Cpx, Ol + Pl, Ol*) and chemical changes in minerals that become progressively more primitive (e.g., plagioclase An_{30} – An_{80}) inwards (Fig. 41a, b). Importantly, both crystallization sequences and compositional trends that are observed in basal reversals are opposite to those expected from internal fractionation of basaltic magma. To resolve this petrological puzzle, igneous petrologists have introduced many different mechanisms including magma undercooling, contamination, compositionally-zoned magma, prolonged magma emplacement, crystal settling, flow differentiation, reaction with varying amounts of intercumulus melt, shrinkage-induced magma inflow, Soret fractionation, thermal gradient-induced compositional reconstitution of solidifying cumulates and redistribution of interstitial melt in solidifying rocks (see a review in Latypov, 2015). Most recently, the basal reversals have been interpreted as a result of open-system development of magma chambers at their initial stage (e.g., Latypov, 2015; Latypov et al., 2011; Latypov and Egorova, 2012). In particular, a general "three-factor model" was put forward that explains the reverse compositional trends in basal reversals by operation of three major processes: (1) a progressive change in the composition of melt that replenishes the chamber; (2) a gradual decrease in the melt undercooling that results in a gradual approach towards equilibrium crystallization; (3) effective removal of compositional boundary layers from the surfaces of growing crystals by flowing magma that increases the proportion of cumulus minerals in rocks (Latypov, 2015; Latypov et al., 2011; Latypov and Egorova, 2012).

These three processes are thought to operate along the cooling margins of magma chambers during the initial stages of their development. Importantly, basal reversals do not develop if cooling of the inflowing magma is weak. This is clearly indicated by their absence from intrusions that are produced from magmas that were emplaced into preheated host rocks (e.g., Basistoppen sill). This indicates that a thermal gradient plays a critical role in the origin of reversals in magmatic bodies: no temperature gradient – no basal reversals. Two types of basal reversals occur in layered intrusions which are referred to as fullydeveloped and aborted reversals (Latypov et al., 2015a). Crystallization sequences and mineral compositional trends in fully-developed basal reversals are opposite to those in the overlying Layered Series to which these reversals gradually pass through a crossover horizon (Fig. 41a). This type is characterized by a continuous evolution during the crystallization of the reversal and is very abundant in intrusive bodies (e.g., Latypov, 2003a, 2003b). In contrast, aborted reversals are quite rarer and are produced when the internal differentiation is interrupted by the emplacement of more primitive magma that forms the compositionally distinct Layered Series. For this reason, the aborted reversals show truncated crystallization sequences and mineral compositional trends. They also exhibit a sharp compositional contact with the overlying Layered Series (e.g., Latypov et al., 2011). The basal reversals are interpreted as forming from the leading portions of evolved melts that are generated through fractional crystallization of parental magma as it ascends along feeder conduits (Fig. 41c). In contrast, Layered Series shows products of fractional crystallization of only slightly modified parental magma that arrived into the chamber when basal reversals were already formed (Latypov, 2015).

The "three-factor model" for the formation of basal reversals has important implications for our common practice of interpreting chilled margins as representatives of parental magma compositions. This practice does not appear to be properly justified because mafic sills and layered intrusions are not commonly produced instantaneously from a single pulse of magma of homogeneous composition (Latypov, 2015). They seem to fill progressively with magma that becomes increasingly more primitive in composition with time (Fig. 41c). As a result, chilled margins may represent solid products of evolved fractionates of the parental magma rather than this magma itself. This concept may account for some puzzling features of layered intrusions, namely: (a) the compositional difference between chilled margins and the bulk of the intrusion, with the latter being commonly more primitive than the former; (b) the existence in the same intrusion of chilled margins that show different compositions; (c) the tendency of the evolved chilled margins to be compositionally similar to low temperature cotectics; (d) the compositional similarities of chilled margins in layered intrusions that are formed from the contrasting parental magmas (Latypov et al., 2007). From this it follows that chilled rocks in plutonic bodies are unlikely to be representative of parental magma compositions. Instead, they appear to have formed from evolved precursors of the parental magma (Fig. 41c; Latypov, 2015). If chilled rocks are not reliable, then this raises a question as to what can be used to identify the parental magma composition. There seems to be no general method that can be safely employed to plutonic bodies to obtain a reliable estimate of their parental magma composition. However, irrespective of many drawbacks (e.g., preservation of partly eroded sections, magma chamber replenishment by multiple pulses and the possible entrainment of intratelluric phenocrysts by magmas) the most reasonable approach appears to be the use of the bulk composition of intrusions and their liquid line of descent as deduced from the crystallization sequence and mineral compositions (e.g., Ariskin and Barmina, 2004; Frenkel' et al., 1988; Irvine, 1970b).

4.13. Adcumulus growth theory

Adcumulus growth takes place by a highly efficient process of solute rejection. Numerous models have been proposed over time for the development of adcumulates within the classical mechanicalaccumulation cumulus paradigm. The simplest and most commonly assumed mechanism has adcumulates developing during recrystallisation within the crystal pile, with residual liquid being expelled during compaction (Irvine, 1980b) (Fig. 42a-c). This mechanism can largely be discounted on several lines of evidence: the cumulus composition of oikocrysts (Latypov et al., 2020b), spatial distribution of ortho- and adcumulates within individual intrusions (Campbell, 1977), the absence of microstructures and zoning patterns characteristic of compaction (Holness et al., 2017c) and microstructural and field evidence that the mush layer at the top of the crystal pile is commonly only a few meters thick (Holness et al., 2017a, 2017b) (see section 4.10).

The alternative explanation for the formation of adcumulates and heteradcumulates requires crystal growth to be taking place at or near the top of the crystal pile, where the intercumulus liquid network is in diffusive contact with the main body of parent magma (Campbell, 1978; Morse, 1986). This necessity was recognized during the earliest pioneering work on cumulate rocks (e.g., Wager et al., 1960). The simplest form of this model for monomineralic adcumulates involves nucleation at the temporary top of the crystal pile, followed by convective replenishment of an adjacent boundary layer of magma very close to its liquidus temperature (Fig. 42d, e), such that growth is favored over nucleation and grains grow to fill space. This process gives rise to what is termed "primary adcumulates", in contrast to "secondary adcumulates" formed by compaction and melt expulsion deep in the crystal pile. For poikilitic heteradcumulates, there is an additional complexity whereby the convecting magma is saturated with one phase but supersaturated with the other, such that a poikilitic texture arises from the difference in relative rates of growth of existing grains and nucleation of new ones (Fig. 42f, g). This gives rise to a common observation that chadacrysts (enclosed grains) commonly increase in size from the

centres to edges of oikocrysts. In some cases, oikocrysts preserve the original nucleation and early growth history of the chadacryst phase, particularly plagioclase (Mathison, 1987). Commonly, heteradcumulates involving olivine and orthopyroxene develop at a peritectic where one phase is dissolving while the poikilitic phase is growing; this relationship has also been recognized for orthopyroxene and clinopyroxene (Barnes et al., 2021) (Fig. 22b). In all cases, the resulting textures are the result of primary crystallization close to or just below the liquidus temperature.

Further insight into the origin of common heteradcumulate textures comes from a common rock type in the Upper Critical Zone of the Bushveld Complex, a poikilitic chromite-bearing pyroxenite illustrated in Fig. 4e. In this rock, a peritectic reaction between orthopyroxene and augite results in orthopyroxene being extensively resorbed inside large idiomorphic augite oikocrysts, leaving a halo of orthopyroxene-depleted material around the oikocrysts that is itself preserved within large, also idiomorphic plagioclase oikocrysts with near-cumulus calcic compositions. Evidently orthopyroxene was dissolving within a transient boundary just ahead of the advancing edge of the augite oikocryst, the process being arrested when entrapped by the growing plagioclase. A similar process is likely to apply to the common poikilitic harzburgite, where partially resorbed olivine grains are enclosed within idiomorphic orthopyroxene and augite oikocrysts (Kaufmann et al., 2018).

The significance of the concept of primary adcumulus growth is that in large intrusions such as the Bushveld or Stillwater Complexes, dominated by adcumulates and heteradcumulates, the old concept of the cumulus pile as a compacting crystal mush cannot automatically be assumed. While orthocumulate rocks are certainly present in larger intrusions, particularly close to the margins, and some, such as the trough layered rocks of Skaergaard (Vukmanovic et al., 2018) show compelling evidence for mechanical accumulation, much if not most of the cumulus sequence accreted to the crystal pile as near-solid rock, in a similar way to evaporitic sediments, with only minor proportions of trapped liquid.

The propagating front of the crystal pile can be seen as a “hard-ground” analogous to chemical sediments (see section 4.10). This has important implications for discussions of “crystal mush” processes and particularly for models of PGE and chromite ore formation involving large scale upward mass-transport by expelled intercumulus components (Marsh et al., 2021; Parker et al., 2022). Large volumes of intercumulus liquid were probably never present. This has profound implications for “mush models” of differentiation (Cashman et al., 2017).

4.14. Compositionally stratified magma chambers

In earlier petrogenetic models of layered intrusions, the resident melt was supposed to be of the same composition throughout the entire chamber because of being kept in vigorous convection (e.g., Wager and Brown, 1968). As a result, any cumulate layer forming at the chamber floor was expected to be compositionally identical across the entire strike of a layered intrusion. It has been thought, therefore, that a single cross-section at any place along the strike is sufficient to provide comprehensive information on the phase, modal and cryptic layering of the entire layered intrusion. For this reason, until the mid-1980’s, lateral variations were assumed to be negligible in layered intrusions and researchers were mostly focused on examining the compositional variations normal to the layering – i.e., from the floor to the roof of the magma chamber. The situation was drastically changed, however, after the ground-breaking discovery of Richard Wilson and his co-authors (Wilson and Engell-Sørensen, 1986; Wilson and Larsen, 1982, 1985) who undertook for the first time a two-dimensional study of mineral composition across the Fongen-Hyllingen intrusion, Norway. On the basis of the compositional data from 11 sampling profiles, they have shown that minerals from the same cumulate layer may systematically change their composition along the strike. For instance, a layer of ferrodiorite in the lower part of the intrusion showed a systematic lateral change in An-content of plagioclase from >60% to 20% (not shown) and in Mg-number of clinopyroxene from >70 to 20 over a distance of ~11 km along the strike (Fig. 43a). This phenomenon has been described as an angular discordance between the modal and cryptic layering in this intrusion. The discordance has clearly indicated that the cumulate layers were deposited on the temporary chamber floor which was not an isothermal surface as is commonly assumed in conventional petrogenetic models. Clearly, some novel interpretation of this puzzling feature was required since none of the traditional models could be reconciled with a non-isothermal character of the floor in a magma chamber. Following some earlier studies, Wilson and Larsen (1985) postulated that the resident melt in the chamber was likely compositionally stratified in response to such processes as magma mixing, contamination by country rocks, or sidewall crystallization (e.g., Huppert and Sparks, 1984; Irvine et al., 1983; Irvine, 1980b; McBirney and Noyes, 1979). In contrast to earlier concepts, however, in which magma was assumed to crystallize against the horizontal floor or by lateral accretion from the walls (Irvine et al., 1983), in situ crystallization of magma along the inclined chamber floor has been proposed. A key feature of this idea is that the same cumulate layer may crystallize from several liquid layers that become increasingly more evolved in composition from the base upwards (Fig. 43b). It is this angular discordance between the horizontal stratification of magma in the chamber and an inclined chamber floor that has been attributed as a major cause of an angular discordance between the cryptic and modal layering of the Hyllingen intrusion. This novel concept has subsequently got some support from experimental studies (e.g., Huppert et al., 1987) and field, textural and chemical observations from other layered intrusions (Tegner et al., 1996; Wilson et al., 1996). More recently, compositional stratification of magma in the chamber has been invoked to explain a number of petrological features of the Bushveld Complex (Cawthorn et al., 2016; Latypov et al., 2018b; Tegner et al., 2006). Although compositional stratification in magma chambers has currently fallen off the radar of most igneous petrologists, it is worthwhile to remind here about this important petrological concept especially in the light of the fact that none of the existing layered intrusions has been so far studied in two dimensions at such a great detail as the Fongen-Hyllingen intrusion (Habekost and Wilson, 1989; Meyer and Wilson, 1999; Wilson and Larsen, 1985; Wilson and Sørensen, 1996; Wilson, 2010). It is not inconceivable that some currently puzzling features of layered intrusions may be better understood and explained in the frame of a concept involving in situ crystallization from a compositionally stratified resident melt in the chamber. It would be prudent to conclude with Wilson (2010, p. 17) insightful remark: ‘Probably the most important feature that has emerged from studies of Fongen-Hyllingen is that lateral variations can be very significant, and must be considered if fundamental magma chamber processes, such as crystallisation mechanisms and magma emplacement, are to be understood’. It is largely through such detailed field, textural and chemical studies of igneous intrusions that the knowledge of magma chamber processes can be improved and advanced (see for debates in Latypov, 2009; Latypov et al., 2015b).

4.15. The importance of melt-sediment interactions during the magma chamber construction

By magma-sediment interactions, we generally refer both to the assimilation of sediment by magma and their thermal devolatilization in response to contact metamorphism. Many sedimentary rocks are extremely rich in volatiles (i.e., CO_2 in carbonates, SO_2 in sulfates, C–H species in carbonaceous shales, and Cl in salts) and can potentially provide the interacting magma with amounts of volatiles that markedly exceed magmatic concentrations (e.g., Ganino and Arndt, 2009). Assimilation is proposed to occur via different mechanisms, the two most invoked ones on the basis of field evidence are: (1) partial or total melting of fusible sedimentary xenoliths, such as shales (e.g., Th´ eriault and Barnes, 1998); (2) thermal breakdown of volatile-rich sedimentary rocks, such as carbonates, and incorporation

of the resulting fluids into the magma (e.g., Ganino et al., 2008). In addition, experimental studies show that the chemical dissolution of the sedimentary rock within the magma may occur at magmatic conditions for sulfate (Iacono-Marziano et al., 2017), and carbonate rocks (e.g., Carter and Dasgupta, 2018), accompanying decarbonation (i.e., thermal breakdown) in the latter case. Thermal decomposition and devolatilization of the sediments also occur at temperatures lower than those necessary for assimilation, in the contact aureoles of the intrusions (e.g., Ganino and Arndt, 2009). They have been extensively documented in black shales (e.g., Aarnes et al., 2010; Virtanen et al., 2021). Depending on the nature of the sedimentary rocks, magma-sediment interactions have variable consequences for intra-chamber magmatic processes as described below.

4.15.1. Magma emplacement and reservoir dynamics

Magma-sediment interactions have poorly studied implications for magma emplacement mechanisms. The nature of the sedimentary rocks is likely to play a role in the formation and propagation of sill-like structures (e.g., Hutton, 2009; Schofield et al., 2014), therefore controlling magma intrusion in sedimentary basins. Several large igneous provinces were emplaced through sedimentary basins, forming the socalled volcanic basins that generally occur along rifted continental margins and on lithospheric cratons (e.g., Svensen et al., 2015). Volcanic basins consist of flood basalts and numerous cogenetic intrusions injected into the sedimentary rocks of the upper crust, commonly as sills and dikes. Carbonaceous and evaporitic rocks are the most common rocks observed in the contact aureoles of the sills (Svensen et al., 2009, 2015; Hutton, 2009; Aarnes et al., 2010; Heimdal et al., 2019). The preferential injection into these sedimentary rocks is likely related to their chemical and physical properties: (i) their lower density and mechanical weak behaviour, (ii) their fluidization caused by heating and dehydration (occurring at particularly low temperatures in coals and hydrous salts), and (iii) the creation of a secondary porosity by devolatilization, dissolution and melting (Hutton, 2009; Schofield et al., 2014). Altogether, these processes are suggested to facilitate the lateral propagation of the intrusions; this in turn promotes the interaction of the magma with the sedimentary rocks that are intruded, by creating new interfaces between the magma and the host rock.
Magma chambers can potentially grow by melting of their host rocks. Recent thermodynamic simulations show that ultramafic magmas can assimilate more than their initial weight of pre-heated host rocks with the residual melt still being basaltic in composition (Mungall, 2007; Heinonen et al., 2021) (see also floor cumulate dissolution in sections 3.4. and 4.7). Mafic magmas have lower heat budgets but still can assimilate several tens of weight percents of suitable pre-heated host rocks (Karykowski et al., 2018a; Virtanen et al., 2022). However, the overall process cannot be considered by equilibrium thermodynamics of confined systems and the amount of assimilation, and consequently the growth of the magma reservoir, is ultimately determined by the efficiency of the heat dissipation and reaction kinetics, which are difficult to estimate accurately.

4.15.2. Magma composition and phase equilibria

The assimilation of volatile-rich sedimentary rocks can modify the composition of the magma by affecting the stability of major magmatic minerals. These modifications are generally observed at a small scale (centimeters to meters), but they can affect plutonic bodies up to several kilometers wide (e.g., Barnes et al., 2005). The effects of the assimilation of carbonate rocks are particularly well constrained. Petrological (e.g., Joesten, 1977; Barnes et al., 2005) and experimental (e.g., Iacono Marziano et al., 2007; Iacono-Marziano et al., 2008) studies show that magma contamination by carbonate rocks is marked by the overgrowth of Ca-rich phases on primary minerals. In particular, olivine or orthopyroxene destabilization in favor of clinopyroxene is often described (e. g., Barnes et al., 2005; Iacono Marziano et al., 2007; Iacono-Marziano et al., 2008). Moreover, scapolite has been observed to crystallize at magma-limestone interfaces, whereas melilite, spinel, apatite and magnesian olivine occur at magma-dolomite interfaces (e.g., Joesten, 1977; Barnes et al., 2005; Iacono Marziano et al., 2007; Ganino et al., 2008; Carter and Dasgupta, 2018). The crystallization of extremely Carich plagioclase (up to An_{100}) is also ascribed to carbonate assimilation (e.g., Chadwick et al., 2007).
When the extent of assimilation is significant (> 10 wt%), carbonate incorporation also deeply affects the composition of the residual melt, possibly generating ultracalcic melts (e.g., Iacono-Marziano et al., 2008), or silica undersaturated, alkali-rich magmas (e.g., Iacono Marziano et al., 2007; Iacono-Marziano et al., 2008). Progressive depletion in silica and enrichment in alkali, mostly described at the meter scale, are observed to affect whole plutonic bodies, with degrees of carbonate assimilation proposed to reach 20 wt% (Barnes et al., 2005).
The effect of the assimilation of other sedimentary rocks on magma phase equilibria is markedly less well known. The assimilation of organic matter by magmas reduces iron and the elements with variable valences in the silicate melt, promoting the crystallization of native iron and other reduced phases including graphite, wüstite, armalcolite, carbides, sulfides, ulvospinel, ¨ native copper and native lead (e.g., UlffMøller, 1985; Ryabov and Lapkovsky, 2010).
The effects of a partial or total assimilation of shales by mafic magmas have been investigated using the Magma Chamber Simulator (Virtanen et al., 2022). The simulations show that as H_2O content in the magma increases due to assimilation, olivine stability increases relative to clinopyroxene. Extensive assimilation of silicate material (> 20 wt%) leads to crystallization of orthopyroxene in the place of olivine (Virtanen et al., 2022), as often observed in nature, where norites are commonly spatially associated with shale xenoliths (e.g., Th´eriault and Barnes, 1998). All the chemical changes caused by shale assimilation lower sulfide solubility in the magma facilitating sulfide segregation provided that sulfur content of the magma is not simultaneously diluted (Virtanen et al., 2022).
The main consequence of magmatic assimilation of sulfate rocks is the significant increase in the sulfur content of the silicate melt, accompanied by a less marked enrichment in CaO, eventually leading to anhydrite saturation (Iacono-Marziano et al., 2017). Magmatic anhydrite has been observed in intrusive rocks that experienced the assimilation of evaporite-bearing country rocks (Li et al., 2009). The assimilation of halite-rich evaporitic rocks can be difficult to identify as it does not seem to affect phase equilibria; it mainly enhances the halogen and alkali content of the magma, therefore increasing the Cl content of Cl-bearing minerals, such as biotite (Heimdal et al., 2019).

4.15.3. Ore-forming processes

By making the magma to coexist with important amounts of fluid phase, magma-sediment interactions are able to engender the formation of either "volatile-assisted" magmatic deposits, or magmatichydrothermal deposits. Produced volatiles may indeed strongly affect the phase equilibria and redox conditions of the magma and trigger the segregation/crystallization of magmatic phases that are generally uncommon or represent accessory phases in magmatic rocks. This has been shown to be instrumental to the formation of three types of magmatic deposits: oxide deposits, like those of the Panzhihua intrusion (e.g., Ganino et al., 2008); native iron deposits enriched in siderophile elements, as those observed at Disko Island (Greenland) and the Siberian Platform (e.g., Ulff-Møller, 1985; Ryabov and Lapkovsky, 2010; IaconoMarziano et al., 2012); and magmatic Ni-Cu-*Co* sulfide deposits (Barnes et al., 2023). For the latter

type of deposits, the input of external sulfur is also recognized to be essential, as proposed for Duluth, and Noril'skTalnakh ore deposits among many others (e.g., Th´ eriault and Barnes, 1998; Li et al., 2009; Iacono-Marziano et al., 2017; Virtanen et al., 2021, 2022).

The release of abundant fluids, and the modification of the redox conditions of the magma induced by the fluids also likely occur with other types of deposits, such as skarn deposits generally associated with carbonate rocks (Meinert et al., 2005); magnetite deposits ascribed to the occurrence of strongly oxidizing, high salinity brines derived from magma-evaporite interactions (e.g. Svensen et al., 2009; Li et al., 2015); and graphite mineralization associated with reduced C-O-H-S fluids produced by the interaction with carbonaceous rocks (e.g., Ortega et al., 2010).

4.16. Lateral reactive infiltration in a crystal mush

In layered intrusions and in sills from the oceanic crust, it has been shown that reactive porous fluid flow significantly affects the chemistry and the texture of cumulate rocks (Philpotts and Philpotts, 2005; Tegner et al., 2009; Namur and Charlier, 2012). Such process may also result in the development of discordant mafic/ultramafic bodies (Tegner et al., 1994; Meurer et al., 1997) and the formation of critical metal deposits (Boudreau, 1999). Although examples of vertical porous flow become increasingly described, lateral flow has rarely been documented (Namur et al., 2013).
The box-shaped Skaergaard intrusion (Greenland) is made up three main units (a section 4.2, Fig. 29a, b), one of which, the Marginal Border Series (MBS) having grown inwards from the vertical walls. The MBS is divided into two parts: the outer MBS with no obvious layering features and the inner, banded, MBS. The inner MBS shows steeply dipping or vertical layering looking like colloform features (Fig. 44a). Colloform bands contrast with their gabbroic host rocks by having a different mineralogy and grain size. In general, the bands are always plagioclasepoor and therefore comparatively enriched in mafic minerals. The bulk chemical composition of colloform bands reflects their mineralogy: i.e., colloform bands are enriched in mafic mineral compared to host gabbros and are therefore enriched in elements FeO, MgO and MnO and depleted in Al_2O_3 and Na_2O. In terms of mineral composition, the An-content [molar Ca/(Ca + Na)] of plagioclase in colloforms is identical to that of plagioclase in host gabbros. In contrast, the Fo-content [molar Mg/ (Mg + Fe)] of olivine in colloforms is 2–5% higher compared to the gabbro.
The colloform bands observed in Skaergaard show an obvious morphological evolution from the outer part of the banded MBS (near the contact with the gneissic country rocks) towards the inner part: i.e., the centre of the intrusion. Such morphological evolution would be best described as progressive but still can be described by 4 main stages. Going from the unbanded MBS to the center of the intrusion, one can observe: (1) colloform bands being planar in vertical sections but undulous on horizontal sections. (Fig. 44b); (2) colloform bands then develop a cuspate shape in three-dimensions (egg-box structure), locally forming series of parallel bands; (3) colloform bands then finger-like and less laterally continuous (Fig. 44b); (4) finally the tips of the fingers are detached from the parent colloform, forming structures looking like a series mafic bowls (Fig. 44b).
The morphology of the colloforms observed in Skaergaard, their undulous structure as well as the development of fingers and ultimately bowls are similar to the morphological features of reaction fronts observed in porous rocks. These were reproduced experimentally by infiltration of liquid into a porous medium (Ortoleva et al., 1987; McBirney and Sonnenthal, 1990). In Skaergaard, the melt density is lower than that of the cumulate matrix. As a consequence, the mush shrinks during solidification. Colloform bands are produced by reactive porous flow, i.e., chemical disequilibrium, due to lateral migration of primitive liquid from the main magma body into the crystal mush. The hot, primitive, migrating melt predominantly dissolves olivine and clinopyroxene and less plagioclase. After some degree of dissolution, the melt becomes effectively super-saturated in mafic components (Schmidt et al., 2012) and abruptly starts abundantly crystallizing olivine and pyroxene in the mush. During disequilibrium, fast, crystallization, mineral proportions are dominantly controlled by the relative complexity of mineral structures. This explains the high ratio of simple mafic minerals (olivine, clinopyroxene, Fe–Ti oxides) over plagioclase (Gibb, 1974; Corrigan, 1982; Burkhard, 2005) and leads to the production of ultramafic bands with a mineralogy and composition contrasting with host gabbros.

4.17. Reactions involving conjugate immiscible liquids in crystal mushes

Recent work has highlighted the importance of silicate liquid immiscibility during the fractionation of basalt. The differential movement of unmixed conjugate liquids, one Fe-rich and the other Si-rich, may have profound effects on the spatial variation of bulk rock composition in mafic intrusions (Charlier et al., 2011; Salmonsen and Tegner, 2013; Namur et al., 2012, Nielsen et al., 2015). The majority of the work done on the petrographic and geochemical effects of silicate liquid immiscibility has focussed on the Skaergaard intrusion of East Greenland.
The evolving bulk liquid in the Skaergaard intrusion encountered the binode at a composition equivalent to that of the bulk melt near the base of UZb (Nielsen et al., 2019). The first evidence of the splitting of the magma into two immiscible conjugates was the discovery of coexisting Si- and Fe-rich melt inclusions in primocryst apatite from UZb (Jakobsen et al., 2005). Evidence of co-existing immiscible conjugate liquids in the Skaergaard crystal mush is provided by the presence of clearly distinct pairs of late-crystallizing pockets of interstitial liquid: granophyric pockets (crystallized from the Si-rich conjugate, Fig. 45a) coexist with pockets dominated by ilmenite, with apatite, skeletal Fe–Ti oxides and clinopyroxene (crystallized from the Fe-rich conjugate, Fig. 45b) (Holness et al., 2011). Smaller pockets of interstitial material, commonly very fine-grained, show two diverging trends of plagioclase composition in the pore walls, correlating with their mineralogy: plagioclase adjacent to pockets dominated by granophyre or quartz has a normally zoned rim with low TiO_2, whereas that adjacent to pockets containing mafic phases is reversely zoned, with high TiO_2 (Humphreys, 2011), again interpreted as a consequence of unmixing and the presence of two distinct liquid compositions in the mush.
The two immiscible conjugates have different physical properties: the Si-rich liquid is buoyant and viscous whereas its Fe-rich conjugate is dense and relatively inviscid. This creates the possibility of differential migration. Significant and sustained loss of an exsolved buoyant Si-rich liquid from the fractionating interstitial liquid in the mush on the chamber floor, and its addition to the overlying bulk magma, is argued to have resulted in an overall Fe-enrichment of the Layered Series from LZc upwards, with a corresponding Si-enrichment in UBS (Nielsen et al., 2019). Micro-scale evidence of pervasive differential migration of the interstitial liquid in the lower parts of the crystal mush on the chamber floor is provided by a variety of features denoting chemical disequilibrium (Holness et al., 2011; Nielsen et al., 2015). These include serrated grain boundaries between pyroxene and plagioclase primocrysts (Fig. 45c), fish-hook pyroxenes (Fig. 45d), mafic symplectites formed of anorthitic plagioclase and olivine (or pyroxene) centred on Fe–Ti oxide grains and replacing the surrounding primocrysts of plagioclase and (less commonly) olivine and augite (Fig. 45e), and extensive rims of olivine separating Fe-Ti-oxides from plagioclase and pyroxene (Fig. 45f). These features are attributed to chemical reactivity of dense Fe-rich liquid retained in the mush following the buoyancy-driven upwards loss of its Si-rich conjugate (Holness et al., 2011). Nielsen et al. (2015) suggest that as much as half the volume of the upper MZ gabbros may have solidified from this retained Fe-rich conjugate liquid. Reactive symplectites are absent in the upper parts of the Layered Series (Holness et al., 2011), which instead

contain the co-existing interstitial pockets of granophyre and ilmenite-rich mafic pockets described above (Figs. 45a, b), indicating the retention of the Si-rich unmixed conjugate. In the most evolved cumulates, the ilmenite-rich intergrowths are absent, consistent with the interstitial liquid either having evolved out of the binode, and therefore comprising a single-phase silica-rich liquid, or that the unmixed Fe-rich conjugate was consumed by overgrowth of the grains in the mush.
Similar, but more compositionally variable, reactive features attributable to differential migration of immiscible silicate liquid conjugates are present in the Sept Iles layered intrusion in Quebec, Canada (Namur et al., 2010, 2011b), and comprise two types. Type I symplectites are intergrowths of anorthitic plagioclase with pyroxene, amphibole, or olivine: they grow from the surface of primocryst oxide grains and replace primocryst plagioclase (Fig. 45g). Type II symplectites are intergrowths of anorthitic plagioclase with orthopyroxene or amphibole, and grow from olivine primocrysts, replacing primocryst plagioclase (Fig. 45h). Although both types of symplectites may have formed from the interaction of primocrysts with residual Fe-rich liquid, the presence of abundant hydrous mineral assemblages in the Sept Iles intrusion suggests that redistribution and concentration of hydrous fluids in incompletely solidified rock, or an increase in water activity of the interstitial melt, may have played an important role in their formation.

4.18. Non-traditional Fe-Mg-Cr stable isotopes: sources, mixing and oxygen fugacity

The study of non-traditional stable isotopes has been developed and applied to layered intrusions during the past decade. On average, values for whole rocks of layered intrusions are close to the isotopic composition of basalts (δ^{56}Fe ~ +0.10‰ and δ^{26}Mg ~ - 0.25‰; Dauphas et al., 2017) (Fig. 46). However, significant fractionation of iron isotopes interpreted to be induced by high-temperature magmatic processes was initially described in the Red Hill intrusion in Tasmania (Sossi et al., 2012). Crystal fractionation in closed systems affects the $Fe^{3+}/\Sigma Fe$ of residual melts which controls the evolution of δ^{56}Fe. Indeed, early fractionation of Fe–Mg silicates (olivine and pyroxenes) and plagioclase gives rise to an enrichment of total iron and δ^{56}Fe as well as an increase in oxygen fugacity of residual melts. At latter stages of differentiation, magnetite saturates and becomes the dominant iron-bearing phase which sequesters Fe^{3+} and isotopically heavy iron (Sossi et al., 2012).
The Skaergaard intrusion, commonly interpreted as a typical closedsystem, exhibits a systematic increase of δ^{56}Fe (- 0.019 + 0.253‰) with stratigraphy (Lesher et al., 2014). The Upper and Upper Main Zones of the Bushveld Complex also span a wide δ^{56}Fe range from 0.04 to 0.36‰, principally reflecting modal variations in oxides and silicates (Stausberg et al., 2014). The Upper Zone magmas, which represent a high-degree differentiated product of the Bushveld parental magma, have a higher δ^{56}Fe than magmas parental to the Lower, Critical and Main Zones (Rios et al., 2016). Bilenker et al. (2017) did not observe systematic variation in whole rock δ^{56}Fe with stratigraphic height in the Upper Zone of the Bushveld Complex despite magnetite crystallization. This is interpreted as a result of the competing fractionation by other Fe-bearing cumulus phases as the crystallization of magnetite and mafic silicates lead to magma enrichment in lighter and heavier Fe isotopes respectively. Similar phenomenon was also reported by Chen et al. (2014) for the Baima layered intrusion. Cao et al. (2019) also reported uniform Fe isotopic compositions (0.00–0.15‰) in the Panzhihua Complex regardless of the formation of Fe–Ti oxide layers. Similar δ^{56}Fe homogeneity in rocks from the Windimurra Complex was documented by Nebel et al. (2013), and has been explained by magma replenishment and mixing.
It was proposed that Mg isotope variations reflect the characteristic of mantle sources, with metasomatism by slab-derived fluids generating the heavy δ^{26}Mg (Brzozowski et al., 2022), while metasomatism by carbonate melt contributes to light δ^{26}Mg (Cheng et al., 2018). Cr isotopic data for the whole rocks of layered intrusions are still extremely rare, with only two data in the Bushveld Complex showing basalt-like average values (Schoenberg et al., 2008). The heavier one was interpreted as inherited from mantle-derived chromite for its higher Cr contents (Farka˘s et al., 2013).

4.19. Subsolidus processes constrained by fractionation of Fe-Mg-Cr stable isotopes

Inter-mineral isotope fractionations provide specific constraints on the interplay between early crystal accumulation and later processes occurring within crystal mushes and the extent to which the magmatic record has been overprinted by subsequent post-accumulation processes. Fe–Mg isotopic variations have been used to address this issue for co-existing oxides and silicates. Magnetite and ilmenite generally have heavier and lighter Fe isotopes than mantle peridotites, respectively (Chen et al., 2014, 2018, 2021; Bilenker et al., 2017; Cao et al., 2019; Tian et al., 2020). Remarkably heavier Mg isotopes of Fe–Ti oxides as compared to the average Bulk Solid Earth (BSE) and coexisting mafic silicates have also been extensively reported (Chen et al., 2018, 2021; Tian et al., 2020). This observation rules out equilibrium inter-mineral fractionation because Fe–Ti oxides crystallization does not significantly affect the MgO content in residual melts. Coexisting silicates with heavier Fe isotopes than those in cumulates of komatiites and slightly lighter Mg isotopes than BSE further demonstrate the widespread compositional disequilibrium between these minerals (Fig. 47).

At present, two mechanisms are provided to explain the disequilibrium isotope fractionation: (1) *Re*-equilibration via exchange of Fe^{3+} with $Fe^{2+}$and Ti^{4+} between Fe–Ti oxides, as well as Mg diffusion from oxides to Fe–Mg silicates induced by subsolidus process (Chen et al., 2014, 2018, 2021); (2) Chemical diffusion between minerals and melts during phase segregation caused by interstitial liquid immiscibility (Tian et al., 2020). The Fe–Mg isotope fractionation between silicates and chromite from the Critical Zone of the Bushveld Complex and the Peridotite Zone of the Stillwater Complex were also measured to investigate post-cumulus processes (Albert et al., 2019; Bai et al., 2021).
Large Fe–Mg isotopic variations in silicates and chromite and their complementary trends reveal widespread isotope disequilibrium between coexisting minerals in layered intrusions as a result of subsolidus processes.
Disequilibrium isotope fractionation induced by elemental diffusion is more pronounced in silicates with Cr as a trace element (Fig. 47), generating heavier Cr isotopes in olivine (Bai et al., 2019). Because of the slower diffusion rate of Cr compared to Fe and Mg, the Cr zoning patterns and Cr isotopic variations can be preserved in mineral profiles during the prolonged subsolidus processes of layered intrusions. Based on this property, the Cr isotopic system may be used to assess the time scales of magma cooling, which was shown to be evaluated to 10–100 k years for the Stillwater Complex (Bai et al., 2019).

5. Controversial issues in layered intrusions

5.1. The microstructure of igneous rocks: primary versus secondary

It is generally accepted that microstructures in rapidly cooled lavas and pyroclastic rocks are essentially unmodified from those created during solidification. Additionally, many authors hold that even the more slowly cooled plutonic rocks have undergone only limited subsolidus adjustment, preserving abundant information about their crystallization history (Vernon and Paterson, 2008; Vernon, 2010; Holness et al., 2018). Conversely, others have argued that the protracted cooling histories of plutonic rocks, both above

and below their solidi, result in the microstructures formed during solidification being sufficiently overprinted that they no longer record the full crystallization history (e. g., McBirney, 2009; Boudreau, 2011; Glazner et al., 2017; Bartley et al., 2018, 2020). This overprinting is attributed variously to metasomatic replacement by late-stage liquids generated elsewhere in the intrusion (e.g., McBirney, 1995; McBirney and Hunter, 1995; McBirney and Sonnenthal, 1990), to extensive late-stage magmatic and subsolidus grain growth and recrystallisation (e.g., Bartley et al., 2018, 2020), or to gravitationally-driven dissolution and reprecipitation in the late stages of solidification (e.g., McBirney and Hunter, 1995; Boudreau and McBirney, 1997). An extreme example of this second view is expressed by McBirney (2009) who argued that the textures of most coarse-grained igneous rocks are essentially metamorphic, with the constituent minerals of slowly cooled plutonic rocks passing "through a range of conditions in which a metamorphic petrologist would normally expect there to be conspicuous changes, including both compositional and textural re-equilibration of the kind seen in other rocks under comparable conditions". With the exception of Bartley et al. (2018, 2020), no evidence is presented to support these fundamental changes in microstructure, nor is any detail provided on the mechanism by which such changes may have occurred, despite the abundance of appropriate work in the metamorphic petrology literature. An example of the disconnect between these studies and the work of the metamorphic petrological community is the hypothesis that modal layering may be amplified during compaction, based on the assumption that the energy of a grain boundary between two like grains is always lower than that between two unlike grains (Boudreau and McBirney, 1997). That this assumption is incorrect is shown by measurement of the equilibrium dihedral angle formed at two-phase triple junctions in granulites (e.g., Vernon, 1968). Resolution of the controversy is dependent on a sound analysis of microstructure. Approaching the problem like a metamorphic petrologist requires not only a clear definition of what constitutes a primary microstructure, and how it might be recognized, but also a set of criteria by which the action of later processes that alter this microstructure may be identified. Importantly, microstructures formed during solidification evolve continuously through solidification itself and may also evolve in the subsolidus without the agency of external forces such as deformation (Bartley et al., 2018) or infiltrating fluids (McBirney, 1995): there is, therefore, necessarily a gradation between primary and secondary microstructures. The most informative approach to the controversy is perhaps to outline characteristic microstructural signatures of the different processes which may occur during the entire lifetime of an igneous rock.

Fundamentally, microstructures formed during the solidification of igneous rocks fall on a spectrum between two endmember states. The first is that controlled entirely by the kinetics of crystal growth (with or without reaction between early-crystallizing phases and any residual melt), while the second is that in which the microstructure is governed by the minimisation of internal energies, commonly described as textural equilibrium (Hunter, 1987). Where a rock sits on this spectrum depends on the cooling rate, because the driving force for textural equilibration only becomes significant at low (or non-existent) undercoolings (Means and Park, 1994).

Microstructures formed during solidification generally record a progressive change in liquidus assemblage, with the earliest-nucleating grains exhibiting shapes consistent with growth in a liquid-rich environment, while later-crystallizing phases have shapes dictated by the remaining porosity in the mush (Fig. 48a). Accumulations of earlyformed grains, particularly those acted on by magmatic currents, are characterized by grain boundaries parallel to crystallographic orientations corresponding to known growth faces, with euhedral grain shapes in slowly-cooled magma (Fig. 48a) and shapes characteristic of diffusion-limited growth, such as dendrites or hopper crystals (e.g., Lofgren, 1974; Donaldson, 1976; Faure et al., 2003; Godel et al., 2013) in rocks which underwent more rapid cooling (Fig. 48b). The geometry of three-grain junctions formed by the pseudomorphing of melt-filled pores by late-crystallizing phases provides an unambiguous measure of the extent of any post-solidification microstructural modification (e. g., Holness et al., 2005, 2012a) (Fig. 48c, d).

The initial grain size population formed during solidification is determined by the balance between nucleation and growth but can be modified by Ostwald ripening. This involves the dissolution of small grains, driven by the higher chemical potential of surfaces with a small radius of curvature compared to that of larger grains. Although many crystal size distributions in igneous rocks have the relatively low numbers of the smaller grains expected for systems which underwent Ostwald ripening (e.g., Waters and Boudreau, 1996), there are several possible reasons for this, such as the cessation of nucleation in the later stages of crystallization (Cashman, 1993). The action of Ostwald ripening is recorded in shape variation as a function of size: dissolving grains tend to be rounded whereas growing grains tend to be facetted (Fig. 48e; Holness, 2018). While experimental evidence suggests that Ostwald ripening is significant only for very small grains for cooling timescales typical of crustal intrusions (Cabane et al., 2001, 2005), it has been argued that Ostwald ripening, or competitive particle growth, in a crystal mush with a grain size gradient is responsible for the formation of highly regular cm-scale layering such as the Stillwater inch-scale layering (Boudreau, 1995, 2011), illustrating very clearly the gradation between what might be termed primary and secondary microstructures. A similar process has been advocated for fine-scale layering formed during devitrification (McBirney et al., 1990) though, since this undoubtedly occurred in a fully solidified rock, it should perhaps be considered a true metamorphic process.

The argument that fine-scale layering is a consequence of competitive particle growth in the crystal mush (Boudreau, 1995) has been further developed to suggest that much of the layering in mafic intrusions, defined both by modal variations and by grain fabric, develops in a previously relatively homogeneous crystal mush during fluid advection driven by compaction (Boudreau and McBirney, 1997). This model relies on the incorrect assumption that the energy of grain boundaries between like grains is lower than that between unlike grains (Vernon, 1968). Dissolution and reprecipitation caused by compaction are also argued to have resulted in foliations defined by shape preferred orientations (Boudreau and McBirney, 1997; Meurer and Boudreau, 1998; Boorman et al., 2004). However, as pointed out by Vukmanovic et al. (2018), the particular example of the Skaergaard trough banding, mentioned by Boudreau and McBirney (1997) in support of their hypothesis, is characterized by strong mineral lineations, a sedimentarylike microstructure with abundant interstitial material (Fig. 48a), and abundant outcrop-scale evidence of layer truncation, consistent with sedimentation in channels from crystal-laden magma: these modal layers are thus primary, rather than a secondary feature enhanced during gravitationally-driven compaction of the mush.

Those studies advocating metasomatism during the latest stages of solidification also have not presented any detailed microstructural evidence. However, again by comparison with metamorphic examples, we can set out what might perhaps be expected were this process to have occurred. For example, one might perhaps expect microstructures to record partial dissolution, with evidence of reaction such as those described by Nielsen et al. (2015) and attributed to chemical disequilibrium consequent to differential migration of immiscible conjugate liquids. One might also expect to see examples of incomplete reaction, with a relationship between the extent of metasomatic change and variables such as distance, temperature and timescales. None have so far been reported, and further work is clearly needed to address this lacuna in our understanding.

Microstructures continue to change in fully solidified rocks undergoing slow cooling, as they evolve towards solid-state textural equilibrium. While this evolution can occur without any external drivers such as compaction or the imposition of chemical disequilibrium by infiltrating fluid, it should be described as a secondary process or, perhaps more accurately, a metamorphic process. The end-point of this textural equilibration is a granular microstructure, characterized by equant grains with smoothly curved grain boundaries and the equilibrium dihedral angles established at all triple junctions (with a median value of 120 ◦ for monomineralic

junctions, and median angles close to, but generally less than, 120 ◦ for bi- or tri-mineralic junctions (Vernon, 1968, Figs. 4c,d, 48f). Grain growth in the subsolidus is driven by the overall reduction of interfacial energies, by the process known by materials scientists as normal grain growth. Normal grain growth only occurs in materials with a granular microstructure: rocks with a microstructure that retains evidence of relative timing of mineral growth, such as that typical of granites, cannot have undergone subsolidus grain growth as advocated by Bartley et al. (2018).

5.2. Compaction in layered intrusions: pervasive versus non-existent

The mechanism of formation of adcumulates, containing only minor quantities of interstitial material (Wager et al., 1960), remains unresolved. One group of hypotheses, discussed in section 4.13, involves continued and extensive post-accumulation primocryst growth during efficient chemical communication with the overlying bulk magma, either by diffusion (of both mass and the latent heat of crystallization) (e.g., Wager et al., 1960; Campbell, 1978, 1987; Morse, 1986) or by compositional convection within the mush (Sparks et al., 1985; Tait and Jaupart, 1992), or directly at the magma-crystal pile interface (Fig. 42) (Campbell, 1987). Another group of models postulates the expulsion of evolved interstitial melt from the mush, either during penetrative shearing (B´ edard, 2015) or by gravitationally driven compaction facilitated by crystal plastic deformation (Irvine, 1980a, 1980b; Sparks et al., 1985; Shirley, 1986; Tharp et al., 1998; Tegner et al., 2009; McKenzie, 2011).
Quite apart from the question of adcumulate formation, the process of compaction is widely promoted as a mechanism for extracting large volumes of crystal-free magma from mush zones. Compaction of a porous layer is driven by the imbalance between the lithostatic and hydrostatic pressure that occurs if the (fully interconnected) interstitial liquid has a lower density than the solids. It occurs by two distinct mechanisms: viscous compaction is the process by which the upwards flow of liquid is accompanied by viscous deformation of the solid crystal framework; mechanical compaction is achieved by the mechanical rearrangement of grains which retain their original shape.
The impetus to develop a theoretical treatment of viscous compaction was the need to understand how partial melts are extracted from the mantle (McKenzie, 1984, 1985; Richter and McKenzie, 1984; Scott and Stevenson, 1984, 1986; Fowler, 1990a, 1990b): the concept was first applied to layered intrusions by Sparks et al. (1985). A typical approach in the context of magmatic intrusions is to deduce the bulk viscosity of the crystal mush using the observed stratigraphic variation of bulk rock composition (e.g., Tegner et al., 2009; McKenzie, 2011). The magnitude of the bulk viscosity thus obtained is then be used to infer the mechanisms by which the crystal framework deformed (McKenzie, 2011). For the particular case of the floor cumulates in the Skaergaard intrusion, such an approach resulted in the suggestion that the solid matrix deformed by dislocation creep (McKenzie, 2011).

There has been much experimental work aimed at understanding compaction of igneous systems over the last 40 years (reviewed by Connolly and Schmidt, 2022). A recent experimental study, focussed on the behaviour of monomineralic accumulations of chromite, olivine and plagioclase, the three minerals of greatest importance to understanding compaction in mafic and ultramafic systems (Schmidt et al., 2012; Manoochehri and Schmidt, 2014; Krattli ¨ and Schmidt, 2021), found that compaction occurred by melt-enhanced grain boundary diffusioncontrolled creep, with some grain boundary sliding (Connolly and Schmidt, 2022). A significant porosity-weakening effect was found that enhances compaction rates considerably compared to those estimated from earlier experimental work: despite this, however, only metre-scale olivine-rich layers are likely to compact on timescales ($\sim 10^3$ years) appropriate to igneous intrusions, with compaction of chromite and plagioclase layers requiring loading by additional sedimentation (Schmidt et al., 2012; Manoochehri and Schmidt, 2014; Krattli ¨ and Schmidt, 2021; Connolly and Schmidt, 2022).
As illustrated by the contrast between those studies based on consideration of geochemistry that advocate compaction in gabbroic layered intrusions, and those based on experimental observation which argue that compaction is only important in ultramafic intrusions, there remain many unanswered questions. Perhaps the most pressing issue is that most studies advocating the process are based on theoretical treatments of bulk geochemical data (e.g., McKenzie, 2011). Compaction should leave a clear signature on both the grain scale and in outcrop, but evidence from field or microstructures is rarely presented. An exception is the detailed microstructural work demonstrating ∼10% compaction of a plagioclase-dominated crystal framework in deep (∼100 m) bodies of ponded lava, consistent with geochemical observations (Gray et al., 2003; Philpotts and Philpotts, 2005). Field evidence of compaction of layers under cognate xenoliths sourced from the intrusion roof is well documented (e.g., Irvine et al., 1998; Scoates, 2000) though this observation has not been followed through with detailed microstructural or geochemical investigations to demonstrate the operative mechanism or the difference in adcumulate status of the compacted region. There is no evidence for extensive dislocation creep required by McKenzie (2011) model for the Skaergaard floor cumulates (Holness et al., 2017c). Furthermore, Holness et al. (2017b) showed that the thickness of the floor mush was of the order a few metres in the evolved parts of the stratigraphy for which Tegner et al. (2009) and McKenzie (2011) argued that compaction was particularly effective: this thickness is insufficient to drive compaction (Krattli ¨ and Schmidt, 2021; Connolly and Schmidt, 2022). Vukmanovic et al. (2019) found no difference in the extent of dislocation creep recorded in anorthosites directly below or above metre-scale layers of magnetitite in the Upper Zone of the Bushveld Complex, despite the considerable gravitational load exerted by the magnetitite. The rigidity and strength of the Bushveld anorthosite (as also evidenced by the absence of load structures) is most likely a consequence of a negligible mush thickness. The overwhelming conclusion, in agreement with the analysis of experimental data by Connolly and Schmidt (2022), is that dislocation creep cannot be the principal deformation mechanism by which compaction occurs in magma bodies emplaced in the crust (Holness et al., 2017c; Vukmanovic et al., 2019).
A further question which has not yet been adequately explored concerns the effects on compaction of unmixing of basaltic magma into conjugate immiscible liquids, one Fe-rich and the other Si-rich. There is strong evidence for upwards migration of the buoyant Si-rich liquid, and an associated retention of its relatively dense Fe-rich conjugate in the floor mush (e.g., Holness et al., 2011). Such differential migration will have a significant effect on the gravitational driving force for compaction in basaltic bodies.
Determining the extent of viscous compaction in igneous systems requires a detailed and focussed attempt to detect the action of meltenhanced diffusion-controlled creep in fully solidified cumulates (e.g., Schmidt et al., 2012; Manoochehri and Schmidt, 2014) to complement inferences based on bulk-rock geochemical variation. A preliminary attempt to do this using compositional zoning in plagioclase in the Skaergaard floor cumulates (Holness et al., 2017c) did not uncover any evidence for dissolution-reprecipitation, but a similar investigation should be extended to other examples of adcumulates, particularly in systems such as slow-cooled intrusions in which the magma crystallized abundant dense minerals, to test the predictions of Connolly and Schmidt (2022).

5.3. Large, long-lived and entirely-molten magma chambers?

For over a century, the classic magma chamber paradigm has underpinned models of terrestrial and extraterrestrial magmatism. Magma chambers are envisaged as large bodies of molten, long-lived and slowly fractionating magma ('a big magma tank') that are

enclosed in crustal rocks (Campbell, 1996; Cawthorn, 1996; Charlier et al., 2015b; Gudmundsson, 2012; Marsh, 1996; Parsons, 1987; Wager and Brown, 1968) (Fig. 49a). In recent years, the magma chamber paradigm has been challenged by studies in which largely molten 'big tank' magma chambers are considered as either very short-lived or never existed in Earth's history (Bachmann and Huber, 2019; Cashman et al., 2017; Edmonds et al., 2019; Sparks et al., 2019). Indeed, many volcanologists have abandoned the classic paradigm because geophysical surveys could not identify any present-day chamber with eruptible magma in the Earth's crust (Cashman et al., 2017; Sparks et al., 2019).

As an alternative, some workers propose the existence of trans-crustal mushy systems (including mushy reservoirs for mafic layered intrusions; Cashman et al., 2017) that form in the crust from the coalescence of numerous intrusions (Fig. 49b). The transcrustal systems are thought to contain only small melt lenses that are generated by processes such as compaction (Bachmann and Huber, 2019; Jackson et al., 2018) or tectonic destabilization (Cashman et al., 2017; Sparks et al., 2019) of the crystal mush. The melt lenses exist for only a very short period of time before accumulating and erupting as lavas on the Earth's surface (Bachmann and Huber, 2019; Cashman et al., 2017; Edmonds et al., 2019; Jackson et al., 2018; Sparks et al., 2019). Some workers have also proposed on the basis of out-of-sequence zircon geochronological data (Mungall et al., 2016; Scoates et al., 2021; Wall et al., 2018) and fieldbased observations (Hepworth et al., 2020a, 2020b) that mafic intrusions may be formed without large magma chambers. Instead, the formation of some intrusions has been attributed to the stacking of chaotically-emplaced sills, with successive pulses of crystal-rich slurries invading earlier-formed cumulates (Hepworth et al., 2020a, 2020b; Mungall et al., 2016; Scoates et al., 2021; Wall et al., 2018; Yao et al., 2021).

Studies of layered mafic intrusions have much to offer debates on the existence of magma chambers (O'Driscoll and VanTongeren, 2017b). On the one hand, end member examples such as the ~55 *Ma* Skaergaard (Greenland) and the ~1.3 *Ga* Kiglapait (Labrador) intrusions have been held up as near wholly the products of closed system fractionation. The Skaergaard intrusion exhibits a remarkably smooth trend in mineral chemical variations through its stratigraphy (section 4.2, Fig. 29a, b) that suggests its differentiation as a big tank of crystal-free tholeiitic melt up to 4 km in thickness and up to 300 km^3 in volume (Nielsen, 2004). The Kiglapait intrusion solidified from >8 km thick magma column (~3500 km^3 total volume of magma) whose cumulate products show a continuous fractionation sequence with minimum evidence of magma recharge (Morse, 2015). On the other hand, field relationships and (Sr) isotopic evidence suggests that the ~60 *Ma* Rum layered intrusion was constructed by repeated intrusion of magma as it solidified (B´edard et al., 1988; Hepworth et al., 2018, 2020a, 2020b; Holness et al., 2007a). In particular, the occurrence of lenses and veins of harrisite, a cumulate characterized by dendritic and skeletal olivine crystals, with intrusive relationships against the host peridotite, is an important component of the Rum intrusion in this regard. Unlike the Skaergaard and Kiglapait examples, the Rum intrusion had long been considered to have behaved as an open magmatic system. However, in the context of the ongoing magma chamber debate, the key point is that new magma input need not (ubiquitously) occur at the magma-crystal mush interface but may intrude into the cumulate pile in a stratigraphically random way. Another notable observation from the Rum intrusion is that the length-scales over which magma intrusion (including melt infiltration) occur may vary by several orders of magnitude (millimeters to tens of metres).

Sitting between the two end members described above, there exists a number of open system layered mafic intrusions that are currently at the forefront of active debate in the context of the big magma tank controversy. These include the ~2.05 *Ga* Bushveld Complex (South Africa) and the ~2.7 *Ga* Stillwater intrusion (USA). Both of these intrusions have been the subject of high resolution (U–Pb in zircon) geochronology (Mungall et al., 2016; Scoates et al., 2021; Wall et al., 2018) and appear to reveal the presence of out-of-sequence layering, implying that the magma that formed some of the cumulates in these bodies was emplaced intrusively, rather than along the magma chamber floor. However, the geochronological data have been challenged on the basis of field and petrographic evidence, as well as other phase equilibria and geochemical arguments (see section 4.3). For example, in the Bushveld Complex, it has been proposed that chromite textures in chromitite layers (that are up to 2 m in thickness) grew in situ on the magma chamber floor (Latypov et al., 2022a). An implication of this model relates to mass balance – because of the relatively small concentration of Cr in mafic melts (~1000s ppm), the column of magma required to form each chromitite layers must have been on the order of several km thick. Given that chromitite layers are laterally extensive over ~400 km, this in turn has been taken to signify that the Bushveld Complex developed as a large, long-lived and mostly molten magma chamber (Latypov et al., 2022a).

The Bushveld body is the largest known layered intrusion in the Earth's crust. Even one of its constituent units, the Main Zone, has been attributed to the crystallization of a column of resident melt up to ~5 km thick (see section 3.1) (Latypov et al., 2022b). The formation of such a cumulate sequence, at a typical solidification rate for large mafic intrusions (~1 cm/year, Morse, 2011) would take ~300,000 years indicating that the intrusion was also long-lived. We can estimate the total volume of resident MZ melt in the following way. The MZ melt column varied between ~5.0 km in the thicker and at least 1.0 km thick in the thinner parts of the complex. Using reconstructions of the lateral extent of the MZ (Kruger, 2005), it is calculated that the thicker areas occupied ~70% of the MZ, and the remaining ~30% were thinner zones. Since the estimated Bushveld Complex area is about 100,000 km^2 (Cawthorn and Walraven, 1998), the total volume of the MZ resident melt is ~380,000 km^3 (5 km*70,000 km^2 + 1.0 km*30,000 km^2). This volume is a few orders of magnitude larger than the largest ignimbrite/tuff supereruptions in Earth's history (e.g., Bishop tuff – 600 km^3 and Youngest Toba eruption – up to 13,200 km^3) (Miller and Wark, 2008). The volume can only be compared to that of some of Earth's large igneous provinces, such as the Karoo (367,000 km^3) (Svensen et al., 2014) and Afar (350,000 km^3) (Ross et al., 2005). If the Bushveld Complex did solidify as a magma chamber in the Earth's crust, it would have a true 'big tank' reservoir in terms of size and lifetime.

It remains quite possible that magma chambers have developed throughout Earth's evolution, particularly when the Skaergaard and the Kiglapait examples are considered. Some regions of the Earth's crust may indeed behave as giant crystal mushes (e.g., mid-ocean ridges or deep roots of continental arcs) (Bachmann and Huber, 2019; Cashman et al., 2017; Edmonds et al., 2019; Sparks et al., 2019), but this does not mean that 'big tank' magma chambers should be absent from other regions (e.g., stable cratons with layered intrusions) (Cawthorn, 1996; Charlier et al., 2015b; Parsons, 1987). It should be stressed that such large layered intrusions as the Bushveld Complex, are not common in the geological record (Smith and Maier, 2021) and are relatively short-lived, so it is no wonder that we are not aware of any current examples of equivalent active and detectable magma chambers in Earth's crust (Cashman et al., 2017; Sparks et al., 2019). The classical paradigm of a magma chamber should not yet be discarded. Rather, efforts should be focused on reconciling new field observations, as well as geophysical, geochronological and thermal/diffusion modelling with the idea that a spectrum of intrusion types may exist, from true big tank magma chambers to *syn*-magmatic sill complexes.

6. Future directions of research

A remarkable aspect of the nearly 100-year-old history of the study of layered intrusions is that, to this day, there is still a lack of universal consensus on some of the most fundamental questions about their origins. Are they fossil magma chambers? Are they indeed natural laboratories for processes that produce the wide range of mafic and ultramafic rock types we see in the crust? How does fractional crystallization and magmatic differentiation actually happen? What causes elements like Pt and Cr to be concentrated by factors of hundreds or thousands in remarkably thin, extraordinarily persistent layers? Is layered intrusion petrology actually a

worthwhile field of research, or are the combined uncertainties and ambiguities destined to doom future research to the point where petrologists will still fail to agree on the fundamentals in another 50 years' time? Here are some suggestions for ways to address these problems to move science forward.

• Detailed rigorous testing of existing and emerging hypotheses for origin of layered intrusions using field relationships in surface outcrops and open pit and underground exposures in mines. For instance, the possible role of earthquakes in affecting crystal sorting and cumulate pile compaction in layered intrusions can be explored, since these magmatic processes inherently occur in tectonically active areas. Combining field observations with analogue physical or computational experiments, focussing on the rheology of crystalliquid mixtures at different strain rates, may increase our understanding of this connection.

• Systematic major and trace element mapping to reveal hitherto unseen patterns of zoning, potentially providing information on crystallization and cooling rates. Microbeam XRF provides the ability to image grain-scale variation in slow-diffusing trace elements over large samples in manageable times. There is great potential to use such data for well-constrained diffusion chronometry on intrusions of different sizes, and evaluation of single chamber vs multiple sill injection models.

• The application of X-ray computed microtomography (MicroCT) to layered intrusions and igneous rocks in general is in its infancy. A lot more can be done with this technique as the technical capability improves, particularly for element-specific 3D imaging.

• High resolution 3D images allow precise quantification of previously unmeasured characteristics of crystal aggregates, particularly clustering and coordination parameters (e.g. (Latypov et al., 2022a). In combination with computational modelling, this is a powerful approach for hypothesis-testing using entirely new datasets.

• Microstructural analysis, especially measurement of dihedral angles, has as yet only been applied to a small number of intrusions (not surprisingly, as dihedral angles are laborious to measure and require optical equipment that is not readily available). More of this kind of data is needed to address fundamental issues of compaction and
mush thickness. More generally, we need comparison of microtextures and microstructures between intrusions of different size and cooling rate.

• Computational fluid dynamics – particularly particle codes, extensively used in engineering applications but hardly used at all in layered intrusion research (or in petrology in general). Some very powerful tools are beginning to be applied – (e.g., Schleicher and Bergantz, 2017) including investigation of effects of cohesiveness on rheology of crystal mushes, model packing geometries and rheologies of synthetic crystal packs with realistic particle size distributions. Importantly, CFD simulations can be used to test the ability of analogue fluid dynamic experiments to scale to natural conditions.

• Application of thermodynamically-constrained forward models of putative parent magmas that are based on quantitative assessments of the intensive parameters under which the subject intrusion formed (e.g. Ariskin et al., 2018).

• Experimental petrology in realistic conditions of pressure, temperature and oxygen fugacity is a powerful tool to constrain magma differentiation in layered intrusions (Toplis and Carroll, 1995) as well as processes of ore formation (Hou et al., 2017, 2018).

• More collaboration with materials scientists and chemists with expertise in crystal nucleation and growth in polycomponent systems. A large body of expertise exists on processes of crystal nucleation, growth and deformation that has only begun to be applied to LMIs.

• Making use of large industry-generated data sets. Modern exploration programs, particularly for Ni-Cu-Co ores, often generate very large multi-element data sets over hundreds of drill holes, enabling the construction of 3D chemical and lithological models using advanced automated data handling techniques. Kevitsa in Finland is a good example of this approach (Le Vaillant et al., 2017). This approach will expand with the advent of rapid continuous downhole analytical techniques.

• Data integration – joint inversion of geophysical and geochemical data sets, and integration with classical petrological and mineral chemistry data as well as new techniques like MicroCT, SXFM and EBSD. Multidisciplinary studies are the key to rigorous testing of existing paradigms and to making the next major advances.

Declaration of Competing Interest

The authors declare that they have no known competing financial interests or personal relationships that could have appeared to influence the work reported in this paper.

Data availability

No data was used for the research described in the article.

Acknowledgments

The synchrotron XRF maps presented in this contribution were collected on the X-ray fluorescence microscopy beamline of the Australian Synchrotron, Clayton, Victoria, part of ANSTO. BC is a Research Associate of the Belgian Fund for Scientific Research-FNRS. This work is based on the research supported in part by the National Research Foundation (NRF) of South Africa (Ref/Grant Number: SRUG2204193706-2023-04-19-CPRR). We would like to thank Richard Naslund, Matthew Kohn and an anonymous reviewer for the careful review of various versions of our paper and many critical comments that helped to improve the quality and clarity of the manuscript. The editorial handling by Arturo Gomez-Tuena and Timothy Horscroft is gratefully acknowledged.

References

Aarnes, I., Svensen, H., Connolly, J.A.D., Podladchikov, Y.Y., 2010. How contact metamorphism can trigger global climate changes: Modeling gas generation around igneous sills in sedimentary basins. Geochim. Cosmochim. Acta 74 (24), 7179–7195.

Abernethy, K.E., 2019. Assimilation of Dolomite by Bushveld Magmas in the Flatreef; Implications for the Origin of Ni-cu-PGE Mineralization and the Precambrian Atmosphere. Doctoral dissertation. Cardiff University.

Acosta-Gongora, ´ P., Pehrsson, S.J., Sandeman, H., Martel, E., Peterson, T., 2018. The Ferguson Lake deposit: an example of Ni–Cu–Co–PGE mineralization emplaced in a back-arc basin setting? Can. J. Earth Sci. 55, 958–979.

Agrawal, S., Paterson, A., 2015. Secondary nucleation: mechanisms and models. Chem. Eng. Commun. 202, 698–706.

Ahn, B., Bosetti, L., Mazzotti, M., 2022a. Secondary nucleation by interparticle energies. II. Kinetics. Cryst. Growth Des. 22, 74–86.

Ahn, B., Bosetti, L., Mazzotti, M., 2022b. Secondary nucleation by interparticle energies. III. Nucleation rate model. Cryst. Growth Des. 22, 3625–3636.

Alapieti, T.T., Lahtinen, J.J., 1986. Stratigraphy, petrology, and platinum-group element mineralization of the early Proterozoic Penikat layered intrusion, northern Finland. Econ. Geol. 81, 1126–1136.

Alapieti, T.T., Kujanpaa, J., Lahtinen, J.J., Papunen, H., 1989. The Kemi stratiform chromitite deposit, northern Finland. Econ. Geol. 84, 1057–1077.

Albert, C., Williams, H.M., Kaufmann, F., Hecht, L., Jenner, F.E., 2019. Iron isotope fractionation during magmatic evolution and implications for isotope disequilibrium in the Bushveld complex. In: AGU Fall Meeting 2019. Abstract V23E–0215.

Andersen, J.C.O., Rasmussen, H., Nielsen, T.F.D., Ronsbo, J.G., 1998. The Triple Group and the Platinova gold and palladium reefs in the Skaergaard Intrusion; stratigraphic and petrographic relations. Econ. Geol. 93, 488–509.

Annen, C., Latypov, R., Chistyakova, S., Cruden, A.R., Nielsen, T.F.D., 2022. Catastrophic growth of totally molten magma chambers in months to years. Sci. Adv. 8 eabq0394.

Arai, S., 1997. Origin of podiform chromitites. J. Asian Earth Sci. 15, 303–310.

Arai, S., 2021. Genetic link between podiform chromitites in the mantle and stratiform chromitites in the crust: a hypothesis. Minerals 11, 209.
Ariskin, A.A., Barmina, G.S., 2004. COMAGMAT: development of a magma crystallization model and its petrological applications. Geochem. Int. 42, 1–157.
Ariskin, A., Danyushevsky, L., Nikolaev, G., Kislov, E., Fiorentini, M., McNeill, A., Kostitsyn, Y., Goemann, K., Feig, S.T., Malyshev, A., 2018. The Dovyren Intrusive complex (Southern Siberia, Russia): Insights into dynamics of an open magma chamber with implications for parental magma origin, composition, and Cu-Ni-PGE fertility. Lithos 302–303, 242–262.
Australian Government, Department of Industry, S. and R, 2022. Critical Minerals Strategy. www.industry.gov.au/publications/critical-minerals-strategy-2022.
Azer, M.K., El-Gharbawy, R.I., 2011. The Neoproterozoic layered mafic–ultramafic intrusion of Gabal Imleih, South Sinai, Egypt: implications of post-collisional magmatism in the north Arabian–Nubian Shield. J. Afr. Earth Sci. 60, 253–272.
Bachmann, O., Huber, C., 2019. The inner workings of crustal distillation columns; the physical mechanisms and rates controlling phase separation in silicic magma reservoirs. J. Petrol. 60, 3–18.
Bai, Y., Su, B.X., Xiao, Y., Chen, C., Cui, M.M., He, X.Q., Charlier, B., 2019. Diffusiondriven chromium isotope fractionation in ultramafic cumulate minerals: Elemental and isotopic evidence from the Stillwater complex. Geochim. Cosmochim. Acta 263, 167–181.
Bai, Y., Su, B.X., Xiao, Y., Cui, M.M., Charlier, B., 2021. Magnesium and iron isotopic evidence of inter-mineral diffusion in ultramafic cumulates of the Peridotite Zone, Stillwater Complex. Geochim. Cosmochim. Acta 292, 152–169.
Ballhaus, C.G., 1988. Potholes of the Merensky Reef at Brakspruit Shaft, Rustenburg platinum mines; primary disturbances in the magmatic stratigraphy. Econ. Geol. 83, 1140–1158.
Ballhaus, C.G., Stumpfl, E.F., 1986. Sulfide and platinum mineralization in the Merensky Reef: evidence from hydrous silicates and fluid inclusions. Contrib. Mineral. Petrol. 94, 193–204.
Barnes, S.J., 1986. The effect of trapped liquid crystallization on cumulus mineral compositions in layered intrusions. Contrib. Mineral. Petrol. 93, 524–531.
Barnes, S.J., 1993. Partitioning of the platinum group elements and gold between silicate and sulphide magmas in the Munni Munni complex, Western Australia. Geochim. Cosmochim. Acta 57, 1277–1290.
Barnes, S.J., 2023. Lithogeochemistry in exploration for intrusion-hosted magmatic NiCu-Co deposits. Geochemistry 23 geochem2022-025.
Barnes, S.-J., Gomwe, T.S., 2010. Composition of the Lac des Iles magma and implications for the origin of the ore. In: 11th International Platinum Symposium, Program Abstracts, Ontario Geological Survey, Miscellaneous Release-Data 269.
Barnes, S.-J., Gomwe, T.S., 2011. The Pd deposits of the Lac des Iles complex, northwestern Ontario. In: Li, C., Ripley, E.M. (Eds.), Reviews in Economic Geology 17. Soc Econ Geol, p 351–37.
Barnes, S.-J., Maier, W.D., 2002. Platinum-group elements and microstructures of normal Merensky reef from Impala platinum Mines, Bushveld complex. J. Petrol. 43, 103–128.
Barnes, S.J., Mungall, J.E., 2018. Blade-shaped dikes and nickel sulfide deposits: a model for the emplacement of ore-bearing small intrusions. Econ. Geol. 113, 789–798.
Barnes, S.J., Robertson, J.C., 2019. Time scales and length scales in magma flow pathways and the origin of magmatic Ni-Cu-PGE ore deposits. Geosci. Front. 10, 77–87.
Barnes, S.J., Williams, M., 2023. Postcumulus processes recorded in whole-rock geochemistry: a case study from the Mirabela layered intrusion, Brazil. J. Petrol. (in review).
Barnes, S.J., Keays, R.R., Hoatson, D.M., 1992. Distribution of sulphides and PGE within the porphyritic websterite zone of the Munni Munni complex, Western Australia. Aust. J. Earth Sci. 39, 289–302.
Barnes, C.G., Prestvik, T., Sundvoll, B., Surratt, D., 2005. Pervasive assimilation of carbonate and silicate rocks in the Hortavær igneous complex, North-Central Norway. Lithos 80, 179–199.
Barnes, S.J., Cruden, A.R., Arndt, N.T., Saumur, B.M., 2016a. The mineral system approach applied to magmatic Ni-Cu-PGE sulphide deposits. Ore Geol. Rev. 76, 296–316.
Barnes, S.J., Mole, D.R., Le Vaillant, M., Campbell, M., Verrall, M., Roberts, M., Evans, N. J., 2016b. Poikilitic textures, heteradcumulates and zoned orthopyroxenes in the Ntaka Ultramafic complex, Tanzania: implications for crystallisation mechanisms of oikocrysts. J. Petrol. 57, 1171–1198.
Barnes, S.J., Hoatson, D.M., 1994. The Munni Munni Complex, western Australia: stratigraphy, structure and petrogenesis. J. Petrol. 35 (3), 715–751.
Barnes, S.J., Holwell, D.A., Le Vaillant, M., 2017. Magmatic sulfide ore deposits. Elements 13, 91–97. https://doi.org/10.2113/gselements.13.2.91.
Barnes, S.J., Le Vaillant, M., Godel, B., Lesher, C.M., 2019a. Droplets and bubbles: solidification of sulphide-rich vapour-saturated orthocumulates in the Noril'skTalnakh Ni-Cu-PGE ore-bearing intrusions. J. Petrol. 60, 269–300.
Barnes, S.J., Mole, D.R., Hornsey, R., Schoneveld, L.E., 2019b. Nickel-copper sulfide mineralization in the Ntaka Hill Ultramafic complex, Nachingwea region, Tanzania. Econ. Geol. 114, 1135–1158.
Barnes, S.J., Latypov, R., Chistyakova, S., Godel, B., Schoneveld, L.E., 2021. Idiomorphic oikocrysts of clinopyroxene produced by a peritectic reaction within a solidification front of the Bushveld complex. Contrib. Mineral. Petrol. 176, 5.
Barnes, S.J., Yudovskaya, M., Iacono-Marziano, G., Le Vaillant, M., Schoneveld, L.E., Cruden, A.R., 2023. The role of volatiles in intrusion emplacement and sulfide deposition in the supergiant Norilsk-Talnakh ore deposits. Geology 51, 1027–1032.
Bartley, J.M., Glazner, A.F., Coleman, D.S., 2018. Dike intrusion and deformation during growth of the half Dome pluton, Yosemite National Park, California. Geosphere 14, 3.
Bartley, J.M., Glazner, A.F., Stearns, M.A., Coleman, D.S., 2020. The granite aqueduct and autometamorphism of plutons. Geosciences 10, 136.
Basta, E.Z., Takla, M.A., 1968. Mineralogy and origin of Abu Ghalaga ilmenite occurrence, Eastern Desert. J. Geol. 12, 87–124.
B´ edard, J.H., 2015. Ophiolitic magma chamber processes, a perspective from the Canadian Appalachians. In: Charlier, B., Namur, O., Latypov, R., Tegner, C. (Eds.), Layered Intrusions. Springer, Berlin, pp. 693–732.
B´ edard, J.H., Sparks, R.S.J., Renner, R., Cheadle, M.J., Hallworth, M.A., 1988. Peridotite sills and metasomatic gabbros in the Eastern Layered Series of the Rhum complex. J. Geol. Soc. Lond. 145, 207–224. Begg, G.C., Hronsky, J.M.A., Arndt, N.T., Griffin, W.L., O'Reilly, S.Y., Hayward, N., 2010.
Lithospheric, cratonic, and geodynamic setting of Ni-Cu-PGE sulfide deposits. Econ. Geol. 105, 1057–1070. Begg, G.C., Hronsky, J.M.A., Griffin, W.L., O'Reilly, S.Y., 2018. Global-to deposit-scale controls on orthomagmatic Ni-Cu (-PGE) and PGE reef ore formation. In: Processes and Ore Deposits of Ultramafic-Mafic Magmas through Space and Time. Elsevier, pp. 1–46.
Bilenker, L.D., VanTongeren, J.A., Lundstorm, C.C., Simon, A.C., 2017. Iron isotopic evolution during fractional crystallization of the uppermost Bushveld complex layered mafic intrusion. Geochem. Geophys. 18, 956–972.
Blanks, D.E., Holwell, D.A., Fiorentini, M.L., Moroni, M., Giuliani, A., Tassara, S., Gonzalez-Jim ´ ´enez, J.M., Boyce, A.J., Ferrari, E., 2020. Fluxing of mantle carbon as a physical agent for metallogenic fertilization of the crust. Nat. Commun. 11, 1–11. Bleeker, W., 2003. The late Archean record: a puzzle in ca. 35 pieces. Lithos 71, 99–134.
Bleeker, W., Smith, J., Hamilton, M., Kamo, S., Liikane, D., Hollings, P., Cundari, R., Easton, M., Davis, D., Houl´ e, M.G., 2020. The Midcontinent Rift and its mineral systems: Overview and temporal constraints of Ni-Cu-PGE mineralized intrusions. Target. Geosci. Initiat. 5, 7–35.
Blundy, J.D., Annen, C.J., 2016. Crustal magmatic systems from the perspective of heat transfer. Elements 12, 115–120.
Bodorkos, S., Oliver, N.H.S., Cawood, P.A., 1999. Thermal evolution of the central Halls Creek Orogen, northern Australia. Aust. J. Earth Sci. 46, 453–465.
Bohrson, W., Spera, F., Ghiorso, M., Brown, G., Creamer, J., Mayfield, A., 2014. Thermodynamic model for energy-constrained open-system evolution of crustal magma bodies undergoing simultaneous recharge, assimilation and crystallization: the magma chamber simulator. J. Petrol. 55, 1685–1717.
Bohrson, W.A., Spera, F.J., Heinonen, J.S., Brown, G.A., Scruggs, M.A., Adams, J.V., Takach, M.K., Zeff, G., Suikkanen, E., 2020. Diagnosing open-system magmatic processes using the Magma Chamber Simulator (MCS): part I—major elements and phase equilibria. Contrib. Mineral. Petrol. 175, 104.
Bolle, O., Diot, H., Fransen, W., Higgins, M.D., 2021. Central sagging of a giant mafic intrusion: the ediacaran Sept ˆIles layered intrusion (Qu´ ebec, Canada). J. Geol. Soc. Lond. 178.
Bond, D.P.G., Wignall, P., 2014. Large igneous provinces and mass extinctions: an update. In: Volcanism, Impacts, Mass Extinctions Causes, 505, pp. 29–55.
Boorman, S., Boudreau, A., Kruger, F.J., 2004. The lower Zone - Ccritical Zone transition of the Bushveld complex: a quantitative textural study. J. Petrol. 45, 1209–1235.
Bosetti, L., Ahn, B., Mazzotti, M., 2022. Secondary nucleation by interparticle energies. I. Thermodynamics. Cryst. Growth Des. 22, 87–97.

Botha, B.W., 2010. An overview of andalusite from Southern Africa: geology and mineralogy. In: The Southern African Institute of Mining and Metallurgy, Refractories 2010 Conference (8p).
Boudreau, A.E., 1992. Volatile fluid overpressure in layered intrusions and the formation of potholes. Aust. J. Earth Sci. 39, 277–287.
Boudreau, A.E., 1995. Crystal aging and the formation of fine-scale igneous layering. Mineral. Petrol. 54, 55–69.
Boudreau, A.E., 1999. Fluid mixing of cumulates: the J-M Reef and associated rocks of the Stillwater complex, Montana. J. Petrol. 40, 755–772.
Boudreau, A.E., 2008. Modeling the Merensky Reef, Bushveld complex, Republic of South Africa. Contrib. Mineral. Petrol. 156, 431–437.
Boudreau, A.E., 2011. The evolution of texture and layering in layered intrusions. Int. Geol. Rev. 53, 330–353.
Boudreau, A.E., 2016. The Stillwater complex, Montana – overview and the significance of volatiles. Mineral. Mag. 80, 585–637.
Boudreau, A.E., 2019. Hydromagmatic Processes and Platinum-Group Element Deposits in Layered Intrusions. Cambridge University Press Cambridge, 275 pp. Boudreau, A.E., McBirney, A.R., 1997. The Skaergaard Layered Series. Part III. Nondynamic layering. J. Petrol. 38, 1003–1020.

Boudreau, A.E., McCallum, I.S., 1986. Investigations of the Stillwater complex; III, the Picket Pin Pt/Pd deposit. Econ. Geol. 81, 1953–1975.
Boudreau, A.E., Butak, K.C., Geraghty, E.P., Holick, P.A., Koski, M.S., 2020. Mineral deposits of the Stillwater complex. Mont. Bur. Mines Geol. Spec. Publ. 122, 1–33.
Bowles, J.F.W., Prichard, H.M., Su´arez, S., Fisher, P.C., 2013. The first report of platinum-group minerals in magnetite-bearing gabbro, Freetown Layered complex, Sierra Leone: occurrences and genesis. Can. Mineral. 51, 455–473.
Boyd, R., Mathiesen, C.O., 1979. The nickel mineralization of the Rana mafic intrusion, Nordland, Norway. Can. Mineral. 17, 287–298.
Brothers, R.N., 1964. Petrofabric analyses of Rhum and Skaergaard layered rocks. J. Petrol. 5, 255–274.
Brown, G.M., 1956. The layered ultrabasic rocks of Rhum, Inner Hebrides. Philos. Trans. R. Soc. Lond. B 240, 1–53.
Brügmann, G.E., Reischmann, T., Naldrett, A.J., Sutcliffe, R.H., 1997. Roots of an Archean volcanic arc complex: the Lac des Iles area in Ontario, Canada. Precambrian Res. 81, 223–239.
Brzozowski, M.J., Good, D.J., Yan, W., Wu, C., An, S., Li, W., 2022. Mg-Fe isotopes link the geochemical complexity of the Coldwell Complex, Midcontinent Rift to metasomatic processes in the mantle. J. Petrol. 63 egac081.
Buick, I.S., Maas, R., Gibson, R., 2001. Precise U–Pb titanite age constraints on the emplacement of the Bushveld complex, South Africa. J. Geol. Soc. Lond. 158, 3–6.
Burkhard, D.J., 2005. Nucleation and growth rates of pyroxene, plagioclase, and Fe-Ti oxides in basalt under atmospheric conditions. Eur. J. Mineral. 17, 675–685.
Butt, C.R.M., Cluzel, D., 2013. Nickel laterite ore deposits: weathered serpentinites. Elements 9, 123–128.
Button, A., 1976. Stratigraphy and relations of the bushveld floor in the Eastern Transvaal. S. Afr. J. Geol. 79, 3–12.
Cabane, H., Laporte, D., Provost, A., 2001. Experimental investigation of the kinetics of Ostwald ripening of quartz in silicic melts. Contrib. Mineral. Petrol. 142, 361–373.
Cabane, H., Laporte, D., Provost, A., 2005. An experimental study of Ostwald ripening of olivine and plagioclase in a silicate melts: implications for the growth and size of crystals in magmas. Contrib. Mineral. Petrol. 150, 37–53.
Cameron, E.N., 1964. Chromitite deposits in the eastern part of the Bushveld complex. Geol. Some Ore Depos. S. Afr. 131–168.
Campbell, I.H., 1977. A study of macrorhythmic layering and cumulate processes in the Jimberlana Intrusion, Western Australia, part I: the upper layered series. J. Petrol. 18, 183–215.
Campbell, I.H., 1978. Some problems with the cumulus theory. Lithos 11, 311–323.
Campbell, I.H., 1986. A fluid dynamic model for the potholes of the Merensky Reef. Econ. Geol. 81, 1118–1125.
Campbell, I.H., 1987. Distribution of orthocumulate textures in the Jimberlana intrusion. J. Geol. 95, 35–53.
Campbell, I.H., 1996. Fluid dynamic processes in basaltic magma chambers. In: Developments in Petrology. Elsevier, pp. 45–76.
Campbell, I.H., Barnes, S.J., 1984. A model for the geochemistry of the platinum group elements in magmatic sulphide deposits. Can. Mineral. 22, 151–160.
Campbell, I.H., Murck, B.W., 1993. Petrology of the G and H chromitite zones in the Mountain View area of the Stillwater complex, Montana. J. Petrol. 34, 291–316.
Campbell, I.H., Naldrett, A.J., 1979. The influence of silicate: sulfide ratios on the geochemistry of magmatic sulfides. Econ. Geol. 74, 1503–1506.
Campbell, I.H., Roeder, P.L., Dixon, J.M., 1978. Crystal buoyancy in basaltic liquids and other experiments with a centrifuge furnace. Contrib. Mineral. Petrol. 67, 369–377.
Campbell, I.H., Naldrett, A.J., Barnes, S.J., 1983. A model for the origin of the platinumrich sulfide horizons in the Bushveld and Stillwater Complexes. J. Petrol. 24, 133–165.
Cantor, B., 2003. Heterogeneous nucleation and adsorption. Philos. Trans. R. Soc. Lond. 361A, 409–417.
Cao, Y., Wang, C.Y., Huang, F., Zhang, Z., 2019. Iron isotope systematics of the Panzhihua mafic layered intrusion associated with giant Fe-Ti oxide deposit in the Emeishan large igneous province, SW China. J. Geophys. Res. Solid 124, 358–375.
Cao, Y., Xing, C.-M., Wang, C.Y., 2023. Crystallization and solidification of poikilitic and granular rocks in the ultramafic sequence of the Xinjie layered intrusion (SW China): Constraints from complex growth zoning of clinopyroxene and spatial variation of dihedral angles. J. Petrol. 64 egad007.
Carr, H.W., Groves, D.I., Cawthorn, R.G., 1994. Controls on the distribution of Merensky Reef potholes at the Western platinum Mine, Bushveld complex, South Africa: implications for disruptions of the layering and pothole formation in the complex. S. Afr. J. Geol. 97, 431–441.
Carr, H.W., Kruger, F.J., Groves, D.I., Cawthorn, R.G., 1999. The petrogenesis of Merensky Reef potholes at the Western platinum Mine, Bushveld complex: Srisotopic evidence for synmagmatic deformation. Mineral. Deposita 34, 335–347.
Carter, L.B., Dasgupta, R., 2018. Decarbonation in the Ca-Mg-Fe carbonate system at mid-crustal pressure as a function of temperature and assimilation with arc magmas – Implications for long-term climate. Chem. Geol. 492, 30–48.
Cashman, K.V., 1993. Relationship between plagioclase crystallisation and cooling rate in basaltic melts. Contrib. Mineral. Petrol. 113, 126–142.
Cashman, K., Blundy, J., 2000. Degassing and crystallization of ascending andesite and dacite. Philos. Trans. R. Soc. Lond. A Math. Phys. Eng. Sci. 358, 1487–1513.
Cashman, K.V., Sparks, R.S.J., Blundy, J.D., 2017. Vertically extensive and unstable magmatic systems: a unified view of igneous processes. Science 355 eaag3055.
Cawthorn, R.G., 1994. Growth nodes at the base of magnetitite layers in the Upper Zone of the Bushveld complex. S. Afr. J. Geol. 97, 455–461.
Cawthorn, R.G., 1996. Layered Intrusions, Developments in Petrology. Elsevier, Amsterdam.
Cawthorn, R.G., 2002. Delayed accumulation of plagioclase in the Bushveld complex. Mineral. Mag. 66, 881–893.
Cawthorn, R.G., 2005. Pressure fluctuations and the formation of the PGE-rich Merensky and chromitite reefs, Bushveld complex. Mineral. Deposita 40, 231–235.
Cawthorn, R.G., 2012. Multiple sills or a layered intrusion? Time to decide. S. Afr. J. Geol. 115, 283–290.
Cawthorn, R.G., 2013. The residual or roof zone of the Bushveld complex, South Africa. J. Petrol. 54, 1875–1900.
Cawthorn, R.G., 2015. The Bushveld complex, South Africa. In: Charlier, B., Namur, O., Latypov, R., Tegner, C. (Eds.), Layered Intrusions. Springer Geology. Springer Netherlands, Dordrecht, pp. 517–587.
Cawthorn, R.G., 2018. A non-horizontal floor during accumulation of the Bushveld complex – evidence and implications. Lithos 316–317, 323–329.
Cawthorn, R.G., 2021. Origin of layered mafic intrusions and their mineral deposits. In: Alderton, David, Elias, Scott A. (Eds.), Encyclopedia of Geology, , 2nd editionvol. 5. Academic Press, United Kingdom, pp. 808–822.
Cawthorn, R.G., Ashwal, L.D., 2009. Origin of anorthosite and magnetitite layers in the Bushveld complex, constrained by major element compositions of plagioclase. J. Petrol. 50, 1607–1637.
Cawthorn, R.G., McCarthy, T.S., 1980. Variations in Cr content of magnetitite from the Upper Zone of the Bushveld complex – evidence for heterogeneity and convection currents in magma chambers. Earth Planet. Sci. Lett. 46, 335–343.
Cawthorn, R.G., McCarthy, T.S., 1981. Bottom crystallization and diffusion control in layered complexes: evidence from Cr distribution in magnetite from the Bushveld complex. Trans. Geol. Soc. S. Afr. 84, 41–50.
Cawthorn, R.G., McCarthy, T.S., 2023. Geochemical anatomy of the Main Magnetitite layer, Bushveld complex, South Africa. J. Petrol. 64, 1–19.
Cawthorn, R.G., Miller, J., 2018. Lopolith–A 100 year-old term. Is it still definitive? S. Afr. J. Geol. 121, 253–260.
Cawthorn, R.G., Spies, L., 2003. Plagioclase content of cyclic units in the Bushveld complex, South Africa. Contrib. Mineral. Petrol. 145, 47–60.

Cawthorn, R.G., Walraven, F., 1998. Emplacement and crystallization time for the Bushveld complex. J. Petrol. 39, 1669–1687.
Cawthorn, R.G., Webb, S.J., 2001. Connectivity between the western and eastern limbs of the Bushveld complex. Tectonophysics 330, 195–209.
Cawthorn, R.G., McCarthy, T.S., Davies, G., 1983. Vertical chemical gradients in a single grain of magnetite from the Bushveld complex, South Africa. Mineral. Mag. 47, 27–34.
Cawthorn, R.G., Meyer, P.S., Kruger, F.J., 1991. Major addition of magma at the Pyroxenite Marker in the Western Bushveld complex, South Africa. J. Petrol. 32, 739–763.
Cawthorn, R.G., Lundgaard, K.L., Tegner, C., Wilson, J.R., 2016. Lateral variations in plagioclase compositions, Main Zone, Bushveld complex, South Africa: evidence for slow mixing of magmas in basinal structures. Mineral. Mag. 80, 213–225.
Chadwick, J.P., Troll, V.R., Ginibre, C., Morgan, D., Gertisser, R., Waight, T.E., Davidson, J.P., 2007. Carbonate assimilation at Merapi Volcano, Java, Indonesia: Insights from crystal isotope stratigraphy. J. Petrol. 48, 1793–1812.
Chambers, A.D., Brown, P.E., 1995. The Lilloise Intrusion, East Greenland: fractionation of a hydrous alkali picritic magma. J. Petrol. 36, 932–963.
Charlier, B., Grove, T.L., 2012. Experiments on liquid immiscibility along tholeiitic liquid lines of descent. Contrib. Mineral. Petrol. 164, 27–44.
Charlier, B., Sakoma, E., Sauv´e, M., Stanaway, K., Vander Auwera, J., Duchesne, J.-C., 2008. The Grader layered intrusion (Havre-Saint-Pierre Anorthosite, Quebec) and genesis of nelsonite and other Fe–Ti–P ores. Lithos 101, 359–378.
Charlier, B., Namur, O., Toplis, M.J., Schiano, P., Cluzel, N., Higgins, M.D., Vander Auwera, J., 2011. Large-scale silicate liquid immiscibility during differentiation of tholeiitic basalt to granite and the origin of the Daly gap. Geology 39, 907–910.
Charlier, B., Namur, O., Grove, T.L., 2013. Compositional and kinetic controls on liquid immiscibility in ferrobasalt–rhyolite volcanic and plutonic series. Geochim. Cosmochim. Acta 113, 79–93. Charlier, B., Namur, O., Bolle, O., Latypov, R., Duchesne, J.-C., 2015a. Fe–Ti–V–P ore
deposits associated with Proterozoic massif-type anorthosites and related rocks. Earth-Sci. Rev. 141, 56–81.
Charlier, B., Namur, O., Latypov, R., Tegner, C., 2015b. Layered Intrusions, Springer Geology. Springer Netherlands, Dordrecht.
Chaumba, J.B., 2022. A review of the emplacement and formation of magmatic platinum-group elements-enriched deposits in large layered mafic/ultramafic intrusions, with special reference to the “big three” (Stillwater complex, Great Dike, and Bushveld complex). J. Afr. Earth Sci. 104603.
Cheadle, M.J., Elliott, M.T., McKenzie, D., 2004. Percolation threshold and permeability of crystallising igneous rocks: the importance of textural equilibrium. Geology 32, 757–760.
Chen, L.-M., Song, X.-Y., Zhu, X.-K., Zhang, X.-Q., Yu, S.-Y., Yi, J.-N., 2014. Iron isotope fractionation during crystallization and sub-solidus re-equilibration: Constraints from the Baima mafic layered intrusion, SW China. Chem. Geol. 380, 97–109.
Chen, L.M., Teng, F.Z., Song, X.Y., Hu, R.Z., Yu, S.Y., Zhu, D., Kang, J., 2018. Magnesium isotopic evidence for chemical disequilibrium among cumulus minerals in layered mafic intrusion. Earth Planet. Sci. Lett. 487, 74–83.
Chen, L.M., Teng, F.Z., Song, X.Y., Luan, Y., Yu, S.Y., Kang, J., 2021. Origins and implications of magnesium isotopic heterogeneity in Fe-Ti oxides in layered mafic intrusions. Geochim. Cosmochim. Acta 308, 273–290.
Cheng, Z., Zhang, Z., Xie, Q., Hou, T., Ke, S., 2018. Subducted slab-plume interaction traced by magnesium isotopes in the northern margin of the Tarim large Igneous Province. Earth Planet. Sci. Lett. 489, 100–110. Chernicoff, C.J., Zappettini, E.O., Villar, L.M., Chemale Jr., F., Hernandez, ´ L., 2009. The belt of metagabbros of La Pampa: lower Paleozoic back-arc magmatism in southCentral Argentina. J. S. Am. Earth Sci. 28, 383–397.
Chisenga, C., Jianguo, Y., Fadel, I., van der Meijde, M., Atekwana, E.A., 2020. Updated tectonic terrane boundaries of Botswana determined from gravity and aeromagnetic data. Episodes J. Int. Geosci. 43, 919–933.
Chistyakova, S., Latypov, R., 2022. Pothole-like depressions in the chamber floor of the Sudbury Igneous complex, Canada. Geology 50 (7), 832–836.
Chistyakova, S., Latypov, R., Zaccarini, F., 2015. Chromitite dykes in the Monchegorsk layered intrusion, Russia: *in situ* crystallization from chromite-saturated magma flowing in conduits. J. Petrol. 56, 2395–2424.
Chistyakova, S., Latypov, R., Hunt, E.J., Barnes, S., 2019a. Merensky-type platinum deposits and a reappraisal of magma chamber paradigms. Sci. Rep. 9, 8807.
Chistyakova, S., Latypov, R., Youlton, K., 2019b. Multiple Merensky Reef of the Bushveld complex, South Africa. Contrib. Mineral. Petrol. 174, 26.
Coffin, M.F., Eldholm, O., 1994. Large igneous provinces: crustal structure, dimensions, and external consequences. Rev. Geophys. 32, 1.
Coish, R.A., Taylor, L.A., 1979. The effects of cooling rate on texture and pyroxene chemistry in DSDP Leg 34 basalt: a microprobe study. Earth Planet. Sci. Lett. 42, 389–398.
Coleman, D.S., Gray, W., Glazner, A.F., 2004. Rethinking the emplacement and evolution of zoned plutons: geochronologic evidence for incremental assembly of the Tuolumne Intrusive Suite, California. Geology 32, 433.
Coleman, D.S., Mills, R.D., Zimmerer, M.J., 2016. The pace of plutonism. Elements 12, 97–102.
Condie, K.C., 2001. Continental growth during formation of Rodinia at 1.35-0.9 Ga. Gondwana Res. 4, 5–16.
Connolly, J., Schmidt, M.W., 2022. Viscosity of crystal mushes and implications for compaction-driven flow. J. Geophys. Res. Solid Earth 127 e2022JB024743.
Conrad, M.E., Naslund, H.R., 1989. Modally-graded rhythmic layering in the Skaergaard intrusion. J. Petrol. 30, 251–269.
Corrigan, G.M., 1982. Supercooling and the crystallization of plagioclase, olivine, and clinopyroxene from basaltic magmas. Mineral. Mag. 46, 31–42.
Cottin, J.-Y., Lorand, J.P., Agrinier, P., Bodinier, J.L., Li´egeois, J.-P., 1998. Isotopic (O, Sr, Nd) and trace element geochemistry of the Laouni layered intrusions (PanAfrican belt, Hoggar, Algeria): evidence for post-collisional continental tholeiitic magmas variably contaminated by continental crust. Lithos 45, 197–222.
Courtillot, V., Jaeger, J.J., F´ eraud, G., 1994. The influence of large igneous provinces on mass extinctions: Where do we stand?. In: New Developments Regarding the KT Event and Other Catastrophes in Earth History, p. 27.
Crowson, P., 2001. Mineral Handbook 2000–2001. Mining Journal Books, Edenbridge.
Cruden, A.R., 1998. On the emplacement of tabular granites. J. Geol. Soc. Lond. 155, 853–862.
Cruden, A.R., Weinberg, R.F., 2018. Mechanisms of magma transport and storage in the lower and middle crust-magma segregation, ascent and emplacement. In: Volcanic and Igneous Plumbing Systems, pp. 13–53.
Cruden, A.R., McCaffrey, K.J.W., Bunger, A.P., 2017. Geometric scaling of tabular igneous intrusions: Implications for emplacement and growth. In: Physical Geology of Shallow Magmatic Systems. Springer, pp. 11–38.
Dauphas, N., John, S.G., Rouxel, O., 2017. Iron isotope systematics. Rev. Mineral. Geochem. 82, 415–510.
Davidson, J., Turner, S., Handley, H., Macpherson, C., Dosseto, A., 2007. Amphibole “sponge” in arc crust? Geology 35, 787–790.
Day, J.M.D., O’Driscoll, B., 2019. Ancient high Pt/Os crustal contaminants can explain radiogenic 186Os in intraplate magmas. Earth Planet. Sci. Lett. 519, 101–108.
Day, J.M.D., Pearson, D.G., Hulbert, L.J., 2008. Rhenium-Osmium Isotope and PlatinumGroup Element Constraints on the Origin and Evolution of the 1·27 Ga Muskox Layered Intrusion. J. Petrol. 49, 1255–1295.
De Hoog, J.C.M., Gall, L., Cornell, D.H., 2010. Trace-element geochemistry of mantle olivine and application to mantle petrogenesis and geothermobarometry. Chem. Geol. 270, 196–215.
DeBari, S.M., 1994. Petrogenesis of the Fiambal´ a gabbroic intrusion, northwestern Argentina, a deep crustal syntectonic pluton in a continental magmatic arc. J. Petrol. 35, 679–713.
Deblond, A., 1994. Geologie et petrologie des Massifs basiques et ultra-basiques de la ceinture Kabanga-Musongati au Burundi: Mus´ ee Royal de L’Afrique Centrale. Ann. Sci. Geol. 99, 123 p.
DePaolo, D.J., 1985. Isotopic studies of processes in mafic magma chambers: I. The Kiglapait intrusion, Labrador. J. Petrol. 26, 925–951.
DePaolo, D.J., Wasserburg, G.J., 1979. Sm-Nd age of the Stillwater complex and the mantle evolution curve for neodymium. Geochim. Cosmochim. Acta 43, 999–1008.
Dixon, S., Rutherford, M.J., 1979. Plagiogranites as late-stage immiscible liquids in ophiolite and mid-ocean ridge suites: An experimental study. Earth Planet. Sci. Lett. 45, 45–60.
Djon, M.L.N., Barnes, S.-J., 2012. Changes in sulfides and platinum-group minerals with the degree of alteration in the Roby, Twilight, and High Grade zones of the Lac des Iles complex, Ontario, Canada. Mineral. Deposita 47, 875–896.
Djon, M.L., Olivo, G.R., Miller, J.D., Peck, D.C., Joy, B., 2017. Stratiform platinum-group element mineralization in the layered Northern Ultramafic Center of the Lac des Iles Intrusive complex, Ontario, Canada. Ore Geol. Rev. 90, 697–722.
Donaldson, C.H., 1974. Olivine morphology in the Tertiary harrisites of Rhum and in some Archean spinifex rocks. Geol. Soc. Am. Bull. 85, 1721–1726.

Donaldson, C.H., 1976. An experimental investigation of olivine morphology. Contrib. Mineral. Petrol. 57, 187–213.
Du Plessis, C.P., Walraven, F., 1990. The tectonic setting of the Bushveld complex in Southern Africa, part 1. Structural deformation and distribution. Tectonophysics 179, 305–319.
Duchesne, J.-C., Charlier, B., 2005. Geochemistry of cumulates from the Bjerkreim–Sokndal layered intrusion (S. Norway). Part I: Constraints from major elements on the mechanism of cumulate formation and on the jotunite liquid line of descent. Lithos 83, 229–254.
Duchesne, J.-C., Li´egeois, J.-P., Deblond, A., Tack, L., 2004. Petrogenesis of the Kabanga–Musongati layered mafic–ultramafic intrusions in Burundi (Kibaran Belt): geochemical, Sr–Nd isotopic constraints and Cr–Ni behaviour. J. Afr. Earth Sci. 39, 133–145.
Duchesne, J.-C., Shumlyanskyy, L., Charlier, B., 2006. The Fedorivka layered intrusion (Korosten Pluton, Ukraine): An example of highly differentiated ferrobasaltic evolution. Lithos 89, 353–376.
Eales, H.V., 2000. Implications of the chromium budget of the Western Limb of the Bushveld Complex. S. Afr. J. Geol. 103, 141–150.
Eales, H.V., Cawthorn, R.G., 1996. The Bushveld Complex. In: Cawthorn, Richard Grant (Ed.), Developments in Petrology, Layered Intrusions. Elsevier, pp. 181–229.
Eales, H.V., Costin, G., 2012. Crustally contaminated komatiite: primary source of the chromitites and marginal, lower, and critical magmas in a staging chamber beneath the Bushveld complex. Econ. Geol. 107, 645–665.
Eales, H.V., Reynolds, I.M., 1986. Cryptic variations within chromitites of the upper critical zone, northwestern Bushveld complex. Econ. Geol. 81, 1056–1066.
Eales, H.V., Field, M., de Klerk, W.J., Scoon, R.N., 1988. Regional trends of chemical variation and thermal erosion in the Upper critical Zone, Western Bushveld complex. Mineral. Mag. 52, 63–79.
Edmonds, M., Cashman, K.V., Holness, M., Jackson, M., 2019. Architecture and dynamics of magma reservoirs. Phil. Trans. R. Soc. A 377, 20180298.
Egorova, V., Latypov, R., 2012a. Processes operating during the initial stage of magma chamber evolution: insights from the marginal reversal of the Imandra layered intrusion, Russia. J. Petrol. 53, 3–26.
Egorova, Vera, Latypov, R., 2012b. Prolonged magma emplacement as a mechanism for the origin of the marginal reversal of the Fongen–Hyllingen layered intrusion, Norway. Geol. Mag. 149, 909–926.
Egorova, V., Latypov, R., 2013. Mafic-ultramafic sills: new insights from M- and S-shaped mineral and whole-rock compositional profiles. J. Petrol. 54, 2155–2191.
Ernst, R.E., 2014. Large Igneous Provinces. Cambridge University Press, University Printing House, Cambridge CB2 8BS, United Kingdom.
Ernst, R.E., Buchan, K.L., 2001. Mantle Plumes: Their Identification through Time. Geological Society of America.
Ernst, R.E., Liikane, D.A., Jowitt, S.M., Buchan, K.L., Blanchard, J.A., 2019. A new plumbing system framework for mantle plume-related continental large Igneous Provinces and their mafic-ultramafic intrusions. J. Volcanol. Geotherm. Res. 384, 75–84.
Ersoy, O., ¨ Nikogosian, I.K., van Bergen, M.J., Mason, P.R.D., 2019. Phosphorous incorporation in olivine crystallized from potassium-rich magmas. Geochim. Cosmochim. Acta 253, 63–83.
European Commission, 2020. Critical Raw Materials single-market-conomy.ec.europa. eu/sectors/raw-materials_en.
Evins, P.M., Smithies, R.H., Howard, H.M., Kirkland, C.L., Wingate, M.T.D., Bodorkos, S., 2010. Devil in the detail; the 1150–1000 Ma magmatic and structural evolution of the Ngaanyatjarra Rift, west Musgrave Province, Central Australia. Precambrian Res. 183, 572–588.
Farka˘s, J., Chrastný, V., Novak, ´ M., Cadkova, ˇ E., Pa˘sava, J., Chakrabarti, R., Jacobsen, S. B., Ackerman, L., Bullen, T.D., 2013. Chromium isotope variations (δ53/52Cr) in mantle-derived sources and their weathering products: Implications for environmental studies and the evolution of δ53/52Cr in the Earth's mantle over geologic time. Geochim. Cosmochim. Acta 123, 74–92.
Faure, F., Trolliard, G., Nicollet, C., Montel, J.-M., 2003. A developmental model of olivine morphology as a function of the cooling rate and the degree of undercooling. Contrib. Mineral. Petrol. 145, 251–263.
Faure, F., Schiano, P., Trolliard, G., Nicollet, C., Soulestin, B., 2007. Textural evolution of polyhedral olivine experiencing rapid cooling rates. Contrib. Mineral. Petrol. 153, 405–416.
Ferguson, M.R.M., Ehrig, K., Meffre, S., Feig, S., 2015. From magma to mush to lava: crystal history of voluminous felsic lavas in the Gawler Range Volcanics, South Australia. Lithos 346–347, 105148.
Ferracutti, G., Bjerg, E., Mogessie, A., 2013. Petrology, geochemistry and mineralization of the Las Aguilas ´ and Virorco mafic–ultramafic bodies, San Luis Province, Argentina. Int. J. Earth Sci. 102, 701–720.
Ferracutti, G., Bjerg, E., Hauzenberger, C., Mogessie, A., Cacace, F., Asiain, L., 2017. Meso to Neoproterozoic layered mafic-ultramafic rocks from the Virorco back-arc intrusion, Argentina. J. S. Am. Earth Sci. 79, 489–506.
Ferreira Filho, C.F., Araujo, S.M., 2009. Review of Brazilian chromite deposits associated with layered intrusions: geological and petrological constraints for the origin of stratiform chromitites. Appl. Earth Sci. 118, 86–100.
Finnigan, C.S., Brenan, J.M., Mungall, J.E., McDonough, W.F., 2008. Experiments and models bearing on the role of chromite as a collector of platinum group minerals by local reduction. J. Petrol. 49, 1647–1665.
Fischer, L.A., Wang, M., Charlier, B., Namur, O., Roberts, R.J., Veksler, I.V., Cawthorn, R. G., Holtz, F., 2016. Immiscible iron- and silica-rich liquids in the Upper Zone of the Bushveld complex. Earth Planet. Sci. Lett. 443, 108–117.
Forien, M., Tremblay, J., Barnes, S.-J., Burgisser, A., Pag´e, P., 2015. The role of viscous particle segregation in forming chromite layers from slumped crystal slurries: insights from analogue experiments. J. Petrol. 56, 2425–2444.
Fourny, A., Weis, D., Scoates, J.S., 2019. Isotopic and trace element geochemistry of the Kiglapait Intrusion, Labrador: Deciphering the mantle source, crustal contributions and processes preserved in mafic layered intrusions. J. Petrol. 60, 553–590. Fowler, A., 1990a. A compaction model for melt transport in the Earth's asthenosphere. Part I: The basic model. In: Ryan, M.P. (Ed.), Magma Transport and Storage. John Wiley, Chichester, pp. 4–15. Fowler, A., 1990b. A compaction model for melt transport in the Earth's asthenosphere, part II, applications. In: Ryan, M.P. (Ed.), Magma Transport and Storage. John Wiley, Chichester, pp. 15–32.
Fowler, A.C., Holness, M.B., 2022. The formation of three-grain junctions during solidification, Part II: theory. Contrib. Mineral. Petrol. 177, 58.
Frenkel', M.Y., Yaroshevsky, A.A., Ariskin, A.A., Barmina, G.S., Koptev-Dvornikov, E.V.,
Kireev, B.S., 1988. Dynamics of *In Situ* Differentiation of Mafic Magmas. Nauka, Moscow, 216 pp.
Galerne, C.Y., Neumann, E.-R., Aarnes, I., Planke, S., 2010. Magmatic differentiation processes in saucer-shaped sills: evidence from the Golden Valley Sill in the Karoo Basin, South Africa. Geosphere 6, 163–188.
Ganino, C., Arndt, N.T., 2009. Climate changes caused by degassing of sediments during the emplacement of large igneous province. Geology 37, 323–326.
Ganino, C., Arndt, N.T., Zhou, M.-F., Gaillard, F., Chauvel, C., 2008. Interaction of magma with sedimentary wall rock and magnetite ore genesis in the Panzhihua mafic intrusion, SW China. Mineral. Deposita 43, 677–694.
Ganino, C., Harris, C., Arndt, N.T., Prevec, S.A., Howarth, G.H., 2013. Assimilation of carbonate country rock by the parent magma of the Panzhihua Fe-Ti-V deposit (SW China): evidence from stable isotopes. Geosci. Front. 4, 547–554.
Gibb, F.G., 1974. Supercooling and the crystallization of plagioclase from a basaltic magma. Mineral. Mag. 39, 641–653. Glazner, A.F., 2014. Magmatic life at low Reynolds number. Geology 42, 935–938.
Glazner, A.F., 2021. Thermal constraints on the longevity, depth, and vertical extent of magmatic systems. Geochem. Geophys. Geosyst. 22, 1–12.
Glazner, A.F., Coleman, D.S., Bartley, J.M., 2017. What is a pluton? What is magma? In: Vearncombe, J. (Ed.), Granites2017@Benalla, Bulletin 65–2017. Australian Institute of Geoscientists, Benalla, pp. 53–55.
Godel, B., 2015. Platinum-group element deposits in layered intrusions: recent advances in the understanding of the ore forming processes. Layer Intrus. 379–432.
Godel, B., Barnes, S.-J., 2008. Platinum-group elements in sulfide minerals and the whole rocks of the JM Reef (Stillwater complex): Implication for the formation of the reef. Chem. Geol. 248, 272–294.
Godel, B., Barnes, S.-J., Maier, W.D., 2006a. Analysis of 3-D distribution of sulphide minerals and microstructures in the Merensky Reef: Implication for ore formation. In: Analysis of 3-D Distribution of Sulphide Minerals and Microstructures in the Merensky Reef: Implication for Ore Formation. GAC-MAC.
Godel, B., Barnes, S.-J., Maier, W.D., 2006b. 3-D distribution of sulphide minerals in the Merensky Reef (Bushveld complex, South Africa) and the J-M Reef (Stillwater complex, USA) and their relationship to microstructures using X-ray computed tomography. J. Petrol. 47, 1853–1872.
Godel, B., Barnes, S.-J., Maier, W.D., 2007. Platinum-group elements in sulphide minerals, platinum-group minerals, and whole-rocks of the Merensky Reef (Bushveld complex, South Africa): Implications for the formation of the reef. J. Petrol. 48, 1569–1604.

Godel, B., Barnes, S.J., Barnes, S.-J., Maier, W.D., 2010. Platinum ore in 3D: insights from high-resolution X-ray computed tomography. Geology 38, 1127–1130.
Godel, B., Barnes, S.J., Gurer, D., Austin, P., Fiorentini, M.L., 2013. Chromite in komatiites: 3D morphologies with implications for crystallization mechanisms. Contrib. Mineral. Petrol. 165, 173–189.
Godel, B., Rudashevsky, N.S., Nielsen, T.F.D., Barnes, S.J., Rudashevsky, V.N., 2014. New constraints on the origin of the Skaergaard Intrusion Cu-Pd-Au mineralization: insights from high-resolution X-ray computed tomography. Lithos 190-191, 27–36.
Goldfarb, R.J., Bradley, D., Leach, D.L., 2010. Secular variation in economic geology. Econ. Geol. 105, 459–465.
Good, N., De Wit, M.J., 1997. The Thabazimbi-Murchison lineament of the Kaapvaal craton, South Africa: 2700 Ma of episodic deformation. J. Geol. Soc. Lond. 154, 93–97.
Goutier, J., 2005. G´ eologie de la r´ egion de la baie Ramsay (32F/10) et de la rivi` ere Opaoca (32F/11). G´eologie Qu´ ebec [Ressources naturelles et faune Qu´ebec].
Gray, N.H., Philpotts, A.R., Dickson, L.D., 2003. Quantitative measures of textural anisotropy resulting from magmatic compaction illustrated by a sample from the Palisades sill, New Jersey. J. Volcanol. Geotherm. Res. 121, 293–312.
Grobler, D.F., Brits, J.A.N., Maier, W.D., Crossingham, A., 2019. Litho-and chemostratigraphy of the Flatreef PGE deposit, northern Bushveld complex. Mineral. Deposita 54, 3–28.
Groshev, N.Y., Nitkina, E.A., Mitrofanov, F.P., 2009. Two-phase mechanism of the formation of platinum-metal basites of the Fedorova Tundra intrusion on the Kola Peninsula: New data on geology and isotope geochronology. In: Doklady Earth Sciences. Springer, pp. 1012–1016.
Groshev, N.Y., Rundkvist, T.V., Karykowski, B.T., Maier, W.D., Korchagin, A.U., Ivanov, A.N., Junge, M., 2019. Low-sulfide platinum–palladium deposits of the Paleoproterozoic Fedorova–Pana layered complex, Kola Region, Russia. Minerals 9, 764.
Groshev, N.Y., Stepenshchikov, D.G., Karykowski, B.T., 2021. An Experiment on Thermal Modelling of the Paleoproterozoic Fedorova Layered Intrusion, Kola Region, Russia: Implications for the Origin of Contact Style PGE Mineralisation (This Vol).
Grout, F.F., 1918. The lopolith; an igneous form exemplified by the Duluth gabbro. Am. J. Sci. 4, 516–522.
Gudmundsson, A., 2012. Magma chambers: formation, local stresses, excess pressures, and compartments. J. Volcanol. Geotherm. Res. 237–238, 19–41.
Guice, G.L., Torm ¨ ¨ anen, T., Karykowski, B.T., Johanson, B., Lahaye, Y., 2017. Precious metal mineralisation in the Sotkavaara Intrusion, northern Finland: Peak Pt, Pd, Au and Cu offsets in a small intrusion with poorly-developed magmatic layering. Ore Geol. Rev. 89, 701–718.
Habekost, E.M., Wilson, J.R., 1989. Raft-like metabasaltic inclusions in the FongenHyllingen layered intrusive complex, Norway, and their mplications for magma chamber evolution. J. Petrol. 30, 1415–1441.
Habteselassie, M.M., Mathison, C.I., Gilkes, R.J., 1996. Vanadium in magnetite gabbros and its behaviour during lateritic weathering, Windimurra complex, Western Australia. Aust. J. Earth Sci. 43, 555–566.
Hagen-Peter, G., Tegner, C., Lesher, C.E., 2019. Strontium isotope systematics for plagioclase of the Skaergaard intrusion (East Greenland): a window to crustal assimilation, differentiation, and magma dynamics. Geology 47, 313–316.
Hahn, U.F., Ovendale, B., 1994. UG2 chromitite layer potholes at Wildebeestfontein North Mine, Impala platinum Limited. J. South. Afr. Inst. 3, 195–200.
Halim, A.H.A., Helmy, H.M., Abd El-Rahman, Y.M., Shibata, T., El Mahallawi, M.M., Yoshikawa, M., Arai, S., 2016. Petrology of the Motaghairat mafic–ultramafic complex, Eastern Desert, Egypt: a high-Mg post-collisional extension-related layered
intrusion. J. Asian Earth Sci. 116, 164–180.
Hammer, J.E., Sharp, T.G., Wessel, P., 2010. Heterogeneous nucleation and epitaxial crystal growth of magmatic minerals. Geology 38, 367–370.
Hanski, E., Walker, R.J., Huhma, H., Suominen, I., 2001. The Os and Nd isotopic systematics of c. 2.44 Ga Akanvaara and Koitelainen mafic layered intrusions in northern Finland. Precambrian Res. 109, 73–102.
Harmer, R.E., 2004. The Volspruit PGE-Ni reef: platinum mineralization in the Lower Zone south of Mokopane. In: Geosci. Africa 2004, Abstr. Vol., 256 Univ. Witwatersrand, Johannesburg, South Africa, p. 257.
Harney, D.M.W., Merkle, R.K.W., Von Gruenewaldt, G., 1990. Platinum-group element behavior in the lower part of the upper zone, eastern Bushveld complex; implications for the formation of the main magnetite layer. Econ. Geol. 85, 1777–1789. Harris, C., Chaumba, J.B., 2001. Crustal contamination and fluid–rock interaction during the formation of the Platreef, northern limb of the Bushveld complex, South Africa.
J. Petrol. 42, 1321–1347.
Hasch, M., Latypov, R., 2021. Too large to be seen: regional structures in lower and Middle group chromitites of the Bushveld complex, South Africa. Ore Geol. Rev. 139, 104520.
Haskin, L.A., Salpas, P.A., 1992. Genesis of compositional characteristics of Stillwater AN-I and AN-II thick anorthosite units. Geochim. Cosmochim. Acta 56, 1187–1212.
Hayes, B., Ashwal, L.D., Webb, S.J., Bybee, G.M., 2017. Large-scale magmatic layering in the Main Zone of the Bushveld complex and episodic downward magma infiltration. Contrib. Mineral. Petrol. 172, 1–16.
Heimdal, T.H., Callegaro, S., Svensen, H.H., Jones, M.T., Pereira, E., Planke, S., 2019. Evidence for magma-evaporite interactions during the emplacement of the Central Atlantic Magmatic Province (CAMP) in Brazil. Earth Planet. Sci. Lett. 506, 476–492.
Heinonen, J.S., Spera, F.J., Bohrson, W.A., 2021. Thermodynamic limits for assimilation of silicate crust in primitive magmas. Geology 50, 81–85.
Henderson, R.A., Fergusson, C.L., Leitch, E.C., Morand, V.J., Reinhardt, J.J., Carr, P.F., 1993. Tectonics of the northern New England Fold Belt. New Engl. Orogen East. Aust. 505–515. Hepworth, L.N., O'Driscoll, B., Gertisser, R., Daly, J.S., Emeleus, C.H., 2017. Incremental construction of the Unit 10 peridotite, Rum Eastern Layered Intrusion, NW Scotland. J. Petrol. 58, 137–166.
Hepworth, L.N., O'Driscoll, B., Gertisser, R., Daly, J.S., Emeleus, C.H., 2018. Linking *in situ* crystallization and magma replenishment via sill intrusion in the Rum Western layered intrusion, NW Scotland. J. Petrol. 59, 1605–1642.
Hepworth, L.N., Daly, J.S., Gertisser, R., Johnson, C.G., Emeleus, C.H., O'Driscoll, B., 2020a. Rapid crystallization of precious-metal-mineralized layers in mafic magmatic systems. Nat. Geosci. 13, 375–381.
Hepworth, L.N., Kaufmann, F.E.D., Hecht, L., Gertisser, R., O'Driscoll, B., 2020b. Braided peridotite sills and metasomatism in the Rum Layered Suite, Scotland. Contrib. Mineral. Petrol. 175, 17.
Hess, H.H., 1960. Stillwater Igneous Complex, Montana: A Quantitative Mineralogical Study. Geol. Soc. America Mem, p. 230.
Higgins, M.D., 1991. The origin of laminated and massive anorthosite, Sept Iles layered intrusion, Quebec, Canada. Contrib. Mineral. Petrol. 106, 340–354.
Higgins, M.D., 1994. Numerical modelling of crystal shapes in thin sections: estimation of crystal habit and true size. Am. Mineral. 79, 113–119.
Higgins, M.D., 2000. Measurement of crystal size distributions. Am. Mineral. 85, 1105–1116.
Hinchey, J.G., Hattori, K.H., Lavigne, M.J., 2005. Geology, petrology, and controls on PGE mineralization of the southern Roby and Twilight zones, Lac des Iles mine, Canada. Econ. Geol. 100, 43–61.
Hoatson, D.M., Sun, S.S., 2002. Archean layered mafic-ultramafic intrusions in the West Pilbara Craton, Western Australia: a synthesis of some of the oldest orthomagmatic mineralizing systems in the world. Econ. Geol. 97, 847–872.
Holness, M.B., 2006. Melt-solid dihedral angles of common minerals in natural rocks. J. Petrol. 47, 791–800.
Holness, M.B., 2014. The effect of crystallization time on plagioclase grain shape in dolerites. Contrib. Mineral. Petrol. 168, 1076.
Holness, M.B., 2015. Plagioclase growth rates control three-grain junction geometry in dolerites and gabbros. J. Petrol. 56, 2117–2144.
Holness, M.B., 2018. Melt segregation from silicic crystal mushes: a critical appraisal of possible mechanisms and their microstructural record. Contrib. Mineral. Petrol. 173, 48.
Holness, M.B., Fowler, A.C., 2022. The formation of three-grain junctions during solidification. Part I: observations. Contrib. Mineral. Petrol. 177, 55.
Holness, M.B., Winpenny, B., 2009. The Unit 12 allivalite, Eastern Layered Intrusion, Isle of Rum: a textural and geo-chemical study of an open-system magma chamber. Geol. Mag. 146, 437–450.
Holness, M.B., Cheadle, M.J., McKenzie, D., 2005. On the use of changes in dihedral angle to decode late-stage textural evolution in cumulates. J. Petrol. 46, 1565–1583.
Holness, M.B., Hallworth, M.A., Woods, A., Sides, R.E., 2007a. Infiltration metasomatism of cumulates by intrusive magma replenishment: the Wavy Horizon, Isle of Rum, Scotland. J. Petrol. 48, 563–587.
Holness, M.B., Nielsen, T.F.D., Tegner, C., 2007b. Textural maturity of cumulates: a record of chamber filling, liquidus assemblage, cooling rate and large-scale convection in mafic layered intrusions. J. Petrol. 48, 141–157.

Holness, M.B., Tegner, C., Nielsen, T.F.D., Stripp, G., Morse, S.A., 2007c. A textural record of solidification and cooling in the Skaergaard Intrusion, East Greenland. J. Petrol. 48, 2359–2377.
Holness, M.B., Stripp, G., Humphreys, M.C.S., Veklser, I.V., Nielsen, T.F.D., Tegner, C., 2011. Silicate liquid immiscibility within the crystal mush: late-stage magmatic microstructures in the Skaergaard Intrusion, East Greenland. J. Petrol. 52, 175–222.
Holness, M.B., Humphreys, M.C.S., Sides, R., Helz, R.T., Tegner, C., 2012a. Toward an understanding of disequilibrium dihedral angles in mafic rocks. J. Geophys. Res. 117, B06207.
Holness, M.B., Richardson, C., Helz, R.T., 2012b. Disequilibrium dihedral angles in dolerite sills: a new proxy for cooling rate. Geology 40, 795–798.
Holness, M.B., Namur, O., Cawthorn, R.G., 2013. Disequilibrium dihedral angles in layered intrusions: a microstructural record of fractionation. J. Petrol. 54, 2067–2093.
Holness, M.B., Tegner, C., Namur, O., Pilbeam, L., 2015. The earliest history of the Skaergaard magma chamber: a textural and geochemical study of the Cambridge drill core. J. Petrol. 56, 1199–1227.
Holness, M.B., Cawthorn, R.G., Roberts, J., 2017a. The thickness of the crystal mush on the floor of the Bushveld magma chamber. Contrib. Mineral. Petrol. 172, 102.
Holness, M.B., Tegner, C., Nielsen, T.F.D., Charlier, B., 2017b. The thickness of the mushy layer on the floor of the Skaergaard magma chamber at apatite saturation. J. Petrol. 58, 909–932.
Holness, M.B., Vukmanovic, Z., Mariani, E., 2017c. Assessing the role of compaction in the formation of adcumulates; a microstructural perspective. J. Petrol. 58, 643–674.
Holness, M.B., Clemens, J.D., Vernon, R.H., 2018. How deceptive are microstructures in granitic rocks? Answers from integrated physical theory, phase equilibrium, and direct observations. Contrib. Mineral. Petrol. 173, 62.
Holness, M.B., Morris, C., Vukmanovic, Z., Morgan, D.J., 2020. Insights into magma chamber processes from the relationship between fabric and grain shape in troctolitic cumulates. Front. Earth Sci. 8, 352.
Holness, M.B., Humphreys, M.C.S., Namur, O., Andersen, J.C.Ø., Tegner, C., Nielsen, T.F. D., 2022. Crystal mush growth and collapse on a steep wall: the marginal Border Series of the Skaergaard Intrusion, East Greenland. J. Petrol. 63, 1–21.
Holness, M.B., Vukmanovic, Z., O'Driscoll, B., 2023. The formation of chromite chains and clusters in igneous rocks. J. Petrol. 64, 1–24.
Holwell, D.A., Blanks, D.E., 2021. Emplacement of magmatic Cu-Au-Te (-Ni-PGE) sulfide blebs in alkaline mafic rocks of the Mordor complex, Northern Territory, Australia. Mineral. Deposita 56, 789–803.
Holwell, D.A., McDonald, I., Armitage, P.E.B., 2006. Platinum-group mineral assemblages in the Platreef at the Sandsloot Mine, northern Bushveld complex, South Africa. Mineral. Mag. 70, 83–101.
Holwell, D.A., Boyce, A.J., McDonald, I., 2007. Sulfur isotope variations within the Platreef Ni-Cu-PGE deposit: Genetic implications for the origin of sulfide mineralization. Econ. Geol. 102, 1091–1110.
Holwell, D.A., Keays, R.R., Firth, E.A., Findlay, J., 2014. Geochemistry and mineralogy of platinum group element mineralization in the River Valley intrusion, Ontario, Canada: a model for early-stage sulfur saturation and multistage emplacement and the implications for "Contact-Type" Ni-Cu-PGE sulfide mineralization. Econ. Geol. 109, 689–712.
Holwell, D.A., Keays, R.R., McDonald, I., Williams, M.R., 2015. Extreme enrichment of Se, Te, PGE and au in Cu sulfide microdroplets: evidence from LA-ICP-MS analysis of sulfides in the Skaergaard Intrusion, East Greenland. Contrib. Mineral. Petrol. 170, 1–26.
Holwell, D.A., Barnes, S.J., Le Vaillant, M., Keays, R.R., Fisher, L., Prosser, R., 2016. 3D textural evidence for the formation of ultra-high tenor precious metal bearing sulfide microdroplets in offset reefs: an extreme example from the Platinova Reef, Skaergaard Intrusion, Greenland. Lithos 256, 55–74.
Holwell, D.A., Fiorentini, M., McDonald, I., Lu, Y., Giuliani, A., Smith, D.J., Keith, M., Locmelis, M., 2019. A metasomatized lithospheric mantle control on the metallogenic signature of post-subduction magmatism. Nat. Commun. 10, 1–10.
Honour, V.C., Holness, M.B., Charlier, B., Piazolo, S.C., Namur, O., Prosa, T.J., Martin, I., Helz, R.T., Maclennan, J., Jean, M.M., 2019a. Compositional boundary layers trigger liquid unmixing in a basaltic crystal mush. Nat. Commun. 10, 4821.
Honour, V.C., Holness, M.B., Partridge, J.L., Charlier, B., 2019b. Microstructural evolution of silicate immiscible liquids in ferrobasalts. Contrib. Mineral. Petrol. 174, 77.
Hoshide, T., Obata, M., 2014. Spinel inclusions in olivine and plagioclase crystals in a layered gabbro: a marker and a tracer for primary phenocrysts in a differentiating magma reservoir. Contrib. Mineral. Petrol. 168.
Hou, T., Charlier, B., Namur, O., Schutte, P., Schwarz-Schampera, U., Zhang, Z., Holtz, F., 2017. Experimental study of liquid immiscibility in the Kiruna-type Vergenoeg ironfluorine deposit, South Africa. Geochim. Cosmochim. Acta 203, 303–322.
Hou, T., Charlier, B., Holtz, F., Veksler, I., Zhang, Z., Thomas, R., Namur, O., 2018. Immiscible hydrous Fe-Ca-P melt and the origin of iron oxide-apatite ore deposits. Nat. Commun. 9, 1415.
Howarth, G.H., Gross, J., 2019. Diffusion-controlled and concentric growth zoning revealed by phosphorous in olivine from rapidly ascending kimberlite magma, Benfontein, South Africa. Geochim. Cosmochim. Acta 266, 292–306.
Huang, H., Fryer, B.J., Polat, A., Pan, Y., 2014. Amphibole, plagioclase and clinopyroxene geochemistry of the Archean Fiskenæsset complex at Majorqapqava,ˆ southwestern Greenland: implications for Archean petrogenetic and geodynamic processes. Precambrian Res. 247, 64–91. Hughes, H.S.R., Andersen, J.C.Ø., O'Driscoll, B., 2021. Mineralization in layered maficultramafic intrusions. In: Encyclopedia of Geology, 2nd edition. Elsevier, pp. 823–839.
Hulbert, L.J., 1983. *A petrological investigation of the Rustenburg Layered Suite and associated mineralization south of Potgietersrus: Unpub* (Doctoral dissertation. D. Sc. dissertation, Univ. Pretoria), pp. 511.
Humphreys, M.C.S., 2009. Chemical evolution of intercumulus liquid, as recorded in plagioclase overgrowth rims from the Skaergaard intrusion. J. Petrol. 50, 127–145.
Humphreys, M.C.S., 2011. Silicate liquid immiscibility within the crystal mush: evidence from Ti in plagioclase from the Skaergaard intrusion. J. Petrol. 52, 147–174.
Hunt, E., Latypov, R., Horv´ ath, P., 2018. The Merensky Cyclic Unit, Bushveld complex, South Africa: reality or a myth? Minerals 8, 144.
Hunter, R.H., 1987. Textural equilibrium in layered igneous rocks. In: Parsons, I. (Ed.), Origins of Igneous Layering. Reidel, Dordrecht, pp. 473–503.
Huppert, H.E., Sparks, R.S.J., 1984. Double-diffusive convection due to crystallization in magmas. Annu. Rev. Earth Planet. Sci. 12, 11–37.
Huppert, H.E., Spark, R.S.J., Wilson, J.R., Hallworth, M.A., Leitch, A.M., 1987. Laboratory experiments with aqueous solutions modelling magma chamber processes II. Cooling and crystallization along inclined planes. In: Parsons, I. (Ed.), Origins of Igneous Layering, NATO ASI Series. Springer Netherlands, Dordrecht, pp. 539–568.
Hutton, D.H.W., 2009. Insights into magmatism in volcanic margins: bridge structures and a new mechanism of basic sill emplacement – Theron Mountains, Antarctica. Pet. Geosci. 15, 269–278.
Iacono Marziano, G., Gaillard, F., Pichavant, M., 2007. Limestone assimilation and the origin of CO_2 emissions at the Alban Hills (Central Italy): constraints from experimental petrology. J. Volcanol. Geotherm. Res. 166, 91–105.
Iacono-Marziano, G., Gaillard, F., Pichavant, M., 2008. Limestone assimilation by basaltic magmas: an experimental re-assessment and application to Italian volcanoes. Contrib. Mineral. Petrol. 155, 719–738.
Iacono-Marziano, G., Gaillard, F., Scaillet, B., Polozov, A.G., Marecal, V., Pirre, M., Arndt, N., 2012. Extremely reducing conditions reached during basaltic intrusion in organic matter-bearing sediments. Earth Planet. Sci. Lett. 357–358, 319–326.
Iacono-Marziano, G., Ferraina, C., Gaillard, F., Di Carlo, I., Arndt, N.T., 2017. Assimilation of sulfate and carbonaceous rocks: Experimental study, thermodynamic modeling and application to the Noril'sk-Talnakh region (Russia). Ore Geol. Rev. 90, 399–413.
Ihlenfeld, C., Keays, R.R., 2011. Crustal contamination and PGE mineralization in the Platreef, Bushveld complex, South Africa: evidence for multiple contamination events and transport of magmatic sulfides. Mineral. Deposita 46, 813–832.
Iljina, M.J., Lee, C.A., 2005. PGE deposits in the marginal series of layered intrusions. Explor. Platin. Gr. Elem. Depos. Mineral. Assoc. Can. Short Course Ser. 35, 75–96.
Iljina, M.J., Alapieti, T.T., McElduff, B.M., 1992. Platinum-group element mineralization in the Suhanko-Konttija¨rvi intrusion, Finland. Aust. J. Earth Sci. 39, 303–313.
Iljina, M., Maier, W.D., Karinen, T., 2015. PGE-(Cu-Ni) deposits of the TornioNar ¨ ank ¨ avaara ¨ belt of intrusions (Portimo, Penikat, and Koillismaa). In: Mineral Deposits of Finland. Elsevier, pp. 133–164.
Irvine, T.N., 1970a. Heat transfer during solidification of layered intrusions. I. Sheets and sills. Can. J. Earth Sci. 7, 1031–1061.

Irvine, T.N., 1970b. Crystallization sequences in the Muskox intrusion and other layered intrusions, I. Olivine-pyroxene-plagioclase relations. In: Visser, D.J.L., Gruenewaldt, G. (Eds.), Spec. Publ. Geol. Soc. South Africa 1. Geological Society of South Africa, pp. 441–476.
Irvine, T.N., 1975. Crystallization sequences in the Muskox intrusion and other layered intrusions—II. Origin of chromitite layers and similar deposits of other magmatic ores. Geochim. Cosmochim. Acta 39, 991–1020.
Irvine, T.N., 1976. Crystallization sequences in the Muskox intrusion and other layered intrusions—II. Origin of chromitite layers and similar deposits of other magmatic ores. In: Chromium: its Physicochemical Behavior and Petrologic Significance. Pergamon, pp. 991–1020.
Irvine, T.N., 1977. Origin of chromitite layers in the Muskox intrusion and other stratiform intrusions: a new interpretation. Geology 5, 273–277. Irvine, T.N., 1979. Rocks whose composition is determined by crystal accumulation and sorting. In: Yoder Jr., H.S. (Ed.), Evolution of the Igneous Rocks. 50th Anniversary Perspectives. Princeton University Press, Princeton, N.J, pp. 245–306.
Irvine, T.N., 1980a. Magmatic density currents and cumulus processes. Am. J. Sci. 280-A, 1–58.
Irvine, T.N., 1980b. Magmatic infiltration metasomatism, double-diffusive fractional crystallization, and adcumulus growth in the Muskox intrusion and other layered intrusions. In: Hargraves, R.B. (Ed.), Physics of Magmatic Processes. Princeton University Press, pp. 325–384.
Irvine, T.N., 1981. A liquid-density controlled model for chromitite formation in the Muskox intrusion. In: Carnegie Institute of Washington Year Book, 80, p. 317.
Irvine, T.N., 1982. Terminology for layered intrusions. J. Petrol. 23, 127–162.
Irvine, T.N., 1983a. Observations on the origins of Skaergaard layering. In: Carnegie Institution of Washington Year Book, 82, pp. 284–289.
Irvine, T.N., 1983b. Skaergaard trough-layering structures. In: Yearbook of the Carnegie Institute of Washington, 82, pp. 289–295.
Irvine, T.N., 1987. Layering and related structures in the Duke Island and Skaergaard intrusions: similarities, differences, and origins. In: Parsons, I. (Ed.), Origins of Igneous Layering. Springer-Science+Business Media, B.V, pp. 185–246.
Irvine, T.N., 1992. Emplacement of the Skaergaard intrusion. In: Carnegie Institution of Washington Year Book, 91, pp. 91–96.
Irvine, T.N., Smith, C.H., 1967. The ultramafic rocks of the Muskox intrusion. In: Wyllie, P.J. (Ed.), Ultramafic and Related Rocks. John Wiley & Sons, Inc., New York, pp. 38–49.
Irvine, T.N., Stoeser, D.B., 1978. Structure of the Skaergaard trough bands. In: Yearbook of the Carnegie Institute of Washington, 77, pp. 725–732.
Irvine, T.N., Keith, D.W., Todd, S.G., 1983. The J-M Platinum-Palladium Reef of the Stillwater complex, Montana: II. origin by double-diffusive convective magma mixing and implications for the Bushveld Complex. Econ. Geol. 78, 1287–1334.
Irvine, T.N., Andersen, J.C.Ø., Brooks, C.K., 1998. Included blocks (and blocks within blocks) in the Skaergaard intrusion: Geologic relations and the origins of rhythmic modally graded layers. Geol. Soc. Am. Bull. 110, 1398–1447.
Ivanic, T.J., Wingate, M.T.D., Kirkland, C.L., Van Kranendonk, M.J., Wyche, S., 2010.
Age and significance of voluminous mafic–ultramafic magmatic events in the Murchison Domain, Yilgarn Craton. Aust. J. Earth Sci. 57, 597–614.
Ivanic, T.J., Nebel, O., Jourdan, F., Faure, K., Kirkland, C.L., Belousova, E.A., 2015. Heterogeneously hydrated mantle beneath the late Archean Yilgarn Craton. Lithos 238, 76–85.
Ivanic, T.J., Nebel, O., Brett, J., Murdie, R.E., 2018. The Windimurra Igneous Complex: An Archean Bushveld?, 453 Geol. Soc. London, Spec. Publ, pp. 313–348.
Jackson, E.D., 1961. Primary textures and mineral associations in the ultramafic zone of the Stillwater complex, Montana. U. S. Geol. Surv. Prof. Pap. 358, 108 pp.
Jackson, E.D., 1970. The cyclic unit in layered intrusions—a comparison of repetitive stratigraphy in the ultramafic parts of the Stillwater, Muskox, Great Dyke and Bushveld complexes. In: Geol. Soc. S. Afr. Spec. Pap, 1, pp. 391–424.
Jackson, M.D., Blundy, J., Sparks, R.S.J., 2018. Chemical differentiation, cold storage and remobilization of magma in the Earth's crust. Nature 564, 405–409.
Jakobsen, J.K., Veksler, I.V., Tegner, C., Brooks, C.K., 2005. Immiscible iron- and silicarich melts in basalt petrogenesis documented in the Skaergaard intrusion. Geology 33, 885–888.
Jakobsen, J.K., Veksler, I.V., Tegner, C., Brooks, C.K., 2011. Crystallization of the Skaergaard intrusion from an emulsion of immiscible iron- and silica-rich liquids: evidence from melt inclusions in plagioclase. J. Petrol. 52, 345–373.
J¨ arvinen, V., Halkoaho, T., Konnunaho, J., Heinonen, J.S., Ram ¨ o, ¨ O.T., 2020. Parental magma, magmatic stratigraphy, and reef-type PGE enrichment of the 2.44-Ga maficultramafic N¨ ar¨ ank¨ avaara layered intrusion, Northern Finland. Mineral. Deposita 55, 1535–1560.
Jaupart, C., Tait, S., 1995. Dynamics of differentiation in magma reservoirs. J. Geophys. Res. 100, 17615–17636.
Jenkins, M.C., Mungall, J.E., 2018. Genesis of the Peridotite Zone, Stillwater complex, Montana, USA. J. Petrol. 59, 2157–2189.
Jenkins, M.C., Mungall, J.E., Zientek, M.L., Costin, G., Yao, Z., 2021. Origin of the JM Reef and lower banded series, Stillwater complex, Montana, USA. Precambrian Res. 367, 106457.
Jerram, D.A., Cheadle, M.J., Philpotts, A.R., 2003. Quantifying the building blocks of igneous rocks: are clustered crystal rrameworks the foundation? J. Petrol. 44, 2033–2051.
Jesus, A.P., Mateus, A., Munha, ´ J.M., Tassinari, C., 2014. Internal architecture and Fe–Ti–V oxide ore genesis in a Variscan synorogenic layered mafic intrusion, the Beja Layered Gabbroic Sequence (Portugal). Lithos 190, 111–136.
Jesus, A.P., Mateus, A., Benoit, M., Tassinari, C.C.G., dos Santos, T.B., 2020. The timing of sulfide segregation in a Variscan synorogenic gabbroic layered intrusion (Beja, Portugal): Implications for Ni-Cu-PGE exploration in orogenic settings. Ore Geol. Rev. 126, 103767.
Joesten, R., 1977. Mineralogical and chemical evolution of contaminated igneous rocks at a gabbro-limestone contact, Christmas Mountains, big Bend region, Texas. Geol. Soc. Am. Bull. 88, 1515–1529.
Johnson, T.E., Brown, M., White, R.W., 2010. Petrogenetic modelling of strongly residual metapelitic xenoliths within the southern Platreef, Bushveld complex, South Africa. J. Metamorph. Geol. 28, 269–291.
Junge, M., Oberthür, T., Melcher, F., 2014. Cryptic variation of chromite chemistry, platinum group element and platinum group mineral distribution in the UG-2 chromitite: an example from the Karee Mine, western Bushveld complex, South Africa. Econ. Geol. 109, 795–810.
Juopperi, A., 1977. The Magnetite Gabbro and Related Mustavaara Vanadium Ore Deposit in the Porttivaara Layered Intrusion, North-Eastern Finland.
Kaavera, J., Imai, A., Yonezu, K., Tindell, T., Sanematsu, K., Watanabe, K., 2020. Controls on the disseminated Ni-Cu-PGE sulfide mineralization at the Tubane section, northern Molopo Farms complex, Botswana: Implications for the formation of conduit style magmatic sulfide ores. Ore Geol. Rev. 126, 103731.
Karinen, T., 2010. The Koillismaa Intrusion, Northeastern Finland: Evidence for PGE Reef Forming Processes in the Layered Series. Geological Survey of Finland, 176 pp.
Karinen, T., Moilanen, M., Kuva, J., Lahaye, Y., Datar, B., Yang, S., K¨ apyaho, A., Antti, E., Ojala, Bulletin, 2022. Mustavaara Revisited: A Revised Genetic Model for Orthomagmatic Fe-Ti-V Mineralisation in the Koillismaa Intrusion, Bulletin of Geological Survey of Finland. Geological Survey of Finland.
Karykowski, B.T., Polito, P.A., Maier, W.D., Gutzmer, J., Krause, J., 2017a. New insights into the petrogenesis of the Jameson Range layered intrusion and associated Fe-TiPV-PGE-Au mineralisation, West Musgrave Province, Western Australia. Mineral. Deposita 52, 233–255.
Karykowski, B.T., Yang, S.-H., Maier, W.D., Lahaye, Y., Lissenberg, C.J., O'Brien, H., 2017b. *In situ* Sr isotope compositions of plagioclase from a complete stratigraphic profile of the Bushveld complex, South Africa: evidence for extensive magma mixing and percolation. J. Petrol. 58, 2285–2308.
Karykowski, B.T., Maier, W.D., Groshev, N.Y., Barnes, S.-J., Pripachkin, P.V., McDonald, I., Savard, D., 2018a. Critical controls on the formation of contact-style PGE-Ni-Cu mineralization: evidence from the Paleoproterozoic Monchegorsk complex, Kola Region, Russia. Econ. Geol. 113, 911–935.
Karykowski, B.T., Maier, W.D., Groshev, N.Y., Barnes, S.-J., Pripachkin, P.V., McDonald, I., 2018b. Origin of reef-style PGE mineralization in the Paleoproterozoic Monchegorsk complex, Kola Region, Russia. Econ. Geol. 113, 1333–1358.
Kaufmann, F.E.D., Vukmanovic, Z., Holness, M.B., Hecht, L., 2018. Orthopyroxene oikocrysts in the MG1 chromitite layer of the Bushveld complex: implications for cumulate formation and recrystallisation. Contrib. Mineral. Petrol. 173, 17.
Kerans, C., 1983. Timing of emplacement of the Muskox intrusion: constraints from Coppermine homocline cover strata. Can. J. Earth Sci. 20, 673–683.
Kerr, R.C., 1994. Dissolving driven by vigorous compositional convection. J. Fluid Mech. 280, 287–302.
Kerr, A., Leitch, A.M., 2005. Self-destructive sulfide segregation systems and the formation of high-grade magmatic ore deposits. Econ. Geol. 100, 311–332.
Khedr, M.Z., Takazawa, E., Arai, S., Stern, R.J., Morishita, T., El-Awady, A., 2022. Styles of Fe–Ti–V ore deposits in the Neoproterozoic layered mafic-ultramafic intrusions, south Eastern Desert of Egypt: evidence for fractional crystallization of V-rich melts. J. Afr. Earth Sci. 194, 104620.

Kieffer, M., Dare, S.A.S., Namur, O., 2023. The use of trace elements in apatite to trace differentiation of a ferrobasaltic melt in the Sept-Iles Intrusive Suite, Quebec, Canada: Implications for provenance discrimination. Geochim. Cosmochim. Acta 342, 169–197.
Kinnaird, J.A., 2005. The Bushveld Large Igneous Province. Rev. Pap. Univ, Witwatersrand, Johannesburg, South Africa, 39pp.
Kinnaird, J.A., Kruger, F.J., Nex, P.A.M., Cawthorn, R.G., 2002. Chromitite formation—a key to understanding processes of platinum enrichment. Appl. Earth Sci. 111, 23–35.
Kinnaird, J.A., Hutchinson, D., Schurmann, L., Nex, P.A.M., de Lange, R., 2005. Petrology and mineralisation of the southern Platreef: northern limb of the Bushveld complex, South Africa. Mineral. Deposita 40, 576–597.
Kirkpatrick, R.J., 1977. Nucleation and growth of plagioclase, Makaopuhi and Alae lava lakes, Kilauea Volcano, Hawaii. Geol. Soc. Am. Bull. 88, 78–84.
Kirkpatrick, R.J., Robinson, G.R., Hays, J.F., 1976. Kinetics of crystal growth from silicate melts: anorthite and diopside. J. Geophys. Res. 81, 5715–5720.
Klemm, D.D., Henckel, J., Dehm, R.M., Von Gruenewaldt, G., 1985. The geochemistry of titanomagnetite in magnetite layers and their host rocks of the eastern Bushveld complex. Econ. Geol. 80, 1075–1088.
Kr¨ attli, G., Schmidt, M.W., 2021. Experimental settling, floatation and compaction of plagioclase in basaltic melt and a revision of melt density. Contrib. Mineral. Petrol. 176, 30.
Kruger, F.J., 1994. The Sr-stratigraphy of the western Bushveld Complex. S. Afr. J. Geol. 97, 393–398.
Kruger, F.J., 2005. Filling the Bushveld complex magma chamber: lateral expansion, roof and floor interaction, magmatic unconformities, and the formation of giant chromitite, PGE and Ti-V-magnetitite deposits. Mineral. Deposita 40, 451–472.
Kruger, W., Latypov, R., 2020. Fossilized solidification fronts in the Bushveld complex argue for liquid-dominated magmatic systems. Nat. Commun. 11, 2909.
Kruger, W., Latypov, R., 2021. Magmatic karst reveals dynamics of crystallization and differentiation in basaltic magma chambers. Sci. Rep. 11, 7341.
Kruger, W., Latypov, R., 2022. *In situ* crystallization of non-cotectic, foliated igneous rocks on a magma chamber floor. Commun. Earth Environ. 8, 251.
Kruger, F.J., Marsh, J., 1982. Significance of $^{87}Sr/^{86}Sr$ ratios in the Merensky cyclic unit of the Bushveld complex. Nature 298, 53–55.
Kruger, F.J., Smart, R., 1987. Diffusion of trace elements during bottom crystallization of double-diffusive convection systems: the magnetitite layers of the Bushveld complex. J. Volcanol. Geothem. 34, 133–142.
Lang, S., Mollo, S., France, L., Misiti, V., Nazzari, M., 2022. Partitioning of Ti, Al, P, and Cr between olivine and a tholeiitic basaltic melt: Insights on olivine zoning patterns and cation substitution reactions under variable cooling rate conditions. Chem. Geol. 601, 120870.
Latypov, R., 2003a. The origin of marginal compositional reversals in basic-ultrabasic sills and layered intrusions by Soret fractionation. J. Petrol. 44, 1579–1618.
Latypov, R., 2003b. The origin of basic-ultrabasic sills with S-D- and I-shaped compositional profiles by *in situ* crystallization of a single input of phenocryst-poor parental magma. J. Petrol. 44, 1619–1656.
Latypov, R., 2009. Testing the validity of the petrological hypothesis 'no phenocrysts, no post-emplacement differentiation'. J. Petrol. 50, 1047–1060.
Latypov, R., 2015. Basal reversals in mafic sills and layered intrusions. In: Charlier, B., Namur, O., Latypov, R., Tegner, C. (Eds.), Layered Intrusions. Springer Netherlands, Dordrecht, pp. 259–293. Latypov, R., 2019. Comment on "the Stillwater complex: integrating zircon geochronological and geochemical constraints on the age, emplacement history and crystallization of a large, open-system layered intrusion" by Wall et al. (J. Petrology, 59, 153–190, 2018). J. Petrol. 60, 1095–1098.
Latypov, R.M., Chistyakova, S.Yu., 2020. Origin of non-cotectic cumulates: a novel approach. Geology 48, 604–608.
Latypov, R.M., Chistyakova, S.Yu., 2022. Misinterpretation of zircon ages in layered intrusions. S. Afr. J. Geol. 125 (1), 13–26.
Latypov, R., Egorova, V., 2012. Plagioclase compositions give evidence for *in situ* crystallization under horizontal flow conditions in mafic sills. Geology 40, 883–886.
Latypov, R., Chistyakova, S., Alapieti, T., 2007. Revisiting problem of chilled margins associated with marginal reversals in mafic–ultramafic intrusive bodies. Lithos 99, 178–206.
Latypov, R., Hanski, E., Lavrenchuk, A., Huhma, H., Havela, T., 2011. A "three-increase model" for the origin of the marginal reversal of the Koitelainen layered intrusion, Finland. J. Petrol. 52, 733–764.
Latypov, R., O'Driscoll, B., Lavrenchuk, A., 2013. Towards a model for the *in situ* origin of PGE reefs in layered intrusions: insights from chromitite seams of the Rum Eastern Layered Intrusion, Scotland. Contrib. Mineral. Petrol. 166, 309–327.
Latypov, R., Chistyakova, S., Page, A., Hornsey, R., 2015a. Field evidence for the *in situ* crystallization of the Merensky Reef. J. Petrol. 56, 2341–2372.
Latypov, R., Morse, T., Robins, B., Wilson, R., Cawthorn, G., Tegner, C., Holness, M., Lesher, C., Barnes, S., O'Driscoll, B., Veksler, I., Higgins, M., Wilson, A., Namur, O., Chistyakova, S., Naslund, R., Thy, P., 2015b. A fundamental dispute: A discussion of "On some fundamentals of igneous petrology" by Bruce D. Marsh, Contrib. Mineral. Petrol. (2013a) 166: 665–690. Contrib. Mineral. Petrol. 169.
Latypov, R., Chistyakova, S., Mukherjee, R., 2017a. A novel hypothesis for origin of massive chromitites in the Bushveld Igneous complex. J. Petrol. 58, 1899–1940.
Latypov, R.M., Chistyakova, S.Yu., Barnes, S.J., Hunt, E.J., 2017b. Origin of platinum deposits in layered intrusions by *in situ* crystallization: evidence from undercutting Merensky Reef of the Bushveld complex. J. Petrol. 58, 715–762.
Latypov, R., Chistyakova, S., Kramers, J., 2017c. Arguments against syn-magmatic sills in the Bushveld complex. S. Afr. J. Geol. 120 (4), 565–574.
Latypov, R., Costin, G., Chistyakova, S., Hunt, E.J., Mukherjee, R., Naldrett, T., 2018a. Platinum-bearing chromite layers are caused by pressure reduction during magma ascent. Nat. Commun. 9.
Latypov, R.M., Chistyakova, S.Yu., McIntosh, R., Scogings, A., 2018b. Geochemical evidence for *in situ* growth of LG6 chromitite from the compositionally stratified magma in the Bushveld chamber. In: 13th International Platinum Symposium. Polokwane, South Africa, pp. 103–104.
Latypov, R., Chistyakova, S., Grieve, R., Huhma, H., 2019a. Evidence for igneous differentiation in Sudbury Igneous complex and impact-driven evolution of terrestrial planet proto-crusts. Nat. Commun. 10, 508.
Latypov, R., Chistyakova, S., van der Merwe, J., Westraat, J., 2019b. A note on the erosive nature of potholes in the Bushveld complex. S. Afr. J. Geol. 122, 555–560.
Latypov, R., Chistyakova, S., Costin, G., Namur, O., Barnes, S., Kruger, W., 2020a. Monomineralic anorthosites in layered intrusions are indicators of the magma chamber replenishment by plagioclase-only-saturated melts. Sci. Rep. 10, 3839.
Latypov, R.M., Chistyakova, S.Yu., Namur, O., Barnes, S., 2020b. Dynamics of evolving magma chambers: textural and chemical evolution of cumulates at the arrival of new liquidus phases. Earth Sci. Rev. 210, 103388.
Latypov, R., Chistyakova, S., Barnes, S.J., Godel, B., Delaney, G.W., Cleary, P.W., Radermacher, V.J., Campbell, I., Jakata, K., 2022a. Chromitite layers indicate the existence of large, long-lived, and entirely molten magma chambers. Sci. Rep. 12, 4092.
Latypov, R.M., Chistyakova, S.Yu., Hornsey, R.A., Costin, G., van der Merwe, M., 2022b. A 5-km-thick reservoir with >380,000 km^3 of magma within the ancient Earth's crust. Sci. Rep. 12, 15651.
Latypov, R.M., Heinonen, J.S., Chistyakova, S.Yu., 2022c. Magmatic erosion of hightemperature melting cumulates in the Bushveld complex by chemical dissolution. GeoGeo 1, 100077.
Latypov, R.M., Chistyakova, S.Yu., Barnes, S.J., Letsoele, C., Kruger, W., 2023a. Constraints on hydrodynamic sorting and reactive porous flow from the cumulates in the inward-growing chamber floor of the Bushveld complex. J. Petrol. (in review).
Latypov, R., Chistyakova, S., Kaufmann, F.E.D., Roelofse, F., Kruger, W., Barnes, S., Magson, J., Nicholson, M., 2023b. The use of An-content of interstitial plagioclase for testing slurry models for the origin of Bushveld massive chromitites. Lithos 460- 461, 107374.
Lauri, L.S., Mikkola, P., Karinen, T., 2012. Early Paleoproterozoic felsic and mafic magmatism in the Karelian province of the Fennoscandian shield. Lithos 151, 74–82.
Le Vaillant, M., Hill, E.J., Barnes, S.J., 2017. Simplifying drill-hole domains for 3D geochemical modelling: an example from the Kevitsa Ni-Cu-(PGE) deposit. Ore Geol. Rev. 90, 388–398.
Le Vaillant, M., Barnes, S.J., Mole, D.R., Fiorentini, M.L., Laflamme, C., Denyszyn, S.W., Austin, J., Patterson, B., Godel, B., Hicks, J., 2020. Multidisciplinary study of a complex magmatic system: the Savannah Ni-Cu-Co Camp, Western Australia. Ore Geol. Rev. 117, 103292.
Lee, C.A., Butcher, A.R., 1990. Cyclicity in the Sr isotope stratigraphy through the Merensky and Bastard Reef units, Atok section, eastern Bushveld complex. Econ. Geol. 85, 877–883.
Leeb-Du Toit, A., 1986. The Impala platinum Mines. In: Anhaeusser, C.R., Maske, S. (Eds.), Mineral Deposits of Southern Africa. Mineral deposits of Southern Africa. Geological Society of South Africa, pp. 1091–1106.

Lenaz, D., O'Driscoll, B., Princivalle, F., 2011. Petrogenesis of the anorthosite-chromitite association: crystal-chemical and petrological insights from the Rum Layered Suite, NW Scotland. Contrib. Mineral. Petrol. 162, 1201–1213.
Lesher, C.M., Burnham, O.M., 2001. Multicomponent elemental and isotopic mixing in Ni-Cu-(PGE) ores at Kambalda, Western Australia. Can. Mineral. 39, 421–446.
Lesher, C.E., Lundstrom, C.C., Barfod, G.C., Glessner, J.J., Brown, E., Thy, P., Salmonsen, L.P., Tegner, C., 2014. Iron isotope systematics of the Skaergaard intrusion. In: 24th Annual VM Goldschmidt Conference: Sacramento, California, USA.
Lesher, C.M., Carson, H.J.E., Houl´e, M.G., 2019. Genesis of chromite deposits by dynamic upgrading of Fe ± Ti oxide xenocrysts. Geology 47, 207–210.
Leuthold, J., Müntener, O., Baumgartner, L.P., Putlitz, B., Ovtcharova, M., Schaltegger, U., 2012. Time resolved construction of a bimodal laccolith (Torres del Paine, Patagonia). Earth Planet. Sci. Lett. 325–326, 85–92.
Li, C., Ripley, E.M., Naldrett, A.J., 2009. A new genetic model for the giant Ni–Cu–PGE sulfide deposits associated with the Siberian flood basalts. Econ. Geol. 104, 291–301.
Li, W., Aud´ etat, A., Zhang, J., 2015. The role of evaporites in the formation of magnetiteapatite deposits along the Middle and lower Yangtze River, China: Evidence from LAICP-MS analysis of fluid inclusions. Ore Geol. Rev. 67, 264–278.
Lightfoot, P.C., 2016. Nickel Sulfide Ores and Impact Melts: Origin of the Sudbury Igneous Complex. Elsevier, New York, NY, 662 pp.
Lightfoot, P.C., Evans-Lamswood, D., 2015. Structural controls on the primary distribution of mafic–ultramafic intrusions containing Ni–Cu–Co–(PGE) sulfide mineralization in the roots of large igneous provinces. Ore Geol. Rev. 64, 354–386.
Lightfoot, P.C., Zotov, I.A., 2005. Geology and geochemistry of the Sudbury Igneous complex, Ontario, Canada: origin of nickel sulfide mineralization associated with an impact-generated melt sheet. Geol. Ore Deposita 47, 349–381.
Lima, H.A.F., Ferreira Filho, C.F., Pimentel, M.M., Dantas, E.L., de Araújo, S.M., 2008. Geology, petrology and geochronology of the layered mafic-ultramafic intrusions in the Porto Nacional area, Central Brazil. J. S. Am. Earth Sci. 26, 300–317.
Lipin, B.R., 1993. Pressure increases, the formation of chromite seams, and the development of the ultramafic series in the Stillwater complex, Montana. J. Petrol. 34, 955–976.
Liu, P.-P., Zhou, M.-F., Chen, W.T., Boone, M., Cnudde, V., 2014. Using multiphase solid inclusions to constrain the origin of the Baima Fe–Ti–(V) oxide deposit, SW China. J. Petrol. 55, 951–976.
Liu, P.-P., Zhou, M.-F., Chen, W.T., Gao, J.-F., Huang, X.-W., 2015. In-situ LA-ICP-MS trace elemental analyses of magnetite: Fe–Ti–(V) oxide-bearing mafic–ultramafic layered intrusions of the Emeishan large Igneous Province, SW China. Ore Geol. Rev. 65, 853–871.
Liu, P.-P., Zhou, M.-F., Ren, Z., Wang, C.Y., Wang, K., 2016. Immiscible Fe-and Si-rich silicate melts in plagioclase from the Baima mafic intrusion (SW China): implications for the origin of bi-modal igneous suites in large igneous provinces. J. Asian Earth Sci. 127, 211–230.
Lofgren, G., 1974. An experimental study of plagioclase crystal morphology: isothermal crystallisation. Am. J. Sci. 274, 243–273.
Lomberg, K.G., Patterson, M.A., Venter, J.E., Martin, E.S., 1999. The morphology of potholes in the UG2 chromitite layer and Merensky Reef (pothole reef facies) at Union Section, Rustenberg platinum Mines. S. Afr. J. Geol. 102, 209–220.
Lundgaard, K.L., Robins, B., Tegner, C., Wilson, J.R., 2002. Formation of hybrid cumulates: melatroctolites in Intrusion 4 of the Honningsvåg Intrusive Suite, northern Norway. Lithos 61, 1–19.
Lundgaard, K.L., Tegner, C., Cawthorn, R.G., Kruger, F.J., Wilson, J.R., 2006. Trapped intercumulus liquid in the Main Zone of the eastern Bushveld complex, South Africa. Contrib. Mineral. Petrol. 151, 352–369.
Lundstrom, C.C., Gajos, N., 2014. Formation of the PGE reef horizon in the Sonju Lake layered mafic intrusion by thermal migration zone refining. Econ. Geol. 109, 1257–1269.
Lundstrom, C.C., Glazner, A.F., 2016. Silicic magmatism and the volcanic–plutonic connection. Elements 12, 91–96.
Lynn, K.J., Garcia, M.O., Shea, T., 2020. Phosphorus coupling obfuscates lithium geospeedometry in olivine. Front. Earth Sci. 8, 135.
Magee, C., Muirhead, J.D., Karvelas, A., Holford, S.P., Jackson, C.A.L., Bastow, I.D., Schofield, N., Stevenson, C.T.E., McLean, C., McCarthy, W., Shtukert, O., 2016. Lateral magma flow in mafic sill complexes. Geosphere (Boulder, CO) 12, 809–841.
Maghdour-Mashhour, R., Hayes, B., Bolhar, R., Ueckermann, H., 2021. Sill intrusion into pyroxenitic mush and the development of the Lower–Upper critical Zone boundary of the Bushveld complex: Implications for the origin of stratiform anorthosites and chromitites in layered intrusions. J. Petrol. 62, 1–30.
Maier, W.D., 2005. Platinum-group element (PGE) deposits and occurrences: Mineralization styles, genetic concepts, and exploration criteria. J. Afr. Earth Sci. 41, 165–191.
Maier, W.D., Barnes, S.-J., 2008. Platinum-group elements in the UG1 and UG2 chromitites, and the Bastard reef, at Impala platinum mine, western Bushveld complex, South Africa: evidence for late magmatic cumulate instability and reef constitution. S. Afr. J. Geol. 111, 159–176.
Maier, W.D., Groves, D.I., 2011. Temporal and spatial controls on the formation of magmatic PGE and Ni–Cu deposits. Mineral. Deposita 46, 841–857.
Maier, W.D., Barnes, S.-J., Gartz, V., Andrews, G., 2003. Pt-Pd reefs in magnetitites of the Stella layered intrusion, South Africa: a world of new exploration opportunities for platinum group elements. Geology 31, 885–888.
Maier, W.D., Barnes, S.-J., Bandyayera, D., Livesey, T., Li, C., Ripley, E., 2008a. Early Kibaran rift-related mafic–ultramafic magmatism in western Tanzania and Burundi: Petrogenesis and ore potential of the Kapalagulu and Musongati layered intrusions.
Lithos 101, 24–53.
Maier, W.D., Barnes, S.-J., Chinyepi, G., Barton, J.M., Eglington, B., Setshedi, I., 2008b. The composition of magmatic Ni–Cu–(PGE) sulfide deposits in the Tati and SelebiPhikwe belts of eastern Botswana. Mineral. Deposita 43, 37–60.
Maier, W.D., Barnes, S.-J., Groves, D.I., 2013. The Bushveld complex, South Africa: formation of platinum–palladium, chrome- and vanadium-rich layers via hydrodynamic sorting of a mobilized cumulate slurry in a large, relatively slowly cooling, subsiding magma chamber. Mineral. Deposita 48, 1–56.
Maier, W.D., Howard, H.M., Smithies, R.H., Yang, S.-H., Barnes, S.-J., O'Brien, H., Huhma, H., Gardoll, S., 2015. Magmatic ore deposits in mafic–ultramafic intrusions of the Giles Event, Western Australia. Ore Geol. Rev. 71, 405–436.
Maier, W.D., Halkoaho, T., Huhma, H., Hanski, E., Barnes, S.-J., 2018a. The Penikat intrusion, Finland: geochemistry, geochronology, and origin of platinum–palladium reefs. J. Petrol. 59, 967–1006.
Maier, W.D., Prevec, S.A., Scoates, J.S., Wall, C.J., Barnes, S.-J., Gomwe, T., 2018b. The Uitkomst intrusion and Nkomati Ni-Cu-Cr-PGE deposit, South Africa: trace element geochemistry, Nd isotopes and high-precision geochronology. Mineral. Deposita 53, 67–88.
Maier, W.D., Abernethy, K.E.L., Grobler, D.F., Moorhead, G., 2020. Formation of the Flatreef deposit, northern Bushveld, by hydrodynamic and hydromagmatic processes. Mineral. Deposita 56, 11–30.
Maier, W.D., Barnes, S.-J., Muir, D., Savard, D., Lahaye, Y., Smith, W.D., 2021. Formation of Bushveld anorthosite by reactive porous flow. Contrib. Mineral. Petrol. 176, 3.
Maier, W.D., Barnes, S.-J., Smith, W.D., 2023. Petrogenesis of the Mesoarchaean Stella layered intrusion, South Africa: implications for the origin of PGE reefs in the upper portion of layered intrusions. Mineral. Deposita 1–21.
Mangler, M.F., Humphreys, M.C.S., Wadsworth, F.B., Iveson, A.A., Higgins, M.D., 2022. Variation of plagioclase shape with size in intermediate magmas: a window into incipient plagioclase crystallisation. Contrib. Mineral. Petrol. 177, 64.
Manoochehri, S., Schmidt, M.W., 2014. Settling and compaction of chromite cumulates employing a centrifuging piston cylinder and application to layered mafic intrusions. Contrib. Mineral. Petrol. 168, 1091.
Mansur, E.T., Ferreira Filho, C.F., Oliveira, D.P.L., 2020. The Luanga deposit, Carajas ´ Mineral Province, Brazil: different styles of PGE mineralization hosted in a mediumsize layered intrusion. Ore Geol. Rev. 118, 103340.
Mao, Y.-J., Schoneveld, L., Barnes, S.J., Williams, M.J., Su, B.-X., Ruprecht, P., Evans, N. J., Qin, K.-Z., 2022. Coupled Li-P zoning and trace elements of olivine from magmatic Ni-Cu deposits: Implications for postcumulus re-equilibration in olivine. J. Petrol. 63 egac018.
Marks, M.A.W., Hettmann, K., Schilling, J., Frost, B.R., Markl, G., 2011. The mineralogical diversity of alkaline igneous rocks: critical factors for the transition from miaskitic to agpaitic phase assemblages. J. Petrol. 52, 439–455.
Marques, J.C., Dias, J.R.P., Friedrich, B.M., Frantz, J.C., Queiroz, W.J.A., Botelho, N.F., 2017. Thick chromitite of the Jacurici complex (NE Craton Sao ˜ Francisco, Brazil): Cumulate chromite slurry in a conduit. Ore Geol. Rev. 90, 131–147. Marsh, B.D., 1996. Solidification fronts and magmatic evolution. Mineral. Mag. 60, 5–40. Marsh, B.D., 2006. Dynamics of magmatic systems. Elements 2, 287–292.
Marsh, B.D., 2013. On some fundamentals of igneous petrology. Contrib. Mineral. Petrol. 166, 665–690.
Marsh, B.D., 2015. Magmatism, magma, and magma chambers. Treat. Geophys. 273–323.
Marsh, E., Anderson, E., 2011. Ni-Co Laterite Deposits. US Geological Survey Open-File Report, 1259.

Marsh, J.S., Pasecznyk, M.J., Boudreau, A.E., 2021. Formation of chromitite seams and associated anorthosites in layered intrusion by reactive volatile-rich fluid infiltration. J. Petrol. 62, 1–23.
Martin, D., 1990. Crystal settling and *in situ* crystallization in aqueous solutions and magma chambers. Earth Planet. Sci. Lett. 96, 336–348.
Martin, D., Nokes, R., 1988. Crystal settling in a vigorously convecting magma chamber. Nature (London) 332, 534–536.
Martin, D., Griffiths, R.W., Campbell, I.H., 1987. Compositional and thermal convection in magma chambers. Contrib. Mineral. Petrol. 96, 465–475.
Mathez, E.A., 1995. Magmatic metasomatism and formation of the Merensky reef, Bushveld complex. Contrib. Mineral. Petrol. 119, 277–286.
Mathez, E.A., Kinzler, R.J., 2017. Metasomatic chromitite seams in the Bushveld and Rum layered intrusions. Elements 13, 397–402. Mathieu, L., 2019. Origin of the vanadiferous serpentine–magnetite rocks of the Mt. Sorcerer Area, Lac Dor´e layered intrusion, Chibougamau, Qu´ebec. Geosciences 9, 110.
Mathison, C.I., 1987. Pyroxene oikocrysts in troctolitic cumulates - evidence for supercooled crystallisation and postcumulus modification. Contrib. Mineral. Petrol. 97, 228–236.
Maxeiner, R.O., Rayner, N.M., 2017. Geology, U–Pb zircon geochronology, and geochemistry of PGE-bearing Neoarchean and Paleoproterozoic gabbroic rocks of the Peter Lake domain, southern Hearne craton, Canada. Can. J. Earth Sci. 54, 587–608.
McBirney, A.R., 1987. Constitutional zone refining of layered intrusions. In: Parsons, I. (Ed.), Origins of Igneous Layering. D. Reidel Publishing Company, pp. 437–452.
McBirney, A.R., 1995. Mechanisms of differentiation in the Skaergaard Intrusion. J. Geol. Soc. Lond. 152, 421–435.
McBirney, A.R., 2009. Factors governing the textural development of Skaergaard gabbros. Lithos 111, 1–5.
McBirney, A.R., Creaser, R.A., 2003. The Skaergaard layered series, part VII: Sr and Nd isotopes. J. Petrol. 44, 757–771.
McBirney, A.R., Hunter, R.H., 1995. The cumulate paradigm reconsidered. J. Geol. 103, 114–122.
McBirney, A.R., Nicolas, A., 1997. The Skaergaard layered series. Part II. Magmatic flow and dynamic layering. J. Petrol. 38, 569–580.
McBirney, A.R., Noyes, R.M., 1979. Crystallization and layering of the Skaergaard intrusion. J. Petrol. 20, 487–554.
McBirney, A.R., Sonnenthal, E.L., 1990. Metasomatic replacement in the Skaergaard intrusion, East Greenland: preliminary observations. Chem. Geol. 88, 245–260.
McBirney, A.R., White, C.M., Boudreau, A.E., 1990. Spontaneous development of concentric layering in a solidified siliceous dike, East Greenland. Earth Sci. Rev. 29, 321–330.
McCarthy, T.S., Cawthorn, R.G., Wright, C.J., McIver, J.R., 1985. Mineral layering in the Bushveld complex: implications of Cr abundances in magnetite from closely spaced magnetitite and intervening silicate-rich layers. Econ. Geol. 80, 1062–1074.
McCuaig, T.C., Beresford, S., Hronsky, J., 2010. Translating the mineral systems approach into an effective exploration targeting system. Ore Geol. Rev. 38, 128–138.
McDonald, I., Holwell, D.A., 2011. Geology of the Northern Bushveld Complex and the Setting and Genesis of the Platreef Ni-cu-PGE Deposit.
McDonald, I., Holwell, D.A., Armitage, P.E.B., 2005. Geochemistry and mineralogy of the Platreef and "critical Zone" of the northern lobe of the Bushveld complex, South Africa: implications for Bushveld stratigraphy and the development of PGE
mineralisation. Mineral. Deposita 40, 526–549.
McDonald, I., Harmer, R.E.J., Holwell, D.A., Hughes, H.S.R., Boyce, A.J., 2017. Cu-NiPGE mineralisation at the Aurora Project and potential for a new PGE province in the Northern Bushveld Main Zone. Ore Geol. Rev. 80, 1135–1159.
McKenzie, D., 1984. The generation and compaction of partially molten rock. J. Petrol. 25, 713–765.
McKenzie, D., 1985. The extraction of magma from the crust and mantle. Earth Planet. Sci. Lett. 74, 81–91.
McKenzie, D., 2011. Compaction and crystallization in magma chambers: towards a model of the Skaergaard Intrusion. J. Petrol. 52, 905–930.
Means, W.D., Park, Y., 1994. New experimental approach to understanding igneous texture. Geology 22, 323–326.
Meinert, L.D., Dipple, G.M., Nicolescu, S., 2005. World skarn deposits. Econ. Geol. 299–366, 100th Anniversary Volume.
Menand, T., Annen, C., de Saint Blanquat, M., 2015. Rates of magma transfer in the crust: Insights into magma reservoir recharge and pluton growth. Geology 43, 199–202.
Meshram, T.M., Nannaware, S.B., Nannaware, B., Bhatacharjee, S., Waghmare, M.M., Rajakumar, T., 2015. PGE distribution in the chromite bearing mafic-ultramafic Kondapalli Layered Complex, Krishna district, Andhra Pradesh, India. Open Geosci. 7.
Meurer, W.P., Boudreau, A.E., 1998. Compaction of igneous cumulates Part II: compaction and the development of igneous foliations. J. Geol. 106, 293–304. Meurer, W.P., Meurer, M.E.S., 2006. Using apatite to dispel the "trapped liquid" concept and to understand the loss of interstitial liquid by compaction in mafic cumulates: an example from the Stillwater complex, Montana. Contrib. Mineral. Petrol. 151, 187–201.
Meurer, W.P., Klaber, S., Boudreau, A.E., 1997. Discordant bodies from olivine-bearing zones III and IV of the Stillwater complex, Montana: evidence for postcumulus fluid migration and reaction in layered intrusions. Contrib. Mineral. Petrol. 130, 81–92.
Meyer, G.B., Wilson, J.R., 1999. Olivine-rich units in the Fongen–Hyllingen Intrusion, Norway: implications for magma chamber processes. Lithos 47, 157–179.
Miller, A.R., 2005. Metamorphosed Compositional Layering in the Ferguson Lake Intrusive Complex, Northwestern Hearne Domain, Western Churchill Province, Private Report. Starfield Resources Inc. SEDAR.COM filing.
Miller, A.R., 2007. A Contribution to the Geology of the Ferguson Lake Intrusive Complex (FLIC): A Metamorphosed Archean Ni-cu-PGE Bearing Leucocratic to Melanocratic Mafic-Ultramafic Layered Complex, Northwestern Hearne Subdomain, Western Churchill Province, Nunavut, Utiliz. Report, Starfield Resources Inc.. SEDAR.COM filing.
Miller, J.D., Ripley, E.M., 1996. Layered intrusions of the Duluth complex, Minnesota, USA. In: Developments in Petrology, vol. 15. Elsevier, pp. 257–301.
Miller, C.F., Wark, D.A., 2008. Supervolcanoes and their explosive supererruptions. Elements 4, 11–15.
Milman-Barris, M.S., Beckett, J.R., Baker, M.B., Hofmann, A.E., Morgan, Z., Crowley, M. R., Vielzeuf, D., Stolper, E., 2008. Zoning of phosphorus in igneous olivine. Contrib. Mineral. Petrol. 155, 739–765.
Mitchell, A.A., Scoon, R.N., 2007. The Merensky Reef at Winnaarshoek, Eastern Bushveld complex: a primary magmatic hypothesis based on a wide reef facies. Econ. Geol. 102, 971–1009.
Mitchell, A.A., Henckel, J., Mason-Apps, A., 2019. The Upper critical Zone of the Rustenburg Layered Suite in the Swartklip Sector, north-western Bushveld complex, on the farm Wilgerspruit 2JQ: I. Stratigraphy and PGE mineralization patterns. S. Afr. J. Geol. 122, 117–142.
Mithen, J.P., Sear, R.P., 2014. Epitaxial nucleation of a crystal on a crystalline surface. EPL (Europhysics Letters) 105, 18004.
Mokatse, T., 2017. Archean Boninite-like Mafic-Ultramafic Rocks from the Lechana Layered Intrusion, Motloutse Complex, Botswana. Doctoral dissertation. Botswana International University of Science & Technology, Botswana.
Mokchah, N., Mathieu, L., 2022. Origin and evolution of the iron-rich upper unit and Fe–Ti–V mineralization of the Neoarchean Lac Dor´e layered intrusion, Chibougamau, Qu´ebec. J. Petrol. 63 egac006. Molyneux, T.C., 1972. X-ray-data and chemical analysis of some titanomagnetite and ilmenite samples from the Bushveld complex, South Africa. Mineral. Mag. 38, 863–871.
Mondal, S.K., Mathez, E.A., 2007. Origin of the UG2 chromitite layer, Bushveld complex. J. Petrol. 48, 495–510.
Mondal, S.K., Zhou, M.-F., 2010. Enrichment of PGE through interaction of evolved boninitic magmas with early formed cumulates in a gabbro–breccia zone of the Mesoarchean Nuasahi massif (eastern India). Mineral. Deposita 45, 69–91.
Mondal, S.K., Baidya, T.K., Rao, K.N.G., Glascock, M.D., 2001. PGE and Ag mineralization in a breccia zone of the Precambrian Nuasahi ultramafic-mafic complex, Orissa, India. Can. Mineral. 39, 979–996.
Mondal, S.K., Ripley, E.M., Li, C., Frei, R., 2006. The genesis of Archean chromitites from the Nuasahi and Sukinda massifs in the Singhbhum Craton, India. Precambrian Res. 148, 45–66.
Morse, S.A., 1969. The Kiglapait layered intrusion, Labrador, 112. Geological Society of America, p. 146. Memoir.
Morse, S.A., 1973. The feldspar/magma density paradox. In: Morse, S.A. (Ed.), The Nain Anorthosite Project, Labrador: Field Report 1972. University of Massachusetts at Amherst, Amherst, MA, pp. 113–116.
Morse, S.A., 1979. Kiglapait geochemistry I: systematics, sampling, and density. J. Petrol. 20, 555–590.
Morse, S.A., 1980. Basalts and Phase Diagrams: An Introduction to the Quantitative Use of Phase Diagrams in Igneous Petrology. Springer-Verlag.
Morse, S.A., 1986. Convection in aid of adcumulus growth. J. Petrol. 27, 1183–1214.
Morse, S.A., 1988. Motion of crystals, solute, and heat in layered intrusions. Can. Mineral. 26, 209–224.
Morse, S.A., 2011. The fractional latent heat of crystallizing magmas. Am. Mineral. 96, 682–689.

Morse, S.A., 2015. Kiglapait Intrusion, Labrador. In: Charlier, B., Namur, O., Latypov, R., Tegner, C. (Eds.), Layered Intrusions. Springer Geology, Springer Netherlands, pp. 589–648.
Morse, S.A., Davidson, J.P., Tepley, F.J., O'Driscoll, B., Vantongeren, J.A., 2017. Plagioclase zonation: an archive of trapped liquid and crustal contamination. Elements 13, 403–408.
Mukherjee, R., Latypov, R., Balakrishna, A., 2017. An intrusive origin of some UG-1 chromitite layers in the Bushveld Igneous complex, South Africa: Insights from field relationships. Ore Geol. Rev. 90, 94–109.
Mungall, J., 2002. A model for co-precipitation of platinum-group minerals with chromite from silicate melts. In: 9th International Platinum Symposium, Abstract with Program, pp. 21–25.
Mungall, J.E., 2007. Crustal contamination of picritic magmas during transport through dikes: the Expo Intrusive Suite, Cape Smith Fold Belt, New Quebec. J. Petrol. 48, 1021–1039.
Mungall, J.E., Brenan, J.M., 2014. Partitioning of platinum-group elements and au between sulfide liquid and basalt and the origins of mantle-crust fractionation of the chalcophile elements. Geochim. Cosmochim. Acta 125, 265–289.
Mungall, J.E., Kamo, S.L., McQuade, S., 2016. U–Pb geochronology documents out-ofsequence emplacement of ultramafic layers in the Bushveld Igneous complex of South Africa. Nat. Commun. 7, 13385.
Mungall, J.E., Jenkins, M.C., Robb, S.J., Yao, Z., Brenan, J.M., 2020. Upgrading of magmatic sulfides, revisited. Econ. Geol. 115, 1827–1833. Mutanen, T., 2005. The Akanvaara intrusion and the Keivitsa – Satovaara Complex, with stops at Kaikkivaltiaanlehto and S¨ arkivaara intrusions. Geological Survey of Finland. Guide 51b.
Myerson, A.S., Erdemir, D., Lee, A.Y. (Eds.), 2019. Handbook of Industrial Crystallization, 3rd ed. Cambridge University Press.
Natural Resources Canada, 2021. Critical minerals. www.nrcan.gc.ca/our-natural-resour ces/minerals-mining/critical-minerals/23414.
Naldrett, A.J., 2004. Magmatic Sulfide Deposits: Geology, Geochemistry and Exploration. Springer, 728 pp.
Naldrett, A.J., Lehmann, J., 1988. Spinel non-stoichiometry as the explanation for Ni-, Cu-and PGE-enriched sulphides in chromitites. In: Geo-Platinum 87. Springer, pp. 93–109.
Naldrett, A.J., Wilson, A., Kinnaird, J., Chunnett, G., 2009. PGE tenor and metal ratios within and below the Merensky Reef, Bushveld complex: implications for its genesis. J. Petrol. 50, 625–659.
Naldrett, A.J., Wilson, A., Kinnaird, J., Yudovskaya, M., Chunnett, G., 2012. The origin of chromitites and related PGE mineralization in the Bushveld complex: new mineralogical and petrological constraints. Mineral. Deposita 47, 209–232.
Namur, O., Charlier, B., 2012. Efficiency of compaction and compositional convection during mafic crystal mush solidification: the Sept Iles layered intrusion, Canada. Contrib. Mineral. Petrol. 163, 1049–1068.
Namur, O., Humphreys, M.C.S., 2018. Trace element constraints on the differentiation and crystal mush solidification in the Skaergaard Intrusion, Greenland. J. Petrol. 59, 387–418.
Namur, O., Charlier, B., Toplis, M.J., Higgins, M.D., Li´ egeois, J.-P., Vander Auwera, J., 2010. Crystallization sequence and magma chamber processes in the ferrobasaltic Sept Iles layered intrusion, Canada. J. Petrol. 51, 1203–1236.
Namur, O., Charlier, B., Pirard, C., Hermann, J., Li´egeois, J.-P., Vander Auwera, J., 2011a. Anorthosite formation by plagioclase flotation in ferrobasalt and implications for the lunar crust. Geochim. Cosmochim. Acta 75, 4998–5018.
Namur, O., Charlier, B., Toplis, M.J., Higgins, M.D., Hounsell, V., Li´egeois, J.-P., Vander Auwera, J., 2011b. Differentiation of tholeiitic basalt to A-type granite in the Sept Iles layered intrusion, Canada. J. Petrol. 52, 487–539.
Namur, O., Charlier, B., Holness, M.B., 2012. Dual origin of Fe-Ti-P gabbros by immiscibility and fractional crystallisation of evolved tholeiitic basalts in the Sept Iles layered intrusion. Lithos 154, 100–114.
Namur, O., Humphreys, M.C.S., Holness, M.B., 2013. Lateral reactive infiltration in a vertical gabbroic crystal mush, Skaergaard intrusion, East Greenland. J. Petrol. 54, 985–1016.
Namur, O., Humphreys, M.C.S., Holness, M.B., 2014. Crystallization of interstitial liquid and latent heat buffering in solidifying gabbros: Skaergaard intrusion, Greenland. J. Petrol. 55, 1389–1427.
Namur, O., Abily, B., Boudreau, A.E., Blanchette, F., Bush, J.W.M., Ceuleneer, G., Charlier, B., Donaldson, C.H., Duchesne, J.-C., Higgins, M.D., Morata, D., Nielsen, T. F.D., O'Driscoll, B., Pang, K.N., Peacock, T., Spandler, C.J., Toramaru, A., Veksler, I. V., 2015a. Igneous layering in Basaltic Magma Chambers. In: Charlier, Bernard, Namur, Olivier, Latypov, R., Tegner, C. (Eds.), Layered Intrusions. Springer Netherlands, Dordrecht, pp. 75–152.
Namur, O., Higgins, M.D., Vander Auwera, J., 2015b. The Sept Iles intrusive suite, Quebec, Canada. In: Charlier, Bernard, Namur, Olivier, Latypov, R., Tegner, C. (Eds.), Layered Intrusions. Springer Netherlands, Dordrecht, pp. 465–515.
Naslund, H.R., 1984. Supersaturation and crystal growth in the roof-zone of the Skaergaard magma chamber. Contrib. Mineral. Petrol. 86, 89–93.
Naslund, H.R., McBirney, A.R., 1996. Mechanisms of formation of igneous layering. In: Cawthorn, R.G. (Ed.), Developments in Petrology, Layered Intrusions. Elsevier, pp. 1–43.
Nebel, O., Arculus, R.J., Ivanic, T.J., Rapp, R., Wills, K.J.A., 2013. Upper Zone of the Archean Windimurra layered mafic intrusion, Western Australia: insights into fractional crystallisation in a large magma chamber. N. Jb. Mineral. (Abh.) 191, 83–107.
Nebel, O., Sossi, P.A., Ivanic, T.J., B´enard, A., Gardiner, N.J., Langford, R.L., Arculus, R. J., 2020. Incremental growth of layered mafic-ultramafic intrusions through melt replenishment into a crystal mush zone traced by Fe-Hf isotope systematics. Front. Earth Sci. 8, 2.
Nicholson, D.M., Mathez, E.A., 1991. Petrogenesis of the Merensky Reef in the Rustenburg section of the Bushveld complex. Contrib. Mineral. Petrol. 107, 293–309.
Nielsen, T.F.D., 2004. The shape and volume of the Skaergaard intrusion, Greenland: implications for mass balance and bulk composition. J. Petrol. 45, 507–530. Nielsen, T.F.D., Andersen, J.C.Ø., Holness, M.B., Keiding, J.K., Rudashevsky, N.S., Rudashevsky, V.N., Salmonsen, L.P., Tegner, C., Veksler, I.V., 2015. The Skaergaard PGE and gold deposit: the result of *in situ* fractionation, sulphide saturation, and magma chamber-scale precious metal redistribution by immiscible Fe-rich melt. J. Petrol. 56, 1643–1676.
Nielsen, T.F.D., Brooks, C.K., Keiding, J.K., 2019. Bulk liquid for the Skaergaard Intrusion and its PGE-Au mineralization: Composition, correlation, liquid line of descent, and timing of sulphide saturation and silicate–silicate immiscibility. J. Petrol. 60, 1853–1880.
Norton, D., Taylor, H.P., Bird, D.K., 1984. The geometry and high-temperature brittle deformation of the Skaergaard Intrusion. J. Geophys. Res. 89, 10178–10192.
Oberthür, T., 2011. Platinum-group element mineralization of the main sulfide zone, Great Dyke, Zimbabwe. Rev. Econ. Geol. 17, 329–349.
O'Driscoll, B., VanTongeren, J.A. (Eds.), 2017a. Elements 13, 371. O'Driscoll, B., VanTongeren, J.A., 2017b. Layered intrusions: from petrological paradigms to precious metal repositories. Elements 13, 383–389.
O'Driscoll, B., Troll, V.R., Reavy, R.J., Turner, P., 2006. The Great Eucrite intrusion of Ardnamurchan, Scotland: reevaluating the ring-dike concept. Geology 34, 189–192.
O'Driscoll, B., Donaldson, C.H., Troll, V.R., Jerram, D.A., Emeleus, C.H., 2007a. An origin for harrisitic and granular olivine in the Rum Layered Suite, NW Scotland: a crystal size distribution study. J. Petrol. 48, 253–270. O'Driscoll, B., Hargraves, R.B., Emeleus, C.H., Troll, V.R., Donaldson, C.H., Reavy, R.J., 2007b. Magmatic lineations inferred from anisotropy of magnetic susceptibility fabrics in units 8, 9, and 10 of the Rum Eastern Layered Series, NW Scotland. Lithos 98, 27–44.
O'Driscoll, B., Day, J.M.D., Daly, J.S., Walker, R.J., McDonough, W.F., 2009a. Rheniumosmium isotopes and platinum-group elements in the Rum Layered Suite, Scotland: implications for Cr spinel seam formation and the composition of the Iceland mantle anomaly. Earth Planet. Sci. Lett. 286, 41–51. O'Driscoll, B., Donaldson, C.H., Daly, J.S., Emeleus, C.H., 2009b. The roles of melt infiltration and cumulate assimilation in the formation of anorthosite and a Cr-spinel seam in the Rum Eastern Layered Intrusion, NW Scotland. Lithos 111, 6–20.
O'Driscoll, B., Emeleus, C.H., Donaldson, C.H., Daly, J.S., 2010. Cr-spinel seam petrogenesis in the Rum Layered Suite, NW Scotland: cumulate assimilation and *in situ* crystallization in a deforming crystal mush. J. Petrol. 51, 1171–1201. O'Hara, M.J., 1998. Volcanic plumbing and the space problem—thermal and geochemical consequences of large-scale assimilation in ocean island development. J. Petrol. 39, 1077–1089.
Ortega, L., Millward, D., Luque, F.J., Barrenechea, J.F., Beyssac, O., Huizenga, J.-M., Rodas, M., Clarke, S.M., 2010. The graphite deposit at Borrowdale (UK): a catastrophic mineralizing event associated with Ordovician magmatism. Geochim. Cosmochim. Acta 74, 2429–2449.
Ortoleva, P., Merino, E., Moore, G., Chadam, J., 1987. Geochemical self-organization I: reaction-transport feedbacks and modeling approach. Am. J. Sci. 287, 979–1007.

Osterero, L., Boudon, G., Balcone-Boissard, H., Morgan, D.J., d'Augustin, Solaro C.,2021. Time-window into the transcrustal plumbing system dynamics of Dominica (Lesser Antilles). Sci. Rep. 11, 11440. Palacz, Z.A., 1985. Sr-Nd-Pb isotopic evidence for crustal contamination in the Rhum intrusion. Earth Planet. Sci. Lett. 74, 35–44.
Pang, K.-N., Zhou, M.-F., Lindsley, D., Zhao, D., Malpas, J., 2008. Origin of Fe-Ti oxide ores in mafic intrusions: evidence from the Panzhihua intrusion, SW China. J. Petrol. 49, 295–313.
Parker, A.P., Clay, P.L., Boudreau, A.E., Burgess, R., O'Driscoll, B., 2022. Magmatic volatiles and platinum-group element mineralization in the Stillwater layered intrusion, U.S.a. Am. Mineral. 107, 797–814.
Parsons, I., 1987. Origins of Igneous Layering. In: Nato Science Series C. Springer, Dordrecht, 687 pp.
Paulick, H., Rosa, D., Kalvig, P., 2015. In: Keiding, J.K., Kalvig, P. (Eds.), Rare earth element projects and exploration potential in Greenland, 2. MiMa Rapp.
Peltonen, P., 1995. Petrogenesis of ultramafic rocks in the Vammala Nickel Belt: implications for crustal evolution of the early Proterozoic Svecofennian arc terrane. Lithos 34, 253–274.
Petford, N., Lister, J.R., Kerr, R.C., 1994. The ascent of felsic magmas in dykes. Lithos 32, 161–168.
Pettigrew, N.T., Hattori, K.H., 2002. Palladium–copper-rich platinum-group element mineralization in Legris Lake mafic–ultramafic complex, Western Superior Province, Canada. Appl. Earth Sci. 111, 46–57.
Philpotts, A.R., 1981. Liquid immiscibility in silicate melt inclusions in plagioclase phenocrysts. Bull. Mineral. 104, 317–324.
Philpotts, A.R., 1982. Compositions of immiscible liquids in volcanic rocks. Contrib. Mineral. Petrol. 80, 201–218.
Philpotts, A.R., 1998. Nature of a flood-basalt-magma reservoir based on the compositional variation in a single flood-basalt flow and its feeder dike in the Mesozoic Hartford Basin, Connecticut. Contrib. Mineral. Petrol. 133, 69–82.
Philpotts, A.R., Dickson, L.D., 2000. The formation of plagioclase chains during convective transfer in basaltic magma. Nature 406, 59–61.
Philpotts, A.R., Doyle, C.D., 1983. Effect of magma oxidation state on the extent of silicate liquid immiscibility in a tholeiitic basalt. Am. J. Sci. 283, 967–986.
Philpotts, A.R., Philpotts, D.E., 2005. Crystal-mush compaction in the Cohassett floodbasalt flow, Hanford, Washington. J. Volcanol. Geotherm. Res. 145, 192–206.
Philpotts, A.R., Shi, J., Brustman, C., 1998. Role of plagioclase crystal chains in the differentiation of partly crystallized basaltic magma. Nature 395, 343–346.
Philpotts, A.R., Brustman, C.M., Shi, J., Carlson, W.D., Denison, C., 1999. Plagioclasechain networks in slowly cooled basaltic magma. Am. Mineral. 84, 1819–1829.
Pin, C., Fonseca, P.E., Paquette, J.-L., Castro, P., Matte, P., 2008. The ca. 350 Ma Beja Igneous complex: a record of transcurrent slab break-off in the Southern Iberia Variscan Belt? Tectonophysics 461, 356–377.
Pina, ˜ R., 2019. The Ni-Cu-(PGE) Aguablanca Ore Deposit (SW Spain). Springer, 78 pp.
Pina, ˜ R., Lunar, R., Ortega, L., Gervilla, F., Alapieti, T., Martínez, C., 2006. Petrology and geochemistry of mafic-ultramafic fragments from the Aguablanca Ni-Cu ore breccia, Southwest Spain. Econ. Geol. 101, 865–881.
Pina, ˜ R., Romeo, I., Ortega, L., Lunar, R., Capote, R., Gervilla, F., Tejero, R., Quesada, C., 2010. Origin and emplacement of the Aguablanca magmatic Ni-Cu-(PGE) sulfide deposit, SW Iberia: a multidisciplinary approach. Bulletin 122, 915–925.
Ping, X., Wang, X., Zheng, J., Liu, Y., Su, Y., Chen, H., Ai, L., 2022. The stable chromium isotope composition of different mantle reservoirs. Geochim. Cosmochim. Acta 338, 24–33.
Plank, T., Kelley, K.A., Zimmer, M.M., Hauri, E.H., Wallace, P.J., 2013. Why do mafic arc magmas contain~ 4 wt% water on average? Earth Planet. Sci. Lett. 364, 168–179.
Pouliquen, G., Key, R.M., Walker, A., 2008. The internal structure and geotectonic setting of the Xade and Tsetseng complexes in the western most part of the Kaapvaal Craton. S. Afr. J. Geol. 111, 345–356.
Prendergast, M.D., 2000. Layering and precious metals mineralization in the; Rincon ´ del Tigre complex, Eastern Bolivia. Econ. Geol. 95, 113–130.
Prendergast, M.D., 2008. Archean komatiitic sill-hosted chromite deposits in the Zimbabwe Craton. Econ. Geol. 103, 981–1004.
Prendergast, M.D., 2021. Variant Offset-Type platinum Group Element Reef Mineralization in Basal Olivine Cumulates of the Kapalagulu Intrusion, Western Tanzania. Econ. Geol. 116, 1011–1033.
Presnall, D.C., Dixon, S.A., Dixon, J.R., O'Donnell, T.H., Brenner, N.L., Schrock, R.L.,
Dycus, D.W., 1978. Liquidus phase relations on the join diopside-forsterite-anorthite from 1 atm to 20 kbar: their bearing on the generation and crystallization of basaltic magma. Contrib. Mineral. Petrol. 66, 203–220.
Prichard, H.M., Mondal, S.K., Mukherjee, R., Fisher, P.C., Giles, N., 2018. Geochemistry and mineralogy of Pd in the magnetitite layer within the upper gabbro of the Mesoarchean Nuasahi Massif (Orissa, India). Mineral. Deposita 53, 547–564.
Pronost, J., Harris, C., Pin, C., 2008. Relationship between footwall composition, crustal contamination, and fluid–rock interaction in the Platreef, Bushveld complex, South Africa. Mineral. Deposita 43, 825–848.
Pupier, E., Duchene, S., Toplis, M.J., 2008. Experimental quantification of plagioclase crystal size distribution during cooling of a basaltic liquid. Contrib. Mineral. Petrol. 155, 555–570.
Qian, R.-Y., Botsaris, G.D., 1997. A new mechanism for nuclei formation in suspension crystallizers: the role of interparticle forces. Chem. Eng. Sci. 52, 3429–3440.
Rao, C.V.D., Santosh, M., 2011. Continental arc magmatism in a Mesoproterozoic convergent margin: petrological and geochemical constraints from the magmatic suite of Kondapalle along the eastern margin of the Indian plate. Tectonophysics 510, 151–171.
Reynolds, I.M., 1985. The nature and origin of titaniferous magnetite-rich layers in the upper zone of the Bushveld complex; a review and synthesis. Econ. Geol. 80, 1089–1108.
Richter, F.M., McKenzie, D., 1984. Dynamical models for melt segregation from a deformable matrix. J. Geol. 92, 729–740.
Rios, K.L., Feineman, M.D., Bybee, G.M., 2016. Iron isotope fractionation in the Bushveld Igneous complex provide insight into fractional crystallization. In: AGU Fall Meeting Abstracts, vol. 2016 pp. V51A–3058.
Ripley, E.M., Li, C., 2018. Metallic ore deposits associated with mafic to ultramafic igneous rocks. In: Processes and Ore Deposits of Ultramafic-Mafic Magmas through Space and Time. Elsevier, pp. 79–111.
Ripley, E.M., Severson, M.J., Hauck, S.A., 1998. Evidence for sulfide and Fe-Ti-P-rich liquid immiscibility in the Duluth complex, Minnesota. Econ. Geol. 93, 1052–1062.
Ripley, E.M., Brophy, J.G., Li, C., 2002. Copper solubility in a basaltic melt and sulfide liquid/silicate melt partition coefficients of Cu and Fe. Geochim. Cosmochim. Acta 66, 2791–2800.
Robertson, J.C., Ripley, E.M., Barnes, S.J., Li, C., 2015. Sulfur liberation from country rocks and incorporation in mafic magmas. Econ. Geol. 110, 1111–1123.
Robins, B., 1972. Crescumulate layering in a gabbroic body on Seiland, northern Norway. Geol. Mag. 109, 533–542.
Roedder, E.W., 1951. Low temperature liquid immiscibility field in the system K_2O-FeOAl$_2O_3$-SiO_2. Am. Mineral. 36, 282–286.
Roedder, E., Weiblen, P.W., 1970. Lunar petrology of silicate melt inclusions, Apollo 11 rocks. Proceedings of the Apollo 11 Lunar Science Conference. Geochim. Cosmochim. Acta 1 (Suppl. 1), 801–837.
Roeder, P., Gofton, E., Thornber, C., 2006. Cotectic Proportions of Olivine and Spinel in Olivine-Tholeiitic Basalt and Evaluation of Pre-Eruptive Processes. J. Petrol. 47, 883–900.
Roelofse, F., Ashwal, L.D., 2012. The lower Main Zone in the Northern Limb of the Bushveld complex - a >1.3 km thick sequence of intruded and variably contaminated crystal mushes. J. Petrol. 53, 1449–1476.
Ross, P.-S., Ukstins Peate, I., McClintock, M.K., Xu, Y.G., Skilling, I.P., White, J.D.L., Houghton, B.F., 2005. Mafic volcaniclastic deposits in flood basalt provinces: a review. J. Volcanol. Geotherm. 145, 281–314.
Ryabov, V.V., Lapkovsky, A.A., 2010. Native iron (- platinum) ores from the Siberian Platform trap intrusions. Aust. J. Earth Sci. 57, 707–736.
S´ a, J.H.S., Barnes, S.-J., Prichard, H.M., Fisher, P.C., 2005. The distribution of base metals and platinum-group elements in magnetitite and its host rocks in the Rio Jacar´ e Intrusion, Northeastern Brazil. Econ. Geol. 100, 333–348.
de Saint Blanquat, M., Horsman, E., Habert, G., Morgan, S., Vanderhaeghe, O., Law, R., Tikoff, B., 2011. Multiscale magmatic cyclicity, duration of pluton construction, and the paradoxical relationship between tectonism and plutonism in continental arcs. Tectonophysics 500, 20–33.
Saleeby, J.B., 1992. Age and tectonic setting of the Duke Island ultramafic intrusion, Southeast Alaska. Can. J. Earth Sci. 29, 506–522.

Salmonsen, L.P., Tegner, C., 2013. Crystallization sequence of the Upper Border Series of the Skaergaard Intrusion: revised subdivision and implications for chamber-scale magma homogeneity. Contrib. Mineral. Petrol. 165, 1155–1171.
Sappin, A.-A., Constantin, M., Clark, T., 2011. Origin of magmatic sulfides in a Proterozoic island arc—an example from the Portneuf–Mauricie Domain, Grenville Province, Canada. Mineral. Deposita 46, 211–237.
Schiavi, F., Walte, N., Keppler, H., 2009. First *in situ* observation of crystallization processes in a basaltic-andesitic melt with the moissanite cell. Geology 37, 963–966.
Schleicher, J.M., Bergantz, G.W., 2017. The mechanics and temporal evolution of an open-system magmatic intrusion into a crystal-rich magma. J. Petrol. 58, 1059–1072.
Schmidt, E.R., 1952. The structure and composition of the Merensky reef and associated rocks on the Rustenburg platinum mine. S. Afr. J. Geol. 55, 233–279.
Schmidt, M.W., Forien, M., Solferino, G., Bagdassarov, N., 2012. Settling and compaction of olivine in basaltic magmas: an experimental study on the time scales of cumulate formation. Contrib. Mineral. Petrol. 164, 959–976.
Schoenberg, R., Kruger, F.J., N¨ agler, T.F., Meisel, T., Kramers, J.D., 1999. PGE enrichment in chromitite layers and the Merensky Reef of the western Bushveld complex; a Re-Os and Rb-Sr isotope study. Earth Planet. Sci. Lett. 172, 49–64.
Schoenberg, R., Zink, S., Staubwasser, M., Von Blanckenburg, F., 2008. The stable Cr isotope inventory of solid Earth reservoirs determined by double spike MC-ICP-MS. Chem. Geol. 249, 294–306.
Schofield, N., Alsop, I., Warren, J., Underhill, J.R., Lehn´ e, R., Beer, W., Lukas, V., 2014. Mobilizing salt: Magma-salt interactions. Geology 42, 599–602.
Schoneveld, L.E., Barnes, S.J., Makkonen, H.V., Le Vaillant, M., Paterson, D.J., Taranovic, V., Wang, K.-Y., Mao, Y.-J., 2020. Zoned pyroxenes as prospectivity indicators for magmatic Ni-Cu sulfide mineralization. Front. Earth Sci. 8.
Schulte, R.F., Taylor, R.D., Piatak, N.M., Seal, R.R., 2010. Stratiform Chromite Deposit Model. US Department of the Interior, US Geological Survey.
Schwindinger, K.R., Anderson, A.T., 1989. Synneusis of Kilauea Iki olivines. Contrib. Mineral. Petrol. 103, 187–198.
Scoates, J.S., 2000. The plagioclase-magma density paradox re-examined and the crystallisation of Proterozoic anorthosites. J. Petrol. 41, 627–649.
Scoates, J.S., Wall, C.J., Friedman, R.M., Weis, D., Mathez, E.A., VanTongeren, J.A., 2021. Dating the Bushveld complex: timing of crystallization, duration of magmatism, and cooling of the world's largest layered intrusion and related rocks. J. Petrol. 62, 1–39.
Scoon, R.N., Costin, G., 2018. Chemistry, morphology and origin of magmatic-reaction chromite stringers associated with anorthosite in the Upper critical Zone at Winnaarshoek, Eastern Limb of the Bushveld complex. J. Petrol. 59, 1551–1578.
Scoon, R.N., Mitchell, A.A., 2012. The Upper Zone of the Bushveld complex at Roossenekal, South Africa: geochemical stratigraphy and evidence of multiple episodes of magma replenishment. S. Afr. J. Geol. 115, 515–534. Scott, D.R., Stevenson, D.J., 1984. Magma solitons. Geophys. Res. Lett. 11, 1161–1164.
Scott, D.R., Stevenson, D.J., 1986. Magma ascent by porous flow. J. Geophys. Res. Solid. 91, 9283–9296.
Seat, Z., Beresford, S.W., Grguric, B.A., Waugh, R.S., Hronsky, J., Gee, M.A., Groves, D.I., Mathison, C.I., 2007. Architecture and emplacement of the Nebo–Babel gabbronorite-hosted magmatic Ni–Cu–PGE sulphide deposit, West Musgrave, Western Australia. Mineral. Deposita 42, 551–581.
Seedhouse, J.K., Donaldson, C.H., 1996. Compositional convection caused by olivine crystallization in a synthetic basalt melt. Mineral. Mag. 60, 115–130.
Sen, G., Presnall, D.C., 1984. Liquidus phase relationships on the join anorthiteforsterite-quartz at 10 kbar with applications to basalt petrogenesis. Contrib. Mineral. Petrol. 85, 404–408.
Setera, J.B., VanTongeren, J.A., 2018. Lateral variability in the Upper Main Zone, Bushveld complex, owing to directional magma recharge and emplacement from north to south. J. Petrol. 59, 1763–1786.
Sharpe, M.R., 1985. Strontium isotope evidence for preserved density stratification in the main zone of the Bushveld complex, South Africa. Nature 316, 119–126.
Shea, T., Hammer, J.E., 2013. Kinetics of cooling- and decompression-induced crystallisation in hydrous mafic-intermediate magmas. J. Volcanol. Geotherm. Res. 260, 127–145.
Shea, T., Hammer, J.E., Hellebrand, E., Mourey, A.J., Costa, F., First, E.C., Lynn, K.J., Melnik, O., 2019. Phosphorus and aluminum zoning in olivine: contrasting behavior of two nominally incompatible trace elements. Contrib. Mineral. Petrol. 174, 85.
Shepherd, K., Namur, O., Toplis, M.J., Devidal, J.L., Charlier, B., 2022. Trace element partitioning between clinopyroxene, magnetite, ilmenite and ferrobasaltic to dacitic magmas: an experimental study on the role of oxygen fugacity and melt composition. Contrib. Mineral. Petrol. 177, 90.
Shirley, D.N., 1986. Compaction of igneous cumulates. J. Geol. 94, 795–809.
Simandl, G.J., Paradis, S., 2022. Vanadium as a critical material: economic geology with emphasis on market and the main deposit types. Appl. Earth Sci. 1–19.
Simkin, T., 1967. Flow differentiation in the picritic sills of North Skye. In: Wyllie, P.J. (Ed.), Ultramafic and Related Rocks. John Wiley and Sons, New York London Sydney, pp. 64–67.
Simkin, T., 1993. Terrestrial Volcanism in Space and Time. Annu. Rev. Earth Planet. Sci. 21, 427–452.
Smith, D.S., Basson, I.J., 2006. Shape and distribution analysis of Merensky Reef potholing, Northam platinum Mine, western Bushveld complex: implications for pothole formation and growth. Mineral. Deposita 41, 281–295.
Smith, W.D., Maier, W.D., 2021. The geotectonic setting, age and mineral deposit inventory of global layered intrusions. Earth Sci. Rev. 220, 103736.
Smith, W.D., Maier, W.D., Bliss, I., 2020. Contact-style magmatic sulphide mineralisation in the Labrador Trough, northern Quebec, Canada: implications for regional prospectivity. Can. J. Earth Sci. 57, 867–883.
Smith, W.D., Maier, W., Barnes, S., Moorhead, G., Reid, D., Karykowski, B., 2021a. Element mapping the Merensky Reef of the Bushveld complex. Geosci. Front. 12, 101101.
Smith, W.D., Maier, W.D., Bliss, I., 2021b. The geology, geochemistry, and petrogenesis of the Huckleberry Cu-Ni-PGE prospect in the Labrador Trough, Canada: Perspectives for regional prospectivity. Ore Geol. Rev. 128, 103905.
Smith, W.D., Maier, W.D., Muir, D.D., Andersen, J.C., Williams, B.J., Henry, H., 2022. New perspectives on the formation of the Boulder Bed of the western Bushveld complex, South Africa. Mineral. Deposita 1–22.
Sossi, P.A., Foden, J.D., Halverson, G.P., 2012. Redox-controlled iron isotope fractionation during magmatic differentiation: an example from the Red Hill intrusion, S. Tasmania. Contrib. Mineral. Petrol. 164, 757–772.
Sotiriou, P., Polat, A., Frei, R., Yang, X.-M., van Vessem, J., 2020. Evidence for Neoarchean hydrous arc magmatism, the anorthosite-bearing Mayville Intrusion, western Superior Province, Canada. Lithos 362, 105482.
Spandler, C.J., Eggins, S.M., Arculus, R.J., Mavrogenes, J.A., 2000. Using melt inclusions to determine parent-magma compositions of layered intrusions: Application to the Greenhills complex (New Zealand), a platinum-group minerals–bearing, island-arc intrusion. Geology 28, 991–994.
Spandler, C., Mavrogenes, J., Arculus, R., 2005. Origin of chromitites in layered intrusions: evidence from chromite-hosted melt inclusions from the Stillwater complex. Geology 33, 893–896.
Sparks, R.S.J., Kerr, R.C., McKenzie, D.P., Tait, S.R., 1985. Postcumulus processes in layered intrusions. Geol. Mag. 122, 555–568.
Sparks, R.S.J., Annen, C., Blundy, J.D., Cashman, K.V., Rust, A.C., Jackson, M.D., 2019. Formation and dynamics of magma reservoirs. Phil. Trans. R. Soc. A 377, 20180019.
Spillar, ˇ V., Dolejˇs, D., 2015. Heterogeneous nucleation as the predominant mode of crystallization in natural magmas: numerical model and implications for crystal–melt interaction. Contrib. Mineral. Petrol. 169.
Stanley, C.R., Russell, J.K., 1989. Petrologic hypothesis testing with Pearce element ratio diagrams: derivation of diagram axes. Contrib. Mineral. Petrol. 103, 78–89.
Stausberg, N., Lesher, C.E., Hoffmann-Barfod, G., Glessner, J.J., Tegner, C., 2014. Iron isotope systematics of the Bushveld Complex, South Africa: Initial results. In: AGU Fall Meeting Abstracts V51C-4798.
Stewart, B.W., DePaolo, D.J., 1990. Isotopic studies of processes in mafic magma chambers: II. The Skaergaard intrusion, East Greenland. Contrib. Mineral. Petrol. 104, 125–141.
Stewart, B.W., DePaolo, D.J., 1992. Diffusive isotopic contamination of mafic magma by coexisting silicic liquid in the Muskox intrusion. Science 255, 708–711.
Stone, D., Lavigne, M.J., Schnieders, B., Scott, J., Wagner, D., 2003. Regional geology of the Lac des Iles area. Open file report 6120.
Stowe, C.W., 1994. Compositions and tectonic settings of chromite deposits through time. Econ. Geol. 89, 528–546.

Svensen, H., Planke, S., Polozov, A.G., Schmidbauer, N., Corfu, F., Podladchikov, Y.Y., Jamtveit, B., 2009. Siberian gas venting and the end-Permian environmental crisis. Earth Planet. Sci. Lett. 277, 490–500.
Svensen, H.H., Polteau, S., Cawthorn, G., Planke, S., 2014. Sub-volcanic Intrusions in the Karoo Basin, South Africa. In: Breitkreuz, C., Rocchi, S. (Eds.), Physical Geology of Shallow Magmatic Systems. Springer International Publishing, Cham, pp. 349–362.
Svensen, H., Fristad, K.E., Polozov, A.G., Planke, S., 2015. Volatile generation and release from continental large igneous provinces. In: Schmidt, A., Fristad, K., ElkinsTanton, L. (Eds.), Volcanism and Global Environmental Change. Cambridge University Press, pp. 177–192.
Svensen, H.H., Jerram, D.A., Polozov, A.G., Planke, S., Neal, C.R., Augland, L.E., Emeleus, H.C., 2019. Thinking about LIPs: a brief history of ideas in large igneous province research. Tectonophysics 760, 229–251.
Swager, C.P., 1997. Structural evolution of greenstone terranes in the southern Eastern Goldfields, Western Australia in Kalgoorlie'97: An International Conference on Crustal Evolution, Metallogeny and Exploration of the Yilgarn Craton–An Update, Extended Abstracts, 49–53; Cassidy, CF et al. Aust. Geol. Surv. Organ. Rec. 41.
Tait, S., Jaupart, C., 1992. Compositional convection in a reactive crystalline mush and melt differentiation. J. Volcanol. Geotherm. Res. 97, 6735–6756.
Talusani, R.V.R., Sivell, W.J., Ashley, P.M., 2005. Mineral chemistry, petrogenesis, and tectonic setting of the Wateranga layered intrusion, Southeast Queensland, Australia. Can. J. Earth Sci. 42, 1967–1985.
Tanner, D., McDonald, I., Harmer, R.E.J., Muir, D.D., Hughes, H.S.R., 2019. A record of assimilation preserved by exotic minerals in the lowermost platinum-group element deposit of the Bushveld complex: the Volspruit Sulphide Zone. Lithos 324, 584–608.
Taranovic, V., Barnes, S.J., Beresford, S., Williams, M., MacRae, C., Schoneveld, L.E., 2022. Nova-Bollinger Ni-Cu sulfide ore deposits, Fraser zone, Western Australia: Petrogenesis of the host intrusions. Econ. Geol. 117, 455–484.
Taubeneck, W.H., Poldervaart, A., 1960. Geology of the Elkhorn Mountains, Northeastern Oregon: part 2, Willow Lake Intrusion. Bull. Geol. Soc. Am. 71, 1295–1322.
Tegner, C., Wilson, J.R., Cawthorn, R.G., 1994. The dunite-clinopyroxenite pegmatoidal pipe, Tweefontein, eastern Bushveld complex, South Africa. S. Afr. J. Geol. 97, 415–430.
Tegner, C., Robins, B., Sorensen, H., 1996. Crystallization from stratified magmas in the Honningsvåg Intrusive Suite, northern Norway: a reappraisal. Mineral. Mag. 60, 41–51.
Tegner, C., Robins, B., Reginiussen, H., Grundvig, S., 1999. Assimilation of crustal xenoliths in a basaltic magma chamber: Sr and Nd isotopic constraints from the Hasvik Layered Intrusion, Norway. J. Petrol. 40, 363–380.
Tegner, C., Cawthorn, R.G., Kruger, F.J., 2006. Cyclicity in the Main and Upper zones of the Bushveld complex, South Africa: crystallization from a zoned magma sheet. J. Petrol. 47, 2257–2279.
Tegner, C., Thy, P., Holness, M.B., Jakobsen, J.K., Lesher, C.E., 2009. Differentiation and compaction in the Skaergaard intrusion. J. Petrol. 50, 813–840.
Teng, F.Z., Li, W.Y., Ke, S., Marty, B., Dauphas, N., Huang, S., Wu, F.Y., Pourmand, A., 2010. Magnesium isotopic composition of the Earth and chondrites. Geochim. Cosmochim. Acta 74, 4150–4166.
Tepley, F.J., Davidson, J.P., 2003. Mineral-scale Sr-isotope constraints on magma evolution and chamber dynamics in the Rum layered intrusion, Scotland. Contrib. Mineral. Petrol. 145, 628–641.
Tharp, T.M., Loucks, R.R., Sack, R.O., 1998. Modeling compaction of olivine cumulates in the Muskox intrusion. Am. J. Sci. 298, 758–790.
Th´eriault, R.D., Barnes, S.-J., 1998. Compositional variations in Cu-Ni-PGE sulfides of the Dunka Road deposit, Duluth complex, Minnesota: the importance of combined assimilation and magmatic processes. Can. Mineral. 36, 869–886.
Therriault, A.M., Fowler, A.D., Grieve, R.A.F., 2002. The Sudbury Igneous complex: a differentiated impact melt sheet. Econ. Geol. 97, 1521–1540.
Thompson, R.N., Patrick, D.J., 1968. Folding and slumping in a layered gabbro. Geol. J. 6, 139–146.
Thordarson, T., Self, S., 1998. The Roza Member, Columbia River Basalt Group - a gigantic pahoehoe lava flow field formed by endogenous processes. J. Geophys. Res. Solid. 103, 27411–27445.
Thy, P., Lesher, C.E., Tegner, C., 2009. The Skaergaard liquid line of descent revisited. Contrib. Mineral. Petrol. 157, 735–747.
Tian, H.C., Zhang, C., Teng, F.Z., Long, Y.J., Li, S.G., He, Y., Yang, W., 2020. Diffusiondriven extreme Mg and Fe isotope fractionation in Panzhihua ilmenite: Implications for the origin of mafic intrusion. Geochim. Cosmochim. Acta 278, 361–375.
Toplis, M.J., Carroll, M.R., 1995. An experimental study of the influence of oxygen fugacity on Fe-Ti oxide stability, phase relations, and mineral-melt equilibria in ferro-basaltic systems. J. Petrol. 36, 1137–1170.
Toplis, M.J., Brown, W.L., Pupier, E., 2008. Plagioclase in the Skaergaard intrusion. Part 1: core and rim compositions in the layered series. Contrib. Mineral. Petrol. 155, 329–340.
Tornos, F., Casquet, C., Galindo, C., Velasco, F., Canales, A., 2001. A new style of Ni-Cu mineralization related to magmatic breccia pipes in a transpressional magmatic arc, Aguablanca, Spain. Mineral. Deposita 36, 700–706.
Tucker, R.D., Boyd, R., Barnes, S.-J., 1990. A U-Pb zircon age for the Råna intrusion, N. Norway: new evidence of basic magmatism in the Scandinavian Caledonides in Early Silurian time. Nor. J. Geol. Geol. Tidsskr. 70, 229–239.
UK Department for Business, E.& I.S, 2022. UK Critical Minerals Strategy. www.gov. uk/government/publications/uk-critical-mineral-strategy.
Ulff-Møller, F., 1985. Solidification history of the Kitdlidt lens: immiscible metal and sulphide liquids from a basaltic dyke on Disko, central West Greenland. J. Petrol. 26, 64–91.
Ulmer, G.C., 1969. Experimental investigations of chromite spinels. Econ. Geol. Monogr. 4, 114–131.
Van der Merwe, M.J., 2007. The occurrence of the critical zone along the exposed southeastern sector of the eastern Bushveld complex. S. Afr. J. Geol. 110, 617–630.
Van der Merwe, J., Cawthorn, R.G., 2005. Structures at the base of the Upper Group 2 chromitite layer, Bushveld complex, South Africa, on Karee Mine (Lonmin platinum). Lithos 83, 214–228.
Vantongeren, J.A., Mathez, E.A., 2013. Incoming magma composition and style of recharge below the Pyroxenite Marker, Eastern Bushveld complex, South Africa. J. Petrol. 54, 1585–1605.
Veksler, I.V., Charlier, B., 2015. Silicate liquid immiscibility in layered intrusions. In: Charlier, B., Namur, O., Latypov, R., Tegner, C. (Eds.), Layered Intrusions. Springer Geology, Dordrecht, pp. 229–258.
Veksler, I.V., Hou, T., 2020. Experimental study on the effects of H_2O upon crystallization in the lower and critical zones of the Bushveld complex with an emphasis on chromitite formation. Contrib. Mineral. Petrol. 175, 1–17.
Vernon, R.H., 1968. Microstructures of high-grade metamorphic rocks at Broken Hill, Australia. J. Petrol. 9, 1–22.
Vernon, R.H., 2010. Granites really are magmatic: using microstructural evidence to refute some obstinate hypotheses. In Forster MA, Fitz Gerald JD, Lister GS (eds) the Science of Microstructure. J. Virtual Explor. 35.
Vernon, R.H., Paterson, S.R., 2008. How extensive are subsolidus grain-shape changes in cooling granites? Lithos 105, 42–50.
Viljoen, M.J., 1999. The nature and origin of the Merensky Reef of the western Bushveld complex based on geological facies and geological data. S. Afr. J. Geol. 102, 221–239.
Viljoen, M.J., Hieber, R., 1986. The Rustenburg section of Rustenburg platinum Mines Limited, with reference to the Merensky Reef. In: Anhaeusser, C.R., Maske, S. (Eds.), Mineral Deposits of Southern Africa. Mineral deposits of Southern Africa. Geological
Society of South Africa, pp. 1117–1134.
Virtanen, V.J., Heinonen, J.S., Molnar, F., Schmidt, M.W., Marxer, F., Skytta, ¨ P., Kueter, N., Moslova, K., 2021. Fluids as primary carriers of Sulphur and copper in magmatic assimilation. Nat. Commun. 2, 1–12.
Virtanen, V.J., Heinonen, J.S., Barber, N.D., Molnar, F., 2022. Complex effects of assimilation on sulfide saturation revealed by modeling with the Magma Chamber Simulator: a case study on the Duluth complex, Minnesota, USA. Econ. Geol. 117, 1881–1899.
Von Gruenewaldt, G., 1973. The Main and Upper zones of the Bushveld complex in the Roossenekal area, eastern Transvaal. Trans. Geol. Soc. S. Afr. 76, 53–61.
Von Gruenewaldt, G., 1993. Ilmenite-apatite enrichments in the Upper Zone of the Bushveld complex: a major titanium-rock phosphate resource. Int. Geol. Rev. 35, 987–1000.
Von Gruenewaldt, G., Hatton, C.J., Merkle, R.K.W., 1986. Platinum-group elementchromitite associations in the Bushveld complex. Econ. Geol. 81 (5), 1067–1079.

Von Gruenewaldt, G., Hulbert, L.J., Naldrett, A.J., 1989. Contrasting platinum-group element concentration patterns in cumulates of the Bushveld complex. Mineral. Deposita 24, 219–229.
Voordouw, R., Gutzmer, J., Beukes, N.J., 2009. Intrusive origin for Upper Group (UG1, UG2) stratiform chromitite seams in the Dwars River area, Bushveld complex, South Africa. Mineral. Petrol. 97, 75–94.
Vukmanovic, Z., Holness, M.B., Monks, K., Andersen, J.C.O., 2018. The Skaergaard trough layering: sedimentation in a convecting magma chamber. Contrib. Mineral. Petrol. 173, 43.
Vukmanovic, Z., Holness, M.B., Stock, M.J., Roberts, R.J., 2019. The creation and evolution of crystal mush in the Upper Zone of the Rustenburg Layered Suite, Bushveld complex, South Africa. J. Petrol. 60, 1523–1542.
Wager, L.R., 1963. The mechanism of adcumulus growth in the Layered Series of the Skaergaard intrusion. Mineral. Soc. Am. Spec. Pap. 1, 1–9.
Wager, L.R., Brown, G.M., 1968. Layered Igneous Rocks. Oliver & Boyd, Edinburgh & London, Edinburgh, 588 pp.
Wager, L.R., Deer, W.A., 1939. Geological investigations in East Greenland. Part III. The petrology of the Skaergaard intrusion, Kangerdlugssuaq, East Greenland. Meddelelser Gronland 105 (4), 335.
Wager, L.R., Brown, G.M., Wadsworth, W.J., 1960. Types of igneous cumulates. J. Petrol. 1, 73–85.
Walker, J.D., Geissman, J.W., Bowring, S.A., Babcock, L.E., 2013. The Geological Society of America geologic time scale. GSA Bull. 125, 259–272.
Wall, C.J., Scoates, J.S., Weis, D., Friedman, R.M., Amini, M., Meurer, W.P., 2018. The Stillwater complex: integrating zircon geochronological and geochemical constraints on the age, emplacement history and crystallization of a large, open-system layered intrusion. J. Petrol. 59, 153–190.
Wang, K., Wang, C.Y., Ren, Z.Y., 2018. Apatite-hosted melt inclusions from the Panzhihua gabbroic-layered intrusion associated with a giant Fe–Ti oxide deposit in SW China: insights for magma unmixing within a crystal mush. Contrib. Mineral. Petrol. 173, 59.
Wang, J., Su, B.-X., Robinson, P.T., Xiao, Y., Bai, Y., Liu, X., Sakyi, P.A., Jing, J.-J., Chen, C., Liang, Z., Bao, Z.-A., 2021. Trace elements in olivine: proxies for petrogenesis, mineralization and discrimination of mafic-ultramafic rocks. Lithos 388-389, 106085.
Waters, C., Boudreau, A.E., 1996. A reevaluation of crystal-size distributions in chromite cumulates. Am. Mineral. 81, 1452–1459.
Waters, L.E., Andrews, B.J., Lange, R.A., 2015. Rapid crystallization of plagioclase phenocrysts in silicic melts during fluid-saturated ascent: phase equilibrium and decompression experiments. J. Petrol. 56, 981–1006.
Watkinson, D.H., Dunning, G., 1979. Geology and platinum-group mineralization, Lacdes-Iles complex, northwestern Ontario. Can. Mineral. 17, 453–462.
Watson, E.B., Cherniak, D., Holycross, M., 2015. Diffusion of phosphorus in olivine and molten basalt. Am. Mineral. 100, 2053–2065.
Watts, K., 2014. A melt inclusion study of the Sudbury Igneous complex (Ontario, Canada): Evidence for two-liquid immiscibility and constraints on trace element distribution. Master Thesis. Saint Mary's University, Halifax, Nova Scotia.
Webb, S.J., Ashwal, L.D., Cawthorn, R.G., 2011. Continuity between eastern and western Bushveld complex, South Africa, confirmed by xenoliths from kimberlite. Contrib. Mineral. Petrol. 162, 101–107.
Welsch, B., Faure, F., Famin, V., Baronnet, A., Bach`elery, P., 2013. Dendritic crystallization: a single process for all the textures of olivine in basalts? J. Petrol. 54, 539–574.
Welsch, B., Hammer, J., Hellebrand, E., 2014. Phosphorus zoning reveals dendritic architecture of olivine. Geology 42, 867–870.
Whitney, D.L., Tepper, J.H., Hirschmann, M.M., Hurlow, H.A., 2008. Late orogenic mafic magmatism in the North Cascades, Washington: Petrology and tectonic setting of the Skymo layered intrusion. Geol. Soc. Am. Bull. 120, 531–542.
Wieser, P.E., Vukmanovic, Z., Kilian, R., Ringe, E., Holness, M.B., Maclennan, J., Edmonds, M., 2019. To sink, swim, twin, or nucleate: a critical appraisal of crystal aggregation processes. Geology 47, 948–952.
Williams, S.R., Philipse, A.P., 2003. Random packings of spheres and spherocylinders simulated by mechanical contraction. Phys. Rev. E67, 051301.
Wilson, J.R., Larsen, S.B., 1985. Two-dimensional study of a layered intrusion – the Hyllingen Series, Norway. Geol. Mag. 122, 97–124.
Wilson, R., 2010. The Fongen-Hyllingen Layered Intrusion, Trondheim Region, Norway: An Excursion Guide. Geological Survey of Norway.
Wilson, J.R., Engell-Sørensen, O., 1986. Marginal reversals in layered intrusions are evidence for emplacement of compositionally stratified magma. Nature 323, 616–618.
Wilson, J.R., Larsen, S.B., 1982. Discordant layering relations in the Fongen–Hyllingen basic intrusion. Nature 299, 625–626.
Wilson, J.R., Sørensen, H.S., 1996. The Fongen-Hyllingen layered intrusive complex, Norway. In: Cawthorn, R.G. (Ed.), Developments in Petrology, Layered Intrusions. Elsevier, pp. 303–329.
Wilson, A.H., Prendergast, M.D., 1989. The Great Dyke of Zimbabwe: I-tectonic setting, stratigraphy, petrology, structure, emplacement and crystallization. Magmatic Sulphides Field Conference, 5, pp. 1–20.
Wilson, J.R., Robins, B., Nielsen, F.M., Duchesne, J.C., Vander Auwera, J., 1996. The Bjerkreim-Sokndal Layered Intrusion, Southwest Norway. In: Cawthorn, R.G. (Ed.), Developments in Petrology, Layered Intrusions. Elsevier, pp. 231–255.
Wilson, A.H., Zeh, A., Gerdes, A., 2017. *In situ* Sr isotopes in plagioclase and trace element systematics in the lowest part of the Eastern Bushveld complex: dynamic processes in an evolving magma chamber. J. Petrol. 58, 327–360.
Woods, K., Keltie, E., Brenan, J., Mungall, J., Weston, R., 2019. The role of country rock assimilation on chromite crystallization in the Ring of Fire, James Bay Lowlands, Ontario, Canada. In: GAC/MAC Meeting, Quebec City.
Wyborn, L.A.I., Heinrich, C.A., Jaques, A.L., 1994. Australian Proterozoic mineral systems: essential ingredients and mappable criteria. In: The AusIMM Annual Conference. AusIMM Darwin, pp. 109–115.
Xiao, Y., Teng, F.Z., Su, B.X., Hu, Y., Zhou, M.F., Zhu, B., He, Y.S., 2016. Iron and magnesium isotopic constraints on the origin of chemical heterogeneity in podiform chromitite from the Luobusa ophiolite, Tibet. Geochem. Geophys. 17, 940–953.
Xing, C.-M., Wang, C.Y., Tan, W., 2017. Disequilibrium growth of olivine in mafic magmas revealed by phosphorus zoning patterns of olivine from mafic–ultramafic intrusions. Earth Planet. Sci. Lett. 479, 108–119.
Xing, C.-M., Wang, C.Y., Charlier, B., Namur, O., 2022. Ubiquitous dendritic olivine constructs initial crystal framework of mafic magma chamber. Earth Planet. Sci. Lett. 594, 117710.
Yang, X.M., Gilbert, H.P., Corkery, M.T., Houl´ e, M.G., 2011. The Mayville mafic–ultramafic intrusion in the Neoarchean Bird River greenstone belt, southeastern Manitoba (part of NTS 52L12): preliminary geochemical investigation and implication for PGE-Ni-Cu-(Cr) mineralization. Rep. Act. 127–142.
Yao, Z., Mungall, J.E., 2022. Magnetite layer formation in the Bushveld complex of South Africa. Nat. Commun. 13, 146.
Yao, Z., Mungall, J.E., Jenkins, M.C., 2021. The Rustenburg Layered Suite formed as a stack of mush with transient magma chambers. Nat. Commun. 12, 505.
Yoder, H.S., 1968. Experimental studies bearing on the origin of anorthosite. In: Isachsen, Y.W. (Ed.), Layered Intrusions and Anorthosite Genesis. New York State Museum and Science, pp. 13–22. Service Memoir.
Yuan, Q., Namur, O., Fischer, L.A., Roberts, R.J., Lü, X., Charlier, B., 2017. Pulses of plagioclase-laden magmas and stratigraphic evolution in the Upper Zone of the Bushveld complex. S. Afr. J. Petrol. 58, 1619–1644.
Yudovskaya, M.A., Naldrett, A.J., Woolfe, J.A.S., Costin, G., Kinnaird, J.A., 2015. Reverse compositional zoning in the Uitkomst chromitites as an indication of crystallization in a magmatic conduit. J. Petrol. 56, 2373–2394.
Zhang, X.-Q., Song, X.-Y., Chen, L.-M., Xie, W., Yu, S.-Y., Zheng, W.-Q., Deng, Y.-F., Zhang, J.-F., Gui, S.-G., 2012. Fractional crystallization and the formation of thick Fe–Ti–V oxide layers in the Baima layered intrusion, SW China. Ore Geol. Rev. 49, 96–108.
Zhang, Y., Namur, O., Charlier, B., 2023. Experimental study of high-Ti and low-Ti basalts: liquid lines of descent and silicate liquid immiscibility in large igneous provinces. Contrib. Mineral. Petrol. 178, 7.
Zhou, M.F., Robinson, P.T., Lesher, C.M., Keays, R.R., Zhang, C.J., Malpas, J., 2005. Geochemistry, petrogenesis and metallogenesis of the Panzhihua gabbroic layered intrusion and associated Fe–Ti–V oxide deposits, Sichuan Province, SW China. J. Petrol. 46 (11), 2253–2280.
Zhou, M.-F., Chen, W.T., Wang, C.Y., Prevec, S.A., Liu, P., Howarth, G.H., 2013. Two stages of immiscible liquid separation in the formation of Panzhihua-type Fe-Ti-V oxide deposits, SW China. Geosci. Front. 4, 481–502.
Zieg, M.J., Marsh, B.D., 2005. The Sudbury Igneous complex: Viscous emulsion differentiation of a superheated impact melt sheet. GSA Bull. 117, 1427–1450.
Zientek, M.L., Cooper, R.W., Corson, S.R., Geraghty, E.P., 2002. Platinum-group element mineralization in the Stillwater complex, Montana. In: Geology, Geochemistry, Mineralogy and Mineral Benefication of Platinum Group Element. Canadian Institute of Mining, Metallurgy and Petroleum, Special Volume, vol. 54, pp. 459–481.

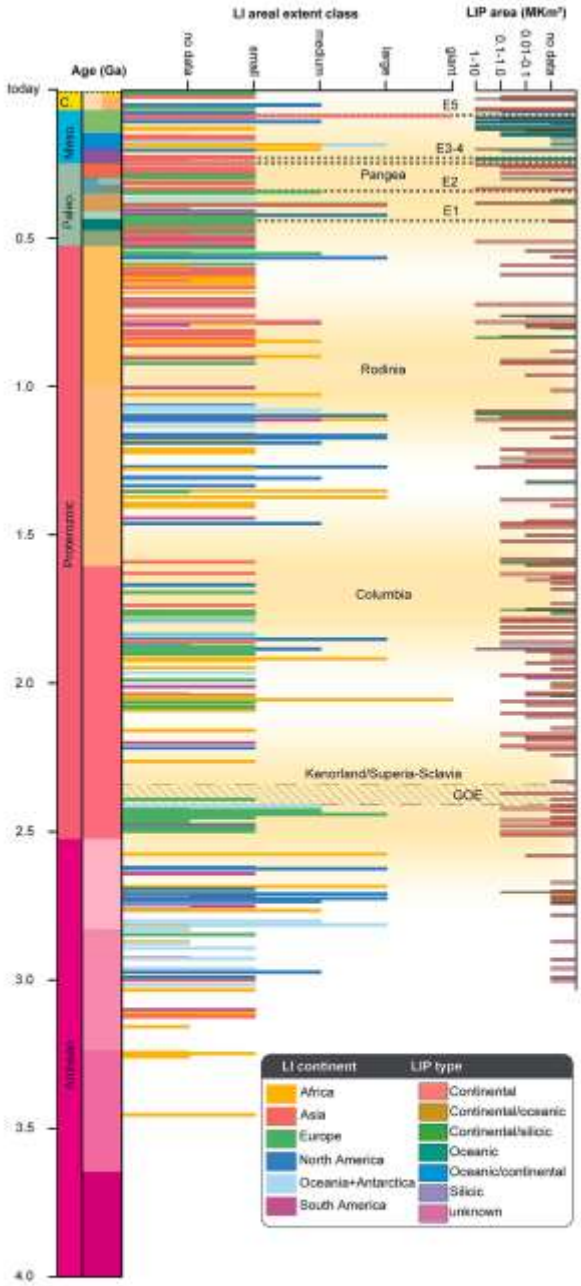

Fig. 1. Distribution of layered intrusions (LI) throughout space (colour) and geological time (y-axis). The x-axis corresponds to areal extent classification (Smith and Maier, 2021), which includes no data (undetermined extent), small (< 100 km^2), medium (> 100 km^2), large (> 1000 km^2), and giant (> 10,000 km^2). The geological time scale was modified from Walker et al. (2013). The age and approximated areal extent of large igneous provinces (LIPs) are modified from Ernst and Bucham (2001). The secular occurrence of supercontinents (Condie, 2001; Goldfarb et al., 2010; Maier and Groves, 2011), the Great Oxidation Event (GOE), and the five major extinction events (E1–5) have been underlain.

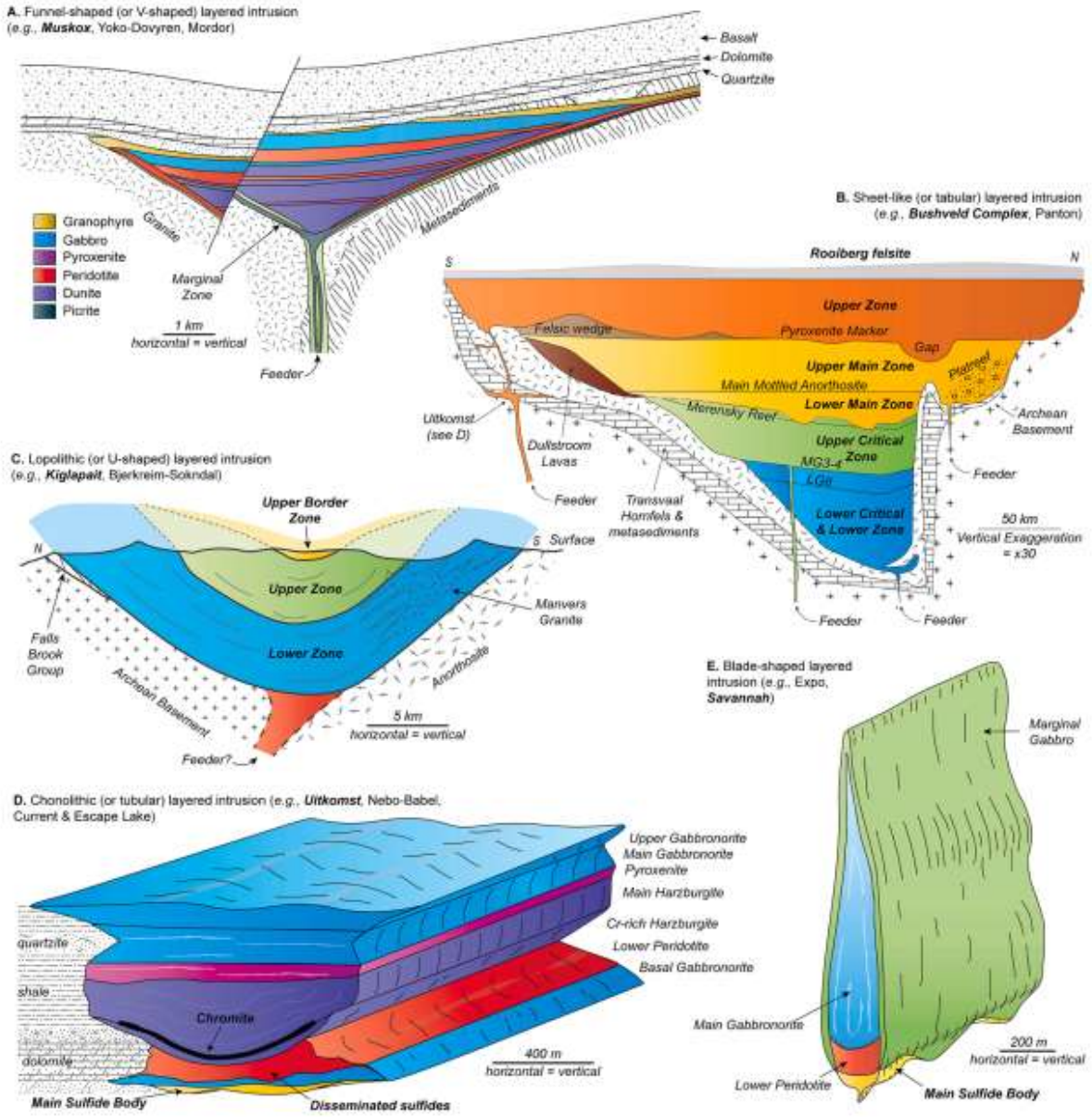

Fig. 2. Illustrated examples of the geometrical diversity of layered intrusions. (A) Funnel-shaped (or V-shaped) intrusion, typified by the Muskox Intrusion (modified from Irvine and Smith, 1967). (B) Sheet-like (or tabular) intrusion, typified by the Bushveld Complex (modified from Kruger, 2005). (C) 'Lopolithic' intrusion, typified by the Kiglapait intrusion (Morse, 1969; Fourny et al., 2019), though, caution should be applied when using this term (see Cawthorn and Miller, 2018). (D) Chonolithic (or tubular) intrusion, typified by the Uitkomst intrusion (modified from Maier et al., 2018b). (E) Bladed intrusion, typified by the Savannah intrusion (modified from Barnes et al., 2016a). Patterns were sourced from the USGS (Doc. No. FGDC-STD-013-2006).

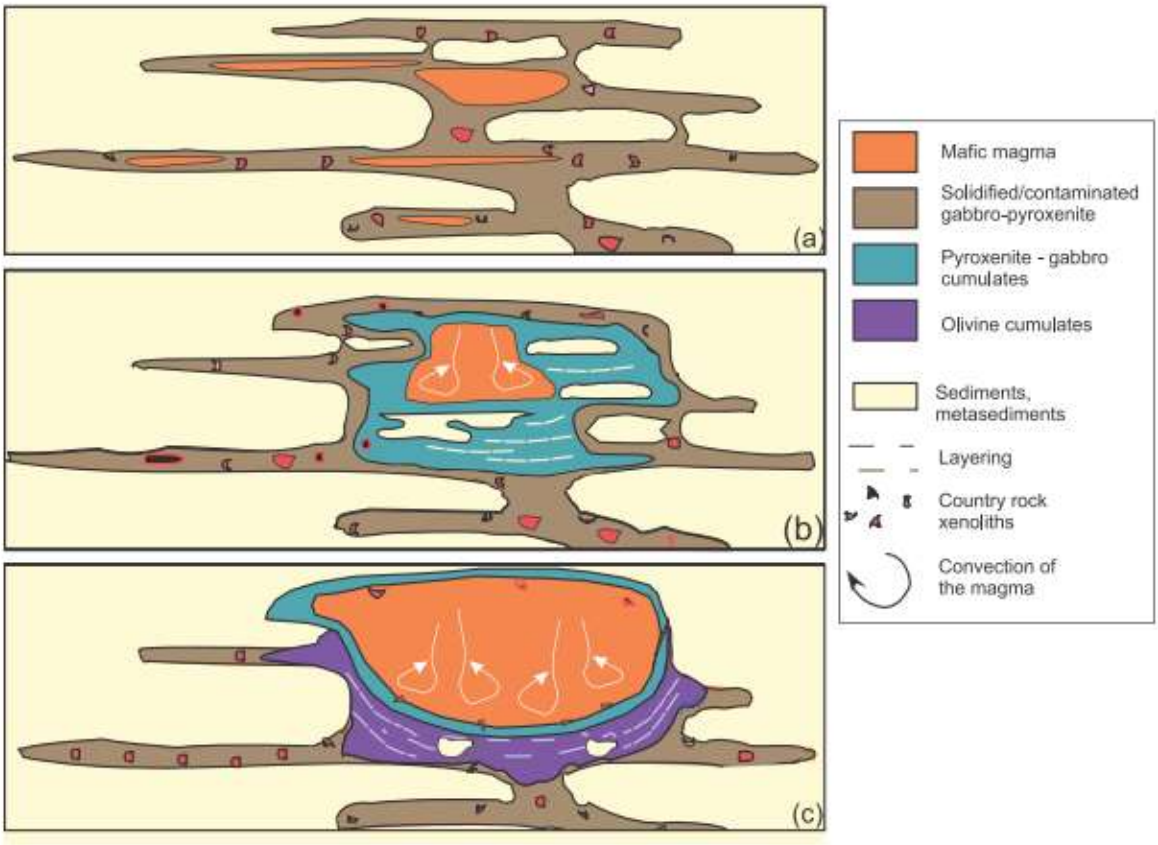

Fig. 3. Emplacement mechanism of a stacked sill complex (A), an intermediate sill-layered intrusion complex (B), and large layered intrusion (C), modified from Barnes et al. (2019a). (A) The episodic arrival of relatively small volumes of magma produces a stack of discrete small intrusions. (B) Magma continuously fluxes into the molten interior of existing sills (A), which allows growth by inflation or country rock stoping to progressively develop into a convecting magma chamber depending on relative rates of cooling and magma arrival. (C) The rate of magma supply surpasses that of magma crystallization, which creates a convecting magma chamber. In this scenario, multiple episodes of emplacement separated by intervals of fractional crystallization gives rise to macrorhythmic layering, typically on a scale of 100 s of m.

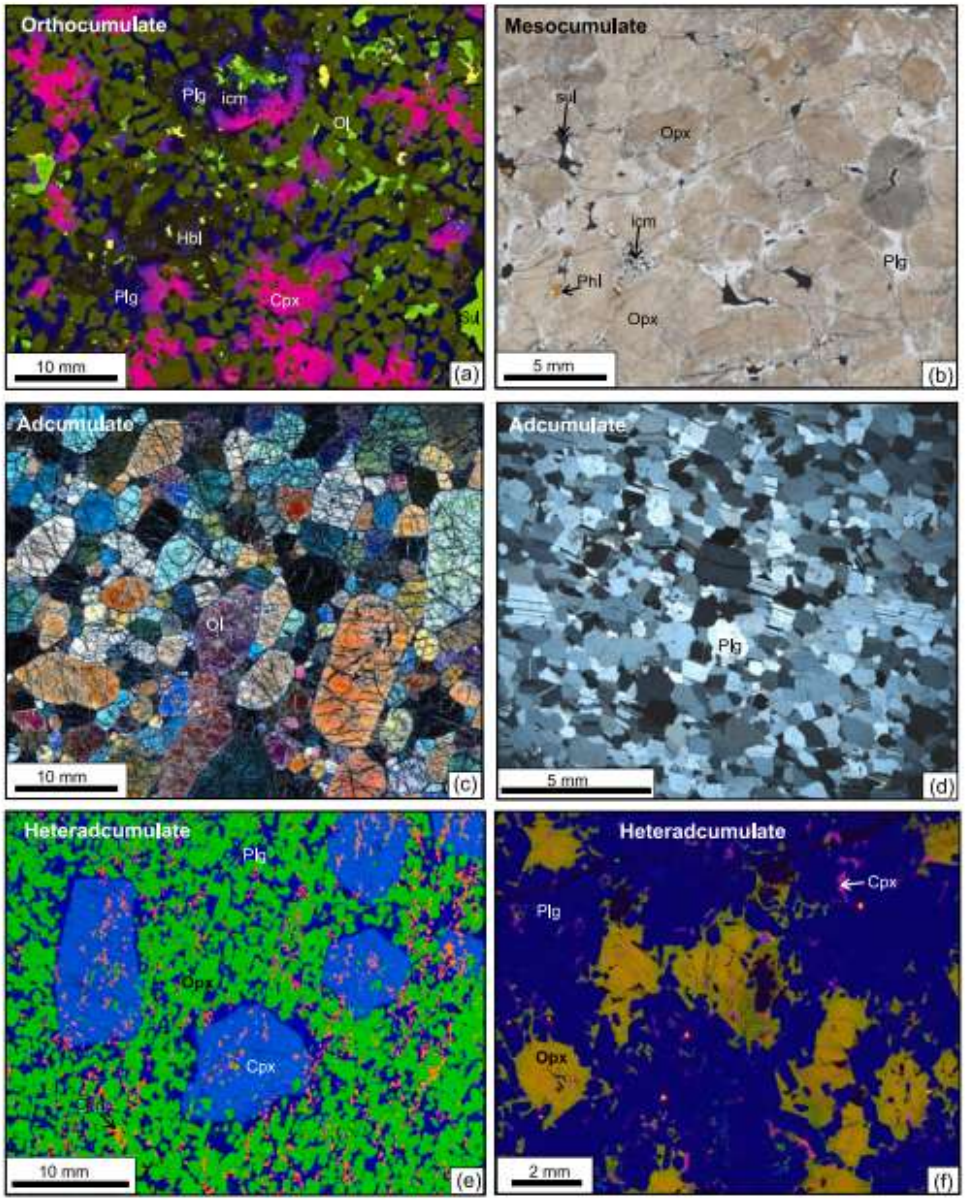

Fig. 4. Examples of orthocumulate, mesocumulate, adcumulate and heteradcumulate textures. (a), olivine orthocumulate from Kharealakh Sill, Norilsk, Siberia. Note distinct zoning (in Cr content – purple to pink, low to high) in intercumulus cpx. Synchrotron X-ray fluorescence (SXRF) false colour image, Cr (red) Fe(green) Ca (blue). (b), orthopyroxene (bronzite) mesocumulate, Mirabela, Brazil. Most grains in face contact, zoned intercumulus plagioclase, fine pockets of late accessory phases. Transmitted light photomicrograph. (c), Olivine adcumulate, Wildara komatiite complex, 100% olivine with characteristic 120° triple points. Transmitted light photomicrograph, crossed polars. (d) adcumulate anorthosite (plagioclase cumulate), Bushveld Complex. 100% unzoned plagioclase. Transmitted light photomicrograph, crossed polars. (e), Opx heteradcumulate, Bushveld. Cumulus bronzite (green) surrounded by chains of chromite grains (orange), idiomorphic oikocrysts of augite (light blue) and larger oikocrysts of plagioclase (dark blue), note extensive resorption of bronzite grains inside augite. Desktop XRF false colour image, Cr (red) Fe(green) Ca (blue). (f), plagioclase-bronzite heteradcumulate, Bushveld. Note bronzite shows zoning from more Cr-rich plagioclase-free cores to relatively slightly Cr-depleted, poikilitic rims. Minor cpx oikocrysts. Rock is almost entirely devoid of late accessory phases. Typical texture of norites in many layered intrusions. SXRF, Cr red, Fe green, Ca blue. Icm = residual intercumulus material. (For interpretation of the references to colour in this figure legend, the reader is referred to the web version of this article.)

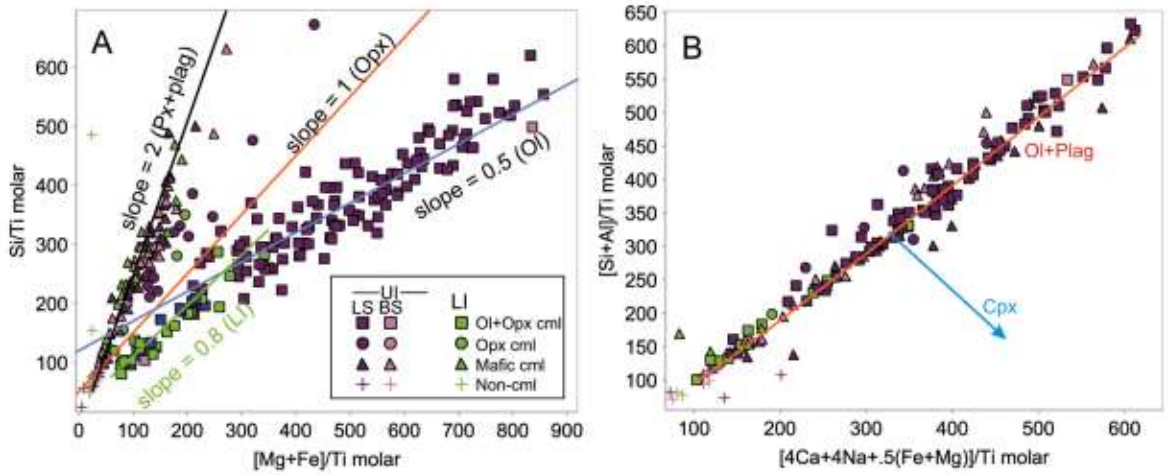

Fig. 5. Example of use of normalised molar ratio (Pearce Element Ratio) plots for determination of cumulus assemblages from whole rock geochemical data. Data are from the Nova intrusive complex in Western Australia (Taranovic et al., 2022). A, plot of molar ratios of Si and Mg + Fe to Ti. Diagonal lines are at constant ratio and show the trends for accumulation of pure olivine (slope 0.5), pure orthopyroxene (1) and a 60:40 mixture of plagioclase plus opx (slope = 2). UI = Upper Intrusion, comprising Layered Series (LS) and Basal Series (BS) and for Lower Intrusion; note that Upper intrusion consists of interlayered olivine and plag+opx cumulates, Lower Intrusion contains mixed olivine+opx cumulates and plag-opx cumulates. B, same data on plot of molar (Si + Al)/Ti vs [(4Ca + 4Na + 0.5(Fe + Mg)]/Ti; this plot shows trend with slope 1 for olivine plus plagioclase cumulates, orthogonal to vector with slope − 1 for accumulation of clinopyroxene; on this evidence the Nova intrusions lack cumulus clinopyroxene. See (Stanley and Russell, 1989) for explanation of the theory behind these and other related diagrams.

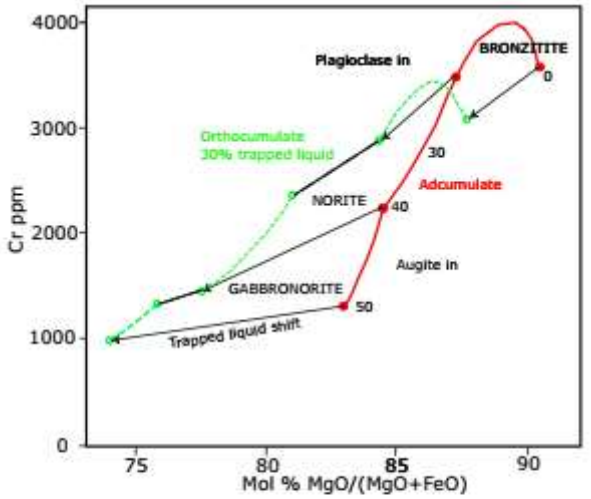

Fig. 6. Illustration of the effect of the "trapped liquid shift" on cumulus mineral compositions. Red curve shows liquidus (adcumulate) composition of orthopyroxene (bronzite) formed by progressive crystallization along the evolving liquidus from a proposed Bushveld Complex parent liquid (numbers indicate % crystallized). Green curve shows the "shifted" composition after re-equilibration with 30% trapped liquid. Note the discontinuous break in the orthocumulate trend corresponding to appearance of new liquidus phases and change in proportion of pyroxene in the cumulus assemblage. Also note the large change in Mg# relative to small change in Cr for the plagioclase-bearing assemblages. For full details see Barnes (1986). (For interpretation of the references to colour in this figure legend, the reader is referred to the web version of this article.)

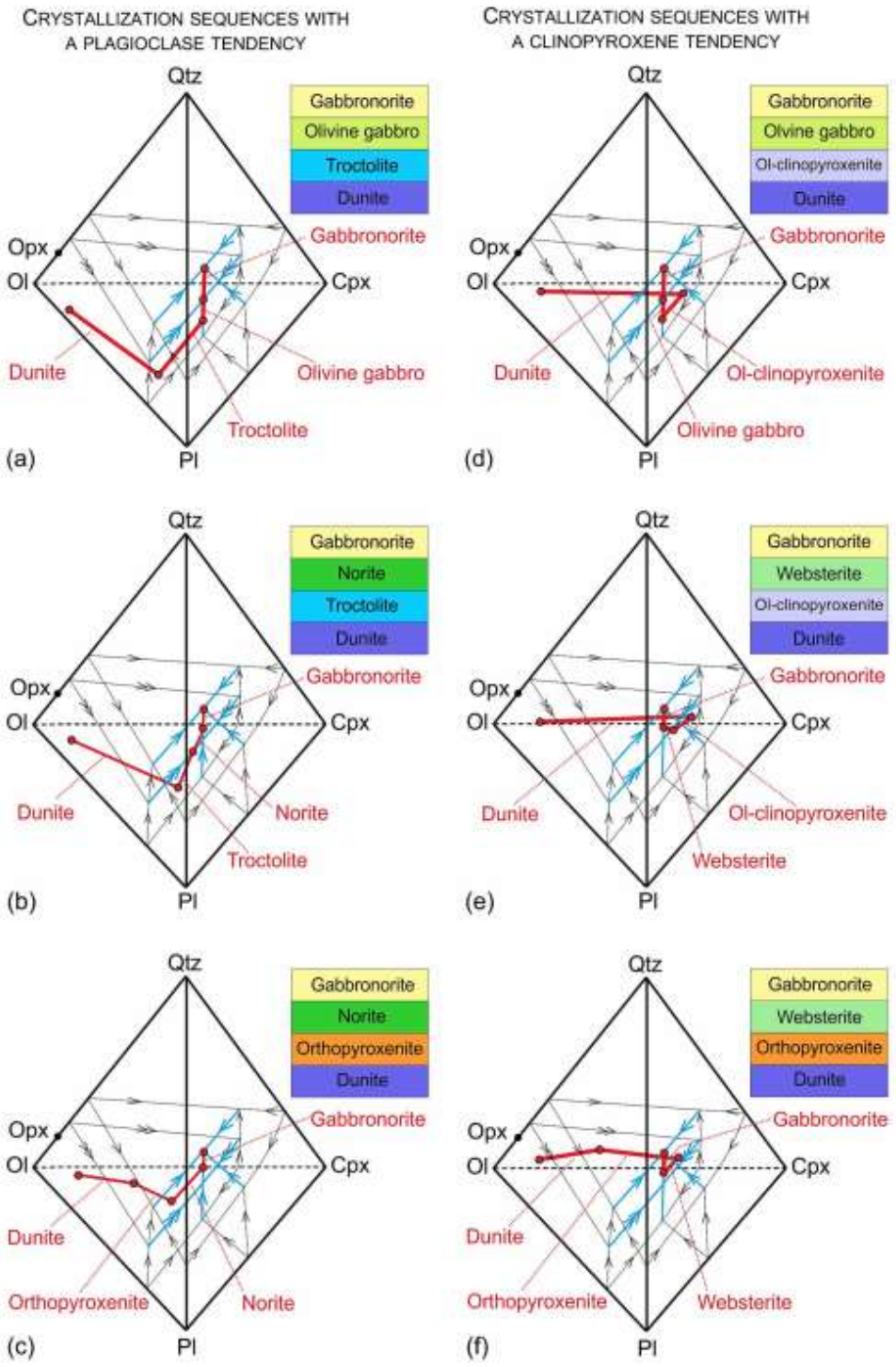

Fig. 7. A quaternary system Ol-Pl-Cpx-Qtz and associated stratigraphic sections illustrating that olivine-saturated basaltic melts may evolve along three crystallization sequences divided into plagioclase (a-c) and clinopyroxene tendencies (d-f). The topology of the diagram is modified and slightly distorted for illustration purposes from Irvine (1979). Black liquidus lines are on ternary sides whereas the blue ones are within a tetrahedron. Red lines are crystallization paths, with dots indicating where changes in mineral assemblages take place. Cotectic and reaction lines are indicated by one or two arrows, respectively.

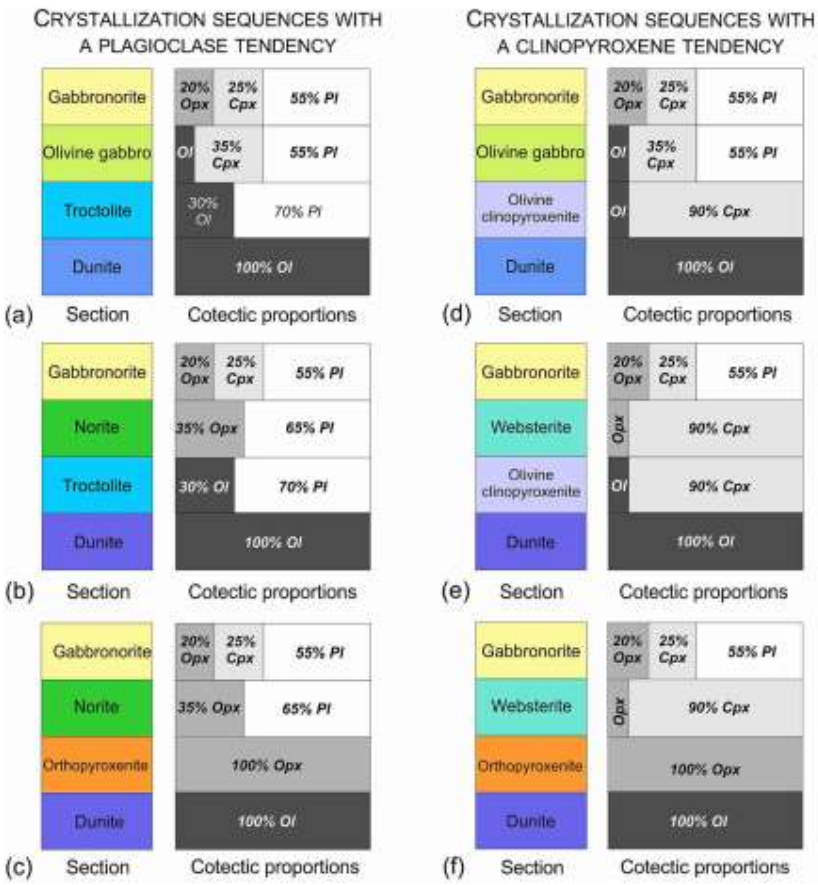

Fig. 8. Theoretically predicted changes in cotectic proportions of phases in cumulates produced from olivine-saturated basaltic melts that follow crystallization sequences along the plagioclase (a-c) and clinopyroxene tendencies (d-f) in a quaternary system Ol-Pl-Cpx-Qtz (see Fig. 7).

Fig. 9. Representative example of layer and layering features. A. Magnetitite layer (Mt) overlying leucogabbronorite, Upper Zone of the Eastern Bushveld Complex, Magnet Heights. Camera bag is 10 cm across. B. Chromitite layers within anorthosite cumulates. UG1 footwall, Critical Zone of the Eastern Bushveld Complex, Dwars River, South Africa.

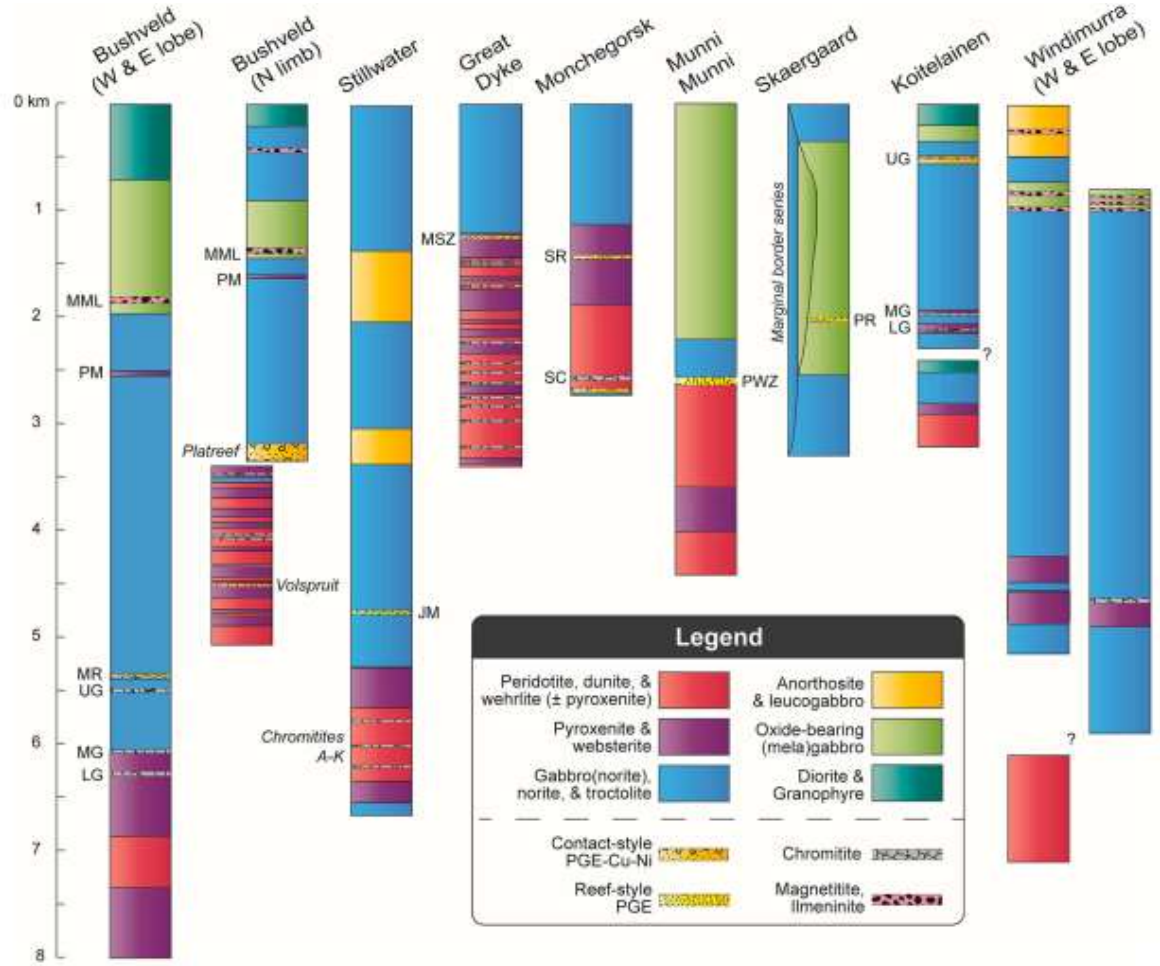

Fig. 10. Schematic stratigraphic sections of some layered intrusions, including the Bushveld western and eastern lobes (modified from Cawthorn and Webb, 2001), Bushveld northern limb (modified after Von Gruenewaldt et al., 1989 and McDonald et al., 2005), Stillwater (modified after Jenkins and Mungall, 2018), Great Dyke (modified after Wilson and Prendergast, 1989), Monchegorsk (modified after Chistyakova et al., 2015 and Karykowski et al., 2018b), Munni Munni (modified after Barnes and Hoatson, 1994), Skaergaard (modified after Salmonsen and Tegner, 2013), Koitelainen (modified after Hanski et al., 2001), and Windimurra (modified after Ivanic et al., 2018). Abbreviations: LG = lower group chromitites; MG = middle group chromitites; UG = upper group chromitites; MML = Main Magnetite Layer; PM = Pyroxenite Marker; MR = Merensky Reef; MSZ = Main Sulfide Zone; SC = Sopcheozero chromitite; SR = Sopcha Reef; PWZ = Porphyritic Websterite Zone; PR = Platinova Reef; SDZ = Shephards Discordant Zone.

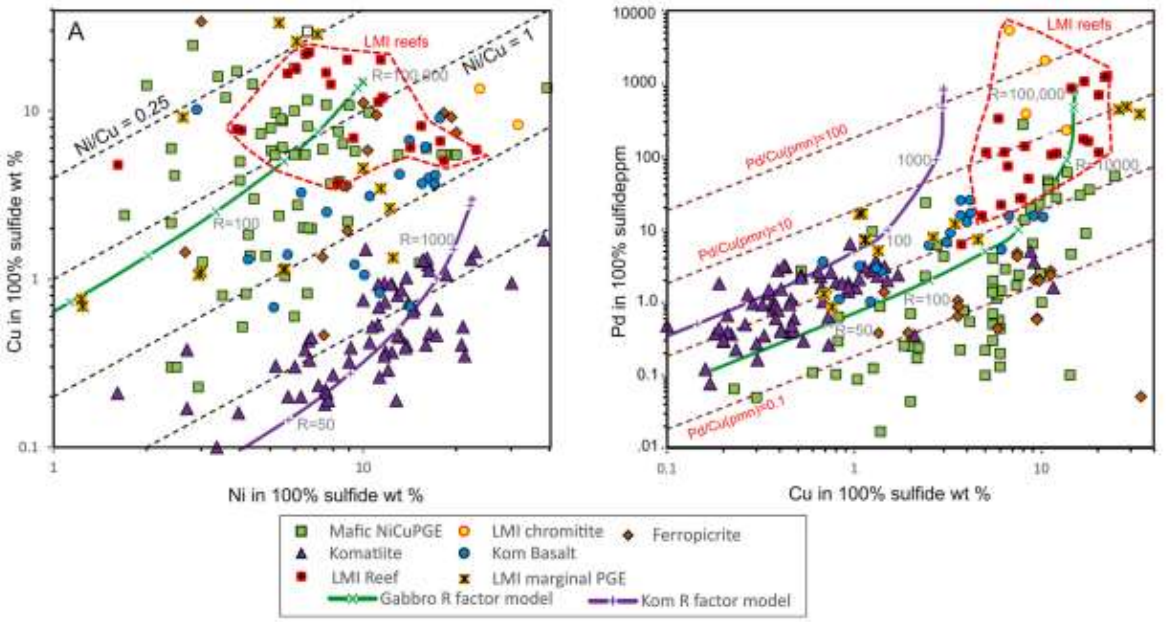

Fig. 11. Ore compositions expressed as bulk metal tenors (concentration of Cu, Ni and Pd in 100% sulfide) from the complete spectrum of magmatic sulfide ore types. (A) Cu vs Ni; (B) Pd vs. Cu. Average bulk compositions of individual ore deposits associated with komatiites, mafic-parented intrusions, komatiitic basalts and ferropicrites. Red symbols are individual deposit data points from PGE-rich reefs in layered mafic intrusions including the Bushveld Complex. Curves show results of simple partition coefficient/mass ratio (D/R) calculations (Campbell and Naldrett, 1979) for model komatiite and mafic magma starting compositions, assuming D values of 150 and 400 for Ni in komatiite and basalt respectively; 1000 for Cu, and 100,000 for Pd, values of R (silicate/sulfide liquid mass ratio) shown in grey text. Pd/Cu(pmn) is Pd/Cu normalised to ratio in primitive upper mantle. (For interpretation of the references to colour in this figure legend, the reader is referred to the web version of this article.)

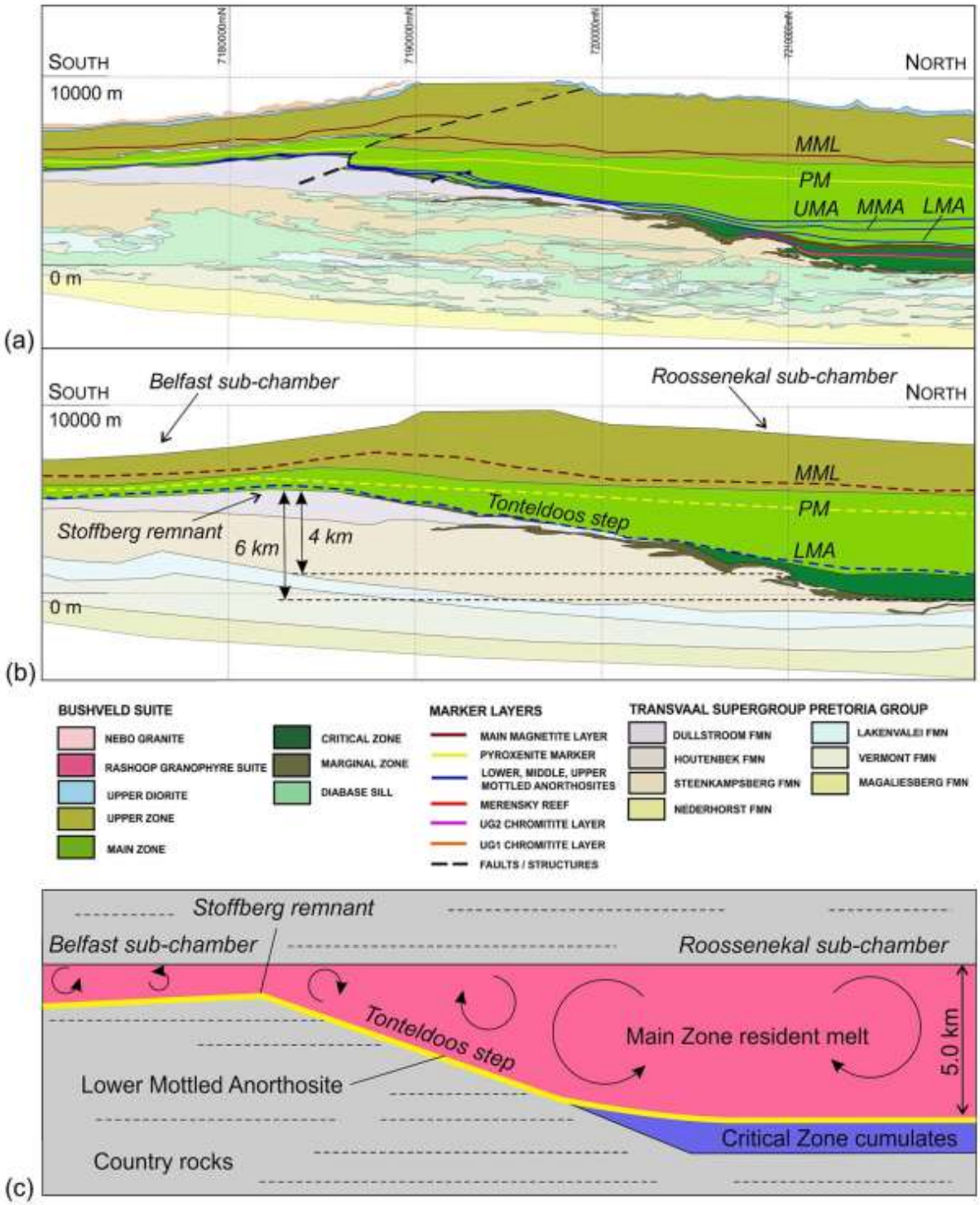

Fig. 12. Geological along-strike section of the southeastern part of the Bushveld Complex in the Tonteldoos area and reconstruction of the magma chamber morphology at the onset of the MZ formation. (a) The section is of the transect line through this area, looking at −11° towards 270° azimuth. The section was constructed by rotating the 3D model to view the detailed geology of the complex and its immediate footwall in their true orientation. The section is not vertically or horizontally exaggerated and shows the true lithology morphology. (b) The schematic section prior to faulting highlights several important features of the complex: (1) the existence of the Roossenekal and Belfast sub-chambers with the intervening Stoffberg remnant of non-deformed host rocks, (2) the ~4-km and ~ 6-km thick vertical distance between the summit of the Stoffberg remnant with the Lower Mottled Anorthosite and the floor of the Roossenekal sub-chamber, respectively, (3) the concave geometry of the Pyroxenite Marker indicating that instantaneous top of the cumulate pile in the two sub-chambers was gently basinal with regards to the Stoffberg remnant. (c) At onset of crystallization, the MZ resident melt column had a total thickness of about 5 km. This resulted in simultaneous deposition of the Lower Mottled Anorthosite along the entire extent of the Roossenekal and Belfast sub-chambers, including the Tonteldoos step and Stoffberg remnant. LMA, Lower Mottled Anorthosite; MMA, Middle Mottled Anorthosite; UMA, Upper Mottled Anorthosite; PM, Pyroxenite Marker; MML, Main Magnetite Layer. Modified from Latypov et al. (2022b).

Fig. 13. Photographs of field evidence for the accumulation of material on the floor of mafic magma chambers. (a) autoliths (examples are arrowed) in the Layered Series on the floor of the Skaergaard intrusion. These blocks are derived from the roof, and their localized concentration suggests they were detached from their source during seismic activity. Pen for scale. (b) Modal layering in the lower part of the floor cumulates of the Skaergaard intrusion. Note the truncation of lower layers by an erosive episode preceding further accumulation. Rifle for scale. (c) Trough banding in the Upper Zone of the Skaergaard intrusion, viewed along the axis of the trough and looking towards the centre of the intrusion. The modally graded trough bands formed by deposition from crystal-rich currents flowing across the floor focussed into channels created by long-lived ridges of homogeneous massive gabbro. The erratic block marked by an asterisk is ~2 m long.

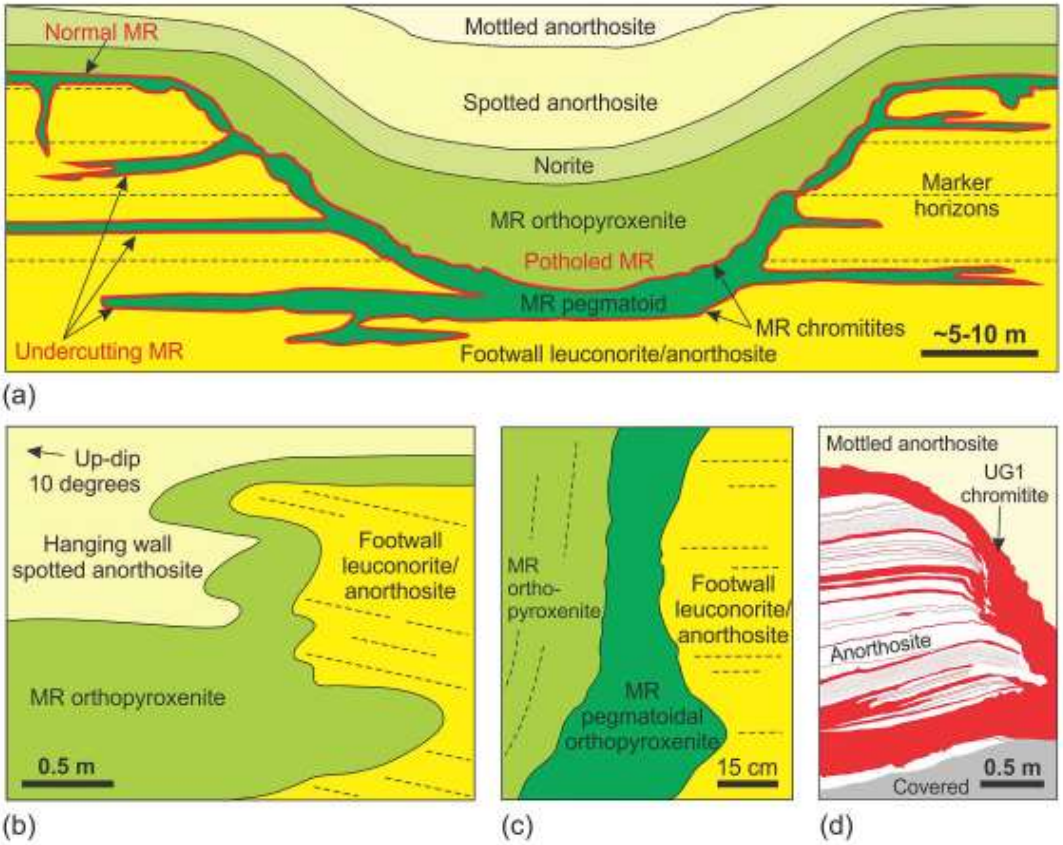

Fig. 14. Sketches of underground exposures illustrating igneous layering that develops on the overturned to undercutting portions of a chamber floor. (a) A generalized morphology of a typical Merensky Reef (MR) pothole at the Impala Platinum Mine, western Bushveld Complex illustrating the transgressive relationship of the normal and potholed MR to its footwall. Note that the potholed MR along the edge of the pothole is accompanied by undercutting MR bodies that are sill-like sulphide- and chromite-mineralised protrusions extending laterally from pothole margins into footwall rocks. Modified from Latypov et al. (2017b). (b) The MR package that develops along subvertical to overhanging margins of a pothole in the western Bushveld Complex. The MR package is of broadly orthopyroxenitic composition and is sandwiched between footwall mottled anorthosites and hanging wall leuconorite. Modified from Chistyakova et al. (2019a). (c) Subvertical to overturned MR package composed of feldspathic orthopyroxenite that is sandwiched between footwall and hanging wall leuconorite in a pothole from the western Bushveld Complex. Modified from Chistyakova et al. (2019a). (d) The UG1 chromitite developing along the subvertical chamber floor without any notable change in its thickness in a pothole from the western Bushveld Complex. Modified from Latypov et al. (2017a).

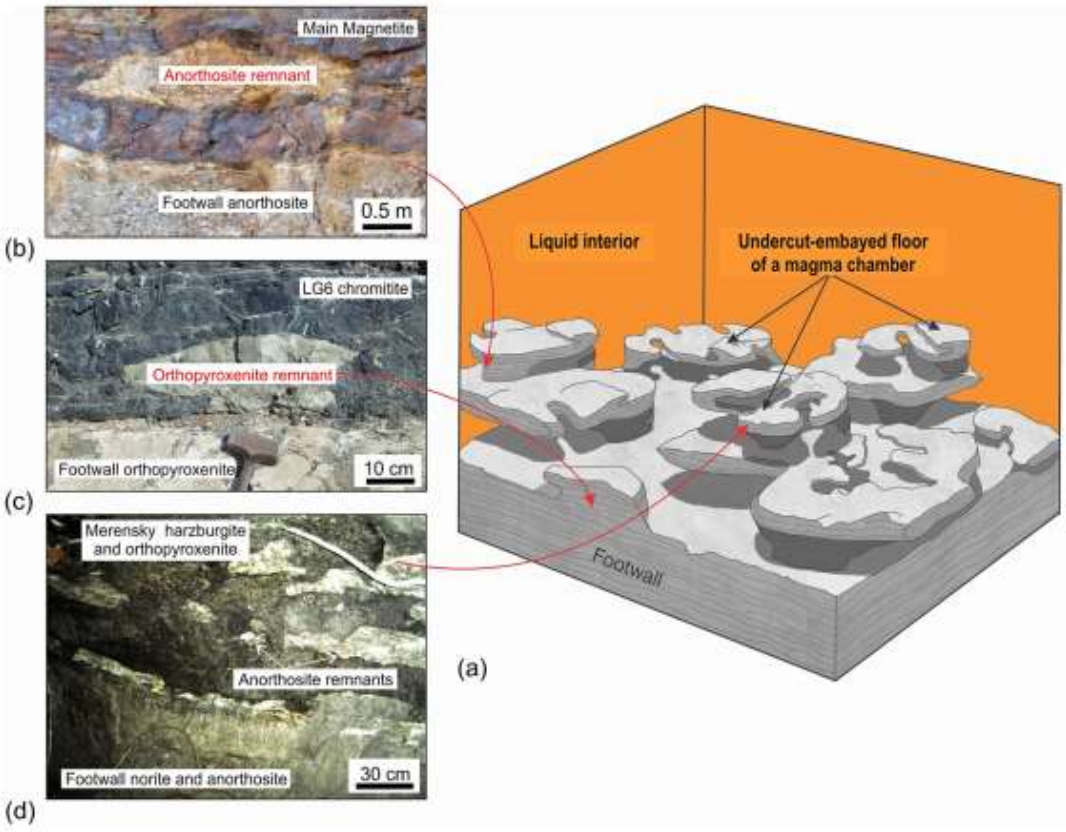

Fig. 15. Artistic impression of the undercut-embayed chamber floor in an evolving magma chamber along with photographs of relevant exposures. (a) When the undercut-embayed floor is observed in three dimensions, it becomes obvious that most seemingly isolated 'inclusions' in two dimensions are actually connected with each other to produce an intricate three-dimensional framework of partially eroded floor cumulates. The process responsible for the formation of such a floor is referred to as here as magmatic 'karstification'. The undercut-embayed floor is expected to be common in open magma chambers. (b) Photograph of an erosional remnant of anorthosite that is hosted by the Main Magnetite Layer and is still attached to the footwall rocks. Vametco Vanadium Mine, Upper Zone of the Western Bushveld Complex. (c) Photograph of an erosional remnant of orthopyroxenite that is hosted by the Lower Group 6 (LG6) chromitite and is still attached to the footwall rocks. Jagdlust area, Lower Critical Zone of the Eastern Bushveld Complex. (d) Photograph of in situ erosional remnants of anorthosite that are hosted by the Merensky Reef orthopyroxenite and seemingly not attached to the footwall rocks in this section. Rustenburg Platinum Mine, Upper Critical Zone of the Western Bushveld Complex. Red arrowed curves indicate possible positions of these 2D exposures in the 3D space of the undercut-embayed chamber floor. Modified from Kruger and Latypov (2021). (For interpretation of the references to colour in this figure legend, the reader is referred to the web version of this article.)

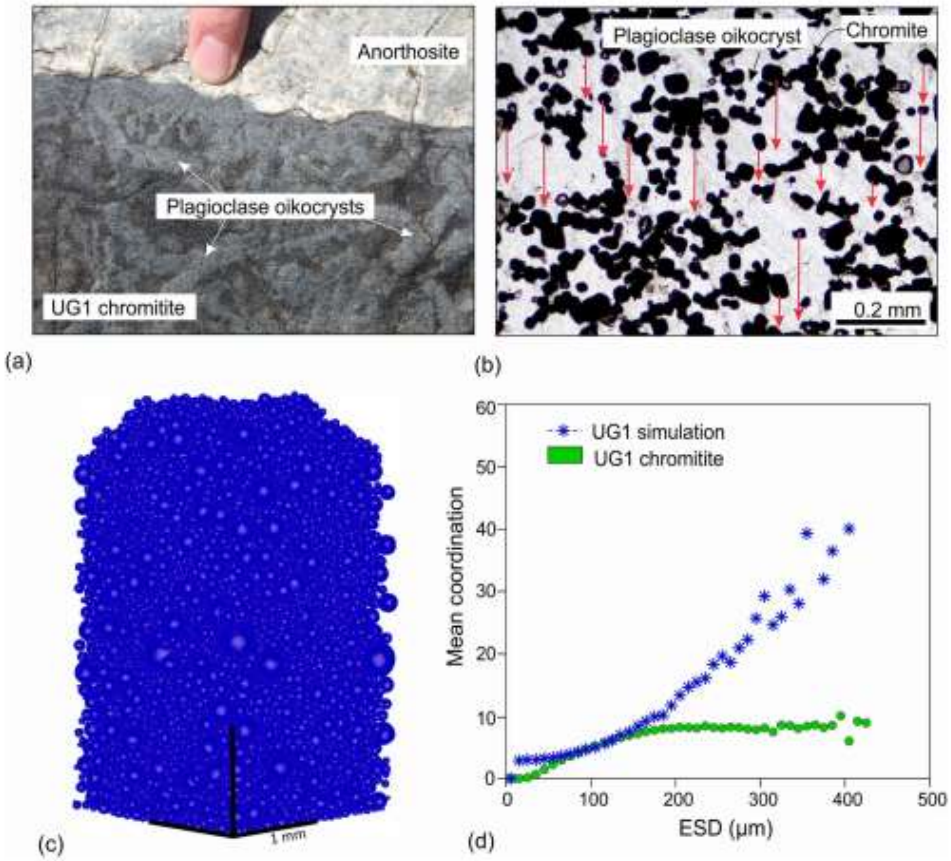

Fig. 16. Comparison of the observed natural data and results of numerical simulation indicating the absence of evidence for the mechanical accumulation of isolated single grains of chromite crystals within the UG1 chromitite of the Bushveld Igneous Complex. (a) The top of the UG1 chromite sublayer, Dwars River, eastern Bushveld Complex. Note large plagioclase oikocrysts enclosing numerous small crystals of cumulus chromite (chadacrysts). (b) Photomicrograph (under plane polarised light) of the UG1 chromitite, with a chromite mode of 27 vol% showing apparently isolated chromite grains and loose clusters enclosed by a single large oikocryst of plagioclase. Red arrows emphasize chromite grains that are apparently isolated and unsupported in the 2D section, most likely because they are attached to others out of the plane of the section. (c) 3D simulation of spheres of the same size distribution as chromite grains in the UG1 chromitite, forming a maximum random packing, which results in a chromite mode of ~60%. (d) Plot showing mean coordination number (i.e., the number of other chromite grains each grain touches) of all grains within each size range bin, as a function of size range of chromite grains in the maximum random packing assuming accumulation of isolated grains and in the UG1 chromitite (ESD: equivalent sphere diameter). Modified from Latypov et al. (2022a). (For interpretation of the references to colour in this figure legend, the reader is referred to the web version of this article.)

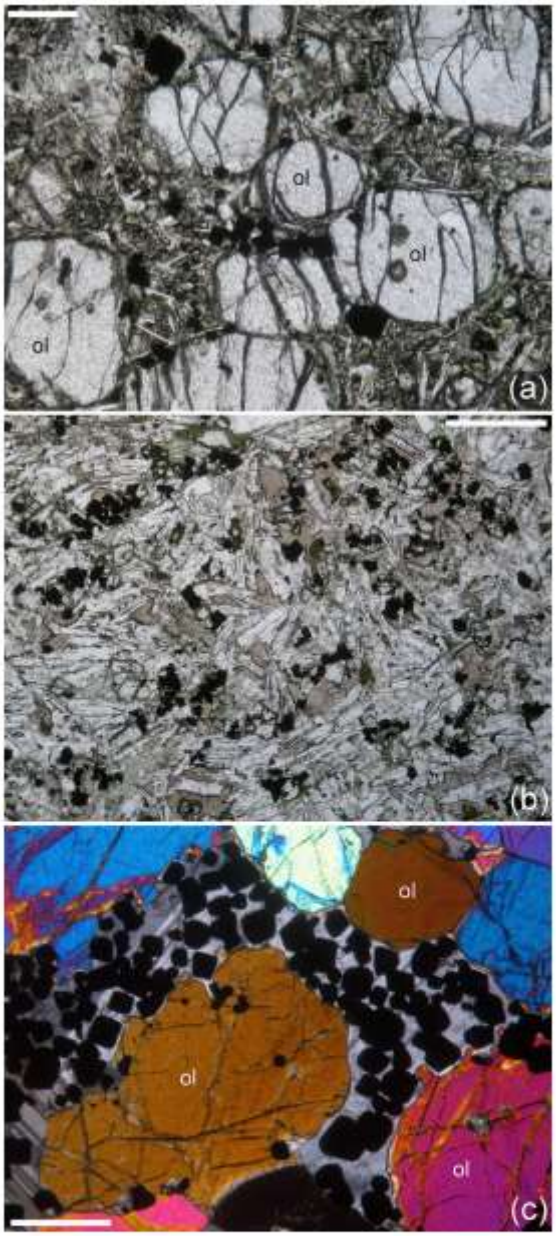

Fig. 17. Photomicrographs of chains and clusters of spinel-group minerals. (a) clusters of olivine (ol) and chromite (opaque) crystals forming the cargo of the Palaeogene 2 m thick Applecross Sill, NW Scotland, hosted by a fine-grained groundmass. Note how the chromite grains form elongate clusters that appear as chains in the 2D section. Plane polarised light. Scale bar is 250 μm long. (b) Palaeogene basaltic lava flow from Skye Main Lava Series, Talisker, Skye, comprising elongate euhedral plagioclase (clear) with anhedral pyroxene (pale brown) and clusters of euhedral magnetite grains (black). Plane polarised light. Scale bar is 500 μm long. (c) Detail of a 1 cm thick chromite stringer in the Unit 10 peridotite of the Rum Eastern Layered Series, photographed under crossed polars. The euhedral chromite grains (black) form clusters in the pore spaces between larger olivine primocrysts. Scale bar is 1 mm long. (For interpretation of the references to colour in this figure legend, the reader is referred to the web version of this article.)

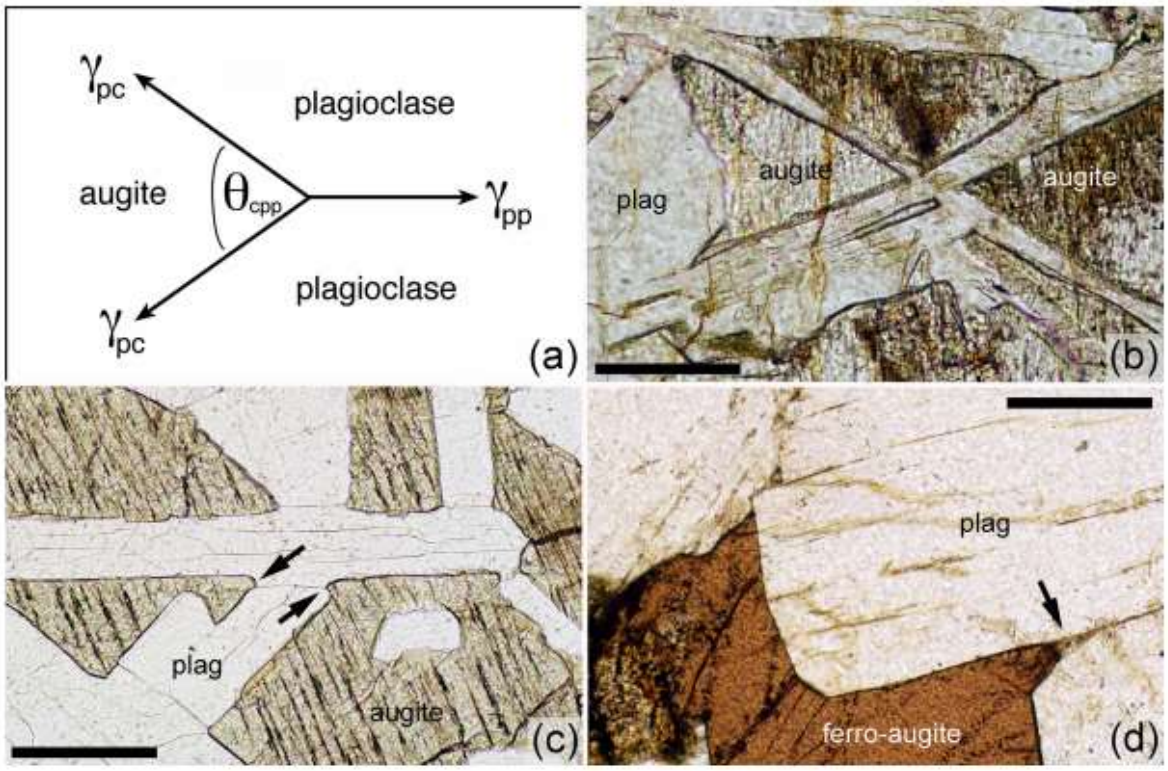

Fig. 18. (a) Cartoon showing the geometry of three-grain junctions formed of augite and plagioclase: the dihedral angle is denoted Θ_{cpp}. (b), (c) and (d) are photomicrographs of thin sections, taken in plane polarised light. (b) Dolerite from the Portal Peak sill, Antarctica. All three-grain junctions between two grains of plagioclase (plag) and one of augite are formed by the meeting of planar plagioclase-augite grain boundaries. Scale bar is 200 mm long. (c) Gabbro from the Lower Zone of the Skaergaard intrusion, East Greenland, showing details of junctions between augite and plagioclase. Note the pronounced curvature of the augite-plagioclase grain boundaries into the three-grain junction (examples are arrowed). Some of this curvature is asymmetric, typical of gabbros in which augite grows as a primocryst phase (Fowler and Holness, 2022). Scale bar is 200 mm long. (d) Ferro-gabbro from the Upper Zone of the Skaergaard intrusion, East Greenland. The three-grain junctions are formed by the meeting of planar grain boundaries between ferro-augite and plagioclase, despite the slow cooling rate: this is attributable to the cessation of plagioclase growth from the highly evolved late-stage liquid. Note the pocket of granophyric material (arrowed) in the pore corner, showing that growth of both pyroxene and plagioclase ceased before the three-grain junction could form. Scale bar is 200 mm long.

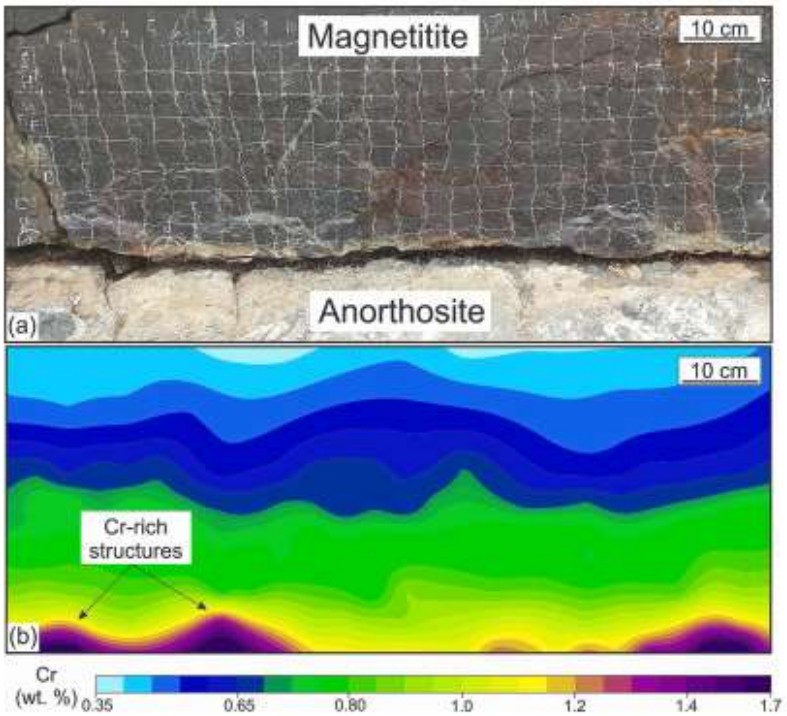

Fig. 19. Magnetitite Layer and corresponding geochemical contour map. (a) Photograph of the Main Magnetite Layer and underlying anorthosite. The magnetitite was analyzed using a portable XRF spectrometer on the grid pattern. (b) Geochemical map based on the distribution of Cr in the layer. Notice at least three Cr-rich, dome-shaped structures at the base of the layer. Modified from Kruger and Latypov (2020).

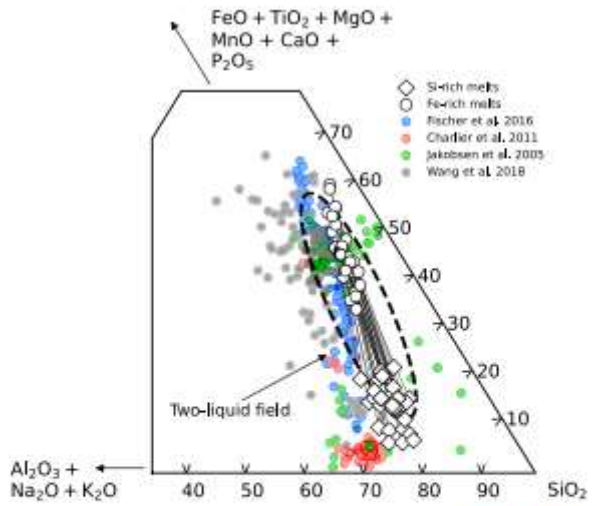

Fig. 20. Pseudo-ternary diagram with immiscibility field of Roedder (1951) in the leucite-fayalite-silica system. Full black circles illustrate immiscible inclusions from Jakobsen et al. (2005), Charlier et al. (2011), and Fischer et al. (2016). Full grey circles are immiscible inclusions from Wang et al. (2018). Open circles are experimental Fe-rich immiscible melts in equilibrium with Si-rich melt (open diamonds) from experimental studies of Dixon and Rutherford (1979), Philpotts and Doyle (1983), Charlier and Grove (2012), and Zhang et al. (2023).

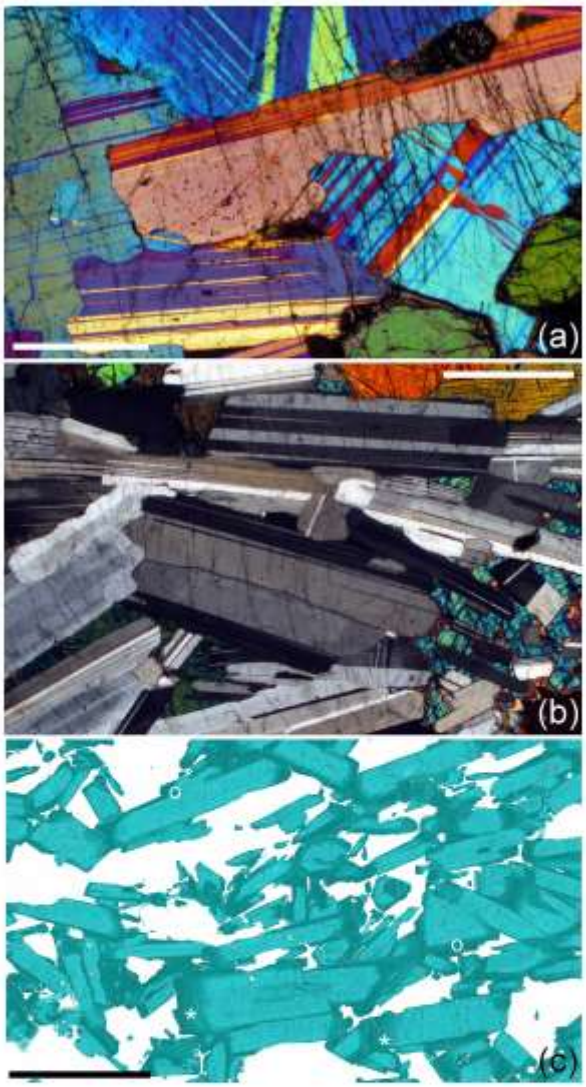

Fig. 21. Images of thin sections from the Skaergaard Intrusion of East Greenland. (a) Gabbro from the Marginal Border Series, which grew in situ on the vertical walls of the Intrusion, photographed under crossed polarised light with a sensitive tint plate inserted. Note the highly irregular grain boundaries between adjacent plagioclase grains. Very few of these grain boundaries are parallel to growth faces of the plagioclase. Scale bar is 1 mm long. (b) Gabbro from the Skaergaard floor cumulates, in which plagioclase primocrysts show a well-developed shape preferred orientation. The grain boundaries are either parallel, or close to, (010), which is the dominant growth face. Any late-stage growth, evident by compositional zoning, is confined to the ends of the elongate laths, demonstrating that grain boundaries parallel to the large (010) faces were formed by the mechanical juxtaposition of equant grains. Scale bar is 1 mm long. (c) Chemical map of plagioclase primocrysts from the lower part of the Skaergaard floor cumulates, with the darker shades of teal showing a more albitic composition (the white areas denote phases other than plagioclase). Note the constant composition cores, and the albitic rims. While many grains show continuous normal zoning (examples are shown by an asterisk), others show an outer rim of constant composition, formed during thermal buffering by latent heat release (examples are shown by white circles). Scale bar is 2 mm long. (For interpretation of the references to colour in this figure legend, the reader is referred to the web version of this article.)

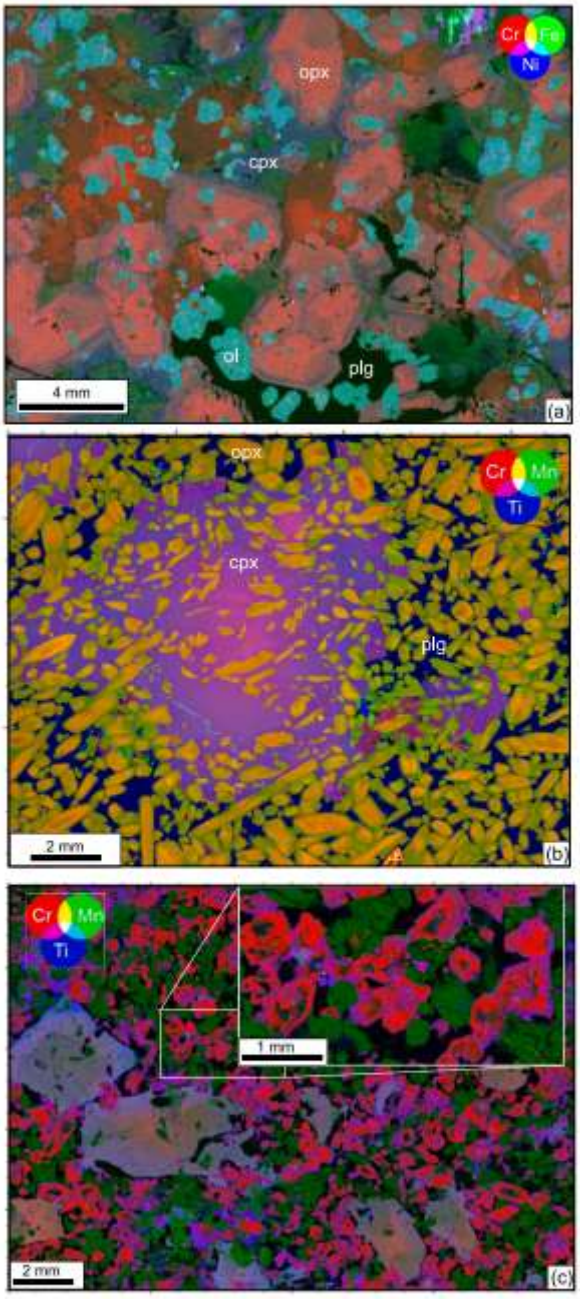

Fig. 22. Pyroxene zoning (in progress). (a) Combined sector and oscillatory zoning in Opx, Huangshanxi, China. (b), Sector and normal zoning in cpx oikocryst, normal zoning (high to low Cr) in Opx, Rytky Intrusion, Finland. (c) Sector zoning in euhedral opx oikocrysts, complex oscillatory zoning in cumulus Cpx, Kevitsa, Finland. SXRF false-colour element maps.

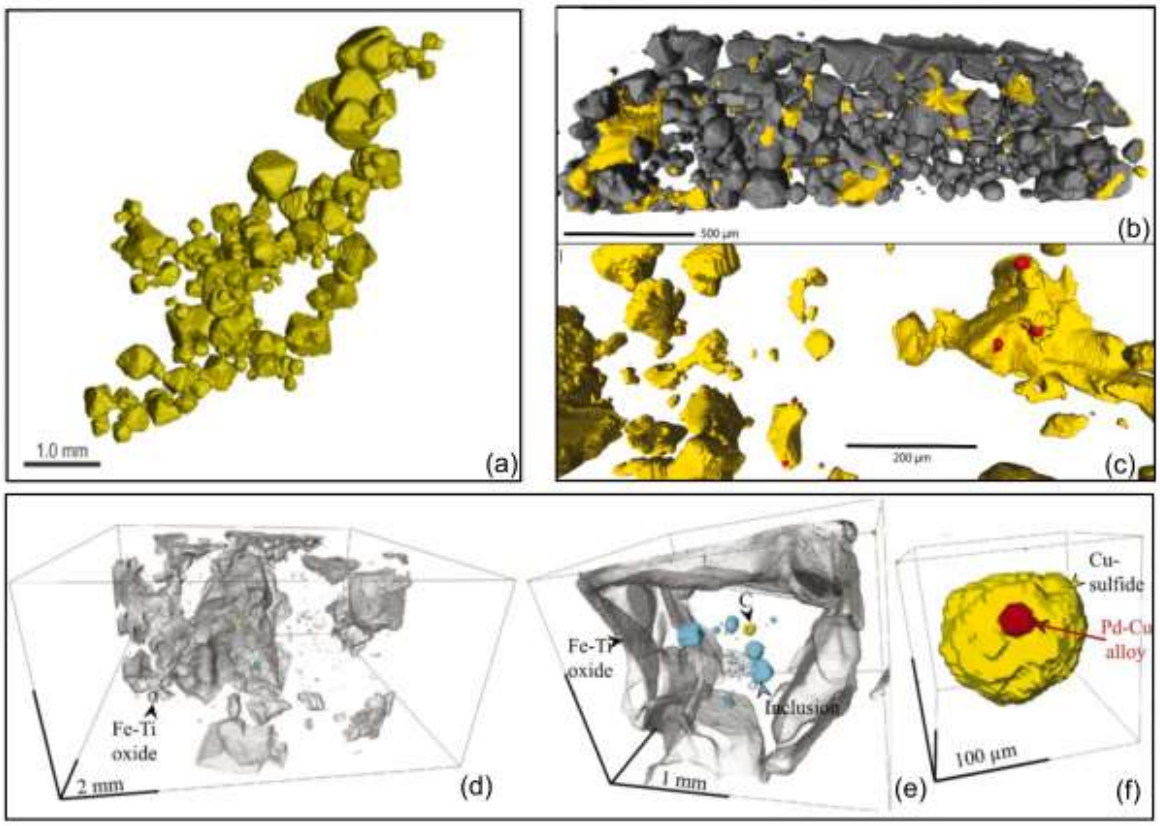

Fig. 23. Images from X-ray microtomography on magmatic PGE-Au and chromite. (a) chromite (yellow) from the UG1 seam, Bushveld, showing characteristic open framework structure of connected grains. (b, c) – Merensky Reef, Bushveld Complex - chromite (grey), sulfide (yellow), PGMs (red) showing the location of most PGMs at the margins of sulfide blebs in contact with chromite, modified from (Godel et al., 2010). (d, e, f) Platinova Reef, Skaergaard, showing location of composite Cu sulfide- Cu—Pd alloy droplets and silicate melt inclusions inside cumulus ilmenite (grey). Modified from Godel et al. (2014). (For interpretation of the references to colour in this figure legend, the reader is referred to the web version of this article.)

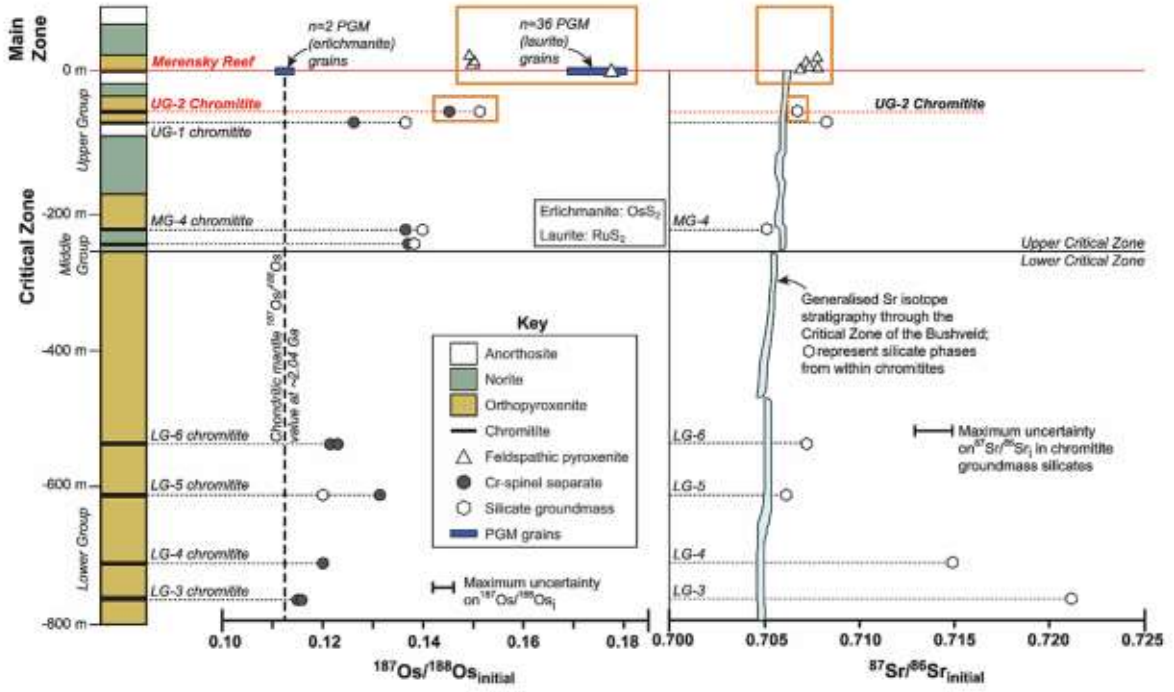

Fig. 24. Sketch of a portion of the Bushveld stratigraphy (left), showing the variation of $^{187}Os/^{188}Os_{initial}$ and $^{87}Sr/^{86}Sr_{initial}$ in the Critical Zone, modified from Schoenberg et al. (1999). The key observation is that there are positive step-changes in both isotopic ratios (in $^{187}Os/^{188}Os_{initial}$, relative to chondrite, and in $^{87}Sr/^{86}Sr_{initial}$) for the Merensky Reef and the UG-2 chromitite (both horizons highlighted in red), relative to the bulk stratigraphy of the Bushveld cumulates). These data are signposted by the orange boxes in the figure. Notably, other Bushveld chromitites show excursions to more radiogenic compositions for both isotopic systems as well. The plot of *Sr* isotope variation with stratigraphy (in grey) are replotted from Kruger (1994). (For interpretation of the references to colour in this figure legend, the reader is referred to the web version of this article.)

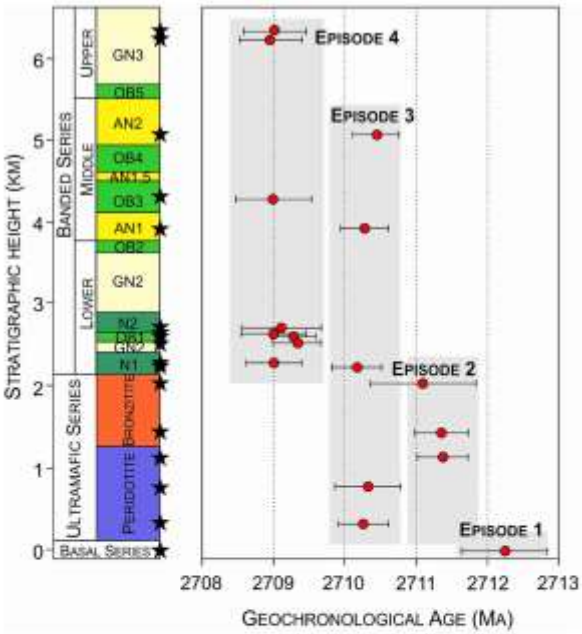

Fig. 25. Chronostratigraphic summary of high-precision U—Pb dating results for zircon from mafic-ultramafic rocks of the Stillwater Complex (data from Wall et al., 2018 but modified from Latypov, 2019). Simplified stratigraphic column of the Stillwater Complex; solid lines indicate contacts between major zones and series. Stars indicate the relative stratigraphic locations of the dated samples. Abbreviations on the section: N1 = Norite zone 1, GN1 = Gabbronorite zone 1, OB1 = Olivine-bearing zone 1, N2 = Norite zone 2, GN2 = Gabbronorite zone 2, OB2 = Olivine-bearing zone 2, AN1 = Anorthosite zone 1, OB3 = Olivine-bearing zone 3, AN1.5 = Anorthosite zone 1.5, OB4 = Olivine-bearing zone 4, AN2 = Anorthosite zone 2, OB5 = Olivine-bearing zone 5, GN3 = Gabbronorite zone 3. Weighted $^{207}Pb/^{206}Pb$ dates for samples at their relative stratigraphic height; width of error bars indicates ±2σ uncertainties. The ages are subdivided into four major time episodes - at about 2712, 2711, 2710, and 2709 *Ma*. The ages do not become systematically younger from the base towards the top of the complex and are, therefore, referred to as out-of-sequence.

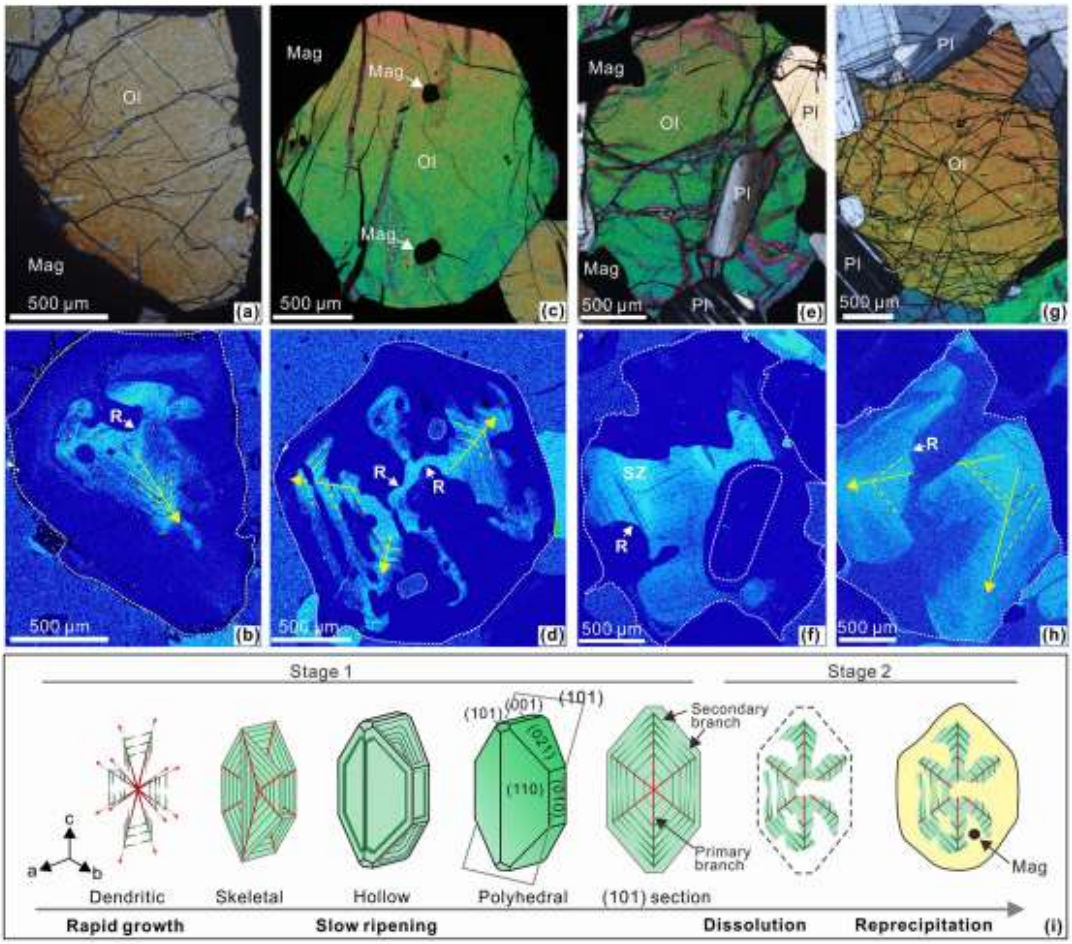

Fig. 26. Phosphorus zoning of olivine (Ol) from layered intrusions. Photomicrographs (a, c, e, g) and P intensity maps (b, d, f, h) of olivine from the Baima intrusion (a, b), the Sept Iles intrusion (c-f) and the Bushveld complex (g, h). The P-rich zones can be clearly identified as skeletal (b, h), dendritic (d) and sector-zoned (SZ) (f) patterns despite of variable degrees of dissolution in olivine. Primary P-rich branches propagating towards crystal corners are marked as yellow arrow and secondary branches developing along the plane are shown in yellow dash line (b, d, h). The resorption surface is marked as R (b,d,f,h). Note that fine-grained magnetite (Mag) and plagioclase (Pl) are enclosed in the P-poor olivine domains (d, f). A schematic cartoon illustrating a two-stage growth process of olivine (i): Stage 1 initiates with rapid growth of dendritic olivine and slow ripening to polyhedral olivine (adopted from Xing et al., 2022); Stage 2 is triggered by chemical dissolution of polyhedral olivine and subsequent reprecipitation of P-poor olivine domains from ambient, evolved interstitial liquid. (a-b) are modified from Xing et al. (2017), and (c-f) are modified from Xing et al. (2022). (For interpretation of the references to colour in this figure legend, the reader is referred to the web version of this article.)

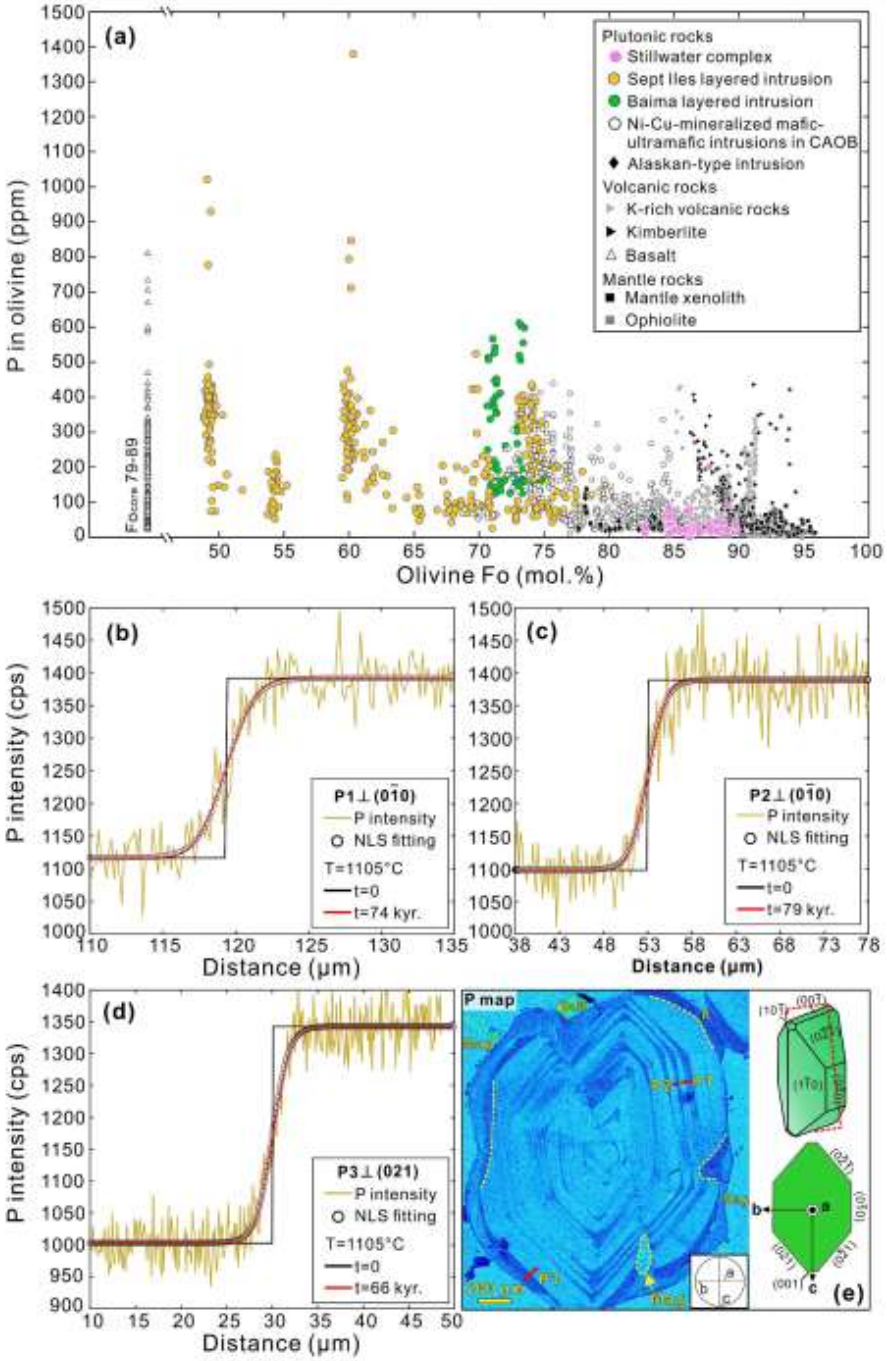

Fig. 27. Binary plot of *Fo* content versus P concentration for the olivine from different types of the rocks (a) and 1-D diffusion modelling for P gradients of olivine from the Sept Iles layered intrusion (b-e). The positions of P X-ray intensity profiles in (b-d) are marked in the P map of olivine (e), which is surrounded by a matrix of magnetite (Mag), ilmenite and sulphide (Sulf). The resorption surface (R) is marked by dashed line. The inset in (e) showing lower hemisphere equal area projection of crystallographic axes obtained by electron backscattered diffraction (EBSD). A 3-D olivine crytstal model in (e) showing the cross section of the P map. Data sources in (a): Stillwater complex, Alaskan-type intrusion and ophiolite (Wang et al., 2021), Sept Iles (Xing et al., 2022), Baima (Xing et al., 2017), Ni-Cu-mineralised mafic-ultramafic intrusions in CAOB (Mao et al., 2022), K-rich volcanic rocks (Ersoy et al., 2019), kimberlite (Howarth and Gross, 2019), basalt (Lynn et al., 2020), mantle xenolith (De Hoog et al., 2010; Wang et al., 2021). (b-e) are modified from Xing et al. (2022).

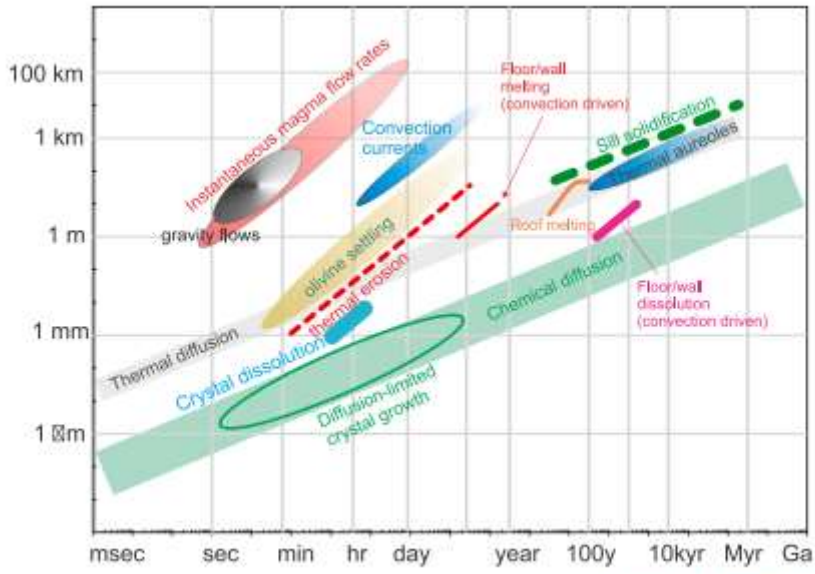

Fig. 28. Length and time scale plot for layered intrusion processes, modified from Barnes and Robertson (2019).

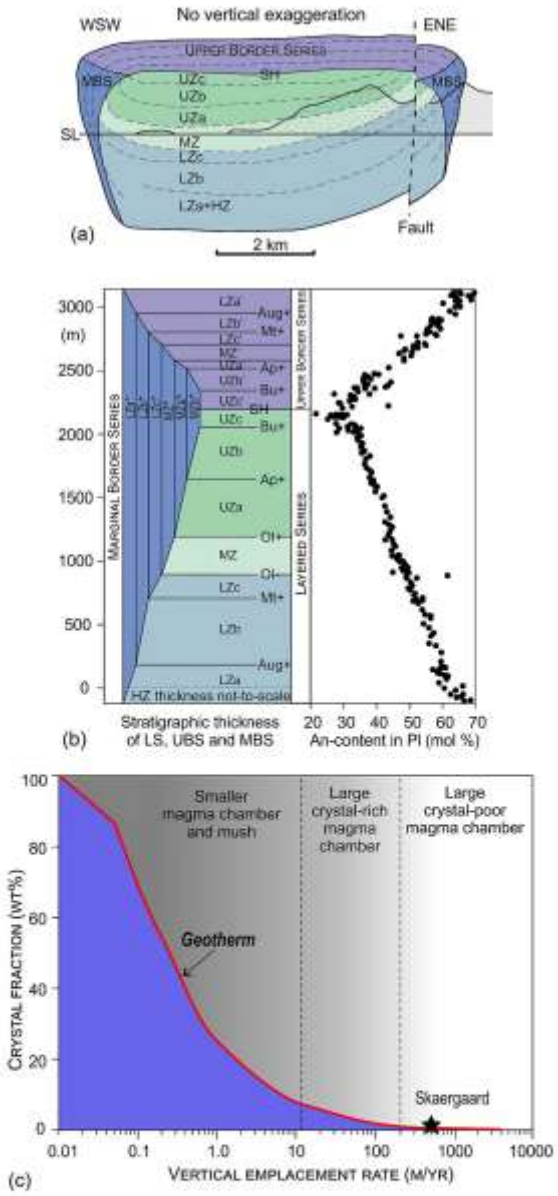

Fig. 29. Geology and stratigraphic section of the Skaergaard layered intrusion and the crystal fraction (wt%) versus magma emplacement rate (m/yr) in its magma chamber. The Skaergaard intrusion is subdivided into three major petrological units: the Layered Series (LS), Upper Border Series (UBS), and Marginal Border Series (MBS), crystallized concurrently along essentially parallel trends of differentiation. The LS formed on the floor, while the UBS crystallized under the roof and MBS at the wall. (a) E–W section through the Skaergaard intrusion. (b) The three fronts of crystallization converged at the Sandwich Horizon (SH) as indicated by the mirror images of the cumulus phase arrivals and An-content of plagioclase in LS and UBS, the MBS follows a similar trend (not shown). (c) The results of numerical simulation show that the minimum vertical emplacement rate that allows for a large, crystal-free chamber to grow without onset of crystallization along its margins is of the order of several 100 s to a few 1000s m/yr (black star for Skaergaard). HZ – Hidden Zone, LZ – Lower Zone, MZ – Main Zone, UZ – Upper Zone, SL – Sea Level; Ol, olivine, Aug, augite; Mt., magnetite, Ap, apatite, Bu, (ferro)bustamite. An-content = 100An/(An+Ab). Modified from Annen et al. (2022).

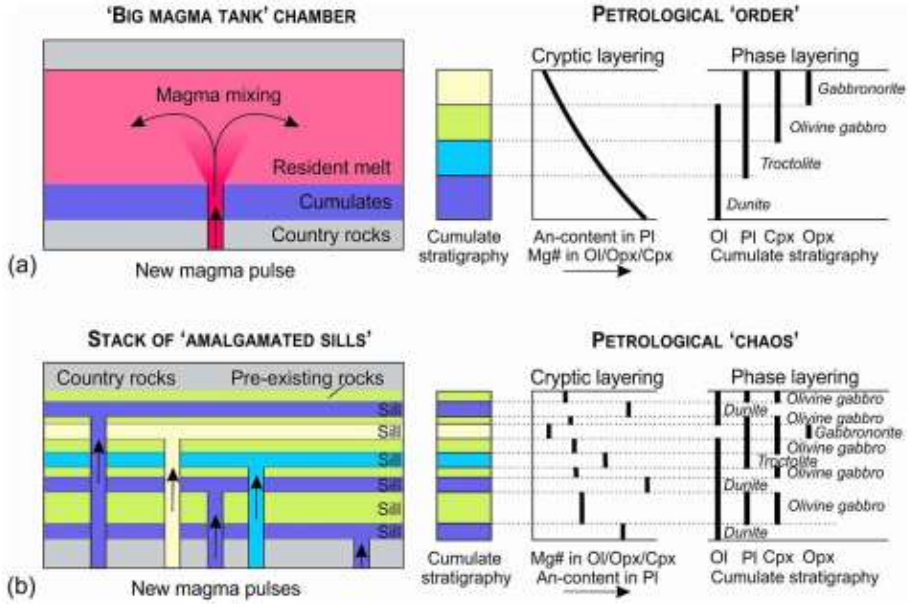

Fig. 30. Two contrasting views on development of mafic layered intrusions in Earth's crust. (a) A "big magma tank" is supposed to develop as a large magma chamber either from the very beginning (e.g., Skaergaard intrusion) or grow incrementally through the numerous magma replenishments as indicated in this figure (e.g., Bushveld Complex). This second scenario is much more common in nature. The crystallization and differentiation of resident melt in the "big magma tank" chamber results in the formation of a layered intrusion with a systematic crystallization sequence (phase layering) and mineral compositional trends (cryptic layering) as expected from liquidus phase equilibria. (b) A stack of 'amalgamated sills' is supposed to form by random emplacement of sills into pre-existing, already solidified rocks. The sills are free to intrude any time, any place and have any size and chemical composition and, therefore, a magmatic body produced in this way is expected to show chaotic crystallization sequences (phase layering) and mineral compositional trends (phase layering) that have little to do with those expected from liquidus phase equilibria. Abbreviations are used in figures and text: Ol, olivine, Opx, orthopyroxene; Pl, plagioclase; Cpx, clinopyroxene; Mg-number = 100 Mg/(Mg + Fe); An-content = 100An/(An+Ab). Modified from Latypov and Chistyakova (2022).

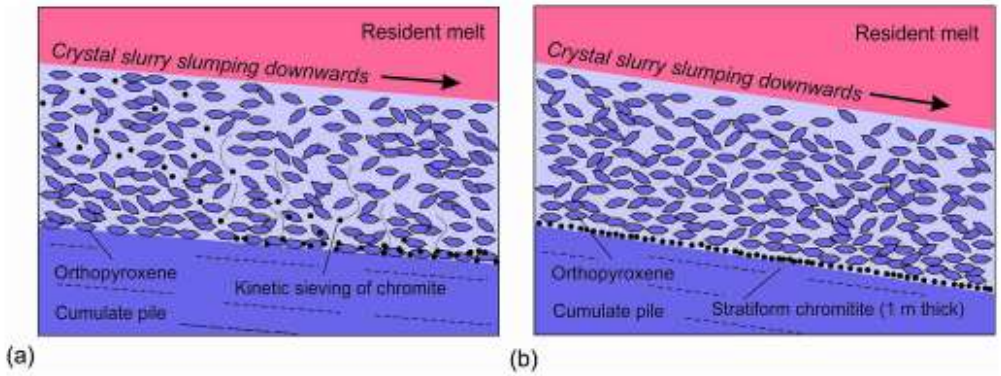

Fig. 31. A sketch of the model proposed by Maier et al. (2013) for the formation of igneous layering involving massive chromitites. They suggest that crystal-free melt replenishes a magma chamber and crystallises into a thick pile of crystal-rich slurry. In response to central subsidence the slurry slums downwards (a) and chromite segregates from silicate minerals by kinetic sieving to form the massive chromitite at the base of the slurry (b). Modified from Latypov et al. (2017b).

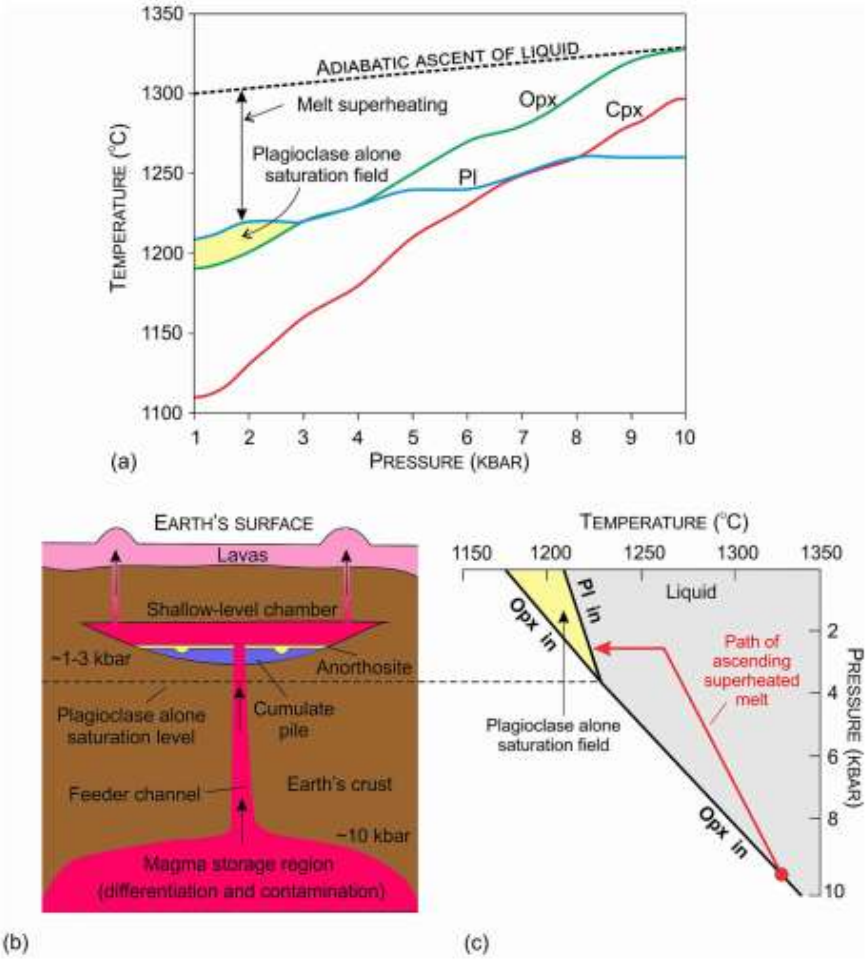

Fig. 32. (a) Thermodynamic modelling illustrating the mechanism via which alumina-rich, basaltic-andesite melts become saturated in plagioclase alone by pressure reduction. The curves show the temperature of the first appearance for each mineral phase at any pressure from 1 to 10 kbar. The alumina-rich basaltic-andesite melt saturated in orthopyroxene at high pressure conditions (along the interval from 10 to 3 kbar) becomes saturated in plagioclase alone as the first liquidus phase, followed by orthopyroxene, at low pressures (P < 3 kbar). Note that adiabatic ascent of the crystal-free melts from a deep-seated storage region towards the Earth's surface may result in melt superheating with respect to their liquidus temperature. (b) A physical model for the formation of stratiform anorthosites from basaltic-andesite melts that becomes saturated in plagioclase alone due to reduction in lithostatic pressure. Basaltic-andesite melts ascending from lower crustal storage regions experience reduction in lithostatic pressure. This results in expansion of plagioclase stability volume and, as a result, some basaltic-andesite melts saturated in orthopyroxene at high-pressure regions may become, after some cooling, saturated in plagioclase alone at lower pressure in shallow chambers. Early and almost perfect fractional crystallization of these plagioclase-saturated melts, in an open system where magma can also flow out of the chamber, will produce monomineralic layers of anorthosite. (c) Phase relations for a basaltic melt in P-T space illustrating the model that basaltic-andesite melts saturated in orthopyroxene first become slightly superheated during their ascent and then saturated in plagioclase alone after stalling and cooling in shallow-level chambers. Therefore, allowing for the development of stratiform anorthosite in shallow-level chambers. Modified from Latypov et al. (2020a).

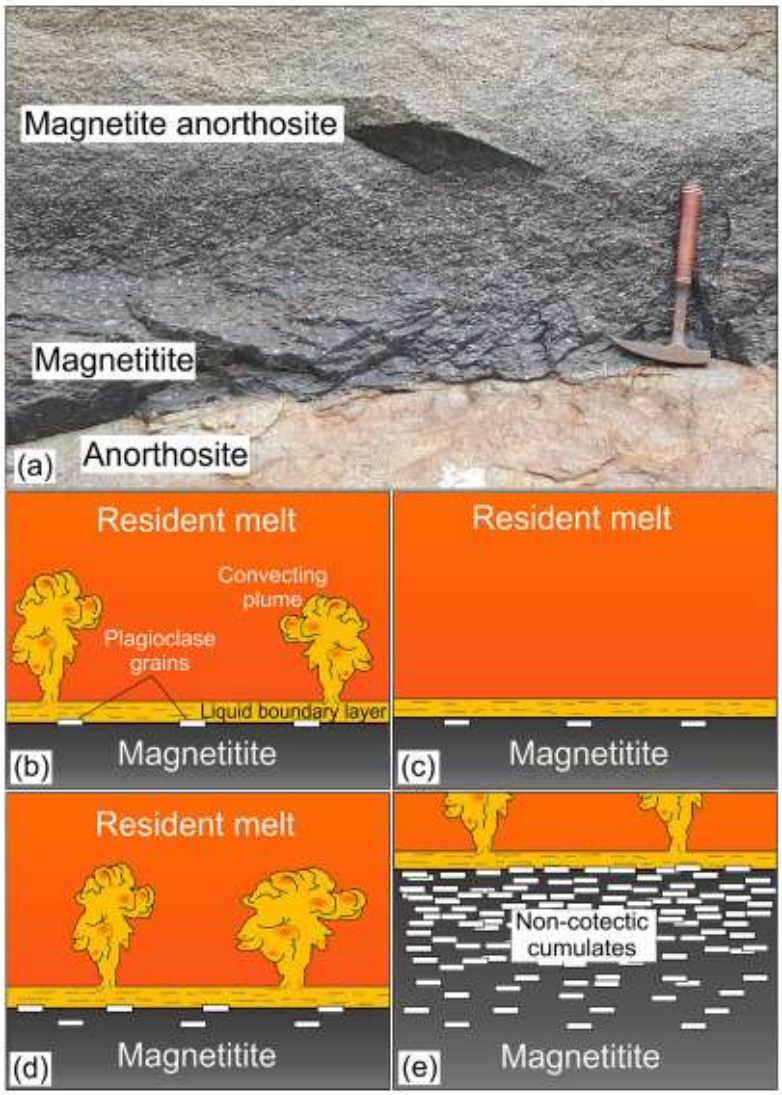

Fig. 33. Appearance of and petrogenetic model for the upper gradational contact of Bushveld massive magnetitite layers. (a) Photograph of a magnetitite layer from the eastern Bushveld Complex. The layer is characterized by a sharp basal contact with an anorthosite layer, and a gradual upwards increase in plagioclase content into a magnetite anorthosite. Hammer measures 40 cm in length. (b) During magnetite crystallization, the liquid undergoes evolution by the convective removal of compositional boundary layers, initially leading to the crystallization of pure magnetite. Eventually, due to magmatic differentiation, plagioclase finally appears in a boundary layer. (c) However, as the boundary layer is removed from the solidification front, liquid saturated in magnetite comes into contact with it, and magnetite-only crystallization resumes. Thus, cumulates are produced that do not correspond to the expected cotectic proportions of magnetite to plagioclase. (d) When plagioclase re-appears in subsequent boundary layers, its abundance increases due to continued differentiation of the resident melt. (e) This process leads to a gradual increase in plagioclase abundance upwards as the layer transitions to magnetite anorthosite. Modified from Kruger and Latypov (2022).

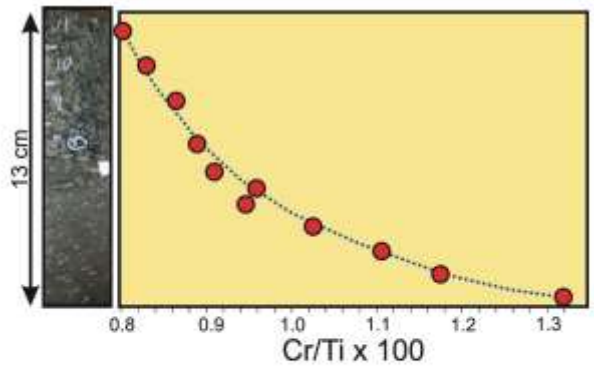

Fig. 34. Variation in the Cr/Ti ratio across the upper gradational contact of the bottom seam (the lowermost magnetitite layer in the Western Limb of the Bushveld Complex). Cr/Ti ratios are plotted to eradicate feldspar contamination. Since Ti concentrations are more or less constant across magnetitite layers, the ratio largely reflects variation in the Cr content of magnetite. The results reveal a remarkably regular and steep depletion upwards which suggests very short distance settling or in situ crystallization. Such a chemical pattern poses a problem for the origin of non-cotectic cumulates by the means of crystal settling or sorting of crystal slurries. Modified from Kruger and Latypov (2022).

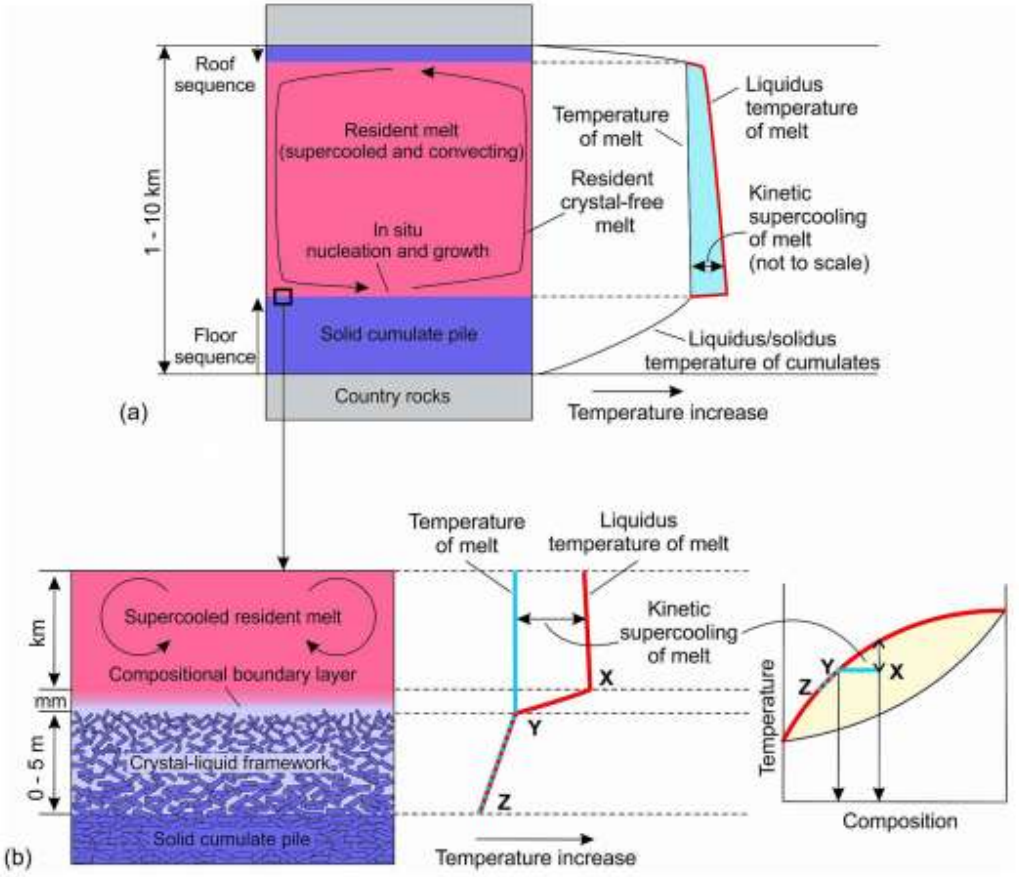

Fig. 35. A generalized view of a long-lived and largely molten basaltic magma chamber. (a) The magma chamber is considered to develop as a central body of the crystal-free resident melt which predominantly nucleates and crystalizes in situ along the margins of the chamber. This occurs because such magma chambers cool slowly and cannot, therefore, attain the degree of supercooling that is necessary for homogeneous nucleation within the resident melt. The resident melt passes to solidifying rocks at the margins through an inward advancing solidification front. The resident melt is kept persistently supercooled with respect to both newly-arriving liquidus phases and the existing ones that are already crystallizing in a solidification front along the chamber margins. In a homogeneous magma the melt temperature changes at about 0.3 °/km, whereas the liquidus temperature changes at about 3.0 °/km. A small rectangle indicates a position of a panel (b) which shows a schematic profile of a solidification front separating the crystal-free resident melt from the solid cumulate pile. A crystal-liquid framework is taken to vary in thickness from zero to a few meters. Minerals in a crystal-liquid framework tend to be in equilibrium with interstitial liquid Z-Y so that only very low supercooling occurs there (not shown). A crystal-liquid framework passes upwards into the resident melt through a few mm thick compositional boundary layer. With moving upwards from in situ growing crystals, the melt in the compositional boundary layer (from Y to X) becomes increasingly more supercooled with respect to liquidus minerals of a crystal-liquid framework. The supercooling of the melt is additionally illustrated using a binary diagram with complete solid solution between two endmembers (e.g., An-Ab). Note that the width of a compositional boundary layer and the degree of its kinetic supercooling are highly exaggerated for illustration purposes. Modified from Latypov et al. (2020b).

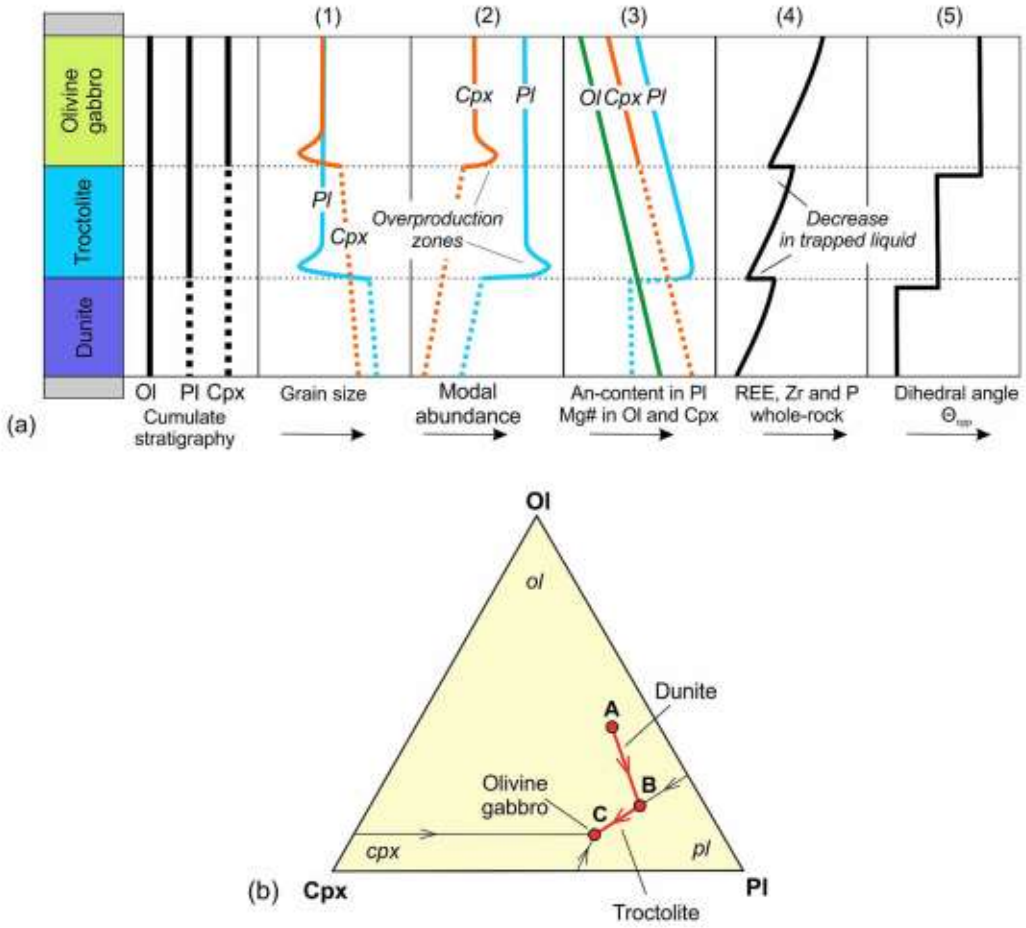

Fig. 36. Summary of textural and chemical features associated with the arrival of new liquidus phases shown against the stratigraphy of a hypothetical layered intrusion produced by closed system fractional crystallization. (a) The cumulate stratigraphy of a layered intrusion produced by internal differentiation of an olivine-saturated basaltic melt A in (b). Solid lines indicate primocrysts (cumulus phases) while dotted lines show oikocrysts (interstitial phases); (b) Fractional crystallization of olivine-saturated basaltic melt A along a crystallization trend Ol (dunite, path A-B), Ol + Plag (troctolite, path B—C), and Ol + Plag+Cpx (olivine gabbro, point C). Abbreviations: Pl, plagioclase; Ol, olivine; Cpx, Ca-rich clinopyroxene; An-content = 100*Ca/(Ca + Na), Mg-number = 100*Mg/ (Mg + Fe^{2+}). Modified from Latypov et al. (2020b).

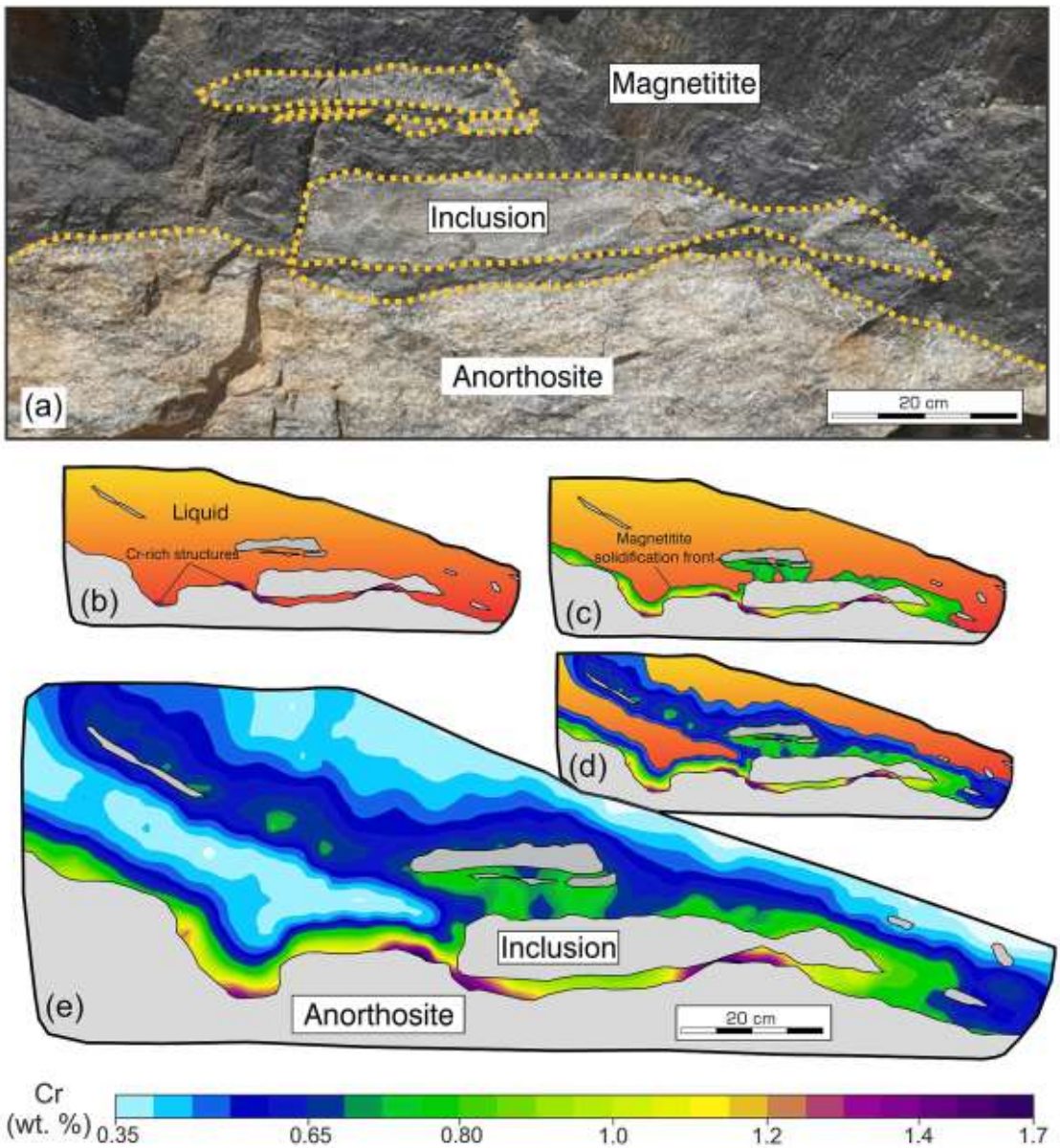

Fig. 37. The progressive propagation of a solidification front within a magmatic karst environment. (a) An outcrop of anorthosite that has undergone magmatic karstification to produce an undercut-embayed chamber floor with interconnected anorthosite inclusions. Rhovan Vanadium mine, Western Bushveld Complex. (b) Magnetite crystallization within the undercut-embayed floor initiates where cooling will be most effective, thus producing growth nodes directly on the floor below the most prominent anorthosite inclusion in the profile and another in a depression to the left. (c) Continued crystallization causes the lower inclusions to become engulfed in magnetite. (d) Growth appears to proceed on unseen inclusions hidden behind the face of the outcrop or have been removed by mining, producing the apparently suspended band of magnetite shown here. (e) Eventually, solid magnetitite wholly fills the entire karst environment. Modified from Kruger and Latypov (2021).

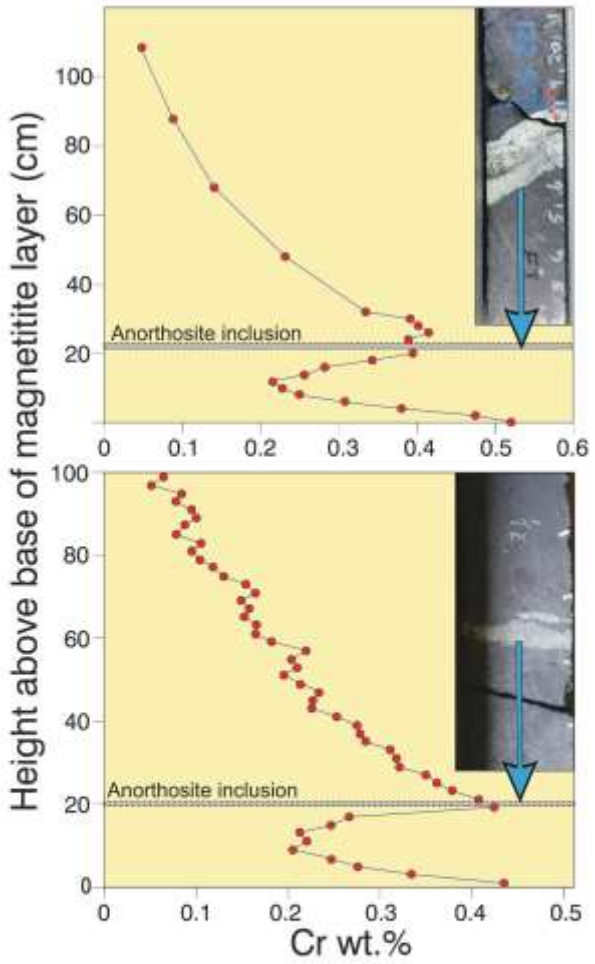

Fig. 38. Variation in Cr contents analyzed by a portable XRF spectrometer throughout the bottom seam (the lowermost magnetitite layer in the Western Limb of the Bushveld Complex) where it contains inclusions of anorthosite. From the bottom upwards, both profiles initially show a decrease in Cr content due to fractional crystallization of the layer. Closer to the inclusions, the trend reverses, and Cr starts increasing. This is attributed to the simultaneous growth of the magnetitite from the chamber floor upwards and from the inclusions downwards. Upwards from the inclusions, Cr contents continue to decrease with continued growth of the magnetitite layer. Modified from Kruger and Latypov (2021).

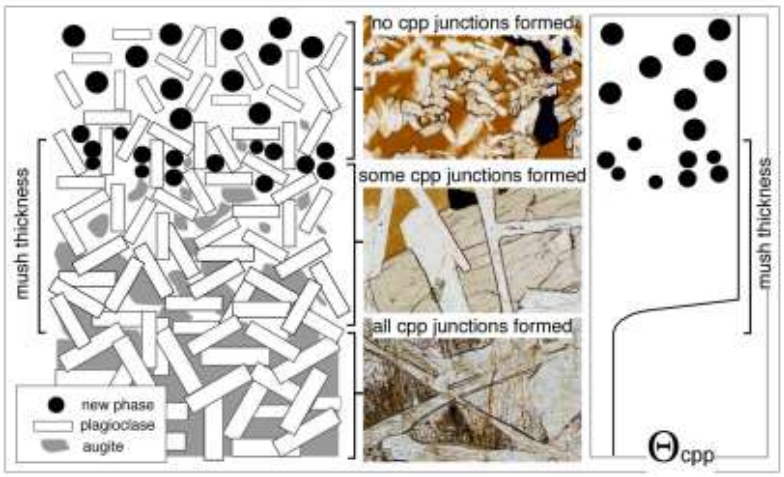

Fig. 39. Schematic cartoon of microstructural variation through a mush zone shortly after the saturation of the bulk magma in a new phase, with illustrative photomicrographs from the crust of the Kilauea Iki lava lake (Hawaii) and the Portal Peak Sill (Antarctica). Immediately before the bulk liquid becomes saturated in the new phase, it nucleates and grows in the highly porous upper layers of the mush. The number of clinopyroxene (augite)–plagioclase–plagioclase (cpp) junctions increases with depth in the mush: all possible junctions have been formed when solidification is almost complete, and therefore marks the base of the mush. The stratigraphic position of the base of the mush at the moment the bulk magma becomes saturated in the new liquidus phase is recorded in the fully solidified cumulate pile by the start of the step-change in Θcpp. The top of the mush at that moment is the horizon where the first homogeneously distributed and abundant primocrysts of the new phase are found.

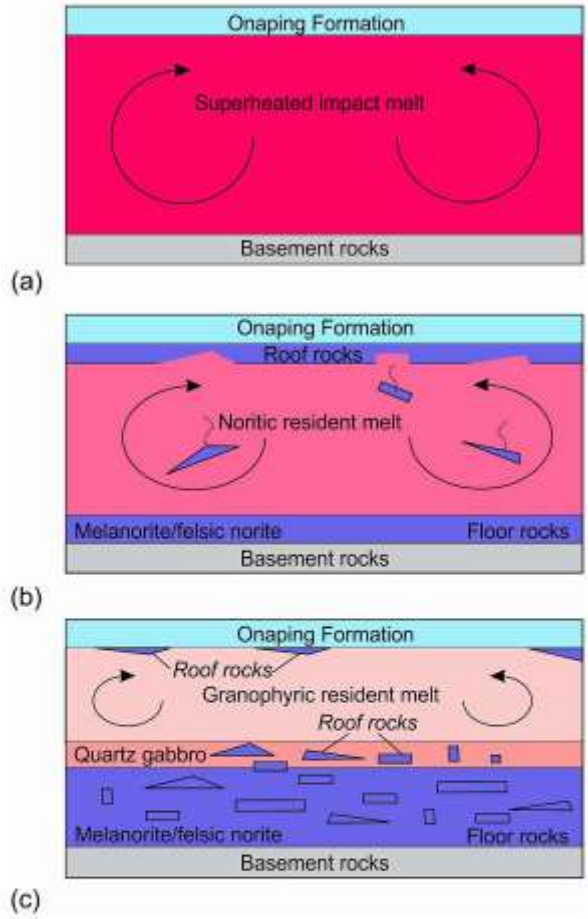

Fig. 40. Model for the proposed formation and disruption of the roof sequence in the SIC. (a) A single, homogeneous layer of superheated impact melt is sandwiched between the shocked basement rocks and overlying fall-back breccia of Onaping Formation. (b) After cooling, the impact melt starts crystallizing melanorite/felsic norite from all margins inwards. Tectonic activity results in the occasional disruption of the gravitationally-unstable roof sequence of melanorite/felsic norite and it collapses as angular blocks on the temporary chamber floor. (c) The process of roof sequence disruption continues during crystallization of quartz gabbro and by the time of granophyre crystallization, almost the entire roof sequence was destroyed and contributed to the total sequence of the floor cumulates. The remnants of the original roof sequence of melanoritic composition are still locally preserved along the top contact of the SIC. Modified from Latypov et al. (2019a).

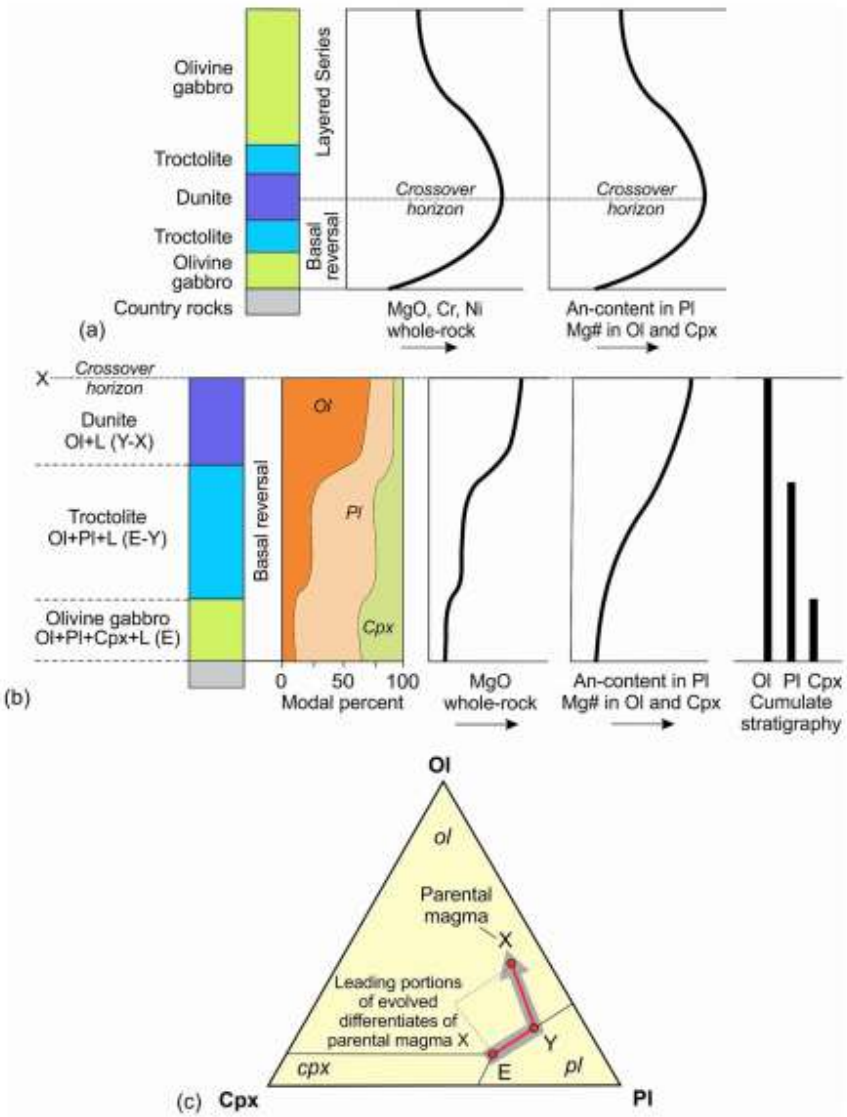

Fig. 41. Section (a) illustrating a fully-developed basal reversal in mafic sills and layered intrusions. It shows crystallization sequences and whole-rock compositional trends that are the opposite of those in the overlying Layered Series into which they pass via a crossover horizon with the most primitive rock composition. The anatomy of the basal reversal is shown at greater detail at (b). The reversal is interpreted as produced from the batches of evolved magma, following the path E, Y, X in (c), derived from parental magma X lying in the olivine field in the ternary system *Ol-Pl-Cpx*. The evolved differentiates are supposed to have resulted from fractional crystallization of the parental magma during its ascent through feeder channels. The basal reversal shows a reverse crystallization sequence *Ol + Pl + Cpx*, *Ol + Pl*, *Ol* with approximately cotectic proportions of the crystallizing phases, reverse trends in whole-rock MgO, and reverse trends in An-content in plagioclase and Mg# of olivine and clinopyroxene. Abbreviations: Pl = plagioclase, Ol = olivine, Cpx = Ca-rich pyroxene, An = 100*An/(An+Ab); Mg# = 100*Mg/ (Mg + Fe). Modified from Latypov (2015).

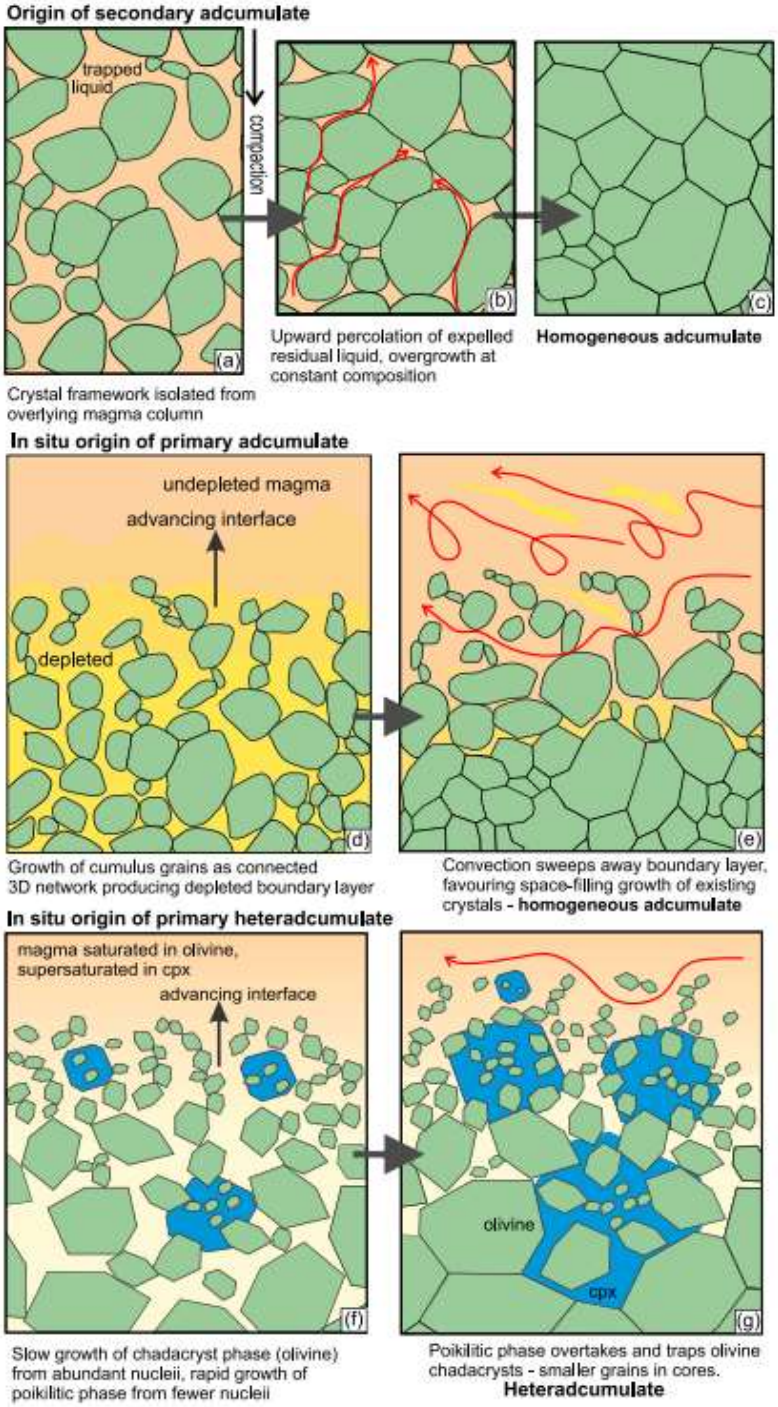

Fig. 42. Models for adcumulate/ heteradcumulate growth. (a-c) conventional cumulus theory model for formation of accumulate by compaction, annealing and liquid expulsion of original mechanically accumulated crystals within the crystal pile, (d, e) model for origin of adcumulate textures by in situ nucleation and growth of cumulus crystals (assumed to be olivine in this example) at top of crystal pile, aided by convective removal of depleted boundary layer around growing cumulus grains. (f, g) competitive in situ growth model for heteradcumulate at top of crystal pile. Olivine (green) grows slowly from abundant nuclei. Cpx (blue) grows rapidly from sparse nuclei due to supersaturation of the liquid in this phase. Hence large augite grains overtake small olivines to produce poikilitic texture. (For interpretation of the references to colour in this figure legend, the reader is referred to the web version of this article.)

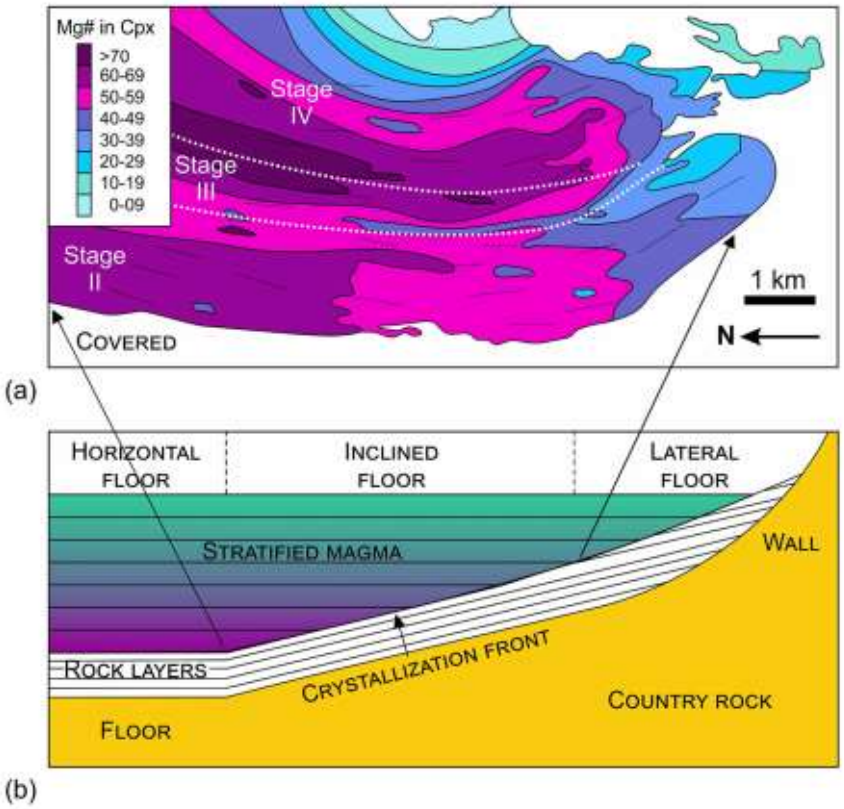

Fig. 43. The formation of systematic discordant relationships between modal and cryptic layering in Fongen-Hyllingen Series as a result of crystallization from compositionally zoned magma along an inclined floor. (a) Contoured compositional variation of Mg-number in Ca-rich pyroxene in the Hyllingen Series. The figure is based on ca. 300 samples from 11 profiles normal to the modal layering. (b) Three modes of crystallization that may occur in a chamber from compositionally zoned magma. Crystallization of a stratified magma along a horizontal floor will result in modal and cryptic layering to be concordant and horizontal. Crystallization along a lateral accretion front will result in modal and cryptic layering to be parallel but discordant to the crystallization front and to the liquid layers. In both above cases, the concordance of modal and cryptic layering in the final solid rocks does not allow to infer their crystallization from a compositionally zoned magma. In contrast, crystallization along an inclined floor will result in modal and cryptic layering to be discordant, a feature that is mappable in the field. Modal layering develops concordant to the sloping floor whereas the cryptic layering develops essentially parallel to the liquid layers. The Fongen-Hyllingen is thought to have followed this third mode of crystallization (a). Modified from Wilson and Larsen (1985).

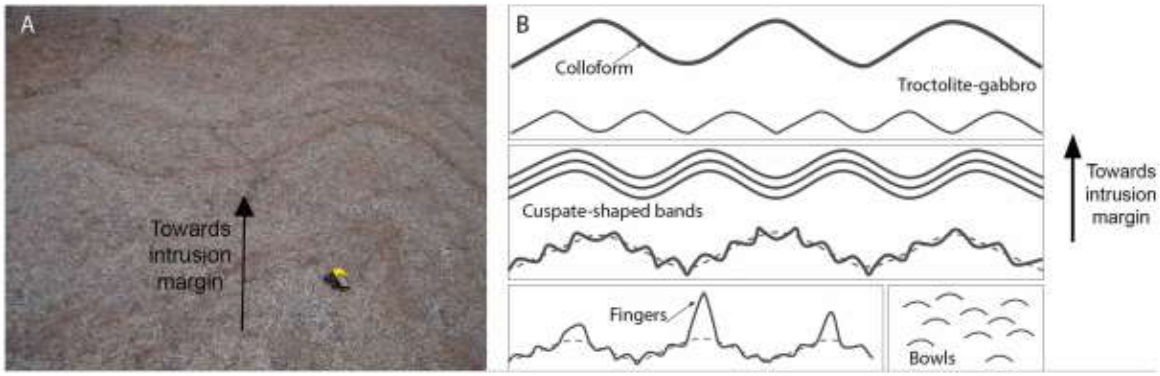

Fig. 44. Colloform banding in the Marginal Border Series of the Skaergaard intrusion. A. Outcrop-scale relationships of colloform bands. Series of closely spaced colloform bands with similar and concordant amplitude and wavelength; Skaergaard Peninsula B. Schematic representation of the morphological evolution of colloform banding with stratigraphic position (i.e., distance from the intrusion margin).

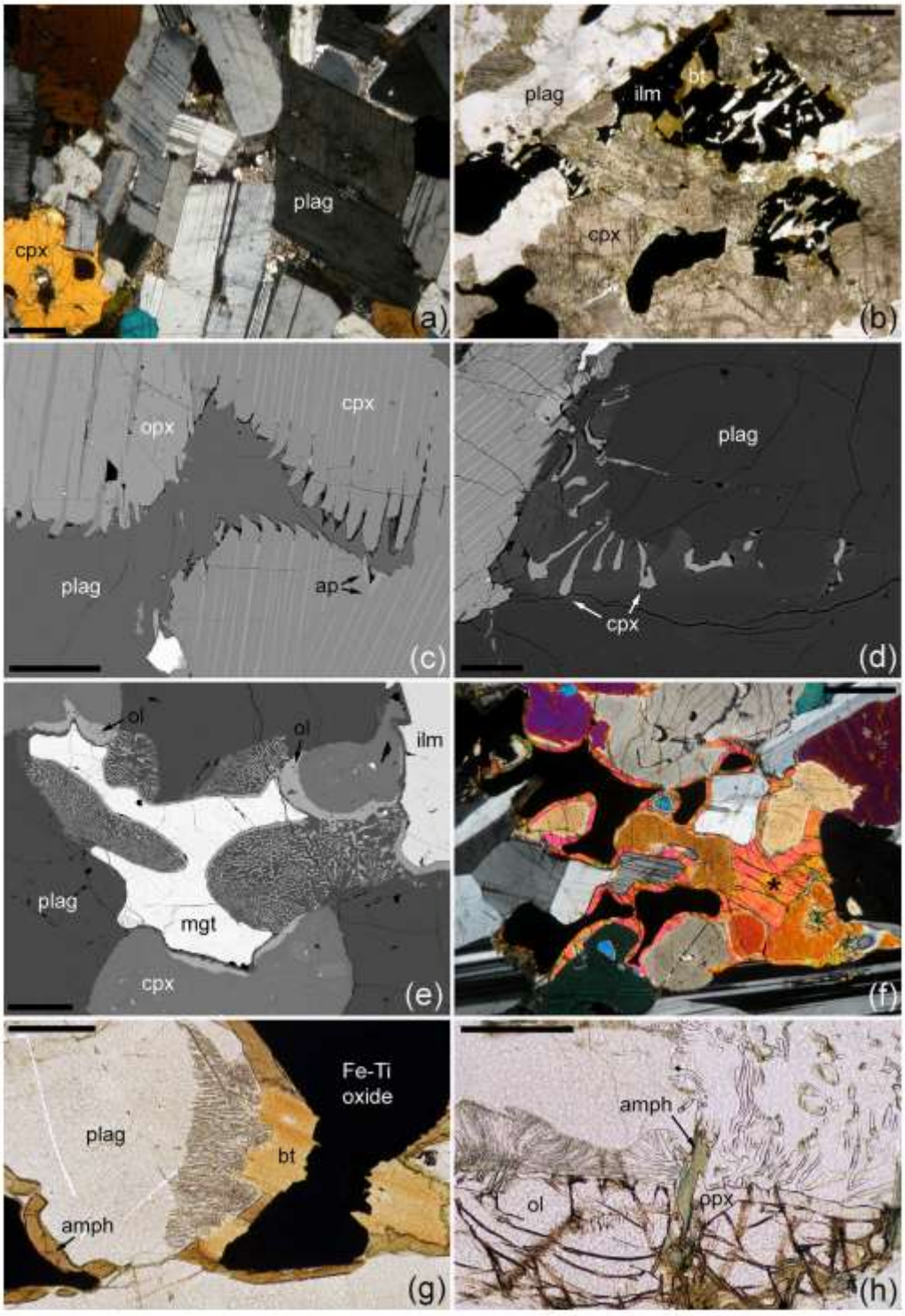

Fig. 45. Images of late-stage microstructures indicative of silicate liquid immiscibility. Abbreviations are plag, plagioclase; cpx, clinopyroxene (augite); opx, orthopyroxene (inverted pigeonite); ilm, ilmenite; mgt, magnetite; bt, biotite; amph, amphibole. (a) Granophyric intergrowths filling planar-sided pockets between plagioclase primocrysts in the upper gabbros of the Skaergaard Layered Series. Crossed polars. Scale bar is 500 mm long. (b) Ilmenite intergrown with plagioclase and biotite, argued to represent the solidified Fe-rich immiscible conjugate in the Skaergaard Layered Series. Plane polarised light. Scale bar is 400 mm long. (c) Back-scattered electron (BSE) image of stepped grain boundaries between pyroxene and plagioclase grains involving growth of augite and dissolution of Ca-poor pyroxene. Skaergaard Layered Series. Scale bar is 100 mm long. (d) BSE image of fish-hook Ca-rich pyroxenes intergrown with An-rich plagioclase extending from a stepped (augite) grain boundary in the Skaergaard Layered Series. Scale bar is 100 mm long. (e) BSE image of replacive symplectites in the Skaergaard Layered Series comprising An-rich plagioclase and olivine surrounding magnetite and ilmenite grains. The development of a poly-crystalline olivine rim where the oxide is adjacent to augite primocrysts should be noted. Scale bar is 200 mm long. (f) Mono-crystalline olivine rims in the Skaergaard Layered Series, extending from a single olivine primocryst (marked with an asterisk), and growing predominantly along oxide-silicate grain boundaries. Crossed polars. Scale bar 300 mm long. (g) A typical Type I symplectite from the Sept Iles intrusion, comprising An-rich plagioclase and orthopyroxene, rooted to a rim of biotite and amphibole surrounding a grain of Fe–Ti oxide. Plane polarised light. Scale bar is 1 mm long. (h) A typical Type II symplectite from the Sept Iles intrusion, comprising An-rich plagioclase, orthopyroxene and minor colourless amphibole, rooted to an orthopyroxene rim surrounding an olivine primocryst. Plane polarised light. Scale bar is 500 mm long.

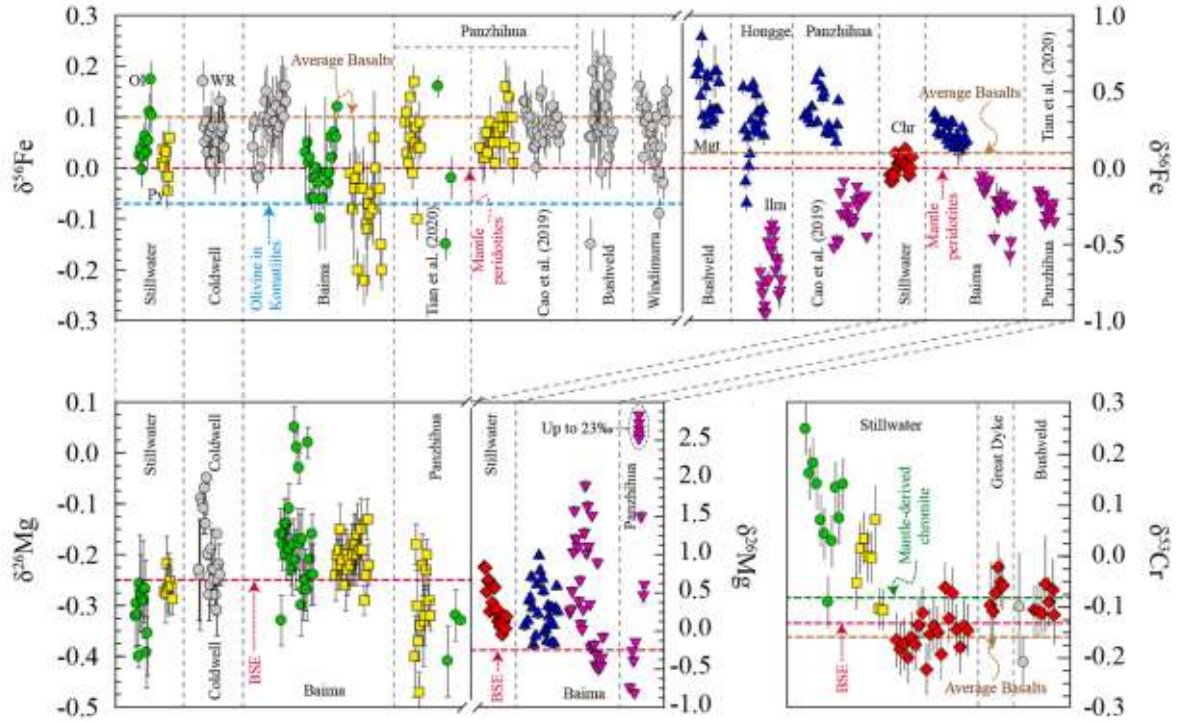

Fig. 46. Iron, magnesium, and chromium isotopic compositions of whole rocks and mineral separates from typical layered intrusions. The average δ^{56}Fe of basalts, mantle peridotite and olivine cumulate in komatiites are from Dauphas et al. (2017). The average bulk silicate earth (BSE) δ^{26}Mg is from Teng et al. (2010). The average δ^{53}Cr in BSE, mantle-derived chromite and basalts are from Schoenberg et al. (2008), Farkaš et al. (2013) and Ping et al. (2022). The Stillwater Complex δ^{56}Fe, δ^{26}Mg and δ^{53}Cr results are from Bai et al. (2019, 2021). The Coldwell Complex δ^{56}Fe and δ^{26}Mg results are from Brzozowski et al. (2022). The Baima Complex δ^{56}Fe and δ^{26}Mg results are from Chen et al. (2014, 2018, 2021). The Panzhihua Complex δ^{56}Fe and δ^{26}Mg results are from Tian et al. (2020) and Cao et al. (2019). The Windimurra and Bushveld Complex δ^{56}Fe results are from Nebel et al. (2020) and Bilenker et al. (2017). The Great Dyke and Bushveld δ^{53}Cr results are from Schoenberg et al. (2008) and Farkaš et al. (2013). Grey circles are whole-rock data and colored circles represent olivine. Squares are for orthopyroxene, and diamonds for chromite. Upwards and downwards triangles represent magnetite and ilmenite, respectively.

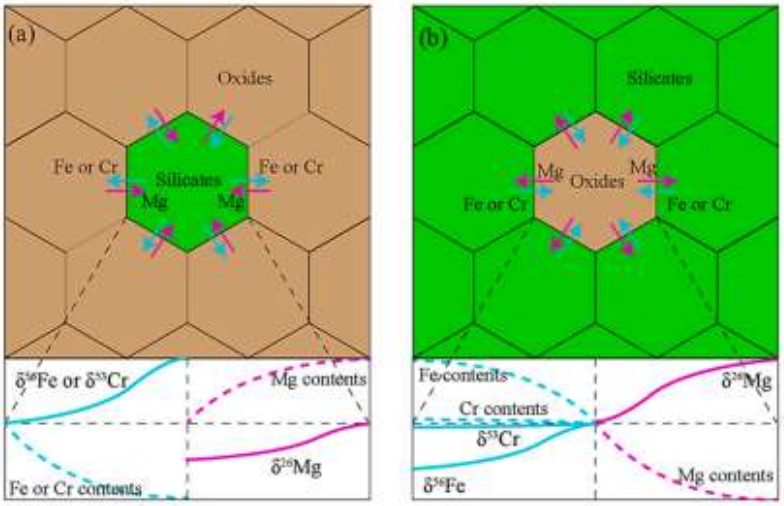

Fig. 47. Schematic illustration of Fe-Mg-Cr elemental and isotopic variations in (a) silicates in an oxide cumulate and (b) oxides in a silicate cumulate. Modelling curves are from Xiao et al. (2016), Chen et al. (2018, 2021) and Bai et al. (2019, 2021). The arrows in minerals indicate the directions of elemental migrations. The compositional effect of inter-mineral diffusion on minerals depends on their elemental contents and relative modal abundances in the rock: Fe—Mg exchange produces obvious changes of δ^{56}Fe and δ^{26}Mg in silicates and oxides, respectively. Similar trends of Cr—Fe contents and δ^{53}Cr-δ^{56}Fe variations for silicates induced by re-equilibration process, however, are unsignificant for oxides with high Fe and Cr concentrations.

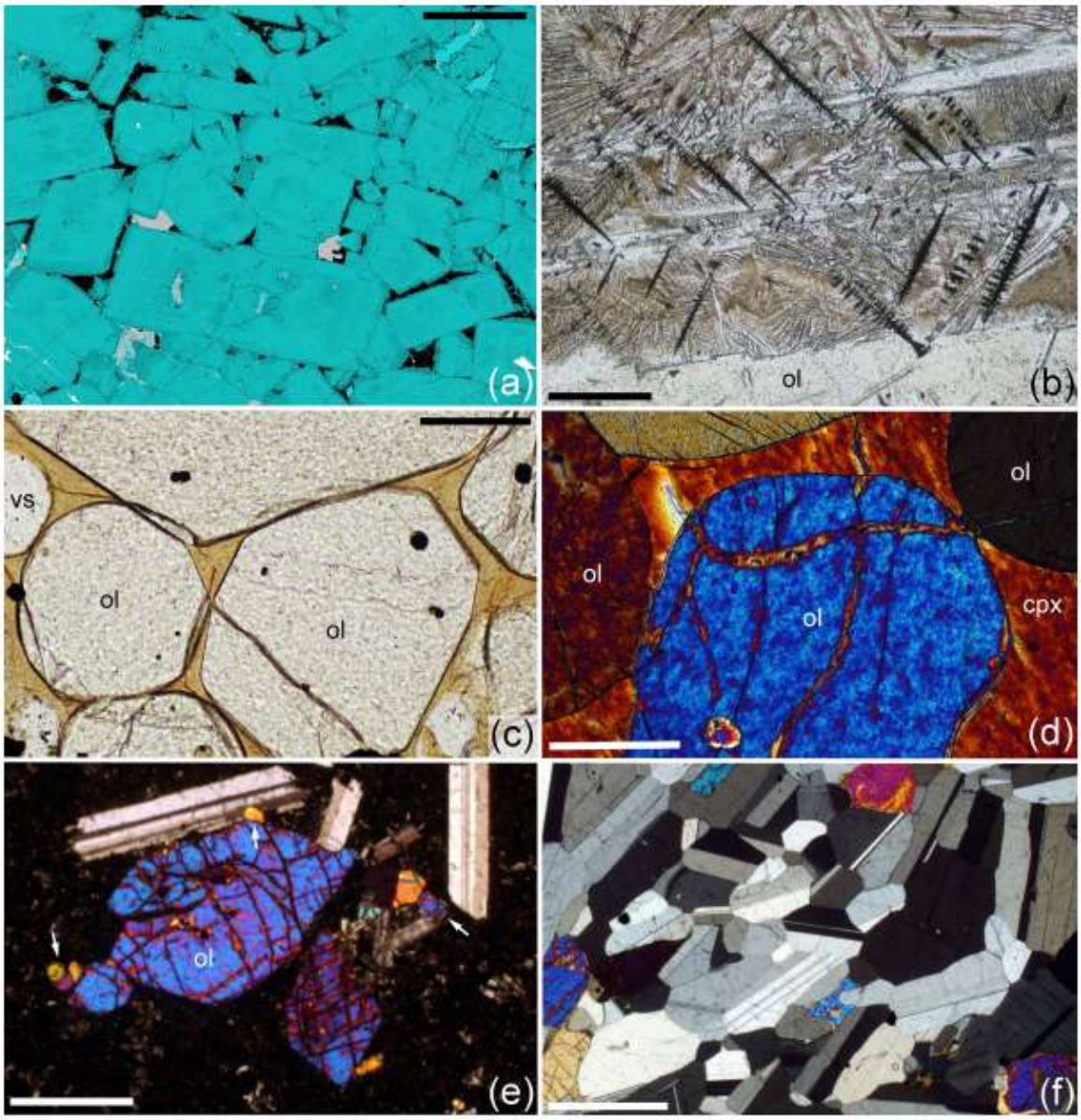

Fig. 48. Micrographs of thin sections. (a) Chemical composition map showing Ca distribution in the leucocratic upper part of a modally graded layer from the trough bands of the Skaergaard Intrusion, East Greenland. Plagioclase is teal (with darker colours showing more sodic compositions), interstitial phases are quartz (black) and clinopyroxene (grey). Note the euhedral shape and randomly oriented grains of the plagioclase, with most grain boundaries formed by the juxtaposition of planar growth faces. The scale bar is 1 mm long. (b) Komatiite flow, Munro Township, Ontario. Serpentinised olivine dendrite branches (ol) are separated by an intergrowth of clinopyroxene (colourless) and chromite (black) dendrites. Note the cubic symmetry of the chromite dendrites: the similar orientation of groups of apparently isolated branches suggests they are connected in 3D and form part of an extensive single grain. Plane polarised light. Scale bar is 100 mm. (c) Olivine-rich glassy enclave from Mauna Loa, Hawaii (the vesicle in the image is labelled vs). The rounded olivine grains, set in a brown glass, display olivine-olivine-glass dihedral angles close to textural equilibrium at pore corners. Plane polarised light. Scale bar is 0.5 mm long. (d) A peridotite cumulate from the Rum Eastern Layered Intrusion, comprising euhedral olivine primocrysts surrounded by interstitial augite (cpx). Note the change in curvature at olivine-olivine-augite three-grain junctions denoting a limited approach to solid-state textural equilibrium following the pseudomorphing of the original texturally equilibrated melt-filled pore (compare with Fig. 48c). Crossed polars. Scale bar is 200 mm long. (e) Cluster of olivine and plagioclase phenocrysts in the margin of a picrite dyke, Skye. The larger olivine grains have well-developed facets, whereas the smaller grains (arrowed) are rounded, suggesting some Ostwald ripening. Crossed polars. Scale bar is 200 μm long. (f) Troctolite from Unit 12 of the Rum Eastern Layered Series. Note the rounded grain boundaries in the plagioclase-rich regions, with significant modification of the original euhedral shape of these primocrysts towards a granular microstructure typical of solid-state textural equilibrium. Crossed polars. Scale bar is 1 mm long. (For interpretation of the references to colour in this figure legend, the reader is referred to the web version of this article.)

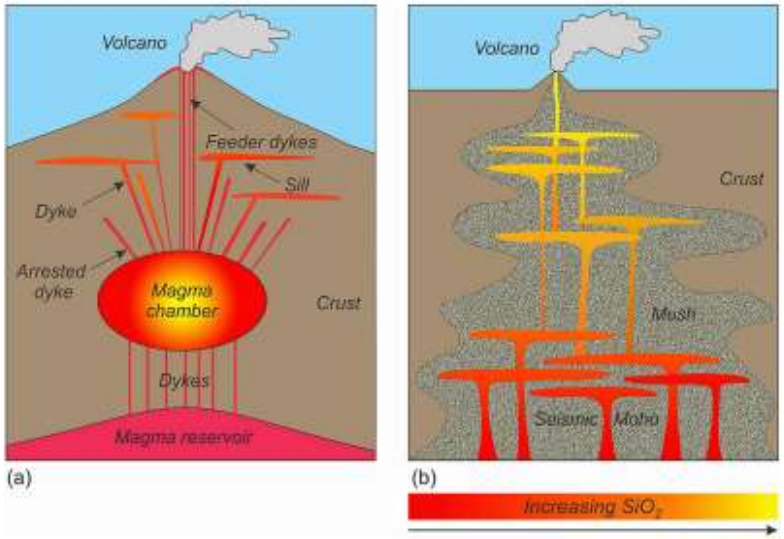

Fig. 49. Two contrasting views on the morphology and architecture of magma chambers in Earth's crust. (a) A magma chamber is a partially or totally molten body located in the crust. It is large, long-lived and liquid-dominated. The magma chamber acts as a sink for magma from a deeper magma accumulation zone (a magma reservoir) and a source for a volcano as well as inclined sheets, sills, and dykes. Modified from Gudmundsson (2012). (b) Transcrustal magmatic system, where melt processing in the deep crust produces melts that are transferred to mid- and finally upper crustal levels. The potential for transient vertical connectivity in this system presents the possibility of successive destabilization of melt lenses. No true magma chambers are supposed to exist in this concept. Modified from Cashman et al. (2017).